UC Santa Barbara

UC Santa Barbara Electronic Theses and Dissertations

Title

Hydrodynamical Study of the Impact of Cosmic Rays on the Stability of Circumgalactic Gas

Permalink

https://escholarship.org/uc/item/8t64b5d3

Author

Tsung, Tsun Hin Navin

Publication Date

2023

Peer reviewed|Thesis/dissertation

eScholarship.org

Powered by the California Digital Library
University of California

UNIVERSITY OF CALIFORNIA, SANTA BARBARA

Hydrodynamical Study of the Impact of Cosmic Rays on the Stability of Circumgalactic Gas

A dissertation submitted in partial satisfaction of the
degree of Doctor of Philosophy in Physics

by

Tsun Hin Navin, Tsung

Committee-in-charge:
Professor Siangpeng Oh, Chair
Professor Lars Bildsten
Professor Timothy Brandt

September 2023

The dissertation of Tsun Hin Navin, Tsung is approved.

Prof. Timothy Brandt

Prof. Lars Bildsten

Committee Chair: Prof. Siangpeng Oh

May 2023

Acknowledgements

I would like to thank my supervisor Prof. Siangpeng Oh, who has supported me throughout my PhD, offering guidance to help me navigate the field and has been very patient with my mistakes. This dissertation would not have been possible without him. I would also like to thank my friends and brothers and sisters at CEFCSB, who have been a great source of emotional support. I am indebted to Choi Kam Kau (Uncle Kam) for his hospitality and care during my stay in Santa Barbara, who provided comfort and a sense of belonging far away from home. I am very grateful to Uncle Shek for his academic advice throughout my life, who has encouraged me to become an explorer of the Universe. There is of course no way to repay the unspeakable love of my parents, Tsung Shun Biu and Shek Wai Tsz Winsy, my wife Chan Mei Ki (Maggie) and the everlasting Father in Heaven.

Curriculum Vitae

☎ *+1 805-886-5920*
✉ *ttsung@ucsb.edu*
LinkedIn:Tsun Hin Navin Tsung
Citizenship: Hong Kong SAR

Education

2017–present **University of California, Santa Barbara**.
Ph.D. Candidate in Physics (Astrophysics Emphasis), Expected July 2023
Thesis title: *Hydrodynamical Study of the Impact of Cosmic Rays on Circumgalactic Gas*
Research interest: Cosmic ray magnetohydrodynamics theory and simulations, galaxy evolution, fluid instability analysis
Advisor: Siangpeng Oh

2013-2017 **University of Oxford, UK**.
Master in Mathematical and Theoretical Physics (MMathPhys)
An undergraduate degree leading to Master qualifications
Part A, B: First Class Honors (Highest classification possible)
Part C: Distinction (Highest classification possible)
Dissertation: Gyrokinetics and the Ion-Temperature-Gradient Instability in a Z-Pinch (Advisor: Prof. Felix Parra Diaz)

Experience

2017–present **Graduate Research Assistant**, *Department of Physics, University of California, Santa Barbara*.
Project leader for 2+ publications, responsible for project management, research idea development, experimental design and operation. Proficient in fluid dynamics theory, simulations and code development. Extensive exposure to analysis and visualization of multi-dimensional data. Experience with parallel and high performance computing.
Supervisor: Dr. Siangpeng Oh

Summer 2016 **Summer Research Intern**, *Department of Physics, University of Oxford*.
Designed and implemented analysis tools for processing images obtained from optical telescopes. Experience with image convolution.
Supervisor: Dr. Martin Bureau

Summer 2015 **Summer Research Intern**, *Department of Physics, the Chinese University of Hong Kong*.
The ODEs governing hydrostatic balance in a self-graviting system is solved using the Runge-Kutta 4-step method.
Supervisor: Dr. Ming Chung Chu

Technical Skills

Programming: Python, C++, Matlab

Tools and Packages: Athena++ (C++ based fluid code), Numpy, Scipy, Matplotlib, Astropy

Version Control: GitHub

Typesetting: LaTeX, Microsoft Office

Publications

2022	**T.H.N.Tsung**, S.P.Oh & Y.F.Jiang, The cosmic ray staircase: outcome of the cosmic ray acoustic instability, *Monthly Notices of the Royal Astronomical Society*, 513, 4464–4493. https://doi.org/10.1093/mnras/stac1123.
2021	**T.H.N.Tsung**, S.P.Oh & Y.F.Jiang, Fluid simulations of cosmic ray modified shocks, *Monthly Notices of the Royal Astronomical Society*, 506, 3282–3300. https://doi.org/10.1093/mnras/stab1926.

Under Review or In Preparation.

Sumbitted	**T.H.N Tsung**, S.P.Oh & C.Bustard, Impact of CR heating on Thermal and Hydrostatic Stability of Galactic Halos, *Submitted to Monthly Notices of the Royal Astronomical Society*.
In Prep	**T.H.N Tsung**, B.Tan & S.P.Oh, Cosmic ray pressure support in turbulent radiative mixing layers.

Awards, Fellowships, and Grants

2017–2018	Regent's Fellowship ($32,000), *UCSB*.
2015–2017	St. Edmund Hall Open Scholarship, *University of Oxford*.
2016	Oxford Physics Practicals Commendation, *University of Oxford*.

Conferences and Invited Talks

Dec 2022	Simulating cosmic rays streaming at the meso-scale, *Faucher-Giguere's group meeting, Northwestern University*.
Dec 2022	Simulating cosmic rays streaming at the meso-scale, *Wisconsin astro seminar, University of of Wisconsin, Madison*.
Dec 2022	Simulating cosmic rays streaming at the meso-scale, *Columbia astro lunch seminar, Columbia University*.
Nov 2022	Simulating cosmic rays streaming at the meso-scale, *Princeton astro lunch seminar, Princeton University*.
Sep 2022	Thermal instability with cosmic ray heating, *What Matter(s) Around Galaxies, Champoluc, Italy*.
Aug 2022	Thermal instability with cosmic ray heating, *6th ICM workshop, Niels Bohr Institute, Copenhagen*.

Aug 2022 Resolved simulations of cosmic rays in the circumgalactic and intracluster medium, *Department of physics seminar, the Chinese University of Hong Kong*.

Jul 2021 The cosmic ray staircase: outcome of the cosmic ray acoustic instability, *Eliot Quataert's Group, Princeton University*.

Jul 2021 The cosmic ray staircase: outcome of the cosmic ray acoustic instability, *Astro Tea, UCSB*.

May 2021 Cosmic ray hydrodynamics, *Geophysical fluid dynamics seminar, UCSC*.

Outreach

Sep–Nov 2020 **School for Scientific Thought**.
Designed a 5-week hands-on course on 'Plasma: the fourth state of matter' for under-privileged high school students in collaboration with UCSB Department of Education.

Referees

Siangpeng Oh.
Professor of Physics
University of California, Santa Barbara
peng@physics.ucsb.edu

Yanfei Jiang.
Associate Research Scientist
Center for Computational Astrophysics, Flatiron Institute
yjiang@flatironinstitute.org

Chad Bustard.
KITP Postdoctoral Fellow
Kavli Institute for Theoretical Physics
bustard@ucsb.edu

Abstract

Hydrodynamical Study of the Impact of Cosmic Rays on the Stability of Circumgalactic Gas

by

Tsun Hin Navin, Tsung

Recently, cosmic rays (CRs) have emerged as a leading candidate for driving galactic winds. Small-scale processes can dramatically affect global wind properties. This thesis investigates how CRs can destabilize hydrodynamical flows in the circumgalactic medium (CGM) and extensively utilizes the newly developed two-moment method to model CR transport by self-confinement (streaming). To ensure the numerical method is robust, a series of tests are conducted to examine the behavior of the code at shocks. This examination led to the discovery of a new class of CR-modified shock solutions which matches with simulation very well. It is then used to study how sound waves are driven unstable by phase-shifted CR forces and CR heating. As the sound waves grow non-linear, they steepen into a quasi-periodic series of propagating shocks; the density jumps at shocks traps CRs by the bottleneck effect, creating staircase like structures in CR pressure profile. The staircase structure redistributes CR heating and forcing to highly localized regions and can enhance the CR pressure push on the CGM gas, driving stronger outflows. It is believed the shocks generated by the CR-driven acoustic instability could have distinct observational signatures, on ∼kpc scales. At last, the CGM is often believed to be unstable to the local thermal instability. Mass dropout from the instability, contrary to other heating or cooling source terms such as radiative cooling, triggers a boost in the CR heating rate and can lead to it dominating the energy budget of CGM gas flow if the magnetic field is sufficiently strong. This loss of thermal equilibrium triggers a loss of hydrostatic equilibrium, driving outflows with properties that vary drastically depending on whether the CR heating timescale is less than the free-fall timescale. If the magnetic field is weak, tangling of the field lines due to local thermal instability can trap CRs, causing a buildup of CR pressure and an uplift and re-circulation of cold gas. These results have implications on the mass and energy loading of winds, and the detection of intermediate velocity clouds at the inner CGM.

Contents

Acknowledgements **iii**

Abstract **vii**

1 Background **1**

2 Fluid Simulations of Cosmic-Ray Modified Shocks **5**

2.1 Introduction 5
2.2 Analytics 12
  2.2.1 Governing Equations 12
  2.2.2 Shock Structure and Solution Method 16
    2.2.2.1 Previous Solution: Uni-directional Streaming 16
    2.2.2.2 New Solution: Bi-directional Streaming 24
  2.2.3 Solution Structure 28
2.3 Simulation 33
  2.3.1 Code 33
  2.3.2 Setup 1: Imposed Shock Profile 34
  2.3.3 Setup 2: Free Flow 39
    2.3.3.1 Uniform Background 42
    2.3.3.2 Gradient Background 43
  2.3.4 Setup 3: 1D Blast Wave 45
  2.3.5 Further Considerations 49
    2.3.5.1 Long Equilibration Times 50
    2.3.5.2 Numerical Resolution 52
    2.3.5.3 Oblique Magnetic Fields 55
    2.3.5.4 Injection of Thermal Particles 57
2.4 Discussion and Conclusion 60

3 The Cosmic-Ray Staircase: the Outcome of the Cosmic Ray Acoustic Instability **65**

3.1 Introduction 66

3.2 Analytic Considerations . . . 69
  3.2.1 CR Acoustic Instability: Linear Theory . . . 72
    3.2.1.1 Diffusion dominated . . . 75
    3.2.1.2 Streaming dominated . . . 78
  3.2.2 CR Bottleneck Effect . . . 83
3.3 Simulation . . . 94
  3.3.1 Setup . . . 94
    3.3.1.1 Initial Profiles . . . 95
    3.3.1.2 Static and Outflow Setup and Boundary Conditions . . . 101
  3.3.2 Acoustic Instability: Comparison with Linear Theory . . . 103
  3.3.3 Acoustic Instability: Non-Linear Outcome . . . 107
    3.3.3.1 General observation of the nonlinear behavior . . . 107
    3.3.3.2 Zoom-in of staircase jumps . . . 110
    3.3.3.3 Staircase Finder . . . 113
    3.3.3.4 Quasi-Static State of the Staircase . . . 116
    3.3.3.5 Bottleneck Effect with a Moving Staircase . . . 119
    3.3.3.6 Jump Widths, Heights and Plateau Widths . . . 122
    3.3.3.7 Dynamical Effect and Averaged Properties . . . 127
3.4 Discussion and Conclusions . . . 136
  3.4.1 Brief Summary . . . 136
  3.4.2 Physical Significance . . . 137
  3.4.3 Applications . . . 138
  3.4.4 Looking Forward . . . 146

4 The Impact of Cosmic Rays on Thermal and Hydrostatic Stability in Galactic Halos 148
4.1 Introduction . . . 149
4.2 Methods . . . 154
  4.2.1 Governing equations . . . 154
  4.2.2 Simulation Setup . . . 158
    4.2.2.1 Initial Profiles . . . 158
    4.2.2.2 Source Terms . . . 162
    4.2.2.3 Simulation Box and Boundary Conditions . . . 164
    4.2.2.4 Resolution, Reduced Speed of Light and Temperature Floors . . . 165
    4.2.2.5 Simulation Runs . . . 165
4.3 Linear Evolution: Thermal Instability . . . 167
  4.3.1 Previous Work; Analytic Expectations . . . 167
  4.3.2 Propagation of modes . . . 173
  4.3.3 Does propagation suppress thermal instability? . . . 177
4.4 Nonlinear Outcomes: Winds and fountain flows . . . 182

4.4.1 Overview of simulation outcomes . . . 186
4.4.2 Energetics and dynamics of the nonlinear steady-state . . . 191
4.4.3 Effect of CR heating . . . 197
4.4.4 Transition to fountain flows . . . 205
4.4.5 Understanding Mass Outflow Rates; 1D Models . . . 207
4.5 Discussion . . . 214
4.5.1 Translating from Code to Physical Units . . . 214
4.5.2 Comparisons against larger scale simulations . . . 219
4.6 Conclusions . . . 221

A Appendix for chapter 3 **227**
A.1 Linear Growth Rates in 1D including Background Gradient . . . 227
A.1.1 Adiabatic EOS for Finite Diffusion Coefficient . . . 227
A.1.2 Adiabatic EOS with a Small Diffusion Coefficient . . . 233
A.1.3 Isothermal EOS with Finite Diffusion Coefficient . . . 235
A.2 Resolution and Reduced Speed of Light Study . . . 235

B Appendix for chapter 4 **242**
B.1 1D Linearized Equations in Uniform Medium . . . 242
B.2 Hydrostatic Boundary Conditions for Eulerian Grid Codes . . . 245
B.3 Simulations fixing the base CR flux instead of pressure . . . 249
B.4 Resolution and 3D . . . 251

Bibliography **256**

Chapter 1

Background

Galaxies are fundamental constituents of the Universe, and a big problem in astronomy is to explain how they form, evolve, and have the observed structure, shape, and composition. Inferring from their luminosity, galaxies appear ellipsoidal or spiral-disk in shape, with sizes spanning a few kpc along the long axis, and a couple hundred pc in thickness. While galaxies appear to contain most of the matter that is gravitationally bounded within the dark matter (DM) halo, this is in fact far from the truth. In reality, observations tell us there is a gigantic halo of rarefied gas around each galaxy, called the 'circumgalactic medium' (CGM), where most of the baryons reside [170]. The CGM was previously unobservable because it is filled with low density gas ($\lesssim 10^{-2}$ cm^{-3}), so it is weak in emissivity. The way observers now study it is through absorption of background quasar spectrum, which one can then infer the CGM gas kinematics and thermodynamics. It was found that the CGM can extend up to $\sim$

300 kpc above a galaxy, and exhibits signs of outflow of order $100-1000$ km s^{-1}. This outflow impacts the intergalactic medium (IGM), where it decelerates and enriches it with metals. At the same time, the CGM gas also exhibits signs of inflow, e.g. through cold streams and infalling clouds, supplying the galaxy with fresh, pristine gas from the IGM. The outflow and inflow of gas combine to form a feedback cycle coupling each galaxy with its surroundings CGM, exchanging mass, momentum and energy. The presence of an outflow can also be deduced by necessity: if there were no outflow to regulate the gas content within galaxies, the amount of CGM gas that would collapse under gravity would trigger a much higher star formation rates than observed.

The source of these outflows could be due to mechanical feedback from supernovae (SNe) [57], radiation pressure from the stars [122], and active-galactic-nuclei (AGN) jets [177]. The way they power an outflow are different and currently under debate, but they all involve, to some degree, direct pushing and heating of the thermal gas in the ISM and CGM. It is very hard to discern one from another from observations. It is unlikely the outflows are entirely powered by just one kind of source; their effects are likely to be cumulative. While these outflow theories apply very well to galaxies with high star formation activities, in more quiescent galaxies such as the Milky Way (MW), some other sources need to be invoked. Moreover, these thermally driven outflows suffer radiative losses, and the ability to sustain a wind decreases as one moves further from the sources, making it hard to explain how there could be enough energy too power gas circulation up to a few hundred kpc from galaxies of typical size of only a few kpc.

Recently, there has been a surge of interest in cosmic rays (CRs) driven outflows. CRs are charged particles moving at relativistic speeds with cosmic origins. In the presence of magnetic turbulence, they could exhibit collective, fluid behaviors just like thermal gas, exerting pressure on the fluid flow and exchange energy. Unlike thermal gas, the relativistic nature of CRs makes them less susceptible to radiative losses, together with their lower adiabatic index makes them good carriers of momentum and energy far away from their sources, and is thought to be a viable source for driving extensive outflows.

Just how viable CRs are in driving outflows depends heavily on their content in the ISM and CGM and their transport mechanism, both of which are poorly constrained and understood. One could imagine it is hard for CRs to drive an outflow if they are subdominant in energy content and highly confined. From observations of the MW, it was found that CRs, at least in the ISM, could have an energy density of 1 eV cm^{-3}, comparable to the energy density of other components in the ISM gas. Although hard to observe, galactic scale simulations have suggested the CGM could even be CR dominated [89]. Regarding their transport, popular theories suggest CRs could be streaming [106] and/or diffusing. Clearly, the correct CR transport depends heavily on the plasma microphysics between CRs and the thermal gas, for which there are up to date, very few kinetic scale numerical studies on due to numerical difficulties [69, 150]. Nevertheless, existing CR transport theories have already presented very rich physics to develop wind models with, and one can speculate what CRs could do to outflows. Multiple galaxy scale studies [17, 89, 140] have suggested they could massively alter wind structures and power strong outflows, but the result is heavily dependent on the CR transport.

Given the numerical difficulties in simulating kinetic scale CR plasma physics and the variable results of large scale simulations, this dissertation focuses on the intermediate scale, much longer than the mean free path of the CRs so that they can be treated as a fluid, but small enough so that small scale fluid behaviors and be resolved. By allowing CRs to adopt a range of transport models, the potential effects of small scale fluid physics, previously unresolved, on the large scale flows are explored. In chapter 2 I set the stage by verifying that the newly developed simulation tool to model CR fluid dynamics is robust, then in chapter 3 I proceed to study the nonlinear ramification of a CR driven acoustic instability, which gives rise to a curious staircase structure in the CR pressure profile. In chapter 4 I explore the effect of CRs on thermal instability, noticing in the nonlinear regime the fluid flow could bifurcate into winds with vastly different properties depending on the CR transport and fluid parameters.

Chapter 2

Fluid Simulations of Cosmic-Ray Modified Shocks

The research constituting this chapter was conducted in collaboration with Dr. Yan-fei Jiang. This chapter has been reformatted and published in the Monthly Notices of the Royal Astronomical Society for which I am the lead author. In the following, I use 'we' to indicate my supervisor Prof. Siangpeng Oh, Dr. Yan-fei Jiang and myself.

2.1 Introduction

Cosmic rays (CR) are close to energy equipartition with thermal gas in the local ISM, and have been observed in many astrophysical scenarios. They are now thought to be dynamically important to galaxy evolution, both in providing non-thermal support to the CGM gas and in driving a wind that initiates a feedback cycle (e.g., see [191] for a recent review), which has become the focus of intense study by numerous groups in recent years. It has even been suggested that the circumgalactic medium is CR dominated [88]. CRs are believed to be accelerated at shocks to high energies through DSA (Diffusive Shock Acceleration). Test particle theories developed in the 1970s [2, 7, 10, 104] were instrumental in explaining the observed power law in CR energy. It was later realized that CR coupling to the background thermal gas through plasma instabilities can affect the acceleration efficiency by generating a shock precursor where upstream thermal particles can be decelerated, compressed and scattered, thus facilitating further acceleration [43]. The two-fluid model and Monte-Carlo simulation were two common methods utilized to study this nonlinear behavior. These variant models all point to the same conclusion, that the non-linear modification of the shock by CRs is substantial.

Magnetic field amplification due to compression, baroclinic vorticity and plasma instabilities can be dynamically important too, and has been seen in X-ray observations [3, 121]. With the growth of computational power it became possible to perform PIC/hybrid simulations which capture the most important microphysics of CR shock acceleration, including various kinetic instabilities and their non-linear evolution into turbulence (e.g., Caprioli and Spitkovsky 25). These simulations continue to show that shock acceleration is very efficient.

In this paper, we study CR modified shocks in the two fluid approximation ubiquitously used in galaxy formation simulations of CR feedback. CRs couple with the background gas through the streaming instability [106]. In this instability, CR bulk drifting at velocity greater than the local Alfven wave speed ($v_D > v_A$) excites magnetic waves which gyro-resonantly scatter the CR, effectively locking the drift motion of the CR to the local wave frame ($(v_D - v_A)/v_A \ll 1$), causing it to 'stream' along the magnetic field at the Alfven speed down the CR pressure gradient, i.e.,

$$\mathbf{v}_s = -\mathbf{v}_A \frac{\mathbf{B} \cdot \nabla P_c}{|\mathbf{B} \cdot \nabla P_c|}. \tag{2.1}$$

This collective streaming causes energy transfer from CR to the gas at the volumetric rate of $\mathbf{v}_s \cdot \nabla P_c$. In steady state, wave growth is balanced by various damping mechanisms (e.g., see Wiener et al. 181). The finite scattering rate of CRs means that they are not perfectly locked to the Alfven frame; slippage with respect to the Alfven frame is expressed in terms of an anisotropic diffusive flux $\bar{\kappa} \nabla P_c$, where $\bar{\kappa}$ is dependent on the CR energy spectrum, the various plasma parameters and the damping mechanisms at play. We forgo these complications and assume the diffusion coefficient is constant in time and space though our work can be extended to account for a more detailed treatment of diffusion.

The two fluid treatment was historically the first method used to study CR modified shocks. However, it has several shortcomings. Since momentum information is integrated out, CR pressure and energy (which are moments of the full distribution function) have to be related by an equation of state, with adiabatic index $\gamma_{\rm c} = 1 + P_{\rm c}/E_{\rm c}$ which is usually assumed to be constant, $\gamma_{\rm c} = 4/3$. In reality, $\gamma_{\rm c}$ depends on the detailed shape of the distribution function and evolves continuously from 5/3 to 4/3 as particles are accelerated. Shock structure, compressibility and acceleration efficiency are all sensitive to assumptions about the adiabatic index [1, 46]. Similarly, the diffusion coefficient $\bar{\kappa}$ is averaged over the CR spectrum. Furthermore, it is not self-consistently calculated[1]. In general it should evolve with the time-dependent distribution function. In particular, since generically $\kappa(p)$ rises with energy, this can lead to a CR flux dominated by the highest-energy particles; in this case a steady state shock structure no longer exists. In this paper, we simply assume a constant, time-steady $\bar{\kappa}$ (and hereafter drop the overbar). Finally, the standard CR hydrodynamic equations ignore microscopic physics such as thermal injection and MHD wave growth which PIC and hybrid simulations take into account[2].

Given these serious shortcomings, it may seem a step backwards to simulate CR modified shocks using the two-fluid approach. Certainly, if our main interest is understanding CR acceleration at shocks, then PIC and hybrid simulations are unquestionably the tools of choice. However, there are still compelling reasons for two-fluid CR shock simulations:

---

[1] The calculation of the diffusion coefficient itself requires calculating wave growth by the resonant streaming instability [106], the current-driven non-resonant Bell instability [8], as well as associated damping mechanisms. Our current study essentially assumes that waves are strongly damped, although kinetic simulations show that waves can be amplified to the non-linear regime [26], which facilitates CR scattering.

[2] They can potentially be modified to include such physics; we implement a very simplified prescription for thermal injection (§2.3.5.4), and one can also analytically model wave growth [27, 28]

Code testing. In recent years, as interest in the role of CRs in galaxy formation has rapidly grown, many new codes for simulating CR transport in the two fluid approximation have been developed (CR streaming with regularization [152]; ENZO [145]; AREPO [127]; GIZMO [29]; GADGET-2 [126]; RAMSES [12, 44]; FLASH [188] among others). These must be subjected to a battery of tests to ensure they are correctly solving the CR transport equations. Perhaps the most demanding test for such codes are CR shocks; this is also one of the few regimes where analytic solutions exists. However, to date codes have only been compared against analytic solutions in the purely advective regime, with both CR streaming and diffusion turned off. Even in this restricted regime, numerical methods do not appear to be robust. When the post-shock CR pressure is a small fraction of the gas pressure, simulations appear to agree with existing analytic solutions [126]. However, once this is no longer true, outcomes are non-unique and dependent on numerical method such as discretization, time-steppping, spatial reconstruction, and CFL number [63, 105]. This was attributed to the fact that the equations can no longer be written in conservative form, due to the presence of a source term involving spatial derivatives. It was therefore suggested that additional assumptions are required at CR shocks to achieve closure, such as constant CR entropy across the shock [105], or a priori prescription of the post-shock CR pressure [63]. We shall clarify this situation by showing that such potentially unphysical assumptions are unnecessary in the full problem where CR transport (diffusion and streaming) is considered.

Even more pressing is the need to compare codes with CR streaming to analytic solutions. In the past, simulations with CR streaming have been afflicted by severe grid-scale instabilities due to the requirement that CRs can only stream down their gradient [152]. The only known cure, adding artificial diffusion, led to severe time-step requirements ($\Delta t \propto (\Delta x)^2$ as well as dependence on the adopted smoothing parameter)[3]. Thus, simulations with CR streaming (and particularly CR shocks with streaming) were infeasible. These problems were resolved with a new two moment method for CR transport [92], which has no arbitrary smoothing and only linear time-step scaling with resolution ($\Delta t \propto \Delta x$); since then similar formulations (albeit with some important differences) have been proposed [29, 165] and employed in galaxy formation simulations. For instance, Thomas and Pfrommer [165] claim that expansion to $\mathcal{O}(v_{\rm A}^2/c^2)$ is necessary, but did not present a specific scenario demonstrating this claim. No codes to date have been compared against existing analytic solutions with streaming [176]. We shall show that these old analytic solutions are in fact incomplete, and develop a new set of solutions. The Jiang and Oh [92] method matches the new analytic solutions we develop.

CR shocks in galaxy formation simulations. Another compelling motivation to understand CR shocks in the two fluid approximation is that at present it is the only one used in galaxy formation simulations; no other method has been shown to be feasible.

---

[3] It is possible to include streaming by modeling it as as diffusion coefficient using a time-implicit scheme [45].

Shocks are also omni-present in such simulations, and it is important to understand the mutual interaction and impact of CRs on shocks and vice-versa, particularly in the presence of CR streaming. For instance, it is usually prescribed in cosmological simulations that $f_{\rm CR} \sim 10\%$ of supernova energy is injected into CR (via a subgrid recipe) and that most of the CRs in the simulation comes from this source. However, in a two fluid code, shocks will enhance CR energy density. Thus, shocks generated by e.g. SNe blast waves, galactic wind termination shocks (e.g., Bustard et al. 21), and structure formation shocks may produce CRs in excess of that from sub-grid injection recipes, and also alter the spatial distribution of CRs. It is important to understand this effect and its dependence on numerical resolution. The simulation results must also be checked to ensure they make physical sense (for instance, that CR acceleration efficiencies are not wildly discrepant with PIC simulations), given the approximations inherent in the two fluid method. It is also important to understand how CRs affect shock jump conditions (e.g., compression ratios, which is *increased* in the presence of CRs), and whether the simulations are handling this correctly. Only by doing so can we assess whether the astrophysical impact of shocks is correctly handled, and the robustness of observational predictions which depend on conditions at the shock (e.g., radio relics; Botteon et al. 14).

The outline of this paper is as follows. In §2.2, we develop analytic solutions for CR modified shocks, and in particular a new solution which takes bi-directional streaming into account. In §2.3, we show simulation results and compare them to the analytic solution. This is followed by a study on the equilibration time, resolution dependence, effect of oblique magnetic fields and injection. We conclude in §2.4.

2.2 Analytics

2.2.1 Governing Equations

Our analytic study follows the treatment by Voelk et al. [176], hereafter VDM84, of CR shocks with streaming, but with some important modifications. We consider 1D adiabatic, non-relativistic, steady-state shocks in the two-fluid approximation. As noted in the Introduction, we do not assume any injection of CRs from the thermal pool; we simply assume a non-zero upstream CR pressure. With a shock finding algorithm, it is possible to include prescriptions for thermal injection (e.g., Pfrommer et al. 127), but we eschew this for the sake of simplicity. At high Mach numbers ($\mathcal{M} > 5$), it has been suggested that the acceleration efficiency is independent of injection, maintaining at or above 50% [1, 47, 48, 50, 99]. We also ignore magnetic field amplification and subsequent back-reaction on the shock, which can alter compressibility and hence CR acceleration efficiency [27, 28]. This is standard in the two fluid formalism.

The time-dependent equations two fluid equations we solve in our 1D numerical simulations are [92]:

$$
\begin{aligned}
&\frac{\partial \rho}{\partial t} + \boldsymbol{\nabla} \cdot (\rho \mathbf{v}) = 0 \\
&\frac{\partial \mathbf{v}}{\partial t} + \mathbf{v} \cdot \nabla \mathbf{v} = -\frac{1}{\rho}\nabla P_g + \frac{1}{\rho}\sigma_c \cdot [\mathbf{F}_c - \mathbf{v}(E_c + P_c)] \\
&\frac{\partial P_g}{\partial t} + \mathbf{v} \cdot \nabla P_g + \gamma_g P_g \boldsymbol{\nabla} \cdot \mathbf{v} = (\gamma_g - 1)\mathbf{v}_s \cdot \sigma_c \cdot [\mathbf{F}_c - \mathbf{v}(E_c + P_c)] \\
&\frac{\partial P_c}{\partial t} + (\gamma_c - 1)\boldsymbol{\nabla} \cdot \mathbf{F}_c = -(\gamma_c - 1)(\mathbf{v} + \mathbf{v}_s) \cdot \sigma_c \cdot [\mathbf{F}_c - \mathbf{v}(E_c + P_c)] \\
&\frac{1}{c^2}\frac{\partial \mathbf{F}_c}{\partial t} + \nabla P_c = -\sigma_c \cdot [\mathbf{F}_c - \mathbf{v}(E_c + P_c)]
\end{aligned} \tag{2.2}
$$

where subscripts g and c denotes the gas and CR respectively; F_c denotes the CR flux. The interaction coefficient tensor is:

$$
\sigma_c^{-1} = \sigma_c'^{-1} + \frac{(E_c + P_c)}{|\mathbf{B} \cdot \nabla P_c|}\mathbf{B}\mathbf{v}_A \tag{2.3}
$$

where $\sigma_c' = (\gamma_c - 1)/\kappa$, and κ is the customary CR diffusion coefficient. There are 5 time-dependent PDEs for the 5 variables ρ, v, P_g, P_c, F_c. Note the presence of source terms in the equations, indicating momentum and energy exchance between the gas and CRs. Total momentum and energy are conserved, since the source terms for gas and CRs are equal and opposite. The last equation in 2.2 is an improvement from the one-moment description [152], taking into account free streaming of cosmic rays when gas and CRs are weakly coupled. The addition of the time-dependent term $\partial \mathbf{F}_c/\partial t\ /c^2$ suppresses a numerical instability associated with the one-moment method. Details for this equation can be found in [92] and references therein.[4]

In our 1D formulation, the B-field is parallel to the shock propagation direction and magnetic pressure/tension is ignored. In steady state, conservation of mass, momentum and energy gives:

$$\rho v = \text{const}, \tag{2.4}$$

$$\rho v^2 + P_g + P_c = \text{const}, \tag{2.5}$$

$$\rho v \left(\frac{1}{2} v^2 + \frac{\gamma_g}{\gamma_g - 1} \frac{P_g}{\rho} \right) + F_c = \text{const}, \tag{2.6}$$

where all quantities are measured in the shock frame. This is supplemented by the steady-state CR energy equation:

$$\frac{\mathrm{d}F_c}{\mathrm{d}x} = (v + v_s) \frac{\mathrm{d}P_c}{\mathrm{d}x}, \tag{2.7}$$

where the steady state CR flux is:

$$F_c = \frac{\gamma_c}{\gamma_c - 1}(v + v_s) P_c - \frac{\kappa}{\gamma_c - 1} \frac{\mathrm{d}P_c}{\mathrm{d}x} \tag{2.8}$$

Equation 2.7 captures energy transferred from CRs to the gas, either by mechanical work done ($v \cdot \nabla P_c$), or heating ($v_s \cdot \nabla P_c$). Transport by streaming and diffusion are captured respectively by the first and second terms on the RHS of eqn.2.8. VDM84 assumed that CRs only stream towards the upstream. However, this assumption is unclear downstream given equation 2.1; CRs can only stream down their gradient. We therefore restrain from presupposing a CR streaming direction. The direction will become clear as we go along. In the following, we take $\gamma_g = 5/3, \gamma_c = 4/3$ to be the adiabatic indices of the gas and CR. 'Upstream' means the fluid state at $x = -\infty$, 'downstream' means the post-subshock fluid state if there is a subshock or $x = +\infty$ if there is not.

---

[4] A recent derivation starting from the CR Fokker-Planck equation [156] can be found in Hopkins et al. [77]. Our equations correspond to the isotropic limit of their results.

The non-conservative form of the CR subsystem leads to the presence of derivatives in equation 2.7 and 2.8. This implies that we cannot simply use conservation laws to determine jump conditions, but must solve for the detailed structure of the front. In particular, we must solve ODEs. For this to be possible, the CR variables P_c, F_c (unlike the gas variables) must be continuous across the front. Physically, the smoothness of P_c, F_c across the shock is guaranteed by the large mean free path of CRs, $\lambda \sim r_{\rm c}/(\delta B/B)^2 \gg \lambda_i$, where r_g is the CR gyroradius and λ_i is the ion mean free path; the (much smaller) thermal ion mean free path sets the characteristic thickness of any gas shock discontinuity. Mathematically, the smooth solutions are guaranteed by the diffusion term in the above equations; we just need to resolve the diffusion length $l_{\rm D} \sim \kappa/c_{\rm s}$. Note that if $P_{\rm c}$ were discontinuous, similar to P_g, then equation 2.8 would imply an infinite CR flux F_c.

2.2.2 Shock Structure and Solution Method

2.2.2.1 Previous Solution: Uni-directional Streaming

Before solving the above equations, we describe the overall features of the shock. CR acceleration implies that P_c is higher in downstream gas. However, downstream CRs can diffuse upstream and affect the flow. The CR precursor significantly affects fluid flow and decelerates incoming gas, from being supersonic with respect to the overall acoustic speed of the plasma (which includes both gas and CR contributions to gas pressure; $c_{\rm s,tot}^2 \approx {\rm d}(p_g + p_c)/{\rm d}\rho$) to subsonic with respect to $c_{\rm s,tot}$. There are two possibilities: (i) in a CR dominated shock, the postshock CR pressure absorbs a significant fraction of the incoming ram pressure. In this case, the 'shock' simply consists of a smooth deceleration and compression; all fluid variables are continuous. After the compression, the flow is still supersonic with respect to the gas sound speed. (ii) The gas must absorb a significant fraction of incoming ram pressure, an amount which is inconsistent with just adiabatic compression. This implies a discontinuous gas subshock *in the gas variables only*, and a jump in gas entropy. The subshock renders the flow subsonic with respect to the gas sound speed. The effect of CR streaming is transfer energy from CRs to the gas in the precursor, preheating the gas and thus increase the importance of gas decelerating the flow, thus increasing the strength of the subshock.

The smooth precursor. The gas is adiabatically compressed. The gas velocity decreases from mass conservation while the gas and CR pressures increase. For a shock propagating in the $-x$ direction, $\nabla P_c > 0$ in the precursor and CR streams towards the upstream ($v_s = -v_A$). The net motion of CR is still towards the downstream as the gas advects faster than v_A ($\mathcal{M}_A \gg 1$). In this region, one can safely take derivatives of the fluid variables, and as shown by VDM84, integrate eqn.2.4 to 2.8 to yield the 'wave adiabat'

$$\left\{1+\frac{\mathcal{M}_A}{\gamma_g-1}\right\}^{2\gamma_g}\left\{P_g+\frac{(\gamma_g-1)B^2(2\gamma_g\mathcal{M}_A+1-\gamma_g)}{\gamma_g(2\gamma_g+1)}\right\} = \text{const}, \tag{2.9}$$

where $\mathcal{M}_A \equiv v/v_A$ is the Alfvenic Mach number. The 'wave adiabat' is an additional conserved quantity which relates gas pressure to density. It reduces to the gas entropy $P_g\rho^{-\gamma_g}$ for $\beta \gg \mathcal{M}_A \gg 1$ – i.e., when $v_{\rm A} \cdot \nabla P_{\rm c}$ is small and there is little energy exchange between CRs and gas, the gas compresses adiabatically. On the other hand, in the limit $\mathcal{M}_A \gg \beta \sim 1$, eqn.2.9 reduces to $\rho = \text{const}$: the gas is incompressible at strong and magnetically significant shocks, due to intense CR heating of the thermal plasma.

Since we have 4 conserved quantities for 5 variables, only a first order differential equation governing the shock precursor is required to close the system. The precursor equation, expressed in terms of the inverse compression ratio $y = \rho_1/\rho$ (subscript 1 denoting upstream), is [176]:

$$\frac{\mathrm{d}y}{\mathrm{d}x} = \frac{(1-y)N(y)}{(\kappa/v_1)D(y)}, \tag{2.10}$$

where $N(y)$ and $D(y)$ are given by eqn.24 and 25 in VDM84; we list them here for completeness:

$$\begin{aligned}N(y) = &\frac{(\gamma_c+1)}{2}\left(y - \frac{\gamma_c - 1}{\gamma_c + 1}\right)\\ &-\frac{\gamma_c}{\gamma_g \mathcal{M}_{s1}^2}\left\{1+\delta - \frac{\gamma_g - \gamma_c}{\gamma_c(\gamma_g - 1)}\frac{1-\bar{P}y}{1-y}\right\}\\ &-\frac{\gamma_c}{\mathcal{M}_{A1}}\left\{y^{1/2} - \frac{1}{\gamma_c \mathcal{M}_{c1}^2 (1+y^{1/2})} + \frac{y^{1/2}\big(1-\bar{P}\big)}{\gamma_g \mathcal{M}_{s1}^2 (1-y)}\right\},\end{aligned} \tag{2.11}$$

$$D(y) = \left(\frac{\bar{P}(y)}{y\mathcal{M}_{s1}^2} - 1\right) \Big/ \left(1 + \frac{(y-1)}{\mathcal{M}_{A1} y^{1/2}}\right) \tag{2.12}$$

where $\delta = P_{c1}/P_{g1}$, $\mathcal{M}_{s1} = v_1/c_{s1}$, $c_{s1}^2 = \gamma_g P_{g1}/\rho_1$, $\mathcal{M}_{c1} = v_1/c_{c1}$, $c_c^2 = \gamma_c P_{c1}/\rho_1$ and $\bar{P} = P_g/P_{g1}$.

The subshock. The subshock is characterized by a set of jump conditions. CR diffusion ensures that only the gas variables jump discontinuously while the CR pressure and flux must be continuous. The jump conditions are therefore:

$$[\rho v] = 0 \tag{2.13}$$

$$\left[\rho v^2 + P_g\right] = 0 \tag{2.14}$$

$$\left[\rho v\left(\frac{1}{2}v^2 + \frac{\gamma_g}{\gamma_g - 1}\frac{P_g}{\rho}\right)\right] = 0 \tag{2.15}$$

$$[P_c] = [F_c] = 0 \tag{2.16}$$

From the jump conditions, one can derive the relation:

$$\gamma_g \langle P_g \rangle = J \langle v \rangle \tag{2.17}$$

where $\langle \cdot \rangle$ denotes the arithmetic mean of the enclosed quantity just before and after the jump and $J = \rho v$ is the conserved mass flux.

What is the criterion for a gas subshock? It occurs when the compression ratio y is discontinuous, i.e. in equation 2.10, $\mathrm{d}y/\mathrm{d}x \to \infty$ when $D(y) = 0$ (it can be shown that $N(y)$ is finite, even in the limit $y \to 1$). From equation 2.12, we see that this happens when:

$$v^2 = \frac{\gamma_g P_g}{\rho} = c_\mathrm{s}^2, \tag{2.18}$$

i.e. the flow hits a sonic point with respect to the *gas* sound speed. We see that this is equivalent to equation 2.17 derived from the jump conditions. Since fluid variables are discontinuous at a shock, the sonic point is defined in terms of the average of pre-shock and post-shock quantities. The upstream flow is of course supersonic; if the downstream flow is still supersonic with respect to the gas sound speed, then there is no sonic transition and no subshock. We still refer to the entire compressive structure as a ‘shock’, since the fluid decelerates from $\mathcal{M} > 1$ to $\mathcal{M} < 1$ with respect to the *total* sound speed[5], given by VDM84:

$$v_p^2 = c_s^2 + c_c^2 \frac{(v - v_A/2)(v + (\gamma_g - 1)v_A)}{v(v - v_A)}, \tag{2.19}$$

where $c_c^2 = \gamma_c P_c/\rho$. However, if the downstream flow is subsonic, then equation 2.10 becomes singular at the sonic point and a subshock occurs.

The sonic point is where P_c is maximized. Physically, this is because at the subshock, the kinetic energy of the flow goes into the gas component rather than the CR component: P_g ungoes a discontinuous increase at the subshock, while P_c is unchanged (continuous) across the subshock. After the subshock, one goes directly to the downstream state where all fluid variables are constant. One can also see this by differentiating equation 2.6 and using equation 2.7 to obtain:

$$\left(\rho v^2 - \gamma_g P_g\right) \frac{\mathrm{d}\rho}{\mathrm{d}x} = \rho \frac{\mathrm{d}P_c}{\mathrm{d}x} \tag{2.20}$$

i.e. as one approaches the sonic point where the term in brackets vanishes, $\boldsymbol{\nabla} P_c \to 0$ and P_c is maximized. Note that if the solution were to remain continuous and differentiable, then $\boldsymbol{\nabla} P_c$ would change sign, implying a non-monotonic precursor profile, which is unphysical in the presence of diffusion. One can also see that at a sonic point, $\mathrm{d}y/\mathrm{d}x$ would change sign since $D(y)$ changes sign (see equation 2.12), again implying a non monotonic profile. However, if a subshock takes place at the sonic

---

[5] Note that this differs from simply summing the gas and CR pressure to get the total pressure in an adiabatic medium, because energy is transferred between the gas and CRs.

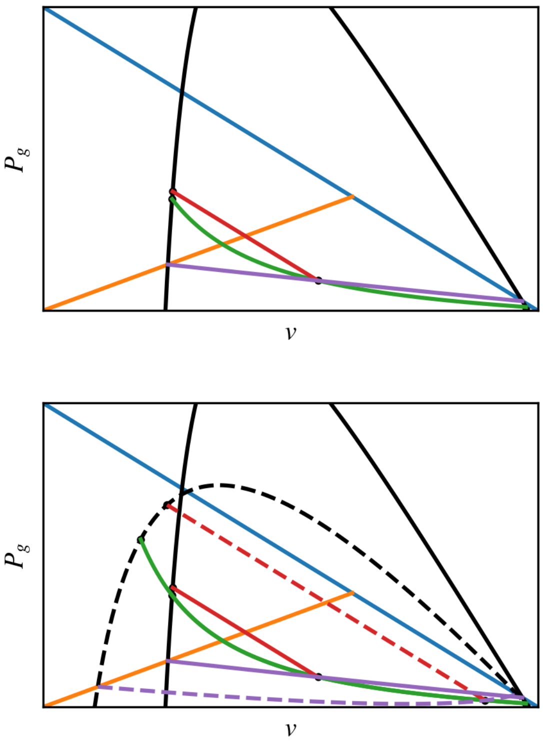

FIGURE 2.1: *Top*: Typical P_g against v diagram without bi-directional streaming. Each colored curve represents a $P_g - v$ relation given a condition, as described in Drury and Voelk [43]. Blue - $P_c = 0$; orange - $\gamma_g P_g = Jv$; black - the Hugoniot, $N(y) = 0$; red - jump in (P_g, v) satisfying the subshock jump conditions 2.13 - 2.16; green - the wave adiabat, eqn.2.9; purple - the reflected Hugoniot. *Bottom*: Same as the top but with bi-directional streaming, which leads to the dotted lines. The dotted black line expresses the $P_g - v$ relation for $\tilde{N}(y) = 0$. Construction of the dotted red and purple line follows that of the solid red and purple line. For reference, $\mathcal{M} = 5, Q = 0.5, \beta = 1$ for these two plots.

point, derivatives involving the gas diverge (in particular, $\mathrm{d}\rho/\mathrm{d}x \to \infty$) and so all equations involving derivatives (including equation 2.10 and 2.20) are no longer valid.

Solution method. In the standard treatment by VDM84, for a given upstream, the downstream can be found by a modification of the procedure described in Drury and Voelk [43] (hereafter DV81). The solution procedure can be expressed graphically, as in the top panel of Fig.2.1, which shows a P_g against v diagram. Each curve on the diagram describes a constraint characteristic to the shock structure:

- $P_c = 0$ *(blue curve).* Pressure must be positive. The plot shows $P_g > 0$ only; another obvious constraint is $P_c > 0$. Thus, all valid solutions must lie below the blue line, which shows $P_c = 0$ (obtained from equation 2.5). Lines parallel to this line correspond to $P_c =$ const, which we will use shortly.

- *Hugoniot (black curve).* The black curve references eqn.2.10, showing where $N(y) = 0$, or equivalently where the gradients of the fluid variables are zero. This corresponds to far upstream and downstream. It is called the Hugoniot. For a given upstream, the Hugoniot encompasses possible downstream states.

- *Wave adiabat (green curve).* The wave adiabat, given by equation 2.9, is set by upstream conditions and conserved throughout the precursor. The initial intersection of the wave adiabat and the Hugoniot at the far right gives the upstream state; the subsequent intersection at the left gives the downstream state if there is no subshock. The ordering of these states is unambiguous, since the shock decelerates the flow.

- *Sonic Boundary (orange line).* The orange line shows the sonic condition given by equation 2.18. If the wave adiabat does not cross this boundary before reaching the Hugoniot, then it never undergoes a sonic transition and there is no subshock. The structure of the shock can then be read off graphically by following the wave adiabat from the upstream to the downstream state. On the other hand, if it crosses this line, then the gas will shock.

- *Reflected Hugoniot (purple line).* If the gas undergoes a sub-shock, how do we proceed? Since P_c is continuous, $[P_c] = [\rho v^2 + P_g] = 0$ across the subshock, the jump in fluid variables must be parallel to the $P_c = 0$ (blue) line. In addition, from equation 2.17, the sonic boundary (orange line) must bisect this line, since the sonic boundary gives the relationship between the *mean* of the pre-shock and post-shock pressure and velocities. From these facts, we can construct a 'reflected Hugoniot' (purple curve), which is the locus of points traced out by lines parallel to the blue $P_c = 0$ line, which start at the Hugoniot (black) and are bisected by the sonic boundary. The reflected Hugoniot shows all the possible pre-subshock states connected to the downstream by the subshock jump conditions eqn.2.13-2.16. The intersection of the wave adiabat (green) and reflected Hugoniot (purple) therefore gives the pre-subshock state.

- *Subshock Jump (red line).* Now that we have identified the pre-subshock state, we insert the subshock jump (red line), which as discussed must be parallel to the $P_c = 0$ (red) line. The intersection of the subshock jump (red line) with the Hugoniot (black line) gives the post subshock (and final downstream) state.

In summary, the solution procedure is: follow the wave adiabat (green) in the direction of decreasing v until it intersects with the reflected Hugoniot (purple), then follow the subshock jump (red) directly to the downstream. In the absence of a subshock, possible if the wave adiabat does not cross the sonic boundary (orange), the downstream is simply given by the intersection of the Hugoniot and the wave adiabat. Such smooth transitions can occur if the shock is CR dominated.

The solution can be parametrized by:

$$\mathcal{M} = \frac{v_1}{v_{p1}}, \quad Q = \frac{P_{c1}}{P_{g1} + P_{c1}}, \quad \beta = \frac{8\pi P_{g1}}{B^2}, \tag{2.21}$$

where v_p is given by eqn.2.19 here. The shock Mach number $\mathcal{M}$ is not to be confused with the Alfvenic Mach number $\mathcal{M}_A$, the sonic Mach number $\mathcal{M}_s$, or the CR acoustic Mach number $\mathcal{M}_c$. Q is the upstream non-thermal fraction of the total pressure. β is the familiar plasma beta.

2.2.2.2 New Solution: Bi-directional Streaming

The aforementioned solution method assumes the direction of CR streaming is the same throughout the shock profile, i.e. towards the upstream. However, post-subshock CR can stream towards the downstream too. At the early stages of shock formation, strong compression at the subshock can cause the CR pressure to overshoot, forming a small spike from which CR stream away in opposite directions (Fig.2.2). This is entirely analogous to the 'Zeldovich spike' [190] which occurs in radiative shocks. The spike is a non-equilibrium state which slowly flattens as CRs stream out. However, it sets up a shock structure where downstream CRs stream *away* from the shock, rather than towards it, as VDM84 assumed. Note that the downstream CR profile is almost

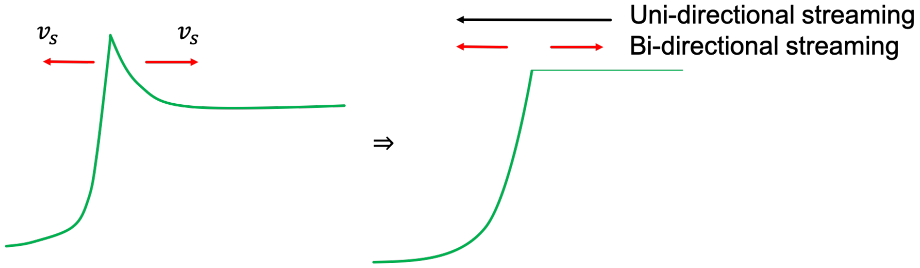

FIGURE 2.2: Conceptual plot of P_c leading to bi-directional streaming. The direction of streaming assumed in VDM84 is added for comparison.

flat ($P_c \rightarrow$ const), so the direction of streaming is set by small changes in the CR profile at the shock.

To capture this new solution graphically, a new Hugoniot curve has to be added (see bottom panel of fig.2.1). This new Hugoniot is derived by setting $\tilde{N}(y) = 0$, where $\tilde{N}(y)$ is the function $N(y)$ with the signs in front of $\mathcal{M}_A$ flipped,

$$\begin{aligned}\tilde{N}(y) = \frac{(\gamma_c+1)}{2}\left(y - \frac{\gamma_c-1}{\gamma_c+1}\right) \\ -\frac{\gamma_c}{\gamma_g \mathcal{M}_{s1}^2}\left\{1+\delta-\frac{\gamma_g-\gamma_c}{\gamma_c(\gamma_g-1)}\frac{1-\bar{P}y}{1-y}\right\} \\ +\frac{\gamma_c}{\mathcal{M}_{A1}}\left\{y^{1/2}-\frac{1}{\gamma_c\mathcal{M}_{c1}^2(1+y^{1/2})}+\frac{y^{1/2}(1-\bar{P})}{\gamma_g\mathcal{M}_{s1}^2(1-y)}\right\},\end{aligned} \tag{2.22}$$

The standard Hugoniot (solid black line in fig.2.1) shows possible downstream solutions for which $v_s = -v_A$, where post-shock CR streams toward the shock. With the sign flip, the new Hugoniot (dotted black line) shows possible downstream solutions for which $v_s = v_A$, and the post-shock CR stream away from the shock. The switch in direction of downstream CRs changes not just the magnitude of the subshock, but also where it occurs. One can see it is not possible to jump, from the standard location where the subshock occurs (intersection between the solid green and purple lines), to the new Hugoniot while satisfying the subshock jump conditions. The sonic boundary (orange) would no longer bisect the line connecting pre-shock and post-shock states. To determine when the subshock occurs, a new reflected Hugoniot (dotted purple line) has to be calculated, in a similar manner as in the standard treatment.

Fluid flow in the precursor conserves the same wave adiabat as before since CR still streams towards the upstream. Therefore precursor fluid states continue to trace the same green curve. The subshock occurs at intersections between the new reflected Hugoniot and the wave adiabat, which brings the fluid directly to the downstream.

Existence of the new solution. In the case of uni-directional streaming, the shock profile can be smooth (i.e. no subshock) if the wave adiabat does not cross the sonic boundary. This happens when the upstream P_c is sufficiently high. However, the new solution always requires a subshock. Bi-directional streaming can only occur if there is a maximum in P_c, at which $\nabla P_c = 0$. As previously discussed (see equation 2.20), unless $\mathrm{d}\rho/\mathrm{d}x = 0$, a maximum in P_c is equivalent to a sonic point in the gas, and thus a subshock must occur, which brings the fluid to its downstream state without further relaxation. Otherwise, the profile will be non-monotonic. This means that in CR dominated regimes, the new solution may cease to exist because the subshock has been smoothed out.

Fig.2.3 shows an example where a new solution is not allowed for the above reasons. The wave adiabat (green) does not cross the sonic boundary before intersecting with

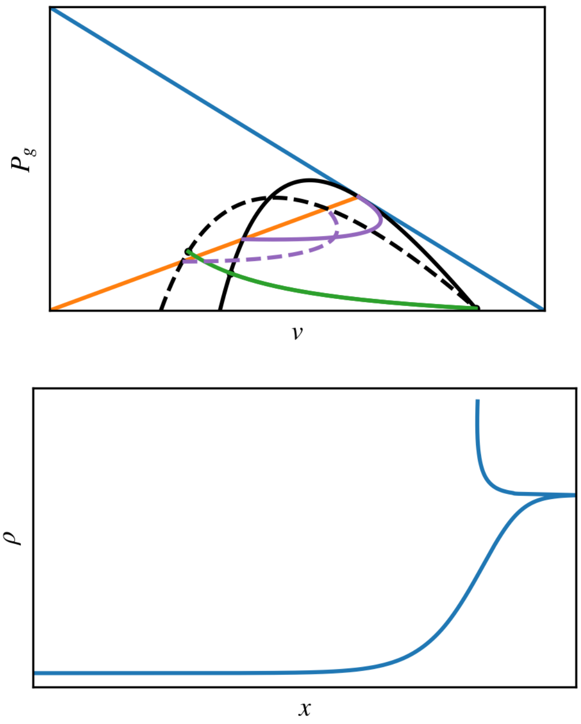

FIGURE 2.3: *Top*: $P_g - v$ diagram for $\mathcal{M} = 2, Q = 0.95, \beta = 1$. The color of the curves mean the same as in fig.2.1. *Bottom*: Density plot of the new solution shows that it is non-monotonic.

the standard Hugoniot (black). Thus, the standard solution involves a smooth transition, with no sub-shock. The wave adiabat (green) does also intersect with the new reflected Hugoniot (dotted purple), but only after crossing the standard Hugoniot (solid black), where $\mathrm{d}P_c/\mathrm{d}x = 0$. Continuing after this would imply a change in sign for $\mathrm{d}P_c/\mathrm{d}x$ and other fluid derivatives, i.e. a non-monotonic profile. This solution therefore has to be rejected.

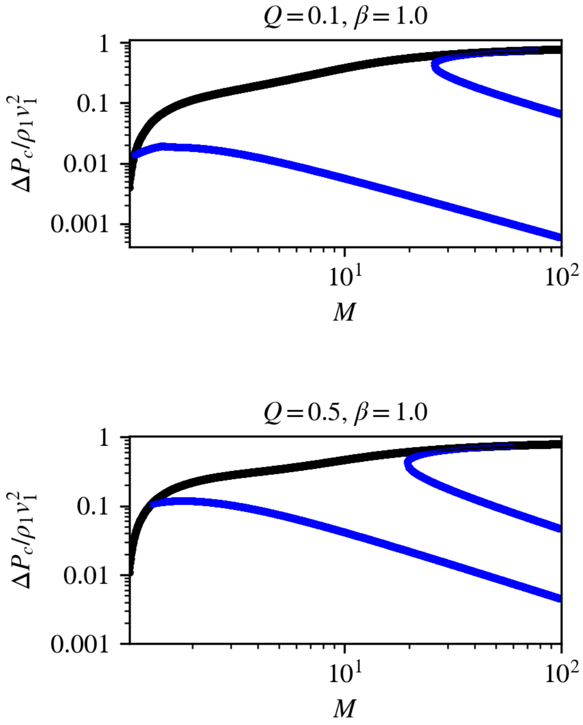

FIGURE 2.4: Acceleration efficiency against mach number $\mathcal{M}$ for $Q = 0.1$ (Top) and $= 0.5$ (Bottom) and $\beta = 1$. The black curve denotes the standard branch while the blue curve denotes the new solution branches (efficient, intermediate and inefficient).

2.2.3 Solution Structure

Fig.2.4 shows the acceleration efficiency, measured by the ratio of the change in CR pressure to the upstream ram pressure ($(P_{c2} - P_{c1})/\rho_1 v_1^2 \equiv \Delta P_c/\rho_1 v_1^2$), against Mach number for upstream non-thermal fraction $Q = 0.1, 0.5$ and $\beta = 1$. Fig.2.5 shows the acceleration efficiency against Q for a sample of Mach number and plasma beta. In these two figures, two different solutions emerge, corresponding to uni-directional (black curves) or bi-directional streaming (blue curves). At high β, the two solutions converge since the contribution of streaming is small in that limit, so it does not

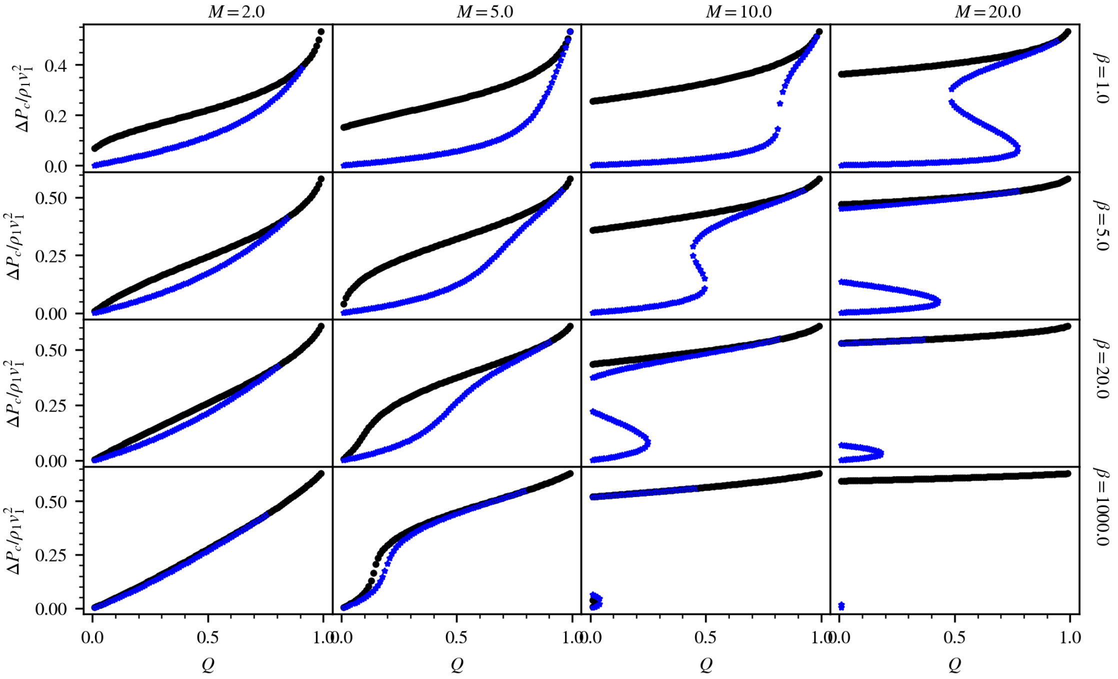

FIGURE 2.5: Acceleration efficiency against upstream non-thermal fraction (Q) for Mach number $\mathcal{M} = 2, 5, 10, 15$ and plasma beta $\beta = 1, 5, 20, 1000$. The black curve denotes the standard branch while the blue curve denotes the new solution branches (efficient, intermediate and inefficient). In each panel, the efficient branch gradually merges with the standard branch as Q increases. At sufficiently CR dominated regimes (high Q), the efficient branch cease to exist by the monotony argument in sec.2.2.2.

matter which way the CRs stream. In magnetically significant regimes ($\beta \sim 1$), the new branch introduces two main differences: first, the acceleration efficiency is in general lower. For bi-directional streaming, downstream CRs stream away from the subshock, and fewer CRs diffuse to the upstream precursor. In the two-fluid formalism, all CR 'acceleration' is essentially compressional (adiabatic) heating. With a smaller precursor, the shock is more hydrodynamic and less compressible (since the $\gamma_g = 5/3$ gas is less compressible than the $\gamma_c = 4/3$ CRs). Lower compression implies less overall less adiabatic heating of the CRs. The difference is small at low Mach numbers ($\mathcal{M} \sim 1-2$) but becomes more apparent as $\mathcal{M}$ increases. At $\mathcal{M} \sim 10$

the acceleration efficiency can drop from $\sim 40-50\%$ for the standard branch to less than 10%. However, at moderate Mach numbers, a transition occurs, and that brings us to the second point: the new solution bifurcates into multiple branches. A similar bifurcation occurs for CR shocks without streaming, which is equivalent to our high β limit (DV81; Becker and Kazanas 4, Donohue and Zank 38, Jones and Ellison 94, Mond and O'C. Drury 120, Saito et al. 144). This does not happen for uni-directional solutions with streaming. Even so, bifurcation in the no streaming case happens only at very small Q, and within an intermediate range of Mach numbers. In contrast, the new bifurcation can occur at high Q (for $\beta \sim 1$, it can occur for equipartition CR energy densities or even in CR dominated regimes) and persists even as $\mathcal{M}$ continue to increase. Fig.2.6 shows a summary of the solution multiplicity for $(\mathcal{M}, Q)$ and $\beta = 1, 20, 1000$. Multiple solutions for the new branch are common, particularly for high Mach numbers and when magnetic fields are significant (lower β). The new branch usually bifurcates into three solutions, and in order of increasing acceleration efficiency we shall call them the inefficient, intermediate and efficient branch.

The uni-directional solution poses a difficulty at low β: a significant downstream non-thermal fraction exists even as $Q \to 0$. This solution has been argued to be physically unrealistic [111]. It is unclear physically how, without injection, one can accelerate particles without an existing CR population. By contrast, the bi-directional solution has at least one branch where $\Delta P_c \to 0$ as $Q \to 0$.

The behaviour of different branches of solution are markedly different. The 'inefficient'

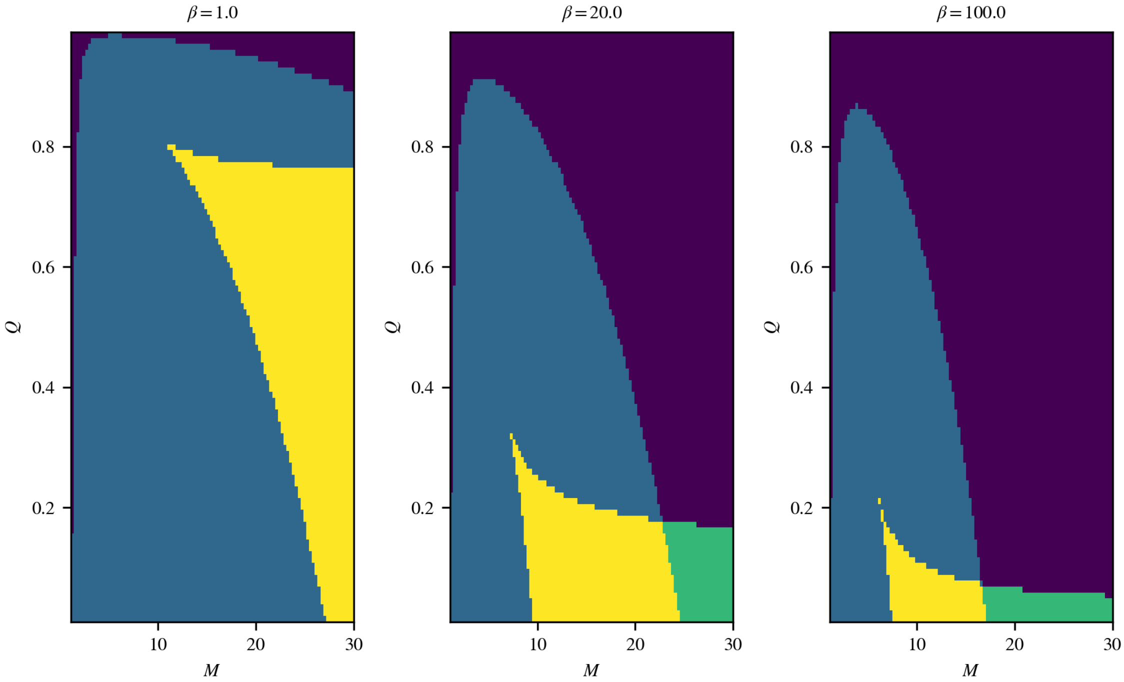

FIGURE 2.6: Color plots showing the multiplicity of the new + standard solution for a given $(\mathcal{M}, Q, \beta)$. Purple = 1, blue = 2, green = 3, yellow = 4.

branch corresponds to the test particle limit where CRs have nearly no effect on the shock structure. The downstream fluid is gas dominated and the shock appears hydrodynamic, giving a compression ratio ~ 4 at high Mach number. At equipartition $(Q \sim 0.5, \beta \sim 1)$, the typical acceleration efficiency $\sim 10\%$ for Mach numbers below 10 and *decreases* with increasing Mach number (see fig.2.4). At low Mach numbers, the acceleration efficiency of this branch appears consistent with PIC/hybrid simulations [25], which found an efficiency of $\lesssim 10\%$ for $\mathcal{M} < 10$. It is however at odds with the behavior at very high Mach numbers $\mathcal{M} > 10$, for which PIC/hybrid simulations show an increase in efficiency. We shall see that if we include thermal injection into DSA (§2.3.5.4), this decline in efficiency at high Mach number goes away. With less ambient CR $(Q = 0.1)$, the acceleration efficiency of the inefficient branch drops to

$\sim 1\%$. This reflects, in the two-fluid model, a substantial ambient CR population is required for efficient acceleration.

The efficient branch is strongly CR modified. Having a smaller adiabatic index $\gamma_c = 4/3$, the fluid is more compressible, so the compression ratio ~ 7 at high Mach number. This leads to much higher adiabatic heating of the CRs. At equipartition, this branch emerge at Mach numbers higher than ~ 12 and has a typical efficiency of $\gtrsim 60\%$. The acceleration efficiency continues to increase with Mach number such that at Mach number of a few tens and above the subshock is smoothed out by the dominating CR population and the efficient branch merges with the standard branch. In the following, we shall often refer to the efficient branch and standard solution collectively as the efficient/standard branch due to their similarity in acceleration efficiency. An acceleration efficiency of this order has been found in previous works, both analytically (Caprioli et al. 27, in a two-fluid model; Caprioli et al. 28, in a kinetic description; both works include magnetic field amplification) and in simulations (Ellison and Eichler 48, in a Monte Carlo approach).

While some previous analytics have assumed CR entropy (P_c/ρ^{γ_c}) to be constant [63, 126] across the shock, we find this to be untrue; CR entropy increases across the shock for all branches of solution (in ascending order of increase: inefficient, intermediate and efficient branch).

The downstream P_c can be different by decades across branches of solution, so knowing which one will be selected is important. We seek to answer this with simulation. In the following sections, we will demonstrate numerically that the standard and new solutions are all valid steady state shock profiles, but the intermediate branch of the new solution is unstable. We also illustrate, with different initial setups, how various branches can be captured. They turn out to be sensitive to local upstream conditions, but generically, the inefficient branch of the new solution is the one most likely to be realized in realistic settings.

2.3 Simulation

2.3.1 Code

The following simulations were performed with Athena++ [160], an Eulerian grid based MHD code using a directionally unsplit, high order Godunov scheme with the constrained transport (CT) technique. CR streaming was implemented with the two moment method introduced by Jiang and Oh [92]. This code solves equation 9 in Jiang and Oh [92], which reduces to our equation 2.2 in 1D (where the B-field is constant and parallel to the shock normal). Unless otherwise specified, a 1D Cartesian grid is used and the magnetic field points in the $+x$ direction.

2.3.2 Setup 1: Imposed Shock Profile

We begin by verifying the analytic standard and new solutions, by imposing the steady-state analytic profiles as initial conditions and verifying that they are time-steady in the code. For a given upstream state, the downstream state can be determined by the method described in §2.2.2. The shock profiles can be calculated from eqn.2.10 supplemented by a subshock that brings the fluid to the downstream state. This profile is input into the simulation domain and evolved in time. Since the shock structure depends only on $\mathcal{M}, Q, \beta$, we fix the upstream $\rho = 100, P_g = 1$ in code units, implying an unstream gas sound speed of $c_s = 0.13$. We set the reduced speed of light $\tilde{c} = 100$[6]. Some simulations were rerun with $\tilde{c} = 1000$ with no apparent difference. The diffusion coefficient (which we set to $\kappa = 0.1$) has no effect on downstream values, it only sets the shock width. The number of grid cells is 4096; at this resolution the diffusive length is typically resolved with $n_{\rm shock} \equiv \kappa / v_1 \Delta x \gtrsim 40$ cells. Previously, $n_{\rm shock} \sim 10 - 20$ was found to be sufficient for convergence [56]. Outflow boundary conditions were used on both sides. The result is independent of the boundary conditions as increasing the domain size and imposing the ghost zones yield no difference. Unless specified, the following simulations assume $\beta = 1$. CR transport at high β is purely diffusive, a limit that has been extensively studied, which we will not investigate in this work.

---

[6] The reduced speed of light $\tilde{c}$ is a free simulation parameter governing the CR free stream speed in the decoupled limit. It should be much greater than other characteristic speeds. See [92] for a detailed discussion.

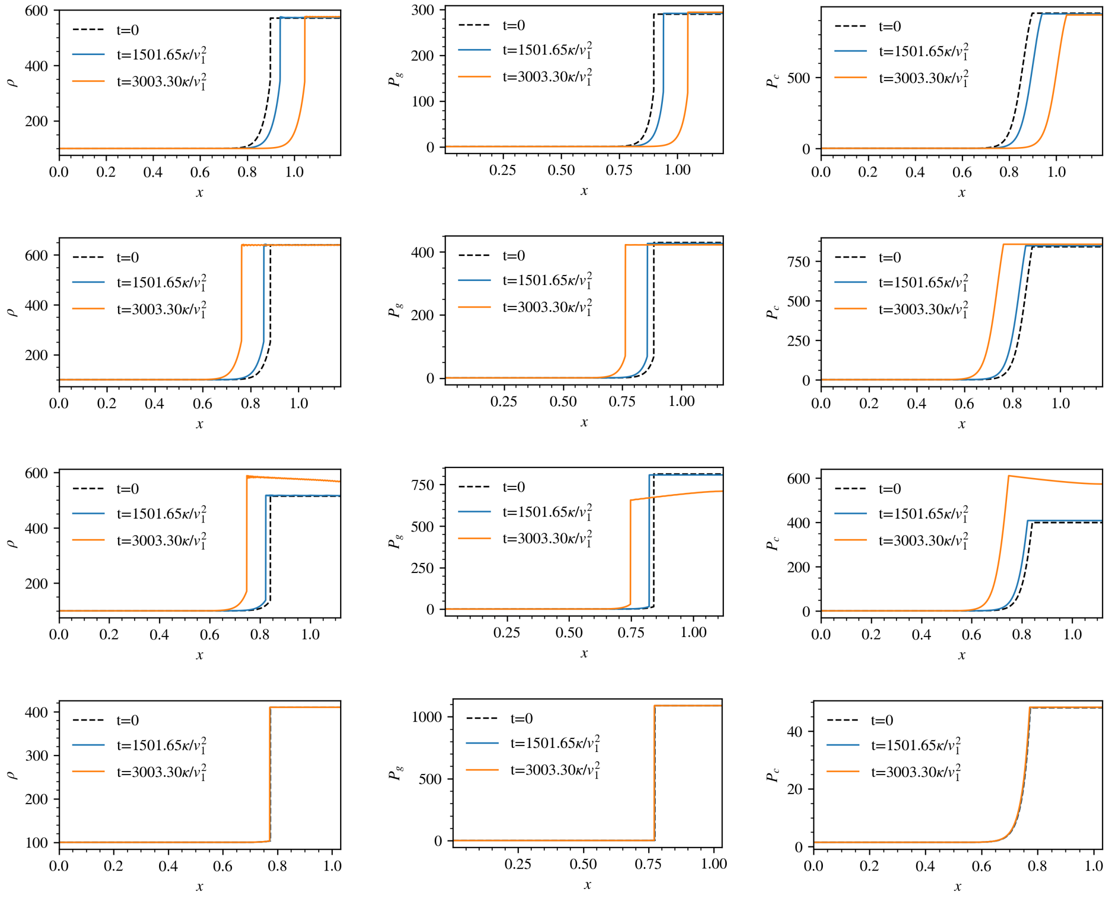

FIGURE 2.7: Simulation results for Setup 1. *Top row*: From left to right: density, gas pressure and CR pressure profiles for the standard branch. *Second row*: Profiles for efficient branch. *Third row*: Profiles for the intermediate branch. *Bottom row*: Profiles for the inefficient branch.

Fig.2.7 shows respectively the shock profiles of the standard, efficient, intermediate and inefficient branch at $t = 0, 1502t_{\text{diff}}, 3003t_{\text{diff}}$ for $\mathcal{M} = 20, Q = 0.6, \beta = 1$, where $t_{\text{diff}} = \kappa/v_1^2$ is the diffusion timescale. The solutions at $t = 1502t_{\text{diff}}$ are relatively well maintained, with a little numerical shift. Such numerical shifts are expected to equilibrate after $\sim 1000t_{\text{diff}}$ [99]. Behavior of the solutions vary drastically after $\sim 2000t_{\text{diff}}$, with the intermediate branch diverging exponentially from its original profile. The standard and efficient branch show small spatial shifts, but overall the profile is maintained, with the same acceleration efficiency. The inefficient branch appears the most robust. In general, solution branches with significant downstream CR fraction tend to be the most susceptible to this numerical shift. Such shift originate at the subshock (we do not observe this for smooth shocks). The problem lies with how the direction of the streaming velocity v_s is determined. The direction is determined by $\mathrm{sgn}(\nabla P_c)$, which is estimated by a finite difference scheme: $\mathrm{sgn}(\nabla P_{c,i}) = \mathrm{sgn}((P_{c,i+1} - P_{c,i-1})/\Delta x)$. The cells at the subshock therefore would still have positive ∇P_c whereas it should, for bi-directional streaming, be negative. This causes v_s to be positive at the subshock and F_c (equation 2.8) to overshoot slightly, hence causing the shift in P_c profile. Since F_c scales linearly with P_c, the overshoot is larger for more CR dominated downstream. The inefficient branch, which has the lowest downstream CR fraction, is therefore the least affected. Another possible source of shift comes from the finite coupling time for F_c to attain its steady state value (eqn.2.8), given roughly by $t_{\rm coup} = 1/\sigma_c \tilde{c}^2$. Across the subshock, σ_c drops abruptly, leading to a rise in the coupling time. Deviations of F_c from the steady state expression (eqn.2.8) causes the tiny discrepancy seen.

The intermediate branch has a profile which does not just translate spatially; it also clearly evolves. Furthermore, in the example above, the acceleration efficiency of the intermediate branch diverges with time and evolves to the standard/efficient branch efficiencies, while the other branches remain close to their initial values. Thus, the intermediate branch is unstable. The same multiplicity (3) of solutions appears in standard solutions with diffusion only, and the intermediate branch is also unstable in this case. Mond and O'C. Drury [120] suggested that this divergent behavior is a consequence of a corrugational instability. Nevertheless, along with Donohue and Zank [38], Saito et al. [144], we have found that the intermediate branch is unstable without invoking a corrugation mode (since our simulations are 1D). It is also unlikely to be due to the acoustic instability [39–41, 100, 178, 189], triggered at the shock precursor by phase shifts between the acoustic disturbances in the gas and CR components due to CR diffusivity: the typical growth time (i.e. e-folding time) of the acoustic instability is $t_{\rm grow} \sim \kappa/c_{c1}^2$. whereas the advection time across the shock precursor is $t_{\rm adv} \sim \kappa/v_1 c_{s1}$. The ratio of these two time scales is $t_{\rm grow}/t_{\rm adv} \sim \mathcal{M} \gg 1$, i.e. there is insufficient time for the instability to grow.

We can understand the instability of the intermediate branch as follows, which is in line with suggestions that the divergent behavior of the intermediate branch is caused by a feedback loop between downstream CR pressure and acceleration efficiency [43]. A clear criterion for a stable solution is $\partial P_{c2}/\partial P_{c1} > 0$, so that for instance the downstream CR pressure P_{c2} decreases if the upstream value P_{c1} decreases. Otherwise, the acceleration efficiency is divergent. In our variables, the stability criterion is:

$$\frac{\partial P_{c2}}{\partial Q} > 0 \Rightarrow \frac{\partial[\Delta P_c/(\rho_1 v_1^2)]}{\partial Q} > -\frac{P_{g1}+P_{c1}}{\rho_1 v_1^2} \approx -\frac{1}{\mathcal{M}^2} \tag{2.23}$$

where $1/\mathcal{M}^2 \ll 1$. From Fig. 2.5, we see that the strong negative slope of the intermediate branch implies that it is unstable, while both of the other branches are stable. Thus, a solution on the intermediate branch will evolve to one of the other

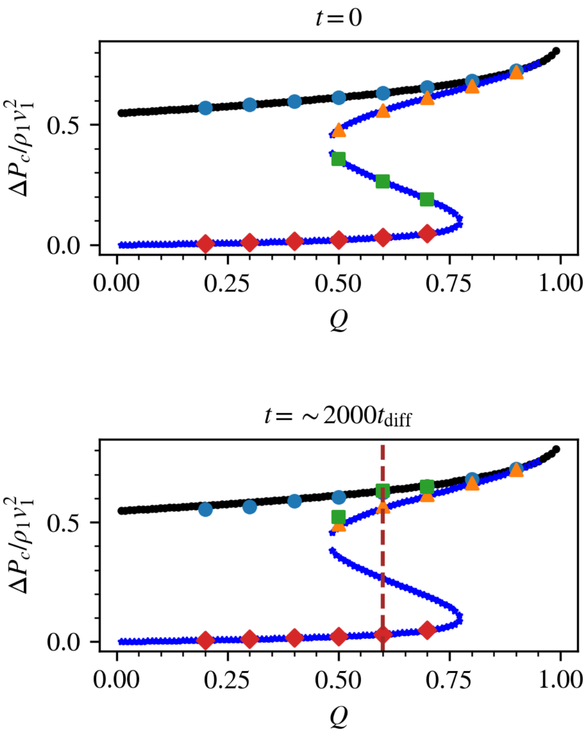

FIGURE 2.8: Acceleration efficiency against Q for $\mathcal{M} = 20, \beta = 1$ at two time instances, at $t = 0$ (Top) and $t \sim 2000 t_{\rm diff}$ (Bottom). The markers denote the simulation data, the different marker shapes represents the solution branch the simulation was set up with (red diamond: inefficient, green squares: intermediate, yellow triangle: efficient, blue circles: standard). The markers are threaded by black and blue lines, denoting the analytic acceleration efficiency (black corresponds to standard branch, blue corresponds to the new solution branches, i.e. efficient, intermediate, inefficient). The vertical brown dashed line indicates the value of Q used in the test cases displayed in fig.2.7.

branches. The instability of the middle branch in an 'S' shaped phase plane curve is generic to many problems, from thermal instability [53] to accretion disk instabilities [157].

We proceed to test the analytic shock profiles for other values of Q. The result is shown in fig.2.8. The acceleration efficiencies of the standard, efficient and inefficient branches are stable and remain close to their initial setups while that of the intermediate branch is unstable, and asymptotes to the standard and efficient branch. These results show that our two-moment code handles this demanding test well, and in agreement with analytic expectations.

2.3.3 Setup 2: Free Flow

Next, we show how initial conditions influence which solution branch is realized. We simulate a fluid moving supersonically towards a reflecting boundary on the right at high speed, as in a converging flow. This causes the fluid to shock. The initial flow is either uniform or has background gradients. The left boundary is set to outflow if the flow is uniform initially, or with linear extrapolation in the ghost zones otherwise. The initial flow speeds are listed in table 2.1 (top table) and P_c is set by Q. The CR flux F_c is determined by eqn.2.8.

For uniform flow, ρ and P_g are set to 1000 and 1 respectively. In the setup with initial gradients, all quantities except for P_c remain constant. P_c was set to be linear:

$$P_c(x) = (P_{c1} - P_{c0})\left(1 - \frac{x}{x_{\text{left}}}\right) + P_{c0}, \tag{2.24}$$

where the subscripts $0, 1$ denote quantities at the left and right boundaries respectively. Equation 2.24 determines the spatially varying CR pressure fraction $Q(x) = P_c(x)/(P_c(x) + P_g)$. The initial profile can equivalently be parametrized by Q_0 and

Case	v	(M, Q, β)	# of sol. branch	Selected branch	Acc. eff.
Fig.2.9(a)	0.5	$(14.8, 0.2, 1)$	2	Inefficient	0.93%
Fig.2.9(b)	1.23	$(26.6, 0.6, 1)$	4	Inefficient	2.1%
Fig.2.9(c)	3.31	$(22.4, 0.95, 1)$	1	Standard	77.0%

θ (deg)	t $(t/t_{\rm diff})$	$(\mathcal{M}_f, Q, \beta)$	r	Acc. eff.	$\theta_{\rm out}$ (deg)
5	60 (1299)	$(7.6, 0.5, 1)$	4.0	1.1%	19.5
45	60 (1304)	$(7.6, 0.5, 1)$	4.0	0.9%	76
5	200 (3435)	$(7.7, 0.5, 100)$	6.8	81.1%	30.8
45	200 (4344)	$(8.65, 0.5, 100)$	4.0	1.2%	76

TABLE 2.1: **Top table**: Summary of test cases with uniform initial flow (§2.3.3). The first column catalogs the corresponding figure. The second column lists the initial flow speed. The third column lists the upstream shock parameters. The forth column enumerates the number of analytical solution branches for each case. The fifth column records the branch selected by simulation. The last column measures the acceleration efficiency by $(P_{c2} - P_{c1})/\rho_1 v_1^2$. **Lower table**: Summary of the oblique shock parameters (§2.3.5.3). Column 1: Angle between upstream magnetic field and shock normal. Column 2: Time of measurement in code unit and in unit of the diffusion time in parenthesis. Column 3: Upstream Mach number (defined relative to the fast magnetosonic speed), non-thermal fraction and plasma beta. Column 4: Compression ratio. Column 5: Acceleration efficiency. Column 6: Angle between downstream magnetic field and shock normal.

Q_1, the non-thermal fraction at the left and right boundaries. Since the shock propagates from right to left, at first $Q = Q_1$, which then declines to $Q = Q_0$ as the shock moves leftward. A background with non-zero P_c gradient will push on the gas, causing the background profile to evolve. We include an external body force on the fluid to counteract the CR push, keeping the background gas in force balance and thus in steady state. We set $\kappa = 0.1$ and use $N = 16384$ grid cells unless otherwise specified.

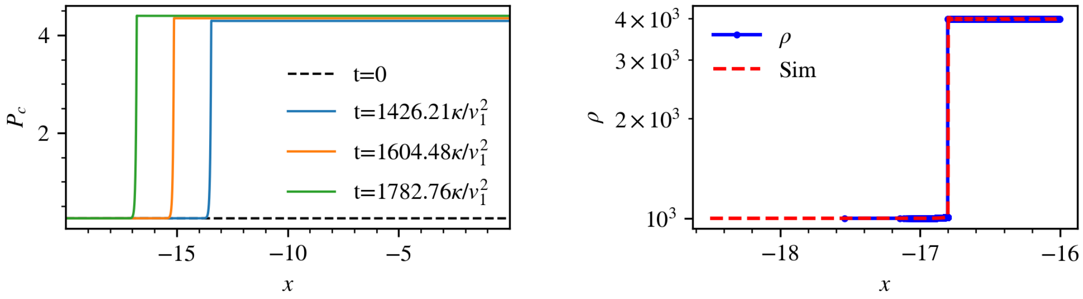

(a) $\mathcal{M} = 14.8$, $Q = 0.2$ and $\beta = 1$

(d) Density

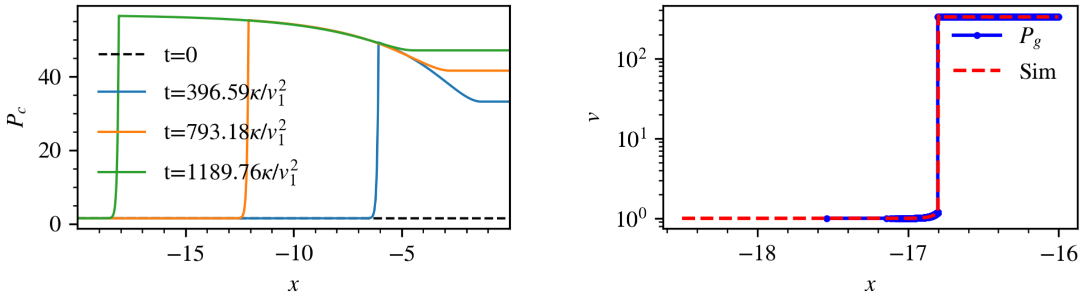

(b) $\mathcal{M} = 26.6$, $Q = 0.6$ and $\beta = 1$

(e) Gas pressure

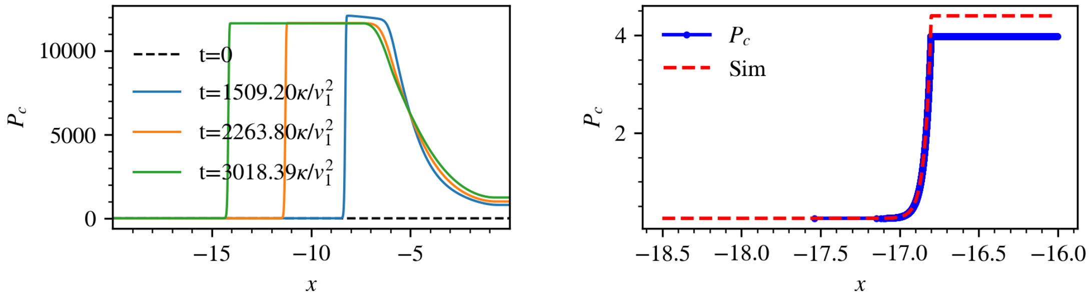

(c) $\mathcal{M} = 22.4$, $Q = 0.95$ and $\beta = 1$

(f) Comparison of simulated shock profile against analytic for the $\mathcal{M} = 14.8$, $Q = 0.2$ and $\beta = 1$ case.

FIGURE 2.9: Simulation results for setup 2 without background gradients, as in Table 2.1.

2.3.3.1 Uniform Background

For initially uniform flow, we show 3 different cases, which are tabulated in Table 2.1 and have profiles in Fig.2.9(a), 2.9(b) and 2.9(c). The Mach number is measured in the shock frame with the shock velocity calculated by imposing continuity: $v_{\rm sh} = [\rho v]/[\rho]$. In each case, it took $\sim 1000 t_{\rm diff}$ for the shock to equilibrate. We comment further on these long equilibration times in §2.3.5. Equilibration generally takes longer for CR dominated flows. In fig.2.9(c), where there is a transition from low to high CR dominance, the equilibration time is extended by a factor of two. We compare the simulated shock profile against the analytic prediction well after equilibration, and find good agreement. We show an example in fig. 2.9(f). This shows that bi-directional streaming is indeed necessary to understand the shock profiles. The slight discrepancy in the P_c profile is due to fluctuations at the subshock associated with $\mathrm{sgn}(\nabla P_c)$, as discussed in §2.3.2. In Table 2.1, it appears the inefficient branch is favored whenever it is a possible solution of the shock equations. We have found in all other shock simulations with uniform flow that the simulation indeed selects the inefficient branch whenever possible. It is unclear physically why this is the case, but could be related to the fact that the inefficient branch maximizes the wave entropy (the quantity on the LHS of equation 2.9), and in particular has strongest subshock and hence the largest jump for the gas entropy. Consistent with the results of the previous section, the intermediate branch is never selected.

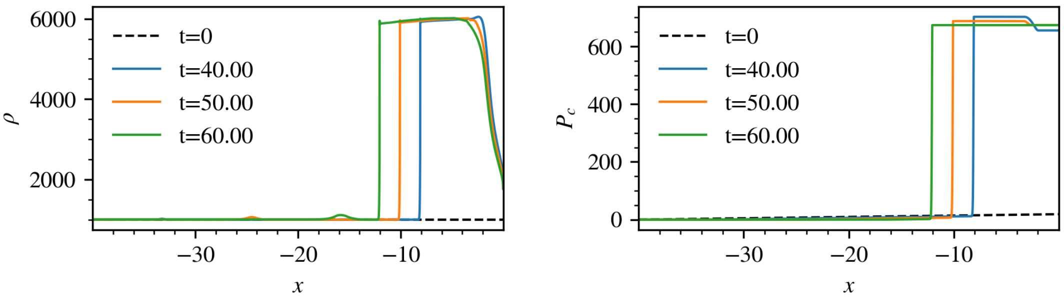

(a) The mach number $\mathcal{M} \approx 15$, $Q_0 = 0.2, Q_1 = 0.95$ simulation. The acceleration efficiency $\sim 57\%$, indicating the efficient/standard branch is selected.

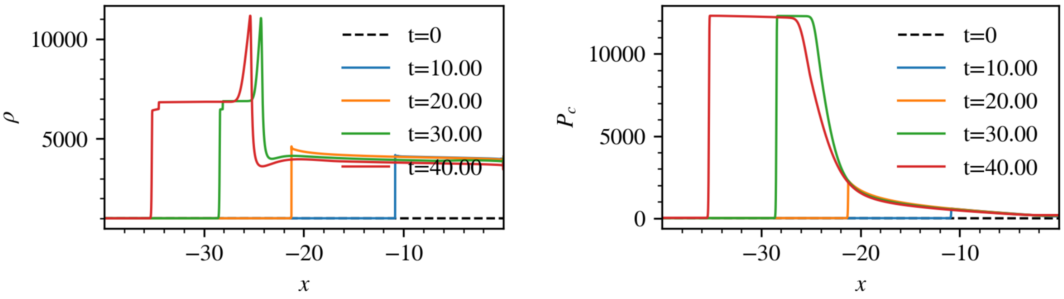

(b) The mach number $\mathcal{M} \approx 20$, $Q_0 = 0.95, Q_1 = 0.75$ simulation. The acceleration efficiency transitions from $\sim 3\%$ to $\sim 77\%$, indicating the inefficient branch is selected at first, then the standard/efficient branch.

FIGURE 2.10: Simulation of setup 2 with background gradient. Time is given in code units because there isn't a well-defined κ/v_1^2 due to varying background.

2.3.3.2 Gradient Background

Fig.2.10(a) shows the evolution of a shock in a background P_c gradient, where Q_0, the initial non-thermal fraction at the left boundary, was 0.2, while Q_1, that at the right boundary, was 0.95. This was meant to simulate a shock propagating from a CR dominated region ($Q_1 = 0.95$), where only the efficient/standard branch is permissible, to a progressively gas dominated area, where the inefficient branch also exists. It is clear that the efficient/standard branch is picked throughout. As a comparison, a similar test where $Q_1 = 0.8$ was performed (not shown). The inefficient branch is selected throughout for this case. The reason for this discrepant solution pick is as follows: as shown in fig.2.11, at $Q_1 = 0.95$, only the efficient/standard branch is possible, so the shock will pick this solution. Under continuously varying background conditions (in this case the gradually decreasing P_c), the shock will shift to a proximate point on the same branch. The shock remains on the same branch even if subsequent upstream conditions permit the inefficient branch. The same logic applies to the case $Q_1 = 0.8$. At $Q_1 = 0.8$, there are 4 possible branches. As in our uniform background tests, the inefficient branch is picked. Subsequent evolution of the shock down the P_c gradient follows the same branch. These two test cases have been repeated without the balancing source terms, causing the shock and the background to co-evolve with time. Nevertheless, the same result applies: the inefficient branch is selected for $Q_1 = 0.8$ while the efficient/standard branch is selected for $Q_1 = 0.95$. Branch selection is unaffected by source terms.

The reverse is also true. A shock beginning at the inefficient branch can, as in fig.2.10(b), transition to the efficient/standard branch provided the upstream has shifted to conditions where only the efficient/standard branches are permissible. This could happen if the upstream is more CR dominated, or has higher plasma β.

The findings of these simulations are summarized in Fig. 2.11. The branch selected by the shock is dependent on the local upstream conditions where the shock is formed. Where possible, the inefficient branch is picked. The shock will remain on the same branch unless the upstream transitions into conditions where only the efficient/standard branches are permissible. It will then switch to these branches and remain there.

Thus, a shock passing through a CR dominated region (e.g., a cold cloud) will change its properties and continue to efficiently accelerate CRs, even after leaving the cloud. Two-fluid shock simulations appear to have hysteresis, likely because downstream conditions set boundary conditions for CR streaming which impact the shock itself. We will not consider the physics of this hysteresis, or the preference for the inefficient branch, further in this paper. The full realism of these properties is unclear, given the limitations of the standard two-fluid approach. For now, it is important to be aware of them, given that two-fluid CR hydrodynamics is essentially the only approach used in galaxy formation simulations.

2.3.4 Setup 3: 1D Blast Wave

Thus, far, we have focussed on the properties of steady-state shocks, and not examined properties of the time-dependent stage. We have already seen that the equilibration time of shocks can be long, $\sim 1000 t_{\rm diffuse}$. Thus, the acceleration efficiency of shocks will be time-dependent in a realistic setting. Here, as the simplest possible example, we consider a plane-parallel analog to a blast wave.

In cosmological simulations, an SN event is typically prescribed to deposit mass, metals, momentum and energy to nearby cells of gas, generating an expanding shock wave. The energy deposited to CR (i.e. acceleration efficiency) is often taken to be 10% of the total energy $\sim 10^{51}$ erg. If CR is treated as a fluid coupled to the thermal gas, additional CR will be generated at the expanding shock. As we have seen, this can

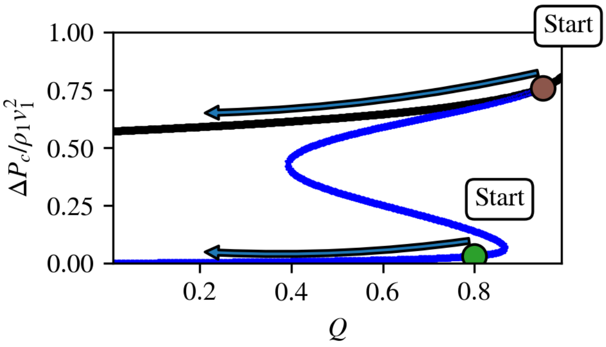

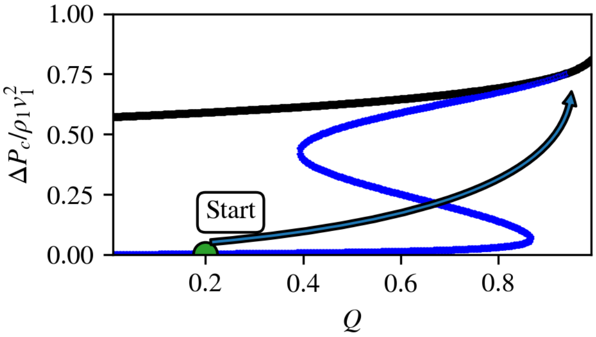

FIGURE 2.11: Acceleration efficiency against Q plot showing how various solution branches are captured. *Top*: A shock beginning at the efficient/standard branch (brown dot) would, under continuously varying background conditions, shift to another point on the same branch. The same holds for the green dot on the inefficient branch. *Bottom*: A shock beginning at the inefficient branch (green dot) can transition to the efficient/standard branch if the background transitions into one for which only the efficient/standard branch is permissible. As before, the black solid line denotes the standard branch while the blue line denotes the new solution branches (efficient, intermediate and inefficient).

be handled self-consistently by a fluid code without a sub-grid prescription, though whether the acceleration efficiency is correct as compared to PIC/hybrid simulations is another matter.

In our setup, a total energy of $E_{\rm ej} = 10^{51}$ erg was deposited uniformly over a volume of radius $R = 10$ pc. 70% of this was deposited into thermal energy, 10% into CR energy and the remaining 20% into kinetic energy. For a swept-up mass to be $50 M_{\odot}$, the average density was $\rho = 8.12 \times 10^{-25}$ $\mathrm{g\,cm^{-3}}$. The average outflow velocity was therefore $v = 632$ $\mathrm{km\,s^{-1}}$, yielding a temperature of $T = 5.64 \times 10^{7}$ K from the ideal gas law for a gas of molecular weight $\mu = 1$. The surrounding ISM was assumed to have density $\rho_{\rm ISM} = 10^{-25}$ $\mathrm{g\,cm^{-3}}$ and $P_{g,\rm ISM} = P_{c,\rm ISM} = 10^{3}\,k_B$ $\mathrm{K\,cm^{-3}}$. The Mach number of the expanding remnant is ≈ 40. We consider both $\beta_{\rm ISM} = 2, 100$ cases. Following the analytic solution method described in §2.2, there are 4 solution branches for the $\beta_{\rm ISM} = 2$ case, of which we expect the inefficient branch to be picked. For the $\beta_{\rm ISM} = 100$ case, only the efficient/standard branch is permissible. The whole domain spanned -2000 pc $< x <$ 2000 pc, with outflow boundary conditions and $\kappa = 3 \times 10^{25}$ $\mathrm{cm^{2}\,s^{-1}}$. The acceleration efficiency is independent of the diffusion coefficient; the specific value chosen allowed the precursor to be resolved without an equilibration time which is too long (and requires a large box). It is also consistent, but on the low side, with the value used in [62] and observations of SN shocks cited therein. A smaller diffusion coefficient is reasonable given the shorter mean free path of CRs at strong shocks, due to the amplification of magnetic perturbations. The domain was resolved with $N = 65536$ cells (i.e. 0.06pc per grid cell). For simplicity and to avoid computational cost, the calculation is done in planar 1D geometry, and only meant to be illustrative.

The top and bottom rows of fig.2.12 shows the time evolution of an expansion shock from a top-hat SNR setup for $\beta_{\rm ISM} = 2$ and $\beta_{\rm ISM} = 100$ respectively. After an initial transient of ~ 1000 kyr, the SNR settles onto a relatively stable structure. For $\beta_{\rm ISM} = 2$, the forward shock at $t = 5871$ kyr has a compression ratio ~ 4 and

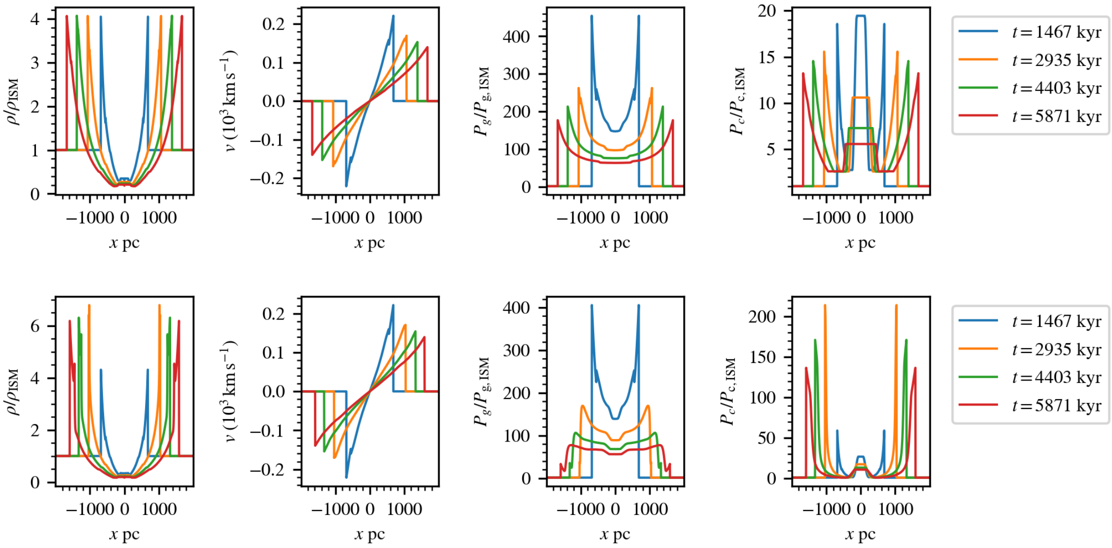

FIGURE 2.12: Evolution of 1D blast wave. *Top row*: $\beta_{\rm ISM} = 2$ *Bottom row*: $\beta_{\rm ISM} = 100$. The compression ratio and acceleration efficiency taken at 5871 kyr are ~ 4 and 4.6% for $\beta = 2$ and ~ 6 and 67.3% for $\beta = 100$.

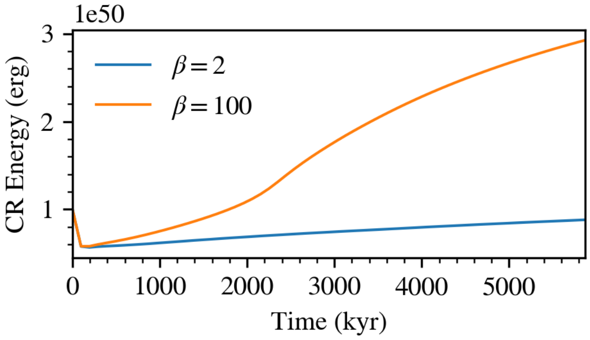

FIGURE 2.13: CR energy enclosed by the blast wave as a function of time for $\beta_{\rm ISM} = 2$ (blue) and $\beta_{\rm ISM} = 100$ (orange). The initial CR energy is 10^{50} erg, i.e. 10% of the total energy ejected. After an initial transient phase, CR energy begins to rise due to particle acceleration.

an acceleration efficiency of $\sim 4.6\%$, indicating the inefficient branch is selected as expected. For $\beta_{\rm ISM} = 100$, the compression ratio rises to ~ 6 and the acceleration efficiency to 67.3%, indicating the efficient/standard branch is selected. As in fig.2.9(c) in §2.3.3, the shock profile for the $\beta_{\rm ISM} = 100$ case underwent an extended transient of ~ 1500 kyr at low post-shock CR dominance before transitioning to the expected efficient/standard branch. Thus, the acceleration efficiency ramps up while the blast wave expands. Comparing the CR energy contained within the SNR of the two test cases (fig.2.13), the high $\beta_{\rm ISM}$ case is clearly much more CR populated (~ 3.5 times in this case).

Our test case is clearly idealized and we expect the simulated profiles to change in realistic 3D spherical geometry, as well as the inclusion of additional physics such as radiative cooling and collisional losses. In particular, the forward shock should decelerate faster from stronger adiabatic cooling, reducing the acceleration efficiency and the net CR produced. Nevertheless, it shows how shocks can potentially add CRs over and above the initial values input by a subgrid recipe, as well as the influence of CR streaming losses (which differ in the low and high β regimes) in reducing acceleration efficiency.

2.3.5 Further Considerations

Through most of this paper, we have considered time-steady, numerically resolved, parallel shocks only involving acceleration of pre-existing CRs (no injection from the

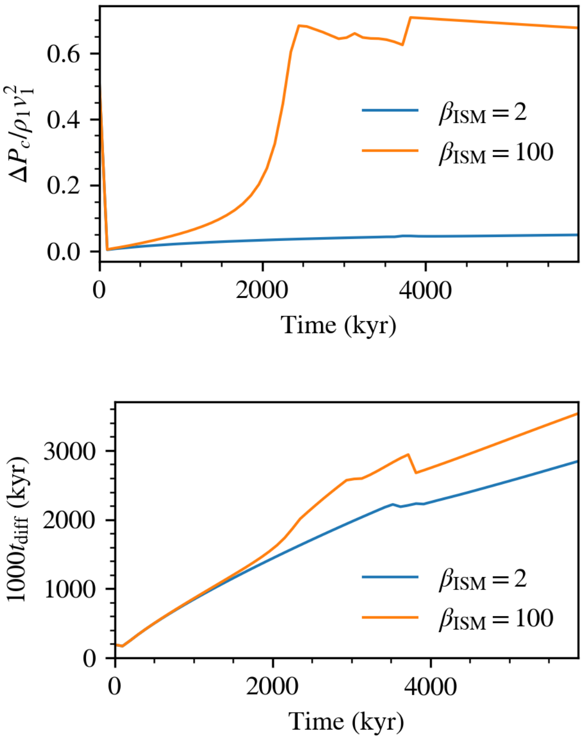

FIGURE 2.14: *Top*: Acceleration efficiency as a function of time for the 1D blast wave example. *Bottom*: Instantaneous diffusion time of the forward shock.

thermal pool). Here, we briefly discuss the impact of relaxing these assumptions.

2.3.5.1 Long Equilibration Times

We have already seen that shocks require $\sim 1000 t_{\rm diff} \sim 1000\kappa/v_1^2$ to equilibrate, where $t_{\rm diff}$ is the diffusion time and v_1 is the upstream velocity in the shock frame. The non-linear build up of the CR precursor, which significantly affects shock structure and CR acceleration, takes many CR diffusion cycles across the shock. The long equilibration time reflects the time required for the upstream flow to respond to the acceleration and diffusion of CR. This has been seen in previous work with diffusion only: for instance, Jones and Kang [95] found it took $\sim 200 - 1000 t_{\rm diff}$ for their solutions to equilibrate, which is very similar to our findings. Fig.2.14 plots the acceleration efficiency and the instantaneous diffusion time of the forward shock in the setup described in §2.3.4. Clearly, the equilibration time for the efficient/standard branch (the $\beta_{\rm ISM} = 100$ case) is longer, ~ 2500 kyr. This timescale is indeed of order $\sim 1000 t_{\rm diff}$.

The equilibration time is longer for the efficient/standard branch because the post-shock CR pressure is higher, leading to a stronger precursor which takes a longer time to build up. By the same token, the more pre-existing CRs there are in the upstream, the more rapidly the precursor equilibrates. As mentioned in §2.3.3 and §2.3.4, when only the efficient/standard branch is permissible, there is usually an extended transient in which the shock transitions from low to high post-shock CR dominance (i.e. low to high CR acceleration efficiency), which coincides with the build-up of the precursor. This behavior was also seen by Dorfi and Drury [39], Jones and Kang [95] in simulations without CR streaming. Jones and Kang [95] derived an approximate analytic formula for the equilibration time and found that the number of diffusion time required is dependent on γ_c as well. The equilibration time is the longest for $\gamma_c = 4/3$ and decreases for a stiffer CR equation of state, when the plasma is less compressible and the precursor plays a smaller role. For instance, in oblique shock simulations assuming $\gamma_c = 4/3$, we find an equilibration time of $\sim 2500 t_{\rm diff}$ for $\theta = 5$ deg, $\beta = 100$ case, whereas Jun and Jones [97] find $t_{\rm eq} \sim 36 t_{\rm diff}$ for $\gamma_c = 5/3$. Thus, in more realistic scenarios where γ_c is self-consistently calculated (and varies continuously from $\gamma_c = 5/3$ to $\gamma_c = 4/3$), equilibration times will be smaller.

Nonetheless, the long equilibration times are important to keep in mind. Before reaching steady-state, shocks will have lower acceleration inefficiencies. One should be careful before grafting the result of steady state shock calculations in many astrophysical settings (for instance, when using a shock-finding algorithm to inject CRs by hand). For example, in SNR presented in §2.3.4, the equilibration time is of order of 1 Myr, comparable to the expansion time, and the acceleration efficiency was clearly time-dependent. Other factors not present in our current simulations will affect whether the standard/high efficiency branch will appear in two-fluid galaxy formation simulations: by 1 Myr, radiative cooling will put the SNR in the snowplough phase, and various instabilities (e.g. Rayleigh-Taylor, CR acoustic instability, corrugational instability), if resolved, can disrupt the shock profile and truncate build-up of a precursor. It is important to bear in mind the use of a galaxy scale CR diffusion coefficient in cosmological simulations, of order $10^{28}\ \mathrm{cm}^2\,\mathrm{s}^{-1}$ or above, would have an equilibration time significantly longer than 1 Myr.

2.3.5.2 Numerical Resolution

It's clear that our high resolution simulations are converged, since they match analytic predictions. However, it is interesting to understand the minimal resolution needed to obtain accurate acceleration efficiencies. To study numerical convergence, we repeated the setup described in 2.3.4 at different resolutions, and compared solutions at $t = 5871$ kyr. The number of grids used were: 512, 2048, 8192, 16384, 32768, 65536, 131072. Equivalently, taking the shock width at this time instance to be $\sim \kappa/v_1 = 3\times10^{25}\ \mathrm{cm}^2\,\mathrm{s}^{-1}/150\ \mathrm{km\,s}^{-1} = 0.67$ pc and a domain size of 4000 pc gives,

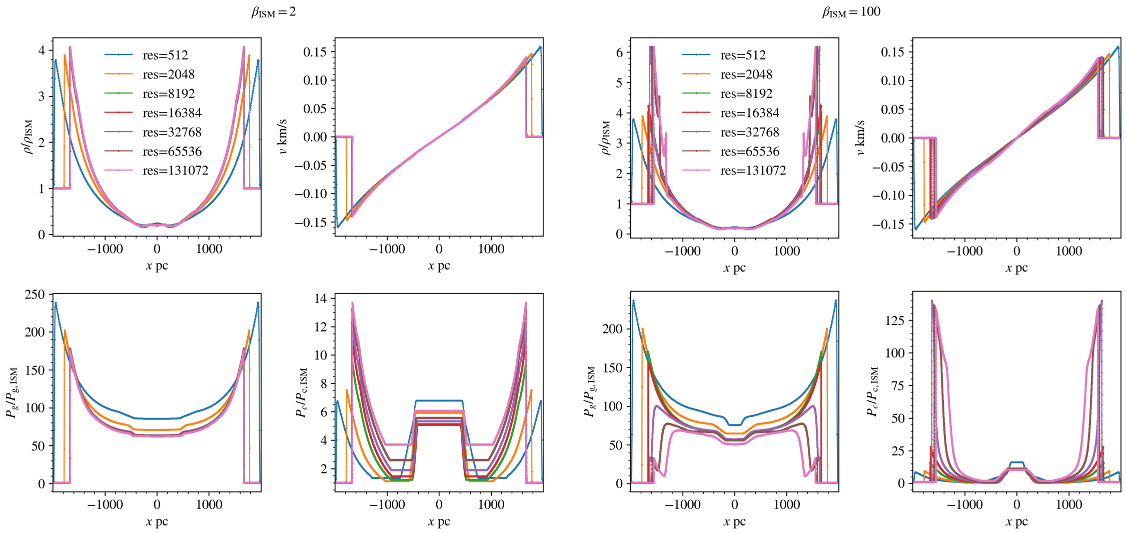

FIGURE 2.15: Plot of density, velocity, gas and CR pressure at $t = 5871$ kyr at different resolutions for $\beta_{\rm ISM} = 2$ (left 4 panels) and $\beta_{\rm ISM} = 100$ (right 4). The legend indicates the number of grids used to resolve the simulation domain. Equivalently, the approximate number of grids the shock is resolved with is: 0.085 (res=512), 0.34 (res=2048), 1.37 (res=8192), 2.73 (res=16384), 5.46 (res=32768), 10.9 (res=65536), 21.9 (res=131072).

in ascending order of resolution, the approximate number of grids $n_{\rm shock}$ the shock was resolved with: 0.085 (res=512), 0.34 (res=2048), 1.37 (res=8192), 2.73 (res=16384), 5.46 (res=32768), 10.9 (res=65536), 21.9 (res=131072). For $n_{\rm shock} < 1$, the shock is unresolved. One can see in fig.2.15 that the solutions converges steadily for the $\beta_{\rm ISM} = 2$ case, whereas for the $\beta_{\rm ISM} = 100$ case, there is an abrupt transition from the inefficient branch to the efficient branch once $n_{\rm shock} > 5.5$. We quantified this by looking at the acceleration efficiency across the forward shock at different resolutions (fig.2.16). The acceleration efficiency converges smoothly for the $\beta_{\rm ISM} = 2$ case, while in the $\beta_{\rm ISM} = 100$ case, there is slow change at low resolution followed by an abrupt rise at $n_{\rm shock} \sim 5$.

Thus, the diffusion length must be resolved by ~ 10 grid cells for convergence in

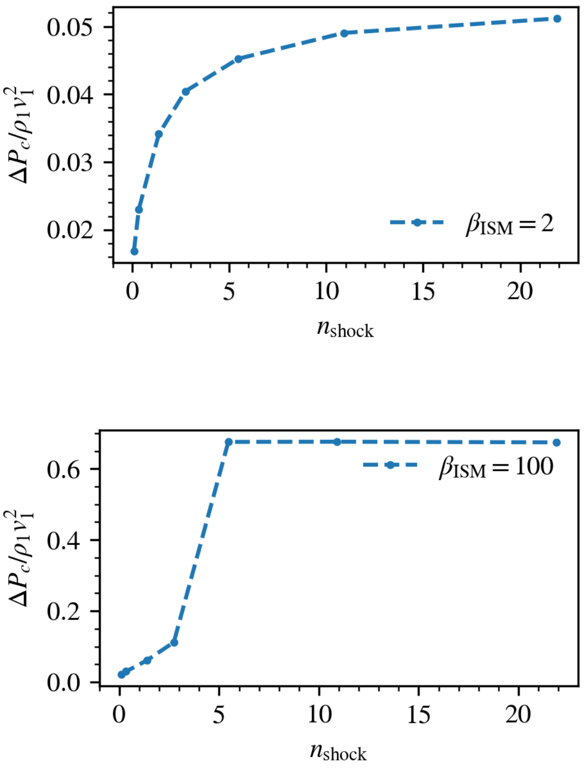

FIGURE 2.16: Acceleration efficiency across the forward shock as a function of $n_{\rm shock}$ for $\beta_{\rm ISM} = 2$ (left) and $\beta_{\rm ISM} = 100$ (right) case.

acceleration efficiency. At a lower Mach number, and if the upstream is highly CR dominated, the precursor is smaller and somewhat lower resolution may suffice. At insufficient resolution, the acceleration efficiency at shocks is underestimated. Except perhaps for very high resolution zoom simulations, most shocks in galaxy scale simulations will not resolve such length-scales and will thus have very low acceleration efficiencies. For this reason alone, it is likely safe to presume that the only source of CRs in such simulations are those injected by a sub-grid recipe.

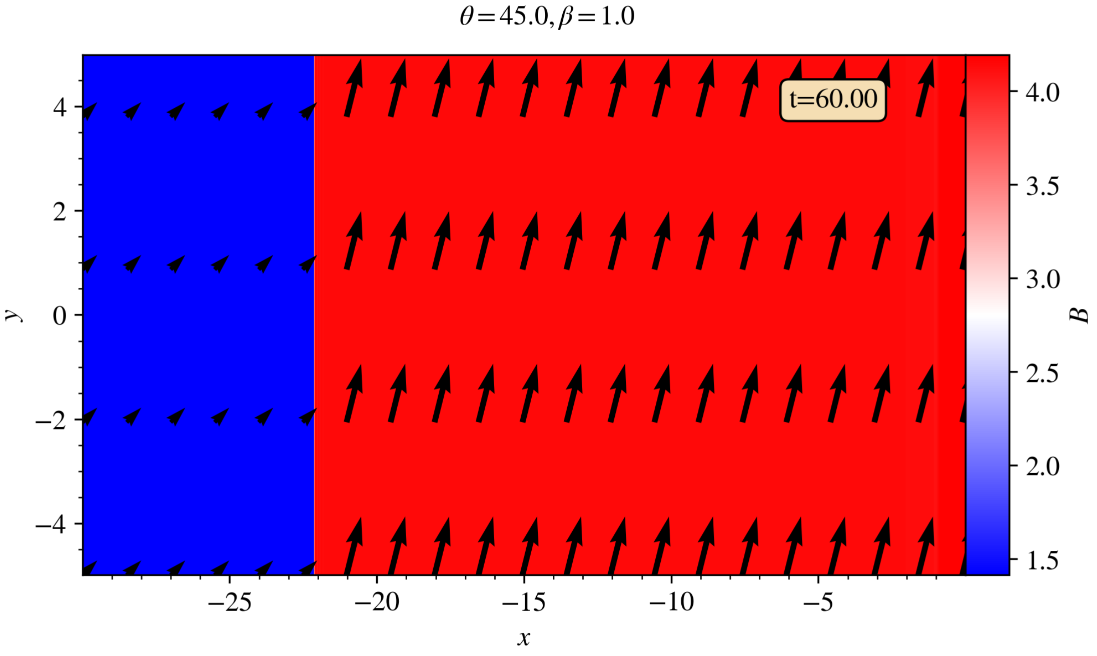

FIGURE 2.17: The shock profile for $\theta = 45$ deg, $\beta = 1$ at $t = 60$ showing the magnetic field. The arrows indicate the orientation of the field.

2.3.5.3 Oblique Magnetic Fields

An oblique shock, where the magnetic field is no longer parallel to the shock normal, suppresses CR acceleration. This is because CR transport across the shock is suppressed. In the post-shock fluid, compression preferentially amplifies the perpendicular B-field component, so the B-fields are aligned parallel to the shock front, suppressing diffusion upstream.

Here we describe four 2D test cases involving oblique magnetic fields. The setups were as follow: We initialized a uniform 2D flow of density $\rho = 1000$, velocity $v = 1.108$, gas pressure $P_g = 1$ and CR pressure $P_c = 1$ (i.e. $Q = 0.5$) crashing towards the right boundary. The magnetic field was oriented at angle $\theta = 5, 45$ deg to the shock normal for plasma beta $\beta = 1, 100$. The reduced speed of light was set to $c = 50$ and CR diffusivity to $\kappa_{\parallel} = 0.1$ along the magnetic field and $\kappa_{\perp} = 1.67 \times 10^{-9}$ perpendicular to it. The domain spanned $-30 < x < 0$, $-5 < y < 5$ for the $\beta = 1$ case and $-90 < x < 0$, $-5 < y < 5$ for the $\beta = 100$ case. The whole domain was resolved with 2048×512 grids for $\beta = 1$ and 8192×512 grids for $\beta = 100$, corresponding to a precursor resolved by $n_{\text{shock}} \approx 6, 8$ grid cells respectively. Reflecting boundary was set at the right and outflow at the left.

A summary of the oblique shock results is given in table 2.1 (lower table). The magnetic field for an example is also shown in fig.2.17. Shock compression deflects the magnetic field away from the shock normal and increases its strength. Compressive amplification of magnetic field is stronger for higher obliquity as only the perpendicular component is boosted. The acceleration efficiencies of the $\beta = 1$ case are very low ($\sim 1.1\%$ for $\theta = 5$ deg and $\sim 0.9\%$ for $\theta = 45$ deg). This is inconsistent with the analytic prediction by Webb et al. [180] (that included oblique magnetic fields and CR diffusion but no streaming), which predicted an efficiency of $\gtrsim 50\%$. The reduction in acceleration efficiency seen in our simulations is caused by bi-directional streaming, with the inefficient branch being picked. For simplicity we eschew repeating the analytic calculation in §2.2 including oblique magnetic fields.

The difference is more marked at different obliquity for $\beta = 100$. At $\theta = 5$ deg, the efficient/standard branch is recovered, achieving an efficiency $\sim 81\%$. The acceleration efficiency decreases drastically at $\theta = 45$ deg to $\sim 1.2\%$. This suggests that the inefficient branch may be more extensive at high obliquity in parameter space

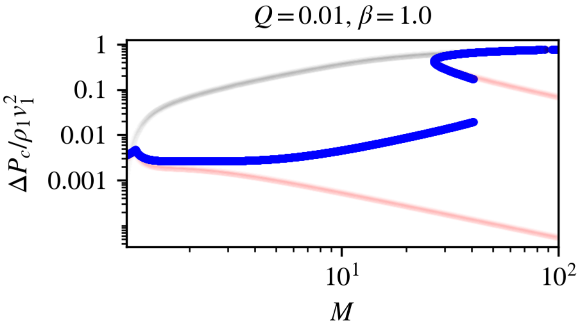

FIGURE 2.18: Acceleration efficiency against Mach number with injection. A fraction of 10^{-3} of the thermal particles is injected at the subshock. Injection is included only for the bi-directional solutions (blue curve). The acceleration efficiency without injection (for the same Q and β) is displayed here for comparison (black and red translucent curves for the uni-directional and bi-directional solutions respectively).

$(\mathcal{M}, Q, \beta)$ than in the 1D case. Given that oblique shocks are the most common case, we expect the inefficient branch to appear more commonly in cosmological simulations than expected from 1D analytics and simulations.

2.3.5.4 Injection of Thermal Particles

Thus far, we only consider acceleration of pre-existing CRs, which can easily take part in diffusive shock acceleration. However, suprathermal particles in the Maxwellian tail of the plasma can also be injected into the DSA process, and contribute to the CR population. This is particularly important when the pre-existing CR population is sparse (small Q). Here, we consider a simple prescription for injection which illustrates some potential effects.

Following Kang and Jones [99], injection can be accommodated in our solution method as follows. First, modify the subshock jump conditions to include injection:

$$[\rho v] = 0, \tag{2.25}$$

$$\left[\rho v^2 + P_g\right] = 0, \tag{2.26}$$

$$\left[\rho v\left(\frac{1}{2}v^2 + \frac{\gamma_g}{\gamma_g - 1}\frac{P_g}{\rho}\right)\right] = -I, \tag{2.27}$$

$$[P_c] = 0, \tag{2.28}$$

$$[F_c] = I, \tag{2.29}$$

where the injected energy flux I is calculated according to

$$I = \frac{1}{2}\epsilon\lambda^2 c_{s2}^2 J, \tag{2.30}$$

for some prescribed injection efficiency ϵ, postshock gas sound speed λc_{s2}, and mass flux $J = \rho v$. Physically, this represents a small fraction ϵ of the incident thermal particles which have λ times the postshock gas sound speed and are injected into the DSA process, contributing to the CR pressure. From the modified jump conditions, one can derive the relation:

$$(1 + \delta_{\mathrm{inj}})J\langle v\rangle = \gamma_g\langle P_g\rangle, \tag{2.31}$$

where

$$\delta_{\mathrm{inj}} = \frac{\gamma_g - 1}{2}\epsilon\lambda^2\frac{c_{c2}^2}{\langle v\rangle|\Delta v|}. \tag{2.32}$$

which is consistent with our previous equation 2.17 , if $\delta_{\text{inj}} = 0$. The symbols $\langle\rangle$ and Δ denote the arithmetic mean and the difference of the relevant quantity before and after the jump.

Graphically, equation 2.31 modifies the sonic boundary by a factor of $(1 + \delta_{\text{inj}})$. However, δ_{inj} is not known a priori, so one must guess a value for δ_{inj} first, then iteratively, using the updated pre and post subshock quantities, find an improved solution until the downstream state stays the same within some tolerance (taken to be 10^{-4} here). A good initial guess would be $\delta_0 = \epsilon\lambda^2/2$.

We inject a fixed fraction $\epsilon \sim 10^{-3}$of the thermal particles into the CR population at the subshock, which is roughly the fraction of particles in a Maxwellian with $\lambda \sim 3$ times the sound speed. This fraction is consistent with the injection parameters in [25]. Fig.2.18 shows a case where most of the CRs come from injection ($Q = 0.01$). The acceleration efficiency including thermal injection as a function of Mach number is displayed by the blue curve. The uni-directional and bi-directional solutions without injection are shown by the translucent black and red curve respectively, for comparison. Two points are worth noting: 1. The acceleration efficiency of the bi-directional solution increases with Mach number instead of the other way around. 2. At high Mach number the inefficient branch vanishes. For small Mach number ($\mathcal{M} < 14$) acceleration efficiency of the bi-directional solution with injection ($\sim 1-2\%$) appear roughly consistent but a few percent lower than that found in hybrid simulations [25]. Our current simulation code not yet include injection; it is left for future work. However, it will improve the realism of two fluid shocks. We believe that most of the properties we have found (in particular, the fact that the inefficient bi-directional branch is favored) will continue to be found in simulations with injection.

2.4 Discussion and Conclusion

In this work, we studied steady-state CR modified shocks in the two fluid approximation, with the inclusion of both CR diffusion and streaming in the CR transport. This is a demanding test of new two-moment CR codes [92] which are the first to be able to handle such shocks with CR streaming; they have never been compared against analytic solutions. It also allows us to understand and quantify the effects of CR modified shocks in galaxy formation simulations. In a two-fluid code, shocks can accelerate CRs, over and above CRs injected via a sub-grid prescription; it is important to understand their contribution quantitatively. We only consider acceleration of pre-existing CRs, although one can modify the code to include thermal injection. Our findings are as follows:

- *New analytic solutions: bi-directional streaming.* Previous analytic solutions [176] assumed uni-direction streaming of CRs toward the upstream. In fact, over-compression at the subshock can lead to a transient spike (similar to the Zeldovich spike in radiative shocks) which seeds bi-directional streaming. The upstream and downstream CRs stream in opposite directions, away from the subshock. We obtain analytic profiles for this new solution. Streaming leads to lower acceleration efficiency with increasing magnetic field (due to increased gas heating and reduced compression). Furthermore, the new solution has a lower acceleration efficiency compared to the standard streaming, since downstream CRs propagate away rather than diffusing back to the shock. The CR precursor is smaller and less compressible. At Mach number $\mathcal{M} \gtrsim 15$, the new solution bifurcates into inefficient, intermediate and efficient acceleration efficiency solution branches (fig. 2.4 and 2.5). The inefficient branch is a hydrodynamic shock only weakly modified by CRs, with acceleration efficiencies that typically do not exceed 10%. The efficient branch is CR dominated, with typical acceleration efficiency $\gtrsim 60\%$, similar to the standard branch. The intermediate branch lies somewhere in between. For weaker magnetic fields (higher β), the standard and new solutions merge closer together. At $\beta \gtrsim 100$ essentially only the efficient branch is left.

- *Simulations match analytic solutions.* The simulations reproduces the standard analytic solution as well as all 3 branches of the new solution. The predicted acceleration efficiency also agrees extremely well with analytic predictions (fig.2.9(f)). It is excellent news that the two-moment method can pass this demanding test, which should lay to rest concerns about solution degeneracy and numerical robustness at CR shocks [63, 105]. As long as explicit diffusion is included (and for Fermi acceleration to operate, diffusion *must* be present), the analytic solution does not require ad hoc closure relations. As long as the diffusion length is resolved, numerical simulations closely match analytic solutions across a wide range of parameters.

- *Inefficient Branch Favored.* Which of the various solution branches is actually realized in nature? The intermediate branch is unstable (perturbations cause the acceleration efficiency to diverge to either the inefficient or efficient branch), so it is not realized. Of the remaining two possibilities, the branch selected is dependent upon the local upstream conditions where the shock is formed. In CR dominated shocks, only the efficient/standard branch is possible, since the compression ratio is high. However, if both branches are possible, the inefficient branch is selected, though transition to the efficient branch is possible if the upstream condition shifts to one for which only the efficient/standard branch is permissible. Once the shock selects the efficient/standard branch, it will remain there. See Fig. 2.11. The reason for this preference for the inefficient branch is unclear, though it is worth noting that it maximizes entropy generation at the shock (see discussion for diffusion only case in Becker and Kazanas 4).

- *Assumptions of time-steady, resolved and parallel shocks often not satisfied.* These calculations focus on well-resolved, steady-state, parallel shocks. These conditions are unlikely to be true in galaxy-scale simulations, and changes to these assumptions all point in the direction of reduced CR modification of the shock and lower acceleration efficiency: 1. The equilibration time for a shock to reach its steady state structure is $t_{\rm equil} \sim 1000 t_{\rm diff}$ (where $t_{\rm diff}$ is the diffusion time); higher for CR dominated shocks with high acceleration efficiency, and somewhat smaller for shocks with lower acceleration efficiency. This is because the build-up of the CR precursor is a non-linear process which requires many diffusion times. This is often longer than shock crossing times (e.g. supernova remnants). Thus, shocks in realistic settings are not time-steady and cannot be compared directly to our results. 2. As shown in §2.3.5.2, the precursor needs to be resolved by at least 10 grid cells for convergence. Lower resolution will lead to lower acceleration efficiency (fig.2.16). 3. High obliquity magnetic fields will suppress formation of the CR precursor and hence acceleration efficiency, since the shock will more closely resemble a hydrodynamic shock with lower compression ratio (table 2.1, lower table). 4. If thermal injection is taken into account, the efficiency of the 'inefficient' branch of the bi-directional solution ($\sim 5 - 10\%$) is in good agreement with hybrid/PIC simulations.

In summary, in a two fluid code, the CR acceleration efficiency of shocks in a galaxy scale simulation is likely small ($\ll 10\%$) and thus the prevailing tendency to assume that they do not contribute significantly is likely reasonable. However, one must be careful to test this assumption, particularly in high resolution simulations, because the high efficiency branch converts such a large fraction ($\sim 60\%$) of the shock kinetic energy to CRs (e.g., see Fig 2.13 where the CR energy rises far above the initial value), far above that obtained by kinetic simulations. In the end, we find that in most settings a two fluid code 'does no harm' at shocks and gives roughly physical reasonable solutions, despite the significant shortcomings of the fluid approach in handling a fundamentally kinetic problem, as discussed in the Introduction. The fluid approach can probably be modified (e.g., introducing thermal injection, as in

§2.3.5.4, and potentially introduce a time-dependent κ and γ_c as the shock evolves) which further improves agreement with kinetic results. In the end, however, the most pragmatic approach for galaxy-scale simulations is to simply leave the code as-is, effectively ignoring CR injection at shocks. If the CR acceleration at shocks is a critical application, then one can simply apply a shock finding algorithm and inject CRs by hand (e.g., Pfrommer et al. 127, Pinzke et al. 128), but carefully taking the time-dependence of shock equilibration into account.

Chapter 3

The Cosmic-Ray Staircase: the Outcome of the Cosmic Ray Acoustic Instability

The research constituting this chapter was conducted in collaboration with Dr. Yan-fei Jiang. This chapter has been reformatted and published in the Monthly Notices of the Royal Astronomical Society for which I am the lead author. In the following, I use 'we' to indicate my supervisor Prof. Siangpeng Oh, Dr. Yan-fei Jiang and myself.

3.1 Introduction

It is generally believed that cosmic rays (CR) should play crucial dynamical roles in the interstellar and circumgalactic medium (ISM, CGM) because the energy density of these high-energy particles is comparable to the thermal energy of the gas or the magnetic field [11]. The coupling between CRs and the thermal plasma is believed to be mediated through the streaming instability [106] in which CRs pitch-angle scattered by hydromagnetic waves causes the waves to grow and thus lead to more scattering. This wave-particle interaction causes energy and momentum to be transferred between the gas and CRs. On global scales, the interaction of waves with CRs are key to the transport and confinement of CRs in a galaxy. Cosmic Rays can provide a significant amount of non-thermal support [35, 89] and is a strong candidate for driving galactic winds [15, 36, 74, 85, 140, 171]. On smaller scales, CRs accelerated by shocks can modify shock structures [11, 43, 64, 68, 176] and impact the entrainment, survival and destruction of cold clouds [16, 19]. Thus CRs can significantly affect the multiphase structure of the ISM and CGM.

Even though details of the wave-particle interaction are inherently kinetic, in the limit of strong scattering a fluid description is possible and more practical for galaxy (or cosmological) scale simulations. CRs, treated as a bulk fluid, have the following general transport modes: 1. Wave-particle interactions lock the bulk of CRs with the local Alfven wave, causing them to advect at the Alfven speed along magnetic fields (streaming). 2. Slippage from perfect wave locking causes CRs to diffuse relative to the local Alfven wave frame, down the CR pressure gradient (diffusion). More detailed transport models in the presence of various wave damping mechanisms have been studied (e.g. ion-neutral damping [19, 51], turbulent damping [70], dust damping [159] or some combination thereof [76]). There is, however, no consensus within the community as to the correct form of CR transport in the ISM and CGM. One important observational constraint lies in reconciliation with gamma ray observations. Gamma-ray emission from pion production by CRs is over-produced in simulations unless CRs can be rapidly transported out of dense star forming regions [29]. Thomas et al. [166] modeled harp-like structures in radio synchrotron maps of the Galactic center. Their analysis suggested streaming dominated transport rather than diffusion.

In the fluid description, CRs have been found to modify well-known fluid instabilities such as the Parker instability [66, 67, 138, 143], magneto-rotational instability [108], thermal instability [22, 101, 149], Kelvin-Helmholtz instability [162], etc., while driving some entirely new instabilities, such as the CR acoustic instability [5, 40]. The CR acoustic instability arises when CRs amplify sound waves, via CR pressure forces and/or CR heating of the gas. This causes acoustic waves to increase in amplitude and steepen into shocks. In this paper, we generalize and test previous linear theory predictions for the CR acoustic instability, and study its non-linear saturation. We find a characteristic staircase structure in the CR pressure profile– a new feature in CR transport – and explain its physical origin.

In the diffusion dominated regime, Drury and Falle [40] found that the acoustic instability occurs when the CR pressure scale height $L_c \equiv P_c/\nabla P_c$ is shorter than the diffusion length $l_{\text{diff}} \sim \kappa/c_s$ (where κ is the diffusion coefficient and c_s is the gas sound speed), a condition not easily met except at shock precursors (see Quataert et al. [131] for application to galactic winds, where they find the instability to be unimportant). Kang et al. [100] performed simulations of its non-linear growth at shocks and found that acoustic waves can steepen into many small scale shocks, resulting in enhanced particle acceleration. Ryu et al. [142] found, in a 2D shock setup, that the steepened acoustic waves can create density inversions, trigger a secondary Rayleigh-Taylor instability and generate turbulence in the downstream. All in all, the CR diffusion driven acoustic instability is mostly relevant at shocks.

On the other hand, Begelman and Zweibel [5] found that in the streaming dominated regime, CR heating can cause acoustic modes to become unstable even without a sharp CR pressure gradient. They speculated that the acoustic modes would, in the non-linear regime, generate constant CR pressure regions (CR plateaus) separated by sudden drops, although they were unable to test this. We shall see in this paper, fulfilment of their prescient predictions.

Numerical simulation of this streaming driven acoustic instability have not yet been conducted to date. In the past, such simulations were infeasible due to a numerical instability which arises at CR pressure gradient zeros. Regularization of this instability [152] requires very high resolution and short time-steps, making the calculation infeasibly expensive. In recent years, a new two-moment method [92, 165] now makes this calculation possible. The two moment method has already been deployed in FIRE simulations of galaxy formation [29, 74].

We will, in this paper, utilize this relatively new tool to study the linear and non-linear growth of the streaming driven acoustic instability. We begin, in §3.2, with an analytic discussion of the CR acoustic instability and relevant physics. In §3.3 we describe our simulation setup and results in the linear and non-linear regime. We proceed in §3.4 a discussion of its astrophysical significance and conclusions. In Appendix A.1, we derive the linear growth rate of the CR acoustic instability. A resolution study is conducted in Appendix A.2.

3.2 Analytic Considerations

Assuming gas flow is non-relativistic and the gyroradii of the CRs to be much smaller than any macro scale of interest, the two-moment equations governing the dynamics of a CR-MHD coupled fluid is given by Jiang and Oh 92

$$\frac{\partial \rho}{\partial t} + \nabla \cdot (\rho \mathbf{v}) = 0, \tag{3.1}$$

$$\frac{\partial (\rho \mathbf{v})}{\partial t} + \nabla \cdot (\rho \mathbf{v}\mathbf{v} - \mathbf{B}\mathbf{B} + P^{*}\mathbf{I}) = \boldsymbol{\sigma}_c \cdot [\mathbf{F}_c - (E_c + P_c)\mathbf{v}] + \rho \mathbf{g}, \tag{3.2}$$

$$\frac{\partial E}{\partial t} + \nabla \cdot [(E + P^{*})\mathbf{v} - \mathbf{B}(\mathbf{B} \cdot \mathbf{v})] = (\mathbf{v} + \mathbf{v}_s) \cdot \boldsymbol{\sigma}_c \cdot$$

$$[\mathbf{F}_c - (E_c + P_c)\mathbf{v}] + \rho \mathbf{g} \cdot \mathbf{v} + \mathcal{L}, \tag{3.3}$$

$$\frac{\partial \mathbf{B}}{\partial t} = \nabla \times (\mathbf{v} \times \mathbf{B}), \tag{3.4}$$

$$\frac{\partial E_c}{\partial t} + \nabla \cdot \mathbf{F}_c = -(\mathbf{v} + \mathbf{v}_s) \cdot \boldsymbol{\sigma}_c \cdot [\mathbf{F}_c - (E_c + P_c)\mathbf{v}], \tag{3.5}$$

$$\frac{1}{c^2}\frac{\partial \mathbf{F}_c}{\partial t} + \nabla P_c = -\boldsymbol{\sigma}_c \cdot [\mathbf{F}_c - (E_c + P_c)\mathbf{v}], \tag{3.6}$$

where c is the speed of light, $\mathcal{L} = \mathcal{H} - \mathcal{C}$ is gas heating minus cooling, $\mathbf{v}_s = -\mathbf{v}_A \mathrm{sgn}(\mathbf{B} \cdot \nabla P_c)$, where $\mathbf{v}_A = \mathbf{B}/\sqrt{\rho}$ is the streaming velocity (the gas is assumed to be fully ionized), $P^* = P_g + B^2/2$, $E = \rho v^2/2 + P_g/(\gamma_g - 1) + B^2/2$ and $\boldsymbol{\sigma}_c$ is the interaction coefficient defined by

$$\begin{aligned} \boldsymbol{\sigma}_c^{-1} &= \boldsymbol{\sigma}_d^{-1} + \frac{\mathbf{B}}{|\mathbf{B} \cdot \nabla P_c|} \mathbf{v}_A (E_c + P_c), \\ \boldsymbol{\sigma}_d^{-1} &= \frac{\boldsymbol{\kappa}}{\gamma_c - 1}. \end{aligned} \tag{3.7}$$

where $\boldsymbol{\kappa}$ is the CR diffusion tensor. Generally, $\boldsymbol{\kappa} = \kappa_{\parallel} \hat{\mathbf{b}}\hat{\mathbf{b}} + \kappa_{\perp} \left(\mathbf{I} - \hat{\mathbf{b}}\hat{\mathbf{b}} \right)$ is anisotropic, but in this 1D study it reduces to a scalar. For simplicity we assume κ to be constant and time-steady, ignoring the dynamics of magnetic waves (see Thomas and Pfrommer 165 for a full inclusion). This assumption can be relaxed by using the equilibrium κ calculated from linear theory (see the appendix of Jiang and Oh 92, and Bustard and Zweibel 19 for an implementation of ion-neutral damping). CRs exchange momentum according to the source term $\boldsymbol{\sigma}_c \cdot [\mathbf{F}_c - (E_c + P_c)\mathbf{v}]$ and energy according to $(\mathbf{v} + \mathbf{v}_s) \cdot \boldsymbol{\sigma}_c \cdot [\mathbf{F}_c - (E_c + P_c)\mathbf{v}]$. We shall call these the generalized CR forcing and heating terms respectively. Microscopically, some degree of anisotropy in the CR distribution is required to trigger the streaming instability; macroscopically, this translates to requiring a finite P_c gradient. As $\nabla P_c \to 0$, the interaction coefficient $\sigma_c \to 0$ (equation 3.2), and CRs can free stream at the speed of light, as encapsulated by the time-dependent term in equation 3.6. The condition for the time-dependent term in equation 3.6 to be negligible is:

$$L_c = \frac{P_c}{\nabla P_c} \ll \frac{c^2}{v_A^2} v_A \Delta t. \tag{3.8}$$

where Δt is a dynamical time. This sets a condition on the strength of the P_c gradient. If it is fulfilled, the equations reduce to the standard one-moment equations [15, 155], and the CR flux, from equation 3.6, reduces to

$$\mathbf{F}_c = (\mathbf{v} + \mathbf{v}_s)(E_c + P_c) - \frac{1}{\gamma_c - 1} \nabla \cdot \boldsymbol{\kappa} \cdot \nabla P_c, \tag{3.9}$$

which shows that in the well-coupled limit, CR transport is given as a sum of advection, streaming and diffusion processes. The CR energy equation (equation 3.5) reduces to:

$$\frac{\partial E_c}{\partial t} + \nabla \cdot \mathbf{F}_c = -(\mathbf{v} + \mathbf{v}_s) \cdot \nabla P_c \tag{3.10}$$

where $\mathbf{F}_c$ is given by equation 3.9. The RHS, written in this form shall be called the coupled CR heating term, while the coupled CR forcing term is ∇P_c. In §3.2.1, we will use this canonical form of the CR equations in the well-coupled limit.

In writing the CR equations as 3.5 and 3.6 we have assumed the CR distribution function to be close to isotropic on scales larger than the scattering mean free path $\sim \kappa/c$. This is not always true, but in the well-coupled limit (which is the context of this study) it is a reasonable assumption. For more general CR equations that take into considering anisotropy in the weakly-coupled limit, see Hopkins et al. [78].

In this study we ignore any CR collisional losses due to Coulomb collisions and hadronic interactions. These losses are important in dense gas, but are unlikely to be important in the diffuse halo gas. Diffusive reacceleration is also not considered as we do not consider the effects of turbulence; the free energy for the instability here comes from the CRs themselves. In any case, reacceleration is strongly suppressed by streaming losses in the low β scenarios we consider (Hopkins et al. 72, Bustard & Oh 2022, in preparation).

We now discuss two key pieces of physics: linear growth rates for the CR acoustic instability (§3.2.1), and the CR bottleneck effect (§3.2.2).

3.2.1 CR Acoustic Instability: Linear Theory

In this section, we make order of magnitude arguments for the threshold and growth rate of instabilities driven primarily by CR diffusion and streaming respectively, in the most physically relevant asymptotic limits for the CGM. The detailed dispersion relations are derived in Appendix A.1, and solutions to these dispersion relations give the growth rates shown in Fig. 3.1. Broadly speaking, in this section we seek to understand the features seen in Fig. 3.1. The reader can get a feel for the physics of the instability here, which are relevant to understanding the simulation results in §3.3; only those interested in the technical details need to consult Appendix A.1.

If CRs were completely locked to the gas, the system would simply behave as a single fluid with adiabatic index intermediate between $\gamma_c = 4/3$ and $\gamma_g = 5/3$, depending

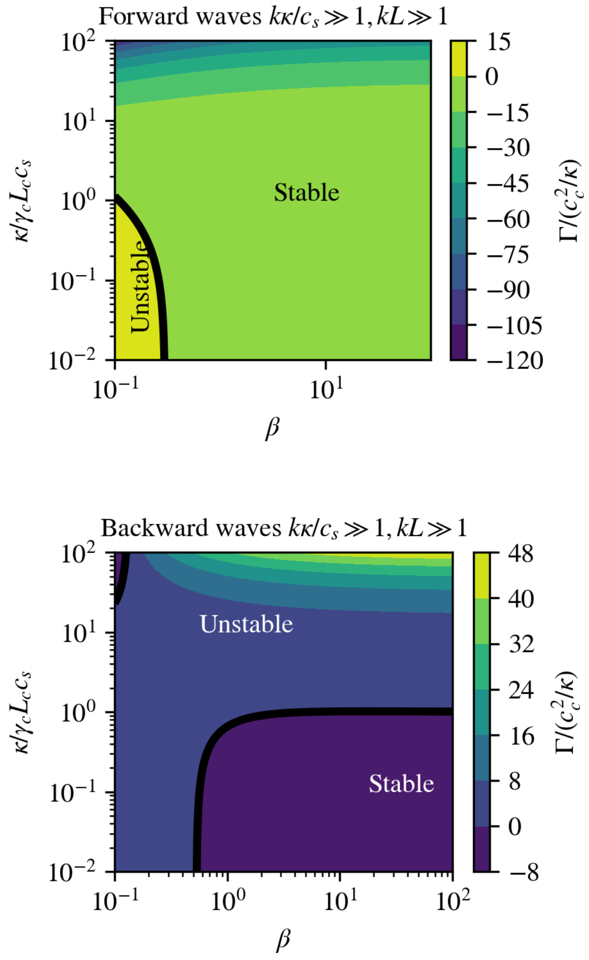

Figure 3.1: Growth rate Γ of the CR acoustic instability (in units of c_c^2/κ) as function of $\eta \equiv \kappa/\gamma_c L_c c_s$ and $\beta \equiv 2P_g/B^2$ of the forward (top) and backward (bottom) acoustic waves in the short wavelength limit ($k\kappa/c_s \gg 1$, $kL \gg 1$). The stable and unstable regimes are demarcated by a thick black line. k is the wavenumber, κ is the diffusion coefficient, $c_s \equiv \sqrt{\gamma_g P_g/\rho}$ is the gas sound speed, $c_c \equiv \sqrt{\gamma_c P_g/\rho}$ is the CR sound speed and $L_c \equiv P_c/|\nabla P_c|$ is the CR scale height. L in the subtitle of each plot is a wildcard for any kind of scale heights (density, gas, CR scale heights etc.), $kL \gg 1$ simply states that the wavelength in consideration here is sufficiently short that WKB analysis holds.

on $\alpha = P_c/P_g$. However, CRs can both stream and diffuse relative to the gas, which leads to a phase offset between gas CR pressure and gas density perturbations. In addition, CRs affect gas pressure perturbations by heating the gas as they stream. Acoustic waves thus experience external forcing. If this forcing is in phase with wave oscillations, they grow; otherwise, they damp.

There are several characteristic lengthscales in the problem:

- The mode wavelength, $\lambda \sim k^{-1}$.
- The CR diffusion length $l_{\rm diff} \sim \kappa/c_s$. This is the lengthscale over which the sound crossing time $t_{\rm sc} \sim L/c_{\rm s}$ and the diffusion time $t_{\rm diff} \sim L^2/\kappa$ are comparable. On scales below $l_{\rm diff}$, diffusion is faster than advection.
- The CR scale height $L_c = |P_c/\nabla P_c|$, as well as the gas pressure scale height $L_{\rm g}$ and the density scale height L_ρ, defined similarly.

Additionally, there are two important dimensionless parameters: $\beta = P_g/P_B$, and $\alpha = P_c/P_g$. Finally, the direction of the sound wave, and in particular whether the sound wave propagates down ('forward' wave) or up ('backward' wave) the CR pressure gradient also affects instability and growth rates.

We work in the WKB approximation $kL_c \gg 1$. Furthermore, we ignore background gas pressure and density gradients, i.e. we assume a uniform background $L_g, L_\rho \to \infty$. In Appendix A, we show that our results are unchanged even if we allow for non-zero gas pressure and density gradients. Essentially, this is because in the WKB approximation, $kL_g, kL_\rho \gg 1$, the background looks locally uniform. We still retain the CR scale height L_c because there is an additional lengthscale in CR dynamics, the diffusion length $l_{\rm diff} \sim \kappa/c_s$. The ratio $\eta \equiv l_{\rm diff}/L_c \sim \kappa/L_c c_s$ impacts CR dynamics and instability growth. If we work in the approximation where besides $kL_c \gg 1$, $kl_{\rm diff} = k\kappa/c_s \gg 1$ (i.e. the diffusion time is much shorter than the wave period), then the ratio $\eta = \kappa/L_c c_s$ is the only dimensionless parameter involving lengthscales which is important. For the purposes of this subsection, we will work in the limit where L_c is small enough that CRs are well-coupled to the thermal gas, and equations 3.9 and 3.10 apply.

For simplicity, we discuss regimes where either CR diffusion and streaming dominate. The diffusion coefficient κ is assumed constant in space and time. Since diffusion rates are independent of B-field strength, while streaming velocities and heating rates are both proportional to $v_{\rm A} \propto B$, we expect that diffusion and streaming dominated regimes correspond to high and low β respectively, a notion we shall quantify.

3.2.1.1 Diffusion dominated

Damping. ‘Drag’ against CRs provides a frictional force which damps sound waves, a phenomenon known as Ptuskin damping [130]. The physics is very similar to radiative damping of sound waves, which famously leads to Silk damping of acoustic waves in the early universe. We can estimate the damping rate as follows. Sound waves are just a simple harmonic oscillator (SHO), where the restoring force is proportional to displacement $F \propto -x$. If CR diffusion produces a perturbed CR force which is instead proportional to velocity, $F \propto -v$, then just as for the SHO, this force will damp oscillations, since it is $\pi/2$ radians out of phase with the restoring force[1]. Since we work in the limit $k\kappa/c_s \gg 1$, where diffusion is much more rapid than advection on scales of the wave period, the Lagrangian time derivative in the CR energy equation (equation 3.10) can be ignored, and CR compression is balanced by diffusion: $i\gamma_c P_{\rm c,0} k u_1 \sim -\kappa k^2 P_{\rm c,1}$, which gives rise to an acceleration:

$$\dot{u}_1 \sim -\frac{1}{\rho}\nabla P_{c,1} \sim -\frac{P_{\rm c,0} u_1}{\rho\kappa} \sim -\frac{c_{\rm c}^2}{\kappa} u_1 \tag{3.11}$$

which is indeed proportional to velocity ($\dot{u}_1 \propto -u_1$), and damps the wave, with damping rate:

$$\Gamma_{\rm damp} \sim \frac{\dot{u}_1}{u_1} \sim -\frac{c_{\rm c}^2}{\kappa}. \tag{3.12}$$

Note that the frictional force, and hence the damping rate, is independent of wavelength in this limit. Using $|P_{\rm c,1}/P_{\rm c,0}| \sim u_1/(\kappa k)$, $P_{\rm g,1}/P_{\rm g,0} \sim u_1/c_s$, we find that rapid diffusion causes the CR pressure perturbation to be suppressed:

$$\left|\frac{P_{\rm c,1}}{P_{\rm g,1}}\right| \sim \frac{c_{\rm s}}{k\kappa}\left(\frac{P_{\rm c,0}}{P_{\rm g,0}}\right) \ll 1. \tag{3.13}$$

Since CR pressure perturbations do not provide a restoring force but a damping force, the acoustic mode is driven by gas pressure perturbations, and propagates at the gas sound speed c_s. Furthermore, since the cosmic ray pressure perturbations are so small, the damping time is much longer than the wave period, $1/t_{\rm damp} c_s k \sim c_s/(k\kappa)(P_{\rm c,0}/P_{\rm g,0}) \ll 1$, even if equipartition holds $P_{\rm c,0} \sim P_{\rm g,0}$. Note also from equation 3.12 that damping is stronger for a weaker diffusion coefficient: the CR pressure perturbations are still $\pi/2$ out of phase, but now have larger amplitude. However, they can now only suppress smaller scale perturbations.

---

[1] Mathematically, this must be true since the diffusion operator brings down an additional factor of i compared to the gradient operator.

Growth with a Background gradient. If sound waves propagate in a medium with a background CR gradient, they can be driven unstable [40]. This can be understood as follows. Consider the limit of rapid diffusion. In this case, the CR gradient is time-steady and simply given by the background gradient, which is much larger than the perturbed CR gradients due to sound waves[2], which are strongly suppressed by diffusion. Since the CR gradient $-\nabla P_c$ is independent of density, any fluctuations in density will result in a differential acceleration, since underdense regions receive a larger force per unit mass:

$$\dot{u}_1 \sim \frac{\rho_1}{\rho^2} \nabla P_{c,0} \sim \mp \frac{u_1}{c_s} \frac{P_{c,0}}{\rho L_c} \sim \mp \frac{u_1}{c_s} \frac{c_c^2}{L_c} \tag{3.14}$$

where we have used $\rho_1/\rho \sim u_1/c_s$, and the $\mp$ sign refers to forward and backward waves respectively. Thus, underdense (overdense) regions having relative acceleration down (up) the gradient. The above force is proportional to velocity, and can either drive or damp sound waves. Consider density maxima, where the velocity perturbation u_1 has the same direction as wave propagation. In a forward wave, the wave and hence u_1 point down the CR gradient, but dense regions are accelerated up the gradient. We have $\dot{u}_1 \propto -u_1$, and the wave is damped. Conversely, for a backward wave, $\dot{u}_1 \propto u_1$, and the wave grows in amplitude. The growth rate is:

---

[2] This is no longer true in the non-linear phase of the instability; we address this in numerical simulations.

$$\Gamma_{\text{growth,diffuse}} \sim \frac{\dot{u}_1}{u_1} \sim \frac{c_c^2}{c_s L_c}. \tag{3.15}$$

For growth driven by a background CR gradient to overcome Ptuskin damping, we see from equation 3.12 and 3.15 that we require:

$$\frac{\kappa}{c_s L_c} > 1 \quad \text{(growth)} \tag{3.16}$$

For the sound wave to see a steady CR gradient ∇P_c independent of density, the diffusion time must be shorter than the sound crossing time across a scale height L_c, which is equivalent to equation 3.16.

3.2.1.2 Streaming dominated

We now consider the streaming dominated regime. For simplicity, and similar to Begelman and Zweibel [5], we consider a weak background gradient (L_c large) which is sufficient to couple CRs to the gas and give the streaming velocity a definite sign[3], but otherwise does not affect CR dynamics. In particular, the force and heating from the background gradient is assumed to be negligible. We will relax this assumption shortly. The magnitude of the background gradient has important implications for CR coupling and non-linear saturation, but here it just complicates matters. We do include diffusion in our WKB analysis, which is essential because otherwise there is no $\pi/2$ phase offset between CRs and density perturbations; streaming with flux $F_{\rm c} \propto P_c$ (rather than $F_{\rm c} \propto \nabla P_c$) cannot introduce a $\pi/2$ phase shift[4]. For any finite scattering rate, CRs are imperfectly locked to the Alfven wave frame, and will always diffuse relative to the wave frame.

---

[3] CRs are assumed to always stream down the background gradient, which is presumed to be larger than any gradients induced by the sound wave. If this is no longer true, very interesting consequences arise, which we explore in §3.3.

CR streaming has two effects. First, it introduces an additional advective component to CR transport which can be either aligned or anti-aligned with gas motions. Thus, it modulates the amplitude and even the sign of CR perturbations. Since the phase shift between CRs and gas depends on the competition between advective and diffusive transport, we might expect that as before, growth/damping depends on whether the wave is forward or backward. Second, CR streaming heats the gas, at a rate $v_{\rm A} \cdot \nabla P_c$, which perturbs the gas pressure. Both of these processes are only important if the streaming velocity $v_{\rm A}$ is large compared to the gas sound speed c_s, or at low $\beta \sim (c_s/v_A)^2$.

Heating is a new consideration, particular to CR streaming. Does it drive growth or damping? CR compression followed by gas heating as CRs stream out of an overdensity is a situation where the adiabatic index of the system is increasing, as energy is transferred from CRs (more compressible) to gas (less compressible). This stiffening of the equation of state is equivalent to a secular increase in the spring constant of a simple harmonic oscillator, which drives overstable oscillations. The peak pressure (arising from CR heating as CRs stream out of an overdensity) lags the peak density, and so work is done on the fluid during the expansion phase. CRs give up more energy streaming out of an overdensity than they receive during compression, and there is net energy transfer from CRs to gas[5]. Unlike the perturbed CR force, these effects are independent of the direction of wave propagation, so we expect heating to be destabilizing for both forward and backward waves.

---

[4] Importantly, stratification can introduce phase shifts, so that sound waves can be destabilized for the pure streaming case in a stratified background [131]. The instability discovered by Quataert et al. [131] is driven purely by phase shifts and does not rely on heating; hence it can operate even in isothermal gas.

We can make order of magnitude estimates for these remarks. Let us write the perturbed acceleration $\dot{u}_1 \approx \dot{u}_{1,a} + \dot{u}_{1,b}$, where $\dot{u}_{1,a}$ arises due to the phase-shifted CR force and $\dot{u}_{1,b}$ arises from gas pressure gradients due to CR heating. The calculation of the phase-shifted, perturbed CR force is the same as for Ptuskin damping, where compression and diffusion balance, except that now:

$$u_1 \rightarrow u_1 + v_{\mathrm{A},1} = u_1 - \frac{1}{2}\frac{\rho_1}{\rho_0} v_A = u_1 \left(1 \mp \frac{v_{\mathrm{A}}}{c_s}\right) \tag{3.17}$$

where we have used $\rho_1/\rho \sim \pm u_1/c_s$, and $\mp$ sign is for forward and backward waves respectively ($v_{\mathrm{A},1}$ always points down the CR gradient, whereas u_1 depends on whether the wave is forward or backward). From substituting this replacement for u_1 into equation 3.11, we obtain a perturbed acceleration from the phase-shifted CR force:

---

[5] This is in contrast to the diffusion case, where CRs expand 'for free', without transferring energy to the gas. In this case, there is net energy transfer from the gas to the CRs, and the wave damps.

$$\dot{u}_{1,a} \sim -\frac{1}{\rho}\nabla P_{c,1} \sim -\frac{c_c^2}{\kappa}\left(1 \mp \frac{v_{\rm A}}{2c_s}\right) u_1 \tag{3.18}$$

The perturbed gas pressure from heating is $\dot{E}_g \sim \omega P_{g,1}/(\gamma_g - 1) \sim v_A \cdot \nabla P_c \sim \pm i v_A k P_c$. Solving for $P_{g,1}$, and using $\omega \sim kc_s$, we obtain a perturbed acceleration from CR heating:

$$\dot{u}_{1,b} \sim -\frac{1}{\rho}\nabla P_{g,1} \sim \pm(\gamma_g - 1)\frac{v_A}{c_s}\dot{u}_{1,a}. \tag{3.19}$$

We thus obtain a net acceleration: $\dot{u}_1 = \dot{u}_{1,a} + \dot{u}_{1,b} = (1 \pm (\gamma_g - 1)v_A/c_s)\dot{u}_{1,a}$. Using equation 3.18 and $\Gamma = u_1/\dot{u}_1$, we obtain:

$$\Gamma_{\rm stream} = -\frac{c_c^2}{2\kappa}\left(1 \mp \frac{1}{2\beta^{1/2}}\right)\left(1 \pm \frac{(\gamma_g - 1)}{\beta^{1/2}}\right) \tag{3.20}$$

as derived by Begelman and Zweibel [5]. Note that instability arises for both forward waves (if $\beta \lesssim 0.25$) and backward waves (if $\beta \lesssim (\gamma_g - 1)^2 = 0.5$, note that we are using $\lesssim$ as this is an approximate calculation). The thresholds differ because u_1 and $v_{\rm A,1}$ can be either aligned or anti-aligned, depending on the direction of wave propagation. The perturbed CR force only destabilizes forward waves, while at sufficiently low β, CR heating destabilizes waves independent of wave direction (as can be seen if the second terms in the two brackets in equation 3.20 dominate).

The growth rate is proportional to the Ptuskin damping rate due to diffusion, $\Gamma_{\rm stream} \sim -\beta^{-1}\Gamma_{\rm damp}$. The diffusive flux $F_{\rm d} \propto \nabla P_c$ is important since it causes a $\pi/2$ phase shift, so that perturbed forces are proportional to velocity rather than displacement. The diffusion time of CRs thus still sets a characteristic timescale. However, by changing the amplitude and sign of total pressure perturbations, CR streaming converts Ptuskin damping ($\dot{u}_1 \propto -u_1$) to a destabilizing force ($\dot{u}_1 \propto u_1$), with a growth rate which depends on the rapidity of streaming and hence heating.

Broadly speaking, in the WKB regime $kL_c \gg 1$ and $k\kappa/c_s \gg 1$, there are two instability regimes, the streaming dominated regime $\beta \lesssim 0.5$, which is unstable regardless of $\kappa/c_s L_c$, and the diffusion dominated regime, $\kappa/c_s L_c > 1$, which is unstable regardless of β. Growth rates, however, can depend on the secondary parameter. This is essentially what we see in Fig 3.1. In both cases, the instability threshold does not depend on P_c/P_g, although growth rates do. The growth rates are simply $c_c^2/\min(2c_s L_c, 6\beta\kappa)$. Where both instabilities are allowed, we anticipate that diffusion dominates when $c_s L_c < 3\beta\kappa$, and vice-versa.

For completeness, we derive in Appendix A.1 an equation governing the growth of an acoustic perturbation as it propagates in an arbitrary background profile in the limit $k\kappa/c_s \gg 1$. Its growth rate can be expressed as

$$\begin{aligned}\Gamma_{\rm grow} = -\frac{c_c^2}{2\kappa}\Bigg\{&\left[1 \pm (\gamma_g - 1)\frac{v_A}{c_s}\right]\left(1 \mp \frac{v_A}{2c_s}\right) \\ &\pm \frac{\kappa}{\gamma_c L_c c_s}\left(1 \pm (\gamma_g - 1)\frac{v_A}{2c_s}\right)\Bigg\}. \end{aligned} \tag{3.21}$$

This quantity has to be greater than zero for growth. In the absence of streaming, we recover the instability condition $\kappa/\gamma_c L_c c_s > 1$ for backward waves as estimated in equation 3.16. In the streaming dominated regime, where $\kappa/\gamma_c L_c c_s \ll 1$, the growth condition are $\beta < 0.3$ for forward waves and $\beta < 0.533$ for backward waves, consistent with the approximate calculation in eqn.3.20. Since waves of both signs are generally present, as a general rule of thumb $\beta \lesssim 0.5$ will result in the CR acoustic instability.

3.2.2 CR Bottleneck Effect

A streaming dominated fluid well-coupled[6] with CRs should in steady state obey, along the B-field, the following[7] [15]

$$P_c(v + v_A)^{\gamma_c} = \text{const} \tag{3.22}$$

This relation can be derived by setting the time-dependent and CR diffusion terms to zero in equation 3.5 and 3.6 and integrating. For a static fluid and for constant B-field (true in our 1D simulations), this reduces to:

$$P_c \rho^{-\gamma_c/2} = \text{const}. \tag{3.23}$$

The CR pressure rises with density.

This property, together with the requirement that CRs can only stream down their gradient, leads to an unusual feature of CR transport known as the 'bottleneck effect',

---

[6] Well-coupled means that CRs have the steady state flux form (eqn.3.9), with a nearly isotropic distribution function.

[7] This conserved quantity is geometry dependent. In spherically symmetric geometry, for example, the conserved quantity is $r^2 P_c(v + v_A)^{\gamma_c}$.

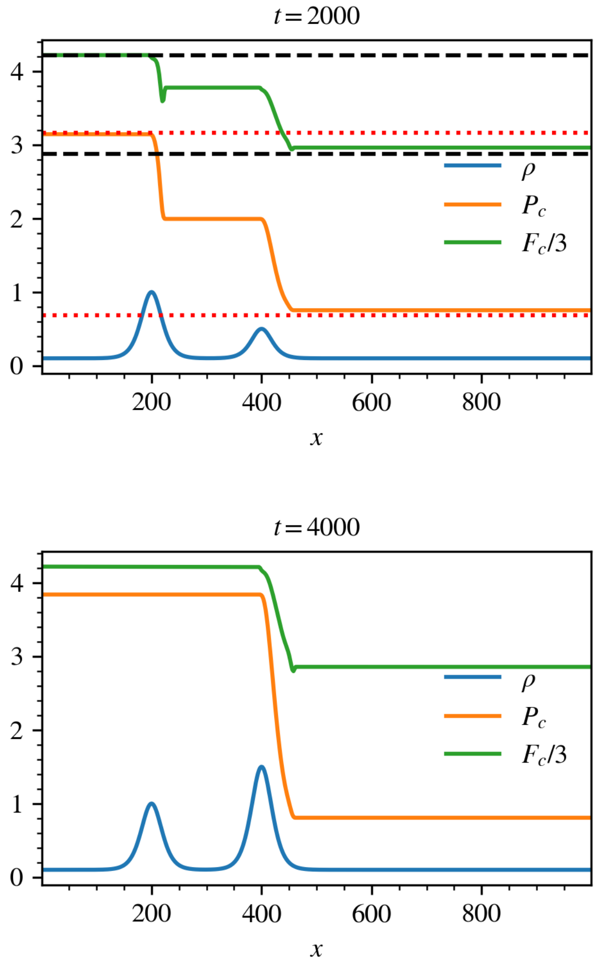

FIGURE 3.2: *The bottleneck effect.* Only the CR variables are evolved while the gas variables are held fixed. A double peak is initialized in the static density field, the denser peak at $x = 200$, the other at $x = 400$. CR pressure responds with a double plateau. Just after $t = 2000$, the peak at $x = 400$ is manually pushed up to 1.5. As seen in the bottom panel, the two P_c plateaus merge. The two panels show the equilibriated P_c, ρ and F_c profiles before and after the push. Note that the upper panel shows the density and CR pressure field *just before* the second peak is modified and F_c has been rescaled for comparison. The bottom panel is the steady-state solution to the updated bump. The region enclosed by the black dashed lines represents ΔF_c predicted using the density profile and equation 3.27. Similarly, the region enclosed by the red dotted lines represents ΔP_c predicted using the density profile and equation 3.26. Both are in good agreement with simulation. If instead we start out with the bump structure in lower panel and manipulate the bumps to end up with that in the upper panel, the CR pressure and flux profiles adjust accordingly to give the results in the upper panel.

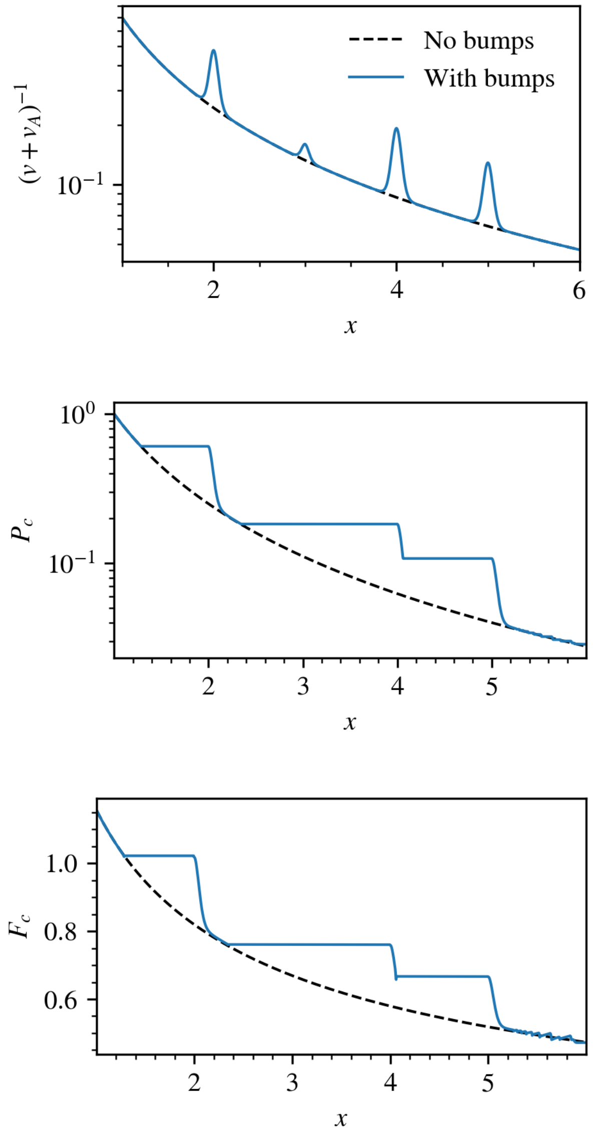

FIGURE 3.3: Steady state profiles of CR sub-system which in one case, denoted by black dashed lines, the $(v + v_A)^{-1}$ profile is initiated without bumps and the other case, denoted by solid blue lines, it is initiated with several bumps. None of the bumps rise above the global maximum of the background profile. The overall ΔP_c and ΔF_c with and without bumps are the same.

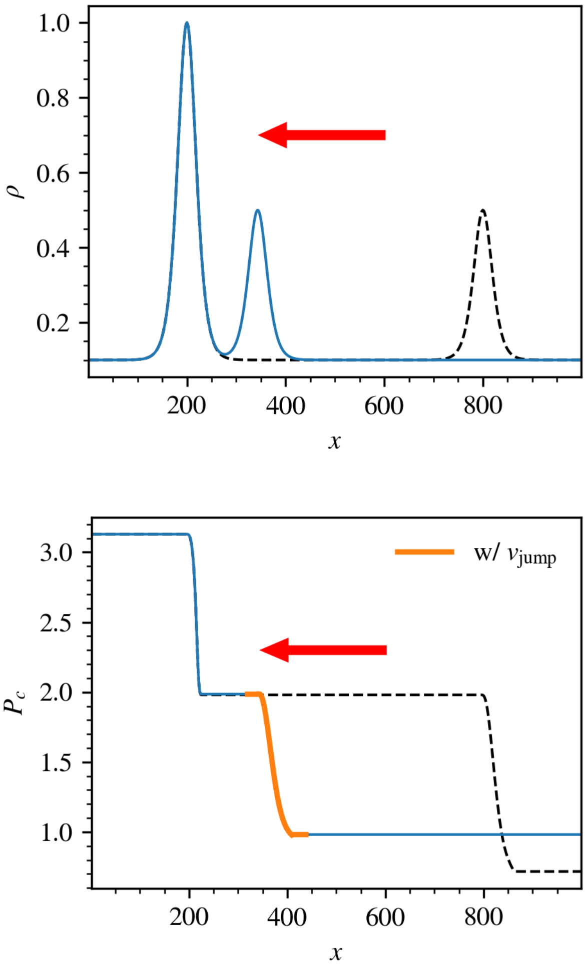

FIGURE 3.4: These two panels denote the possible effect of a moving bump on the P_c jumps. The upper panel shows the density field while the lower panel shows the CR pressure. Similar to the setup in fig.3.2, only the CR variables are evolved while the gas variables remain decoupled. Initially, two density peaks are placed apart at $x = 200$ and $x = 800$ and kept stationary (see the black dashed line in the upper panel). The equilibrated P_c profile is shown by the black dashed line in the lower panel. Some time after the initial equilibrium the peak at $x = 800$ is moved manually at constant speed towards $-x$ while the peak at $x = 200$ remains fixed. The red arrow indicates the direction of motion. The subsequent density and P_c profiles when the peak has moved to $x = 350$ are indicated by the solid blue lines. The orange line denotes the P_c profile across the second bump evaluated using equation 3.28, including the effect of $v_{\rm jump}$.

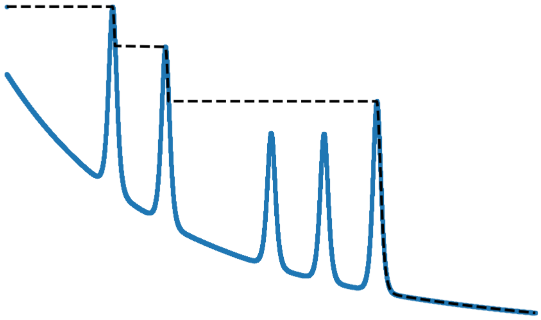

FIGURE 3.5: Constructing a convex hull over wiggly curve, surface, etc. is similar to covering it with a rubber band that connects all the highest peaks. Fluctuations lying in the valley between the ridges are swept under the rubber band. See Vergassola et al. [175]. Note that the convex hull described here is slightly different from the canonical mathematical definition.

predicted analytically by Skilling [156] and first simulated by Wiener et al. [183]. For simplicity, consider a 1D setup with constant B-field pointing in the $+x$-direction, the gas variables held fixed, and CRs streaming towards the $+x$ direction. Now suppose the CRs encounter an overdense bump. Equation 3.23 demands that P_c increases at the rising edge with the density. This contradicts the requirement that CRs only streams down the P_c gradient. The resolution (seen in Fig 3.2) is for P_c to flatten on the incoming side and for CRs to decouple from that gas in that region; they free-stream at the speed of light. CRs recouple to the gas and obey equation 3.22 on the far side of the density bump, where gas density and hence P_c falls, with CRs streaming down the gradient. Physically, the decrease in Alfven speed as the density rises causes a CR traffic jam at the bump, causing CR pressure to build up and flatten out. Simulations of this bottleneck effect in the presence of a single bump have been conducted in 1D by Wiener et al. [183], Jiang and Oh [92], and in 2D[8] by Bustard and Zweibel [19].

---

[8] Note that B-field geometry does affect how well the bottleneck equation 3.22 is obeyed as it influences the magnitude of the streaming velocity along x. Here, we assume that B and ∇P_c

Here, we follow a similar setup as in Jiang and Oh [92] in considering a CR sub-system (i.e. a constant B-field pointing in the $+x$-direction, keeping the gas variables fixed and allow only the CR variables to vary). However, here we consider the impact of multiple density peaks. Two density bumps are placed apart from each other, one higher than the other. The initial CR pressure is set to near zero and the CR flux to zero. CRs are injected by fixing the CR flux at the inner boundary ($x = 0$), while keeping inner CR pressure boundary free. At some time well after the P_c profile has equilibriated, the second density bump is pushed manually down to lower than the first and the P_c profile allowed to adjust and equilibrate. The result is shown in Fig 3.2, and can be described as follows: CRs always bottleneck behind the highest density peak they see from the incoming direction. Specifically, incoming CRs would bottleneck and form a plateau all the way up to the highest density peak they see, and upon climbing down in a fully coupled manner (for which equation 3.23 holds), bottleneck up the next highest peak and so on and so forth, forming a staircase. Should the order of peak heights be changed, manually in fig.3.2, or (in our simulations of the CR acoustic instability) due to rise of some newly seeded unstable modes, for example, then the P_c profile will adjust accordingly such that the above holds true in steady state. Thus, if instead we start out with the bump structure in lower panel of fig.3.2 and manipulate the bumps to end up with that in the upper panel, the CR profiles adjust to give the results in the upper panel. If the fluid has a background flow or

---

are aligned. The general case of a non-aligned mean field which in addition changes direction can introduce additional bottlenecks, but is beyond the scope of 1D simulations.

variable B-fields, equation 3.22 holds, with CR bottlenecks at the deepest minima of $(v + v_A)$.

How is the net momentum and energy transfer from CRs affected by the presence of a staircase? The spatial distribution is obviously affected, since there is no momentum and energy transfer at the plateaus; instead, these only happen at the staircase jumps, where the CRs are coupled [9]. However, we shall now show that in a static setup, the total momentum and energy transfer from CRs to the gas only depends on the net change in Alfven speed across the profile. If the bump structure does not change this, then even if a CR staircase develops, the total momentum and energy transfer is unaffected.

Consider the previous setup in the coupled limit. The net momentum transfer by CR forces, integrated over the profile, is:

$$\int dx \, \nabla P_c = -\Delta P_c \tag{3.24}$$

Similarly, in our static setup, the net amount of CR heating in steady-state is:

$$\int dx \, v_A \cdot \nabla P_c = \int dx \, \nabla \cdot F_c = -\Delta F_c. \tag{3.25}$$

Since we deal exclusively with decreasing P_c and F_c profiles and will make use of ΔP_c and ΔF_c frequently in the following, we defined $\Delta P_c = P_{\text{c,left}} - P_{\text{c,right}}$ and

---

[9] In our subsequent simulations of the acoustic instability, the jumps propagate and eventually all gas fluid elements experience a force and CR heating.

$\Delta F_c = F_{\rm c,left} - F_{\rm c,right}$ to ensure positive definiteness, hence the minus sign.

Fig.3.3 shows a smooth density profile and the associated background P_c profile (without bumps) and the steady-state P_c profile in the presence of bumps. Again, we decouple the hydrodynamics so that the gas distribution does not evolve. While the spatial distribution of P_c (and hence the spatial distribution of CR momentum and energy transfer) is strongly affected by the presence of bumps, the net momentum/energy transfer (ΔP_c and ΔF_c respectively) is almost unchanged. See also Wiener et al. [183] for similar conclusions (their sections 3.6, 3.7). The CR pressure only changes where CRs are coupled; there, $P_c \propto v_{\rm A}^{-\gamma_c}$. Thus, $\Delta P_c \propto \Delta[v_A^{-\gamma_c}]$. Since the net density drop is the same, so is the net change in v_A and hence P_c. Similarly, the net change in the flux is given by $\Delta F_c \approx \Delta(P_c v_A) \propto \Delta[v_A^{1-\gamma_c}]$, so the net heating is also determined by the initial and final Alfven speeds (in our 1D sims with constant B-field, this is equivalent to the net density jump). Since these are almost unchanged by the presence of bumps, the net heating rate is similar.

The net momentum transfer in Fig 3.2, $\Delta P_c \propto \Delta[v_A^{-\gamma_c}]$, is similarly given by the net change in the Alfven speed:

$$\Delta P_{\rm c} = P_{\rm c,left}\left[1 - \left(\frac{v_{A,\rm min}}{v_{A,\rm right}}\right)^{\gamma_c}\right] \tag{3.26}$$

where $P_{c,\rm left} = (\gamma_c - 1)F_{c,\rm inj}/\gamma_c v_{A,\rm min}$. The net energy transfer is likewise $\Delta F_c \approx \Delta(P_c v_A) \propto \Delta[v_A^{1-\gamma_c}]$, or

$$\Delta F_c = F_{c,\rm inj}\left[1 - \left(\frac{v_{A,\rm min}}{v_{A,\rm right}}\right)^{\gamma_c - 1}\right]. \tag{3.27}$$

We show $\Delta P_c, \Delta F_c$ calculated using these equations as dashed black lines in Fig. 3.2; they agree well with the simulations. When the second peak is pushed up in the lower panel of fig.3.2 there is an increase in ΔP_c and ΔF_c, as expected.

In many realistic applications (and certainly in the CR acoustic instability) the density profile is not static but dynamic, and the density peaks are seldom stationary. As we will see in §3.3 the non-linear evolution of the CR acoustic instability often involves density bumps propagating up the CR pressure gradient. The P_c profile develops into a propagating staircase in which equation 3.22 holds only in the respective rest frames of the jumps. The motion of the jumps will have non-negligible effect on the P_c jumps and hence the overall energy and momentum transfer. A simple illustration is given in Fig.3.4, again evolving only the CR sub-system, in which a density peak manually moved at constant speed to the left, incurs a reduced P_c jump at the moving peak.

How can we understand this? The key is to realize that equation 3.22 only holds in the rest frame of the jumps, which is the frame where the density (and hence P_c) is time-steady. In the lab frame, the conserved quantity is therefore:

$$P_c(v + v_A - v_{\rm bump})^{\gamma_c} = \text{const} \tag{3.28}$$

instead, where v is the lab frame velocity profile and $v_{\rm bump}$ is the propagation velocity of the bump. In Fig 3.4, we show the result of applying equation 3.28, which matches the simulation results well.

The conservation law in equation 3.28 has 3 asymptotic limits, when each of the 3 terms $v, v_A, v_{\rm bump}$ dominates. When the CR flux $F_c \sim 4P_c v$ is dominated by gas flows, and the CRs simply advect with the gas, then $P_c \propto v^{-\gamma_c} \propto \rho^{\gamma_c}$, i.e. the CRs are adiabatic with an adiabatic index $\gamma_c = 4/3$ for a relativistic fluid. When the CR flux is dominated by streaming $F_c \sim 4P_c v_A$, then $P_c \propto v_A^{-\gamma_c} \propto \rho^{\gamma_c/2}$ (for constant B), which is a limit most studied in the literature for the bottleneck effect [19, 183]. When $v_{\rm bump} \gg v, v_A$, then the CR flux in the frame of the bump is $F_c \sim 4P_c v_{\rm bump}$, which is constant. As $\nabla \cdot F \to 0$, from equation 3.10, $\nabla P_c \to 0$, i.e. $P_c \to$const at the moving bump, as is also given by equation 3.28. The motion of the bump reduces CR heating of the gas, and when $v_{\rm bump} \gg v, v_A$, there is almost no apparent energy exchange between the two fluids! In this limit, the heating time $\sim l_{\rm bump}/v_A$ is much longer than the bump propagation time $\sim l_{\rm bump}/v_{\rm bump}$ (where $l_{\rm bump}$ is the bump size), so before the CRs have a chance to transfer much energy, the bump has already moved on.

Another perspective is to see that the motion of the density bump weakens the minimum in $(v + v_A - v_{\rm bump})$, and reduces the strength of the bottleneck. The moving bump makes a net time-averaged contribution to the density profile which is much smoother than the density profile of the stationary bump, and approaches the background profile for a rapidly moving bump. If the background profile is already flat, as in this example, then coupling between the CRs and gas becomes weak and there is hardly any CR staircase. In this way, the motion of density bumps alters the CR staircase (and energy and momentum transfer) compared to the stationary case, where staircase heights are maximized. We will return to this when interpreting our simulation results. Note that if bumps are propagating at different velocities, then one must apply a different frame transformation for each bump. Although one can still infer the CR staircase structure given velocity information, the lack of a global reference frame means that it is no longer possible to write $\Delta P_c, \Delta F_c$ in terms of endpoint quantities, as in equation 3.26 and 3.27.

These properties are the basis for the 'staircase' features seen in the non-linear outcome of the CR acoustic instability, and discussed further in §3.3.3. Interestingly, such staircase features are also seen in Lagrangian maps (i.e., correspondence between initial (Lagrangian) and final (Eulerian) particle positions) in adhesion models of cosmological structure formation [175]. They are also seen in doubly diffusive fluids, such as sea water where both salt and heat diffuse [137]. However, we caution that while some mathematical machinery can be used in common, the origin and physics of these staircases is quite different. In particular, the CR staircase arises from features peculiar to CR transport – namely, the bottleneck effect in a two-fluid system.

Mathematically, the P_c staircase is similar to constructing a convex hull (see fig.3.5) of ρ (or $(v + v_A)^{-1}$ for non-zero flow) and then determining P_c from equation 3.23 (or 3.22). A convex hull is the smallest convex set that encloses a particular shape. For our purposes, given a plot of $(v + v_A)^{-\gamma_c}$ as a function of position, the convex hull of this structure is the non-increasing set of lines of minimal length which encloses all points, including the peaks. As shown in Fig 3.5, it is equivalent to connecting the peaks with rubber bands, via horizontal ridge lines.

The reasoning above did not take into account multi-dimensional effects, e.g. that due to magnetic field draping around density enhancements [158]. Bustard and Zweibel [19] show in 2D that magnetic field strength can affect the path CRs choose around density peaks. Particularly, it was shown that a higher magnetic field facilitates penetration of CRs into density peaks, since magnetic tension causes the field lines to resist draping. The bottleneck effect can be important in this case.

3.3 Simulation

The following simulations were performed with Athena++ [160], an Eulerian grid based MHD code using a directionally unsplit, high order Godunov scheme with the constrained transport (CT) technique. CR streaming was implemented with the two moment method introduced by Jiang and Oh [92]. This code solves equations 3.1–3.7. Cartesian geometry is used throughout.

3.3.1 Setup

Our 1D setup consists of a set of initial profiles, source terms and appropriate boundary conditions. Magnetic field is constant both in space and time in 1D Cartesian geometry (as required to maintain $\nabla \cdot B = 0$). Both CR transport modes (streaming and diffusive) are present. We assume that CRs stream at the local Aflven speed v_A. Slippage from perfect wave locking gives rise to CR diffusion, which in the absence of a model for damping, is assumed constant in space and time. In this study we focus mostly on streaming dominated transport; the CR diffusion coefficient is usually taken to be small (in a sense we shall quantify).

The CR acoustic instability is a small scale instability that only depends on local conditions. In the following we will frequently reference our setup to actual galactic halo conditions, obtained mostly from galaxy scale simulations. The purpose of doing so is to provide a context for which this instability could act. Our 1D Cartesian setup can be crudely thought of as mimicking the vertical profile of disk galaxies, though obviously it is highly idealized. However, it allows for high resolution and a detailed scrutiny of the physics in this first study.

3.3.1.1 Initial Profiles

The initial profiles are calculated by solving a set of ODE's assuming time steadiness of the fluid equations. In the absence of any instability, the initial profiles will remain steady in simulations. To simplify our calculations, we assume a power law profile in the gas and CR pressure and calculate the required density, velocity profiles and gravity, cooling/heating source terms required for these profiles to remain time-steady.

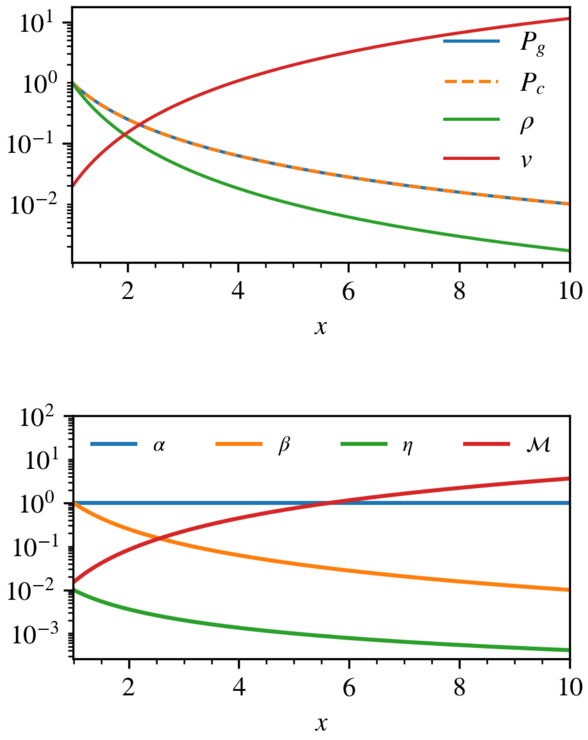

FIGURE 3.6: Top: Typical initial ρ, v, P_g, P_c profiles found by integrating eqn.3.31 from $x = 1$ to 10. The profiles shown are obtained with $\alpha_0 = 1, \beta_0 = 1, \eta_0 = 0.01, \mathcal{M}_0 = 0.015, \phi = 2$. Bottom: Typical variation of $\alpha, \beta, \eta, \mathcal{M}$ with x.

The pressure profiles take the form:

$$P_g = P_{g0}\left(\frac{x}{x_0}\right)^{-\phi}, \tag{3.29}$$

$$P_c = \alpha_0 P_{g0}\left(\frac{x}{x_0}\right)^{-\phi}, \tag{3.30}$$

for some specified ϕ, x_0, P_{g0} and α_0. For pressure to decrease with radius, $\phi > 0$. A power law pressure profile is motivated by galaxy scale simulations (e.g. van de Voort and Schaye 173) and its simplicity in describing a generic halo profile. Since magnetic fields are constant in our model, this implies that $\beta \propto x^{-\phi}$, i.e. the gas becomes magnetically dominated at large x. Physically, magnetically dominated halos can arise in simulations [125, 174] and in analytic solutions [85]; we discuss this further in §3.4.

Specifying the density ρ_0, velocity v_0 and Alfven speed $v_{A0} = B/\sqrt{4\pi\rho_0}$ at x_0, the velocity v and density ρ profiles are found by integrating from x_0 the equations

$$\frac{\mathrm{d}}{\mathrm{d}x}(v+v_A) = \frac{\kappa P_c'' - (v+v_A)P_c'}{\gamma_c P_c}, \tag{3.31}$$

$$\rho v = \text{constant}, \tag{3.32}$$

where the first equation is the steady state version of equation 3.10, and the second from mass conservation. Each prime means an additional derivative with respect to x. As mentioned above, B and κ are constants. An example of the initial profiles is shown in fig.3.6. Using the steady state profiles calculated, the gravity source term g is defined as

$$g = \left(\rho v\frac{\mathrm{d}v}{\mathrm{d}x} + \frac{\mathrm{d}P_g}{\mathrm{d}x} + \frac{\mathrm{d}P_c}{\mathrm{d}x}\right)/\rho \tag{3.33}$$

to ensure momentum balance. To have a sense of what functional form ρ and g have, consider the sub-sonic and sub-Alfvenic limit where we can ignore terms involving the velocity v (for a galactic halo/wind profile this would hold near the base of the profile). For streaming dominated transport the diffusive term in equation 3.31 can be ignored, which then reduces to equation 3.23. We obtain, for the density, a power law profile:

$$\rho = \rho_0\left(\frac{x}{x_0}\right)^{-3\phi/2}, \quad v \ll c_s, v_A. \tag{3.34}$$

The gravity term has a power law form too:

$$g = \frac{\phi P_{g0}(1+\alpha_0)}{\rho_0 x_0}\left(\frac{x}{x_0}\right)^{\phi/2-1}, \quad v \ll c_s, v_A, \tag{3.35}$$

where we have used $\gamma_c = 4/3$. In our fiducial setup ($\phi = 2$), gravity is constant until the critical point (see discussion below equation 3.40).

For cooling, adiabatic processes and CR heating is balanced by a time-independent heating/cooling term $\mathcal{H}(x)$, defined using the steady state profiles,

$$\begin{aligned}\mathcal{H} = \Bigg[& v\frac{\mathrm{d}P_g}{\mathrm{d}x} + \gamma_g P_g \frac{\mathrm{d}v}{\mathrm{d}x} \\ &+ (\gamma_g - 1) v_A \frac{\mathrm{d}P_c}{\mathrm{d}x}\Bigg] / (\gamma_g - 1).\end{aligned} \tag{3.36}$$

In the subsonic and sub-Alfvenic limit this approximates to

$$\mathcal{H} = -\frac{\alpha_0 \phi P_{g0} v_{A0}}{x_0}\left(\frac{x}{x_0}\right)^{-\phi/4-1}, \quad v \ll c_s, v_A. \tag{3.37}$$

Although not fully realistic, it is a simple and attractive setup in global force and energy balance. Note that it *does* have cooling, which in the background profile offsets CR Alfven heating. However, this cooling is simply a function of spatial position, rather than thermodynamic variables. This simplification allows us to initialize arbitrary profiles which are still in energy balance.

Thus, in each scenario the initial profile is determined by the parameters:

- $\rho_0, \mathcal{M}_0,\ P_{g0}, \alpha_0, \beta_0, \eta_0, \phi$.

The subscripts 0 all indicate they are defined at x_0. The dimensionless parameters are defined as

$$\alpha_0 = P_{c0}/P_{g0}, \quad \beta_0 = 8\pi P_{g0}/B^2, \quad \eta_0 = \kappa/\gamma_c L_{c0} c_{s0},$$
$$\mathcal{M}_0 = v_0/c_{s0}, \tag{3.38}$$

where $c_{s0} = \sqrt{\gamma_g P_{g0}/\rho_0}$ is the adiabatic sound speed and $L_{c0} = |P_c/P_c'|_0$ is the CR scale height. Note that $L_{c,0} = x_0/\phi$, so x_0 can also be interpreted as a CR pressure scale-height. In general, $\alpha, \beta, \eta, \mathcal{M}$ (defined similarly as 3.38 but without the subscript 0) vary along the profile. Their typical variation is given by the bottom plot of fig.3.6. β and η usually decrease as x increases while $\mathcal{M}$ increases[10]. α, by construction of the power law pressure profile equations 3.29 and 3.30, is a fixed quantity throughout. Unless otherwise specified, we set $\rho_0 = 1, P_{g0} = 1$ and $x_0 = 1$.

One issue in 1D Cartesian geometry is the transition to supersonic flow. If we combine the Euler equation with equation 3.22 (in the streaming dominated regime), we obtain, after some manipulations, the wind equation

$$\frac{\mathrm{d}v}{\mathrm{d}x} = \frac{g(x)}{v(v^2 - c_{\text{eff}}^2 - c_s^2)}, \quad \text{1D Cartesian} \tag{3.39}$$

---

[10] Note that κ is constant in our setup. Since L_c increases further out in the halo, this causes η to fall with distance. Realistically κ should vary with location (e.g., due to weaker self-confinement, κ is likely to increase further out in the halo), so the overall variation of η is unclear. For simplicity, we do not consider alternate forms of η.

where

$$c_{\text{eff}}^2 = \frac{\gamma_c P_c}{\rho}\frac{v+v_A/2}{v+v_A}, \quad c_s^2 = \frac{\mathrm{d}P_g}{\mathrm{d}\rho}. \tag{3.40}$$

As usual with wind equations, there is some critical point where the wind becomes transonic (i.e. $v^2 = c_{\text{eff}}^2 + c_s^2$ in this case). To avoid any singularity, $g(x)$ has to go through zero at the critical point, and indeed it must change sign if the wind is to keep acceleration $(\mathrm{d}v/\mathrm{d}x > 0)$. This is obviously unphysical. We cannot focus on subsonic flow alone in our simulations; the flow must be supersonic at large x to avoid boundary problems (see §3.3.1.2). In reality, at large radii disk winds transitions to a more spherical geometry, where this problem no longer occurs. But for simplicity, we simply solve for the gravitational field $g(x)$ which maintains a steady wind solution through the sonic point in Cartesian geometry. Our conclusions are unchanged if we focus solely on the subsonic portion of the flow, where the gravitational field is fully realistic (e.g., constant or power law up to the sonic point).

We shall try to answer the following questions with this 1D setup: 1. Verify the linear growth of the CR acoustic instability and study the non-linear growth and saturation. Since we find that the non-linear CR profile exhibits a staircase structure, we follow up with the questions below: 2. How can we understand the staircase structure and characteristic scales? 3. How does the staircase affect the time-averaged momentum and energy transfer between the gas and CR?

Our simulations focus on situations where streaming dominates CR transport, i.e. $\kappa/L_c c_s \sim \eta \ll 1$. The CR diffusion dominated limit (with $\eta \gtrsim 1$) has already been studied [40, 42, 100, 131, 142]. In actual simulations using the two-moment formalism, the diffusion coefficient κ is never set to zero (as that would give `nan` in the calculation of σ_c, equation 3.7). Also, with our boundary conditions, the very fast growth rates for small κ cause the simulations to crash. We find that for stability and numerical convergence, the diffusion length $l_{\rm diff} \sim \kappa/c_s$ has to be resolved with $\gtrsim 4$ grid cells. Thus, the minimum value of κ in our simulations is dictated by resolution. Since the diffusion length is resolved, the fastest growing, small-scale modes in our simulation are in the limit $k\kappa/c_s > 1$. As discussed in Appendix A.1.2, on scales below the diffusion length, growth rates are independent of wave number. In addition, the acoustic mode dominates, $\omega \approx \pm kc_s$, i.e. the wave propagation speed is simply the gas sound speed.

3.3.1.2 Static and Outflow Setup and Boundary Conditions

Linear Growth. To evaluate linear growth rates, we will (mostly) adopt a static background. The initial profiles are first evaluated up to the boundary ghost zones and input into the simulation box. Then an acoustic wave is generated from a boundary and its amplitude tracked as it propagates. We perturb the velocity, gas density and pressure as follows:

$$\delta v = A\zeta(t)\sin(\mp kc_s t), \quad \delta\rho = \pm\rho\frac{\delta v}{c_s}, \quad \delta P_g = \pm\gamma_g P_g\frac{\delta v}{c_s}, \tag{3.41}$$

where A is some injection amplitude and ρ, P_g, c_s are evaluated at the boundary with the top sign for forward propagating waves, and bottom sign for backward waves. The perturbations are multiplied by a buffer function $\zeta(t)$, given by

$$\zeta(t) = 1 - e^{-t/\tau} \tag{3.42}$$

where τ is small (around one wave-crossing time), to ensure the wave profile and its derivatives are continuous when the acoustic perturbation is injected.

Non-Linear Growth. When studying the non-linear growth and saturation, we include a background flow. As we shall explain, this is important to avoid boundary effects; it also mimics a disk wind. We impose the initial density, gas pressure and CR flux onto the inner ghost zones while keeping the CR pressure free by linearly extrapolating from the active zones. The inner velocity is determined by maintaining constant mass flux. For the outer boundary, we copy the density, gas pressure and CR flux from the last active zone and linearly extrapolate the CR pressure. The velocity is again determined from constant mass flux. This set of boundary conditions mimics a stratified disk atmosphere with the inner boundary fixed by galactic disk properties and the outer boundary kept free. To limit boundary effects, a buffer zone with viscosity is added near the boundaries to damp out inbound or outbound unstable acoustic waves[11]. Still, it is important, when the outer boundary is kept free, to initiate a background velocity such that the flow near the outer boundary is supersonic, as

---

[11] Specifically, we add the term $\nu\nabla^2 v$ to the momentum equation, where ν is chosen to be small enough not to affect the overall profile, but large enough to damp out high frequency sound waves.

Identifier	Dir. of prop.	α_0	β_0	η_0	ϕ	λ ($l_{\rm diff,0}$)	Inj. amp.	resolution ($\lambda/\Delta x$)
alpha1beta1eta.01phi2	Up	1	1	0.01	2	1	1.84×10^{-5}	109
alpha1beta1eta.1phi2	Up	1	1	0.1	2	0.1	1.99×10^{-4}	109
alpha10beta1eta.1phi2	Up	5	1	0.1	2	0.1	1.99×10^{-5}	109
alpha1beta.1eta1phi2	Up	1	0.1	1	2	0.01	2.35×10^{-4}	109
alpha1beta.01eta10phi2	Up	1	0.01	10	2	0.003	3.47×10^{-4}	328
alpha1beta.1eta.1phi1	Up	1	0.1	0.1	1	0.1	1.57×10^{-4}	219
alpha1beta.1eta.1phi.5	Down	1	0.1	0.1	0.5	0.1	1.44×10^{-4}	437
alpha1beta.1eta.1phi2	Up	1	0.1	0.1	2	0.1	1.29×10^{-5}	109
alpha1beta.5eta.1phi2ms.03[a]	Up	1	0.5	0.1	2	0.1	1.87×10^{-5}	109

[a] A background flow with $\mathcal{M}_0 = 0.03$ (see eqn.3.38) is initiated for this case.

Table 3.1: Parameters for simulation of linear growth of acoustic waves. Column 1: Case identifier. Column 2: Direction of propagation up or down the CR pressure gradient. Column 3-5: Parameters defined in equation 3.38. Column 6: Power-law index of the background P_c profile defined in eqn.3.30. Column 7: Wavelength of the acoustic wave in units of $l_{\rm diff,0} \equiv \kappa/c_{s,0}$. Column 8: Injection amplitude. Column 9: Resolution, the number of grids each wavelength is resolved with.

otherwise inbound unstable sound wave can cause unphysical effects[12] (e.g. spurious shocks). Despite requiring the flow near the outer boundary to be supersonic, it is possible to initiate the flow at the inner boundary to be highly subsonic (see the bottom of figure 3.6). To further ensure our discussion will not be affected by outer boundary conditions, we focus on the inner (subsonic) half of the simulation domain. Unlike the linear setup, where we explicitly perturb the profile, here all growth is seeded by numerical noise.

3.3.2 Acoustic Instability: Comparison with Linear Theory

Table 3.1 lists the parameters used for simulating the linear growth of acoustic waves. In each case, an acoustic wave with a specified amplitude and wavelength (expressed in units of diffusion length) is injected by a boundary perturbation as described in

---

[12] In keeping the boundary free, the values at the ghost zones should depend on the last active zones. Instead, inbound sound waves carry information from outside in. This usually isn't a problem when the inbound sound waves are stable, but here they are problematic.

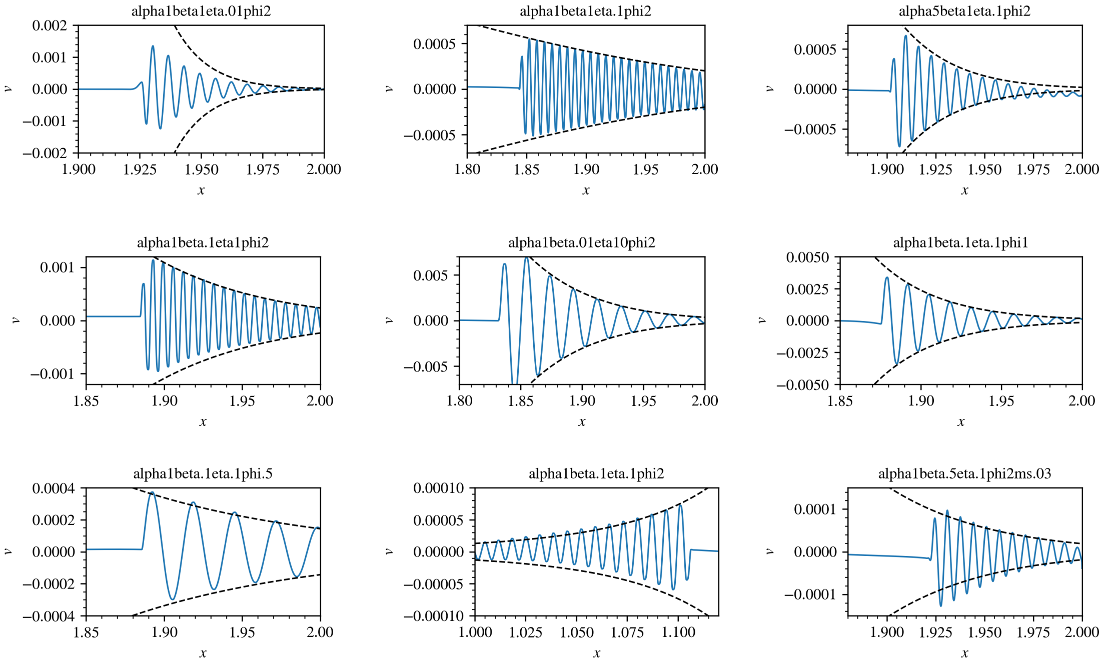

FIGURE 3.7: Simulation of linear growth of acoustic waves. An acoustic wave is injected according to the description described in §3.3.1.2 with the parameters listed in table 3.1. In each panel, the identifier is given at the top. The blue curve shows the simulated velocity profile of the growing acoustic wave. The analytically predicted amplitude (using equation A.23) is displayed in black dashed line for comparison.

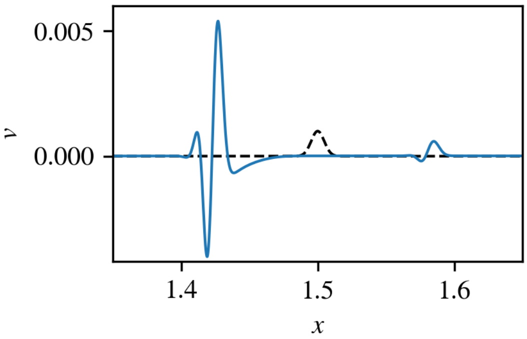

FIGURE 3.8: Growth comparison of forward and backward propagating waves. The black dashed line shows the initial velocity profile with a slight Gaussian perturbation at $x = 1.5$. This perturbation then decomposes into a forward moving (to $+x$) component and a backward (to $-x$) component. Their evolution is captured at a later time by the blue solid line. As expected, the backward component grows more rapidly. The background $\alpha_0 = 1, \beta_0 = 0.5, \eta_0 = 0.01, \phi = 2$. The Gaussian bump has amplitude 10^{-3} and characteristic width of κ/c_{s0}.

§3.3.1.2. The background profile spans $1 < x < 2$. The resolution is given in number of grids used to resolve each wavelength, the whole domain is typically resolved with 16384 grids. The reduced speed of light is $c = 1000$. The results are displayed in fig.3.7. In each panel, the velocity profile is given by the blue solid curve. In the linear growth phase, the velocity amplitude of the acoustic perturbation can be analytically expressed, to first order approximation, as

$$\hat{v}(x) = \hat{v}(x_{\rm inj}) \exp\left\{ \frac{1}{2} \ln \frac{\rho_{\rm inj}}{\rho} + \frac{1}{2} \mathcal{I}(x, x_{\rm inj}) \right\}, \tag{3.43}$$

where $\mathcal{I}(x, x_{\rm inj})$, given in equation A.24, is an integral involving the growth rate from the location of injection $x_{\rm inj}$ to some point x along the path of propagation. Overall there is good agreement between the simulated amplitude growth and analytics, except in the case where $\lambda = l_{\rm diff,0}$ (case `alpha1beta1eta.01phi2`, panel in the upper left corner), for which $k\kappa/c_s \sim 1$ and the growth rate formula (equation 3.21) is no longer valid. In particular, for $k\kappa/c_s \lesssim 1$ the acoustic mode bifurcates into additional hybrid modes (appendix A.1). These modes have lower growth rates than the asymptotic small wavelength $k\kappa/c_s \gg 1$ limit.

In Fig.3.8, rather than injecting a sound wave from the right boundary, we set up a Gaussian perturbation of amplitude 10^{-3} and characteristic width κ/c_{s0} in the middle of the simulation domain. Both the forward and backward acoustic modes are unstable at the Gaussian bump. The background mode clearly grows faster than the forward mode, as expected.

Identifier	α_0	β_0	η_0	ϕ	c	Resolution (Δx)	$\langle \dot{M} \rangle / \dot{M}_0$	$\langle \Delta P_c \rangle / \Delta P_{c0}$	$\langle \Delta F_c \rangle / \Delta F_{c0}$	$\gamma_{\rm eff}$
NL4096alpha.5beta1eta.01phi2c200	0.5	1	0.01	2	200	2.20×10^{-3}	0.969	1.120	0.947	1.28
NL4096alpha.6beta1eta.01phi2c200	0.6	1	0.01	2	200	2.20×10^{-3}	0.977	1.184	0.932	1.20
NL4096alpha.7beta1eta.01phi2c200	0.7	1	0.01	2	200	2.20×10^{-3}	1.063	1.207	0.911	1.17
NL4096alpha.8beta1eta.01phi2c200	0.8	1	0.01	2	200	2.20×10^{-3}	1.123	1.230	0.915	1.20
NL4096alpha.9beta1eta.01phi2c200	0.9	1	0.01	2	200	2.20×10^{-3}	1.175	1.234	0.899	1.19
NL4096alpha1beta1eta.01phi2c200	1	1	0.01	2	200	2.20×10^{-3}	1.384	1.309	0.907	1.25
NL4096alpha1beta1eta.01phi2c400	1	1	0.01	2	400	2.20×10^{-3}	1.382	1.321	0.890	1.22
NL4096alpha1beta1eta.01phi2c800	1	1	0.01	2	800	2.20×10^{-3}	1.375	1.313	0.883	1.22
NL4096alpha1beta1eta.01phi2c1000	1	1	0.01	2	1000	2.20×10^{-3}	1.446	1.310	0.868	1.23
NL4096alpha2beta1eta.01phi2c200	2	1	0.01	2	200	2.20×10^{-3}	1.713	1.269	0.852	1.16
NL4096alpha3beta1eta.01phi2c200	3	1	0.01	2	200	2.20×10^{-3}	1.825	1.210	0.844	1.12
NL4096alpha4beta1eta.01phi2c200	4	1	0.01	2	200	2.20×10^{-3}	1.861	1.186	0.844	1.10
NL4096alpha5beta1eta.01phi2c200	5	1	0.01	2	200	2.20×10^{-3}	1.890	1.187	0.848	1.09
NL4096alpha6beta1eta.01phi2c200	6	1	0.01	2	200	2.20×10^{-3}	1.901	1.175	0.846	1.09
NL4096alpha7beta1eta.01phi2c200	7	1	0.01	2	200	2.20×10^{-3}	1.925	1.158	0.848	1.09
NL4096alpha8beta1eta.01phi2c200	8	1	0.01	2	200	2.20×10^{-3}	1.944	1.141	0.843	1.09
NL4096alpha9beta1eta.01phi2c200	9	1	0.01	2	200	2.20×10^{-3}	1.366	1.120	0.813	1.09
NL4096alpha10beta1eta.01phi2c200	10	1	0.01	2	200	2.20×10^{-3}	1.579	1.107	0.825	1.09
NL1024alpha1beta.02eta.01phi2c4000	1	0.02	0.01	2	4000	8.79×10^{-3}	5.635	1.408	0.671	1.22
NL1024alpha1beta.04eta.01phi2c3000	1	0.04	0.01	2	3000	8.79×10^{-3}	4.318	1.393	0.739	1.25
NL4096alpha1beta.05eta.01phi2c2000	1	0.05	0.01	2	200	8.79×10^{-3}	4.232	1.423	0.752	1.25
NL1024alpha1beta.06eta.01phi2c3000	1	0.06	0.01	2	3000	8.79×10^{-3}	3.943	1.376	0.727	1.25
NL1024alpha1beta.08eta.01phi2c2000	1	0.08	0.01	2	2000	8.79×10^{-3}	3.354	1.364	0.783	1.27
NL2048alpha1beta.1eta.01phi2c1000	1	0.1	0.01	2	1000	4.39×10^{-3}	3.078	1.666	0.858	1.31
NL2048alpha1beta.3eta.01phi2c550	1	0.3	0.01	2	550	4.39×10^{-3}	2.140	1.500	0.888	1.26
NL2048alpha1beta.5eta.01phi2c400	1	0.5	0.01	2	400	4.39×10^{-3}	1.680	1.463	0.919	1.26
NL4096alpha1beta.6eta.01phi2c200	1	0.6	0.01	2	200	2.20×10^{-3}	1.685	1.433	0.889	1.25
NL16384alpha1beta.6eta.01phi2c200	1	0.6	0.01	2	200	5.49×10^{-4}	1.685	1.505	0.926	-
NL4096alpha1beta.8eta.01phi2c200	1	0.8	0.01	2	200	2.20×10^{-3}	1.466	1.352	0.908	1.26
NL4096alpha1beta2eta.01phi2c200	1	2	0.01	2	200	2.20×10^{-3}	1.091	1.117	0.864	1.17
NL4096alpha1beta3eta.01phi2c200	1	3	0.01	2	200	2.20×10^{-3}	0.937	1.053	0.914	1.17
NL4096alpha1beta4eta.01phi2c200	1	4	0.01	2	200	2.20×10^{-3}	0.896	1.036	0.953	1.16
NL4096alpha1beta1eta.02phi2c200	1	1	0.02	2	200	2.20×10^{-3}	1.378	1.299	0.879	1.23
NL4096alpha1beta1eta.04phi2c200	1	1	0.04	2	200	2.20×10^{-3}	1.312	1.271	0.880	1.21
NL4096alpha1beta1eta.06phi2c200	1	1	0.06	2	200	2.20×10^{-3}	1.209	1.271	0.899	1.21
NL4096alpha1beta1eta.08phi2c200	1	1	0.08	2	200	2.20×10^{-3}	1.290	1.255	0.871	1.18
NL4096alpha1beta1eta.1phi2c200	1	1	0.1	2	200	2.20×10^{-3}	1.211	1.260	0.884	1.18

TABLE 3.2: Simulation parameters for non-linear evolution of the acoustic instability. We have listed out only the test cases explicitly mentioned or used for figures in this paper. Column 1: Identifier of the test cases. Column 2-7: $\alpha_0, \beta_0, \eta_0, \phi$ defined in 3.30 and 3.38. Column 8: Resolution given in grid size. Column 9-11: Ratio of the time averaged mass flux, $\langle \Delta P_c \rangle$ and $\langle \Delta F_c \rangle$ to the initial values. Column 12: Effective CR adiabatic index (defined by eqn.3.50).

All in all, we have shown that acoustic perturbations can be amplified by CRs in various settings and the growth rate is consistent with that expected from linear theory. In particular, in the fluid rest frame, waves propagating up the CR gradient are more unstable.

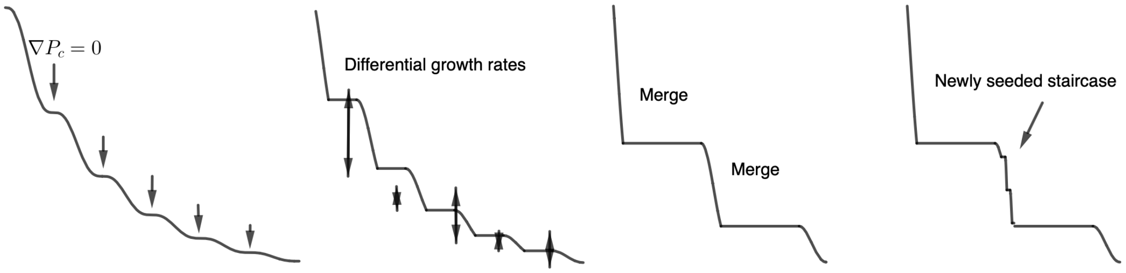

Figure 3.9: Non-linear growth and generation of the staircase. Time proceeds from the left panel to the right. Initial growth of acoustic waves generates a series of ∇P_c zeros, which then expand to form a series of staircases. Differential non-linear growth rates of the jumps causes stronger jumps to expand at the expense of weaker jumps, merging into bigger jumps. Subsequently, as merging slows down and new modes grow, the stair jumps fragment into smaller sub-steps.

3.3.3 Acoustic Instability: Non-Linear Outcome

We list, in Table 3.2 the simulations we have used to probe the non-linear regime, the parameters used and some relevant results. These include the change in mass flux, as well as ΔP_c and ΔF_c of the time averaged profiles. As discussed in §3.2.2, ΔP_c and ΔF_c probe the net momentum and energy transfer. We show the ratios $\Delta P_c/\Delta P_{c0}, \Delta F_c/\Delta F_{c0}$ between the non-linear staircase and the background profile.

3.3.3.1 General observation of the nonlinear behavior

The following proceeds after the linear growth phase. Growth of acoustic waves is slowed when the amplitude becomes large enough such that the CR pressure gradient becomes zero at the wave extrema (left most panel of fig.3.9). At these locations, CRs decouple from the gas, truncating CR heating, which is the source of energy driving the instability. Elsewhere gas and CRs are still coupled, so growth continues, though growth rates become strongly inhomogeneous. The local patches of CR gradient zeros expand, forming a series of CR plateaus separated by jumps in CR pressure, i.e. a staircase structure that travel up the P_c gradient (second left of fig.3.9). Gas and CR remain coupled at the jumps, so the instability continues to act, stretching the jump heights. Each CR jump can be seen to associate with a density spike. Local conditions drive a differential in non-linear growth for each jump, causing the CR plateaus to rise or drop at varying rates. When one plateau levels with another, the jump between them vanishes, they merge and move thereafter as one (second right of fig.3.9). Occasionally, newly seeded modes with wavelengths at or smaller than the jump width would arise at a stair jump, breaking it up into a series of sub-staircases (right most of fig.3.9). When a stair propagates into a region for which $\beta \gtrsim 0.5$, where acoustic waves are damped, the jump will shrink. As the instability saturates, we see continual staircase propagation, breaking and merging of the staircase jumps in an overall time-steady manner.

Fig.3.10 depicts a snapshot which clearly shows the aforementioned staircase structure in the P_c profile (See bottom left panel of fig.3.10). The morphology of the P_c profile is distinct from the other profiles, particularly the gaseous profiles, in several ways. First, P_c decreases monotonically whereas the density exhibits small scale shocks. Second, whereas the P_c jumps, as well as gas density and velocity fluctuations are of order $\Delta P_c/P_c \sim \Delta\rho/\rho \sim \Delta v/v \sim 1$, the gas pressure and temperature exhibit extreme dips, $\Delta P_g/P_g \sim \Delta T/T \gg 1$. The origin of these dips will be discussed in §3.3.3.2.

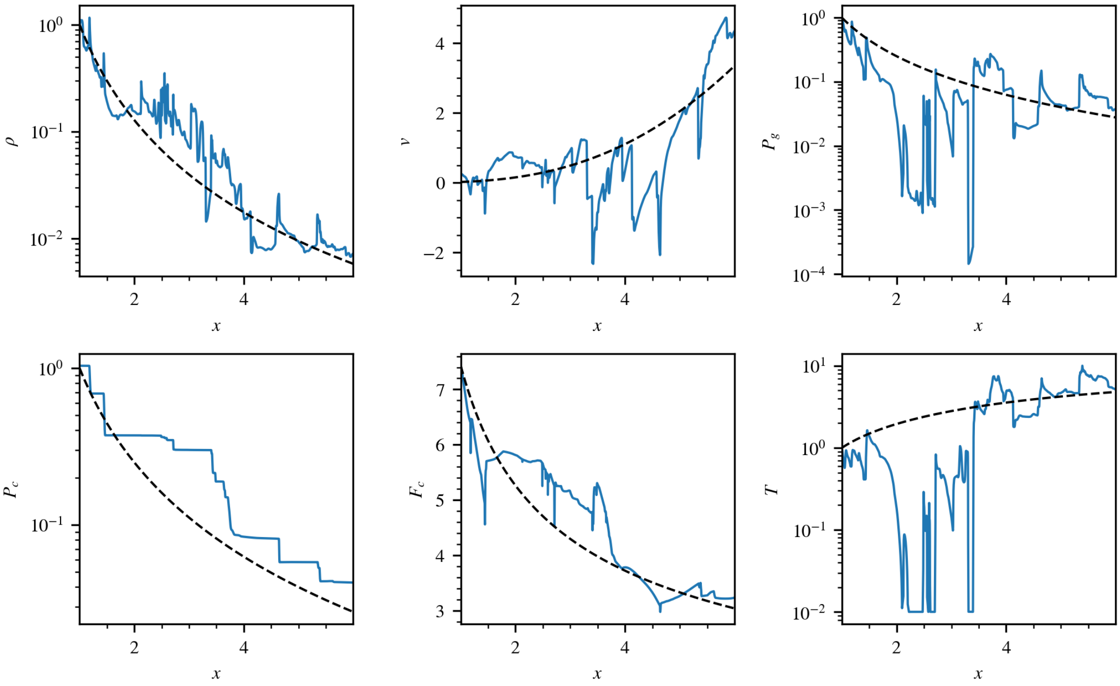

FIGURE 3.10: Density (top left), velocity (top middle), gas pressure (top right) and CR pressure (bottom left), CR flux (bottom middle), temperature (bottom right, defined in code units by $T = P_g/\rho$) plots of the non-linear evolution of the acoustic instability at $t = 2.84$ (blue solid lines). The initial profiles are shown by black dashed lines for comparison ($t = 0$). A staircase structure can be seen in the CR pressure. Plasma β decreases from 0.6 to 0.017 from $x = 1$ to $x = 6$, going below the stability threshold $\beta = 0.53$ at $x \approx 1.1$. The case shown is a time slice taken from `NL4096alpha1beta.6eta.01ms.015psi0c200`.

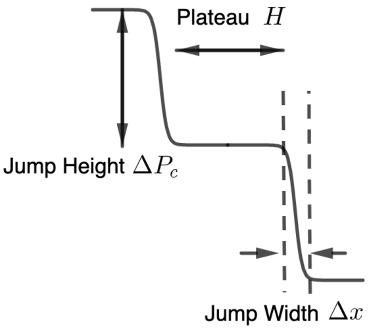

FIGURE 3.11: Clarification of jump width, height and plateau.

In Fig. 3.11, we illustrate the meaning of the terms *jump width* Δx, *jump height* ΔP_c and *plateau* H, which we use throughout the rest of this paper. We often express the jump width as $w \equiv \Delta x / l_{\rm diff}$, normalized with respect to the local diffusion length, while the jump height is often expressed as $h \equiv \Delta P_c / P_c$, i.e. the logarithmic change in P_c.

3.3.3.2 Zoom-in of staircase jumps

The P_c jumps can provide intense local heating and momentum transfer as they propagate, potentially altering the overall dynamics of the gas-CR fluid. In this subsection we zoom-in onto a typical jump and explain the physics behind various features.

Fig.3.12 shows the CR pressure, density and gas pressure profiles across one such jump. Since the instability is dominated by backward propagating waves (see fig 3.8), like most others this jump is propagating to the left, up the CR gradient. We observe for other jumps the direction of propagation is always towards increasing P_c in the *rest* frame of the fluid, such that only in the supersonic part of the flow do the stairs propagate down the P_c gradient in the *lab* frame. Moving across the zoom-in profiles from left to right, the P_c jump is preceded by sharp density and gas pressure increase. These are purely hydrodynamic shocks, across which P_c remains constant and decoupled from the gas. The actual P_c jump begins from the post-shock density

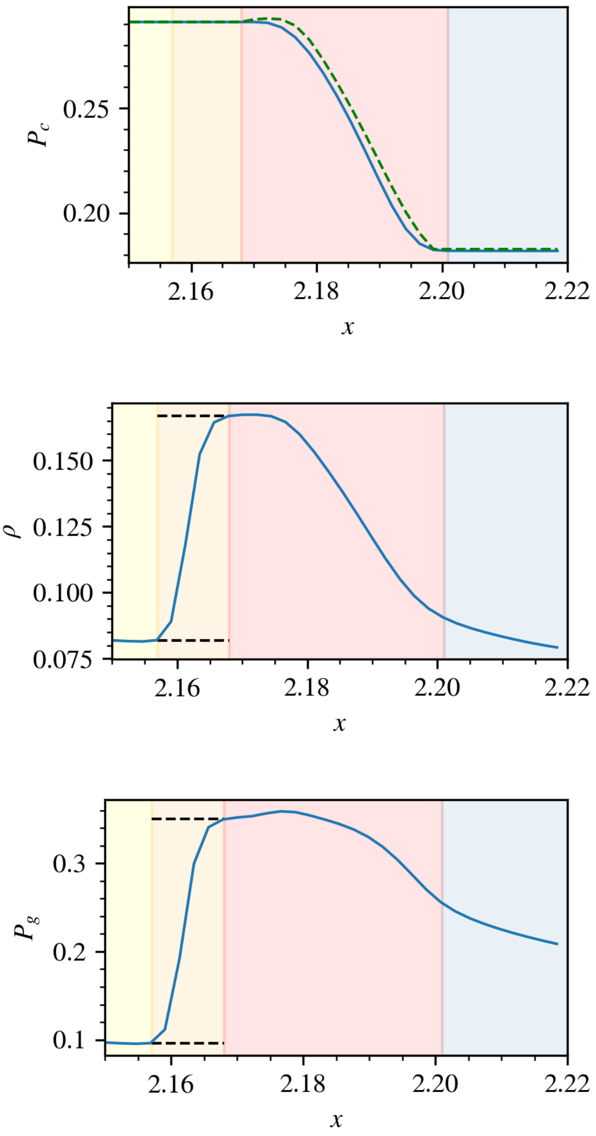

FIGURE 3.12: Zoom-in plot of the CR pressure (top), density (middle) and gas pressure (bottom) across a typical staircase jump that is propagating up the P_c gradient (i.e. left in these plots). The blue solid curves are the simulation data. A stair jump in general consists of 4 sections, color coded by different background shades. The yellow section denotes the pre-jump plateau where CR and gas are uncoupled. The orange section denotes the hydrodynamic shock. The red section denotes the actual stair jump, where CR and gas are coupled. The blue section denotes the entailing plateau where CR and gas becomes uncoupled again. The green dashed curve in the P_c plot (top panel) is the analytic P_c profile calculated from equation 3.22 in the shock's rest frame for the simulated density profile. Given the upstream condition and the shock's Mach number, the Rankine-Hugoniot shock jump relations return the post-shock density and gas pressure, as displayed by the horizontal black dashed lines in the density plot, which closely match those in simulation.

peak, tracing the falling side of the acoustic disturbance. The jump is ensued by a CR plateau.

Across a hydrodynamic shock, one can infer the shock speed $v_{\rm sh}$ by imposing mass continuity

$$v_{\rm sh} = \frac{\rho_2 v_2 - \rho_1 v_1}{\rho_2 - \rho_1}, \tag{3.44}$$

where v_1, v_2 are the fluid velocities in the lab frame and the subscripts 1 and 2 denote the fluid quantities upstream and downstream of the shock respectively. The density and gas pressure increase follow the Rankine-Hugoniot shock jump relations, as shown by the black dashed lines. Proceeding down the jump, CR and gas are coupled. In the rest frame of the shock the bottleneck equation 3.22 is satisfied, as demonstrated by the green dashed line. The gas and CR profiles across other jumps also exhibit similar structure: a purely hydrodynamic shock at a CR plateau, followed by a jump in P_c and an ensuing CR plateau.

The generation of gaseous shocks preceding each P_c jump follows from wave steepening of acoustic waves, where differences in phase velocities between the wave crest and trough causes overtaking and a discontinuity to be formed. Waves generated in this manner are usually weak and propagate at approximately the sound speed in the fluid's rest frame (thus appearing to propagate down the CR gradient only for supersonic flows). However, with thermal cooling these initially weak shocks can evolve into strong shocks, as we describe below.

The CR staircase is characterized by sudden drops in CR pressure (the jumps), connected by regions of constant CR pressure (the plateaus). CR and gas are decoupled at the plateaus and coupled at the jumps. Thus, there are no CR forces or CR heating at the plateaus, but very strong CR momentum and energy transfer to the gas at the jumps, where ∇P_c is much larger than in the background profile. This rearrangement of where CR momentum and heat is deposited causes the entire region to fall out of force and energy balance. Regions of excess cooling (the plateau) abut regions of intense CR heating (the jump). The cooling in plateaus causes gas pressure and temperature to have extreme dips[13], and pressure gradients between the plateau and jump drives a strong shock. This shock can be considerably stronger and different in character from simple steepening of an unstable acoustic wave. It is driven by the thermodynamics of the staircase structure when cooling is present. Cooling itself can create density peaks which create bottlenecks, and further alters the structure of the staircase.

3.3.3.3 Staircase Finder

Before we delve into the dynamical implications of the staircase, we shall determine the saturation of the non-linear staircase structure. To this end we have developed a

---

[13] In our simplified setup, cooling is artificially enforced to be equal to CR heating (plus adiabatic heating) in the initial steady-state profile (see eqn.3.36 and 3.37), and meant to mimic a system initially in thermal equilibrium. Cooling is independent of time. If the initial CR heating is strong, so is cooling and gas pressure and temperature will fall very quickly at the CR plateaus. A more realistic scenario would use standard cooling functions which depend on plasma density and temperature. This would produce initial pressure profiles which are no longer power law, and time-dependent cooling. We are studying this separately (Tsung et al 2022, in preparation), but the current simplified setup illustrates much of the key physics.

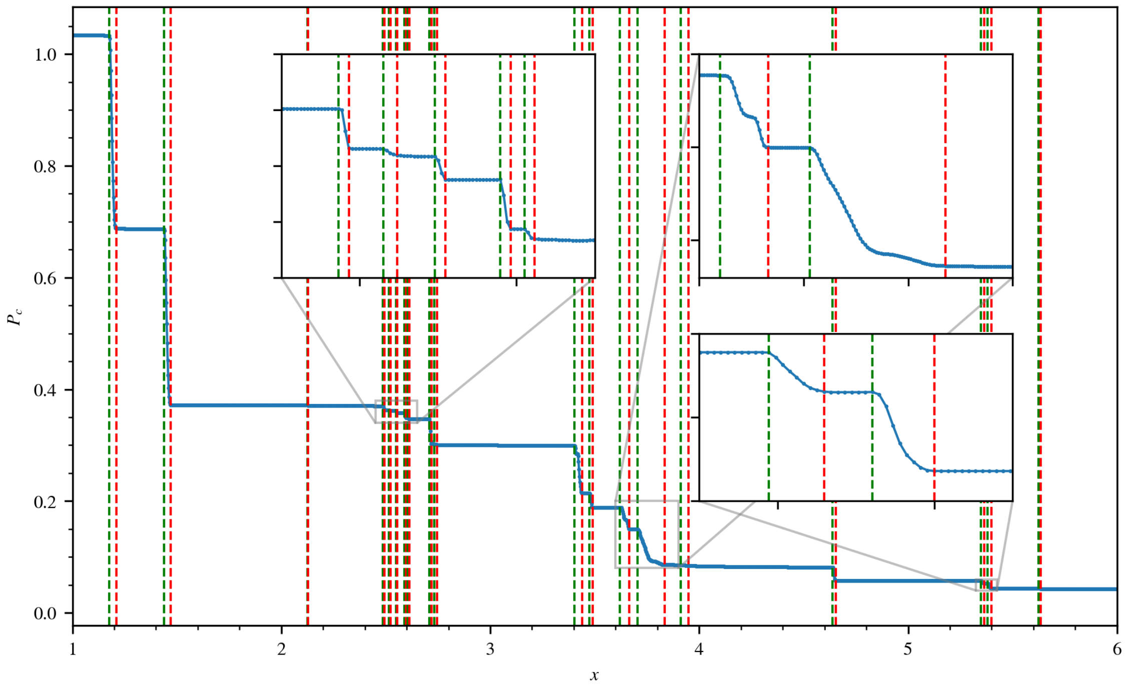

FIGURE 3.13: Staircases are identified using the algorithm described in §3.3.3. The P_c profile is plotted in blue solid line with green (red) dashed lines indicating the beginning (end) of a staircase jump. The zoom-in panels show with greater clarity parts of the P_c profile with the identified jumps, showing the staircase finder to be robust. The case shown is a time slice taken from `NL4096alpha1beta.6eta.01ms.015psi0c200`.

simple staircase finder to identify staircase jumps in a P_c profile. In light of equation 3.8, we deem the gas to be coupled with CRs if the following condition holds:

$$\frac{\Delta x}{L_c} > \theta_{\rm thres} \frac{v_A}{c}, \tag{3.45}$$

where Δx is the grid spacing (of order $c\Delta t$), L_c is the local P_c scale height and $\theta_{\rm thres}$ is some threshold parameter. Physically, this condition determines whether the time-dependent term in equation 3.6 is negligible. If so, there is strong coupling, and the CR flux attains its steady state form (equation 3.9). We have found $\theta_{\rm thres} \approx 0.01$ to

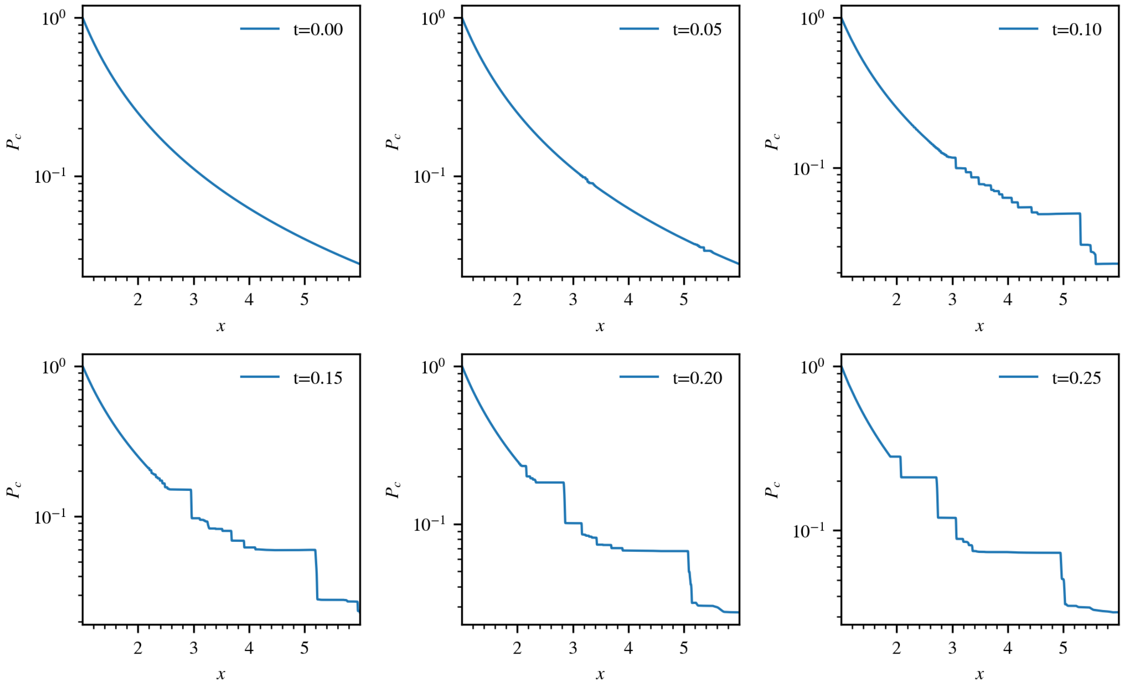

FIGURE 3.14: The evolution of the staircase at the first few time instances is displayed. Starting with smooth a background profile at $t = 0$, ∇P_c zeros begin to appear due to the acoustic instability at $t = 0.05$, followed by a surge of stairs at $t = 0.1$. The stairs subsequently merge, propagate and fragment to new stairs. The case shown is `NL4096alpha1beta.6eta.01ms.015psi0c200`.

work well in identifying jumps in the staircase here, though note that this value is likely situation dependent. Every grid cell is categorized as 'coupled' or 'uncoupled' according to this criterion. If a 'coupled' grid has an 'uncoupled' grid on its left and a 'coupled' grid on its right, it is deemed the start of a jump and vice versa for the end of a jump. Once the stair jumps have been identified we then record the number of jumps along the profile, as well as the jump widths, heights, etc. Fig.3.13 shows a snapshot of P_c with vertical dashed green lines indicating the start of a jump and red dashed lines indicating the end of a jump. This method is quite robust in capturing staircase jumps.

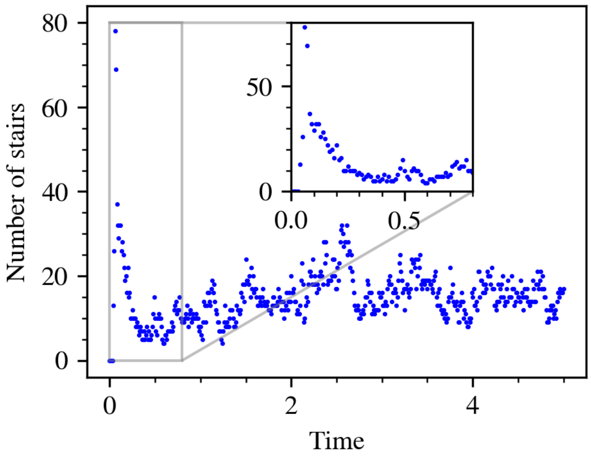

Figure 3.15: Number of staircases as a function of time. There is an initial surge of stairs from $t = 0$ to $t = 0.1$, followed by a merging phase from $t = 0.1$ to $t = 0.5$ and at last a quasi-steady state from $t = 0.5$ onwards where the the number of staircases fluctuates about a constant value. The zoom-in panel is displays the $0 < t < 0.8$ section in greater detail, showing clearly an initial phase of staircase surge $(0 < t < 0.08)$ followed by the merging phase $(0.08 < t < 0.5)$. The case shown is `NL4096alpha1beta.6eta.01ms.015psi0c200`.

3.3.3.4 Quasi-Static State of the Staircase

The staircase finder was applied over time. Fig.3.14 shows the evolution of the staircase at the first few time instances while Fig.3.15 shows the number of stairs (each pair of green and red dashed line is counted as one stair) captured as a function of time. From $t = 0 - 0.1$ there is an initial surge of stair jumps seeded by numerical noise due to the acoustic instability. This time period is consistent with the growth time $t_{\rm grow} \sim \kappa/c_c^2 \sim 0.01$ for the case displayed, where several e-folds are required to reach the non-linear stage. There is a large number of them because small scale perturbations from noise each grow until $\nabla P_c = 0$ is reached, forming plateaus. From $t = 0.1 - 0.5$ the number of jumps drops drastically as the individual CR plateaus expand and merge. Since non-linearly steepened sound waves travel $\sim c_s$, we expect the difference in propagation speed between adjacent jumps to be $\sim c_s$, and the merging timescale $\sim H/c_s$, the sound crossing time across a plateau (the merging timescale in general scales as $H/v_{\rm bump}$, where $v_{\rm bump}$ is the jump propagation speed. In the presence of strong shocks due to cooling at the plateaus, $v_{\rm bump}$ does not scale as c_s. However, at the early stage of staircase formation, before cooling can take action, $v_{\rm bump} \sim c_s$ is generally true). Do all the CR plateaus simply merge into one big jump? The answer is no. From $t = 0.5$ onwards the number of staircase steadied to around 15, fluctuating from 5 to 30. The number steadies due to two main reasons. First, merging of the CR plateaus have slowed down (the time for the stairs to merge lengthens with plateau width H). Second, newly seeded acoustic modes (seeded by numerical noise or propagating acoustic waves) at the CR jumps where CR and gas are still coupled lead to growth of a series of smaller CR stair jumps. This is similar to what happened at $t = 0 - 0.1$, but occurring only at the jumps. This leads to a fragmentation of a stair jump into smaller sub steps. The relative independence of these two factors causes fluctuations in stair numbers for $t > 0.5$. In this way the P_c profile settles into a quasi-steady state marked by occasional merging, fragmentation and propagation of the staircase. In summary, the evolution of a staircase structure is characterized by: 1. an initial surge of jumps seeded by perturbations, scaled by the growth timescale $t_{\rm grow}$, followed by 2. merging of the jumps on some merger timescale $t_{\rm merge}$ and at last 3. a quasi-static state balancing fragmentation and merging of stairs. Since the CR acoustic instability is a local instability, the staircase is agnostic to the simulation box size. Extending the simulation domain at fixed resolution (more specifically at fixed

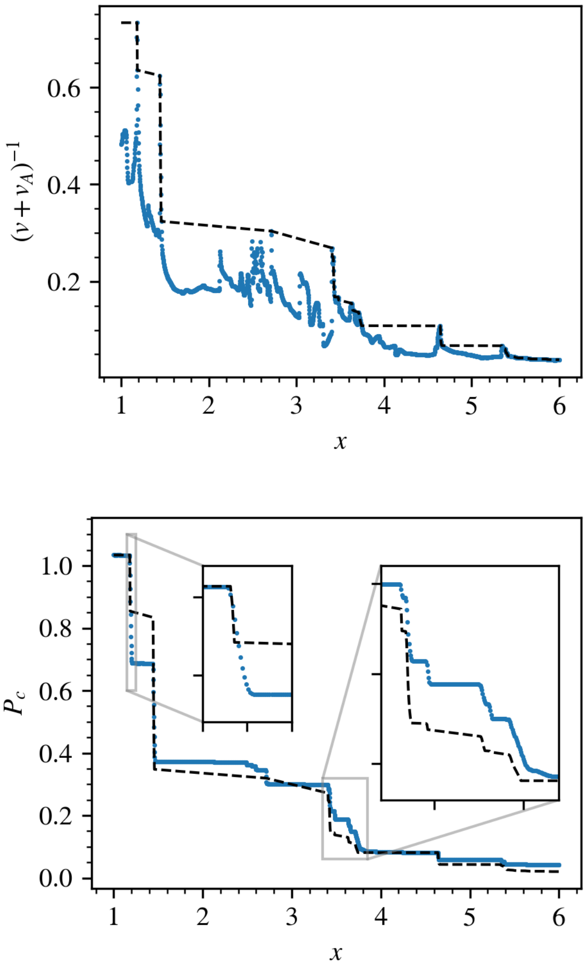

FIGURE 3.16: Top plot: $(v+v_A)^{-1}$ (solid blue line) and its convex hull (black dashed line). Bottom plot: The reconstructed P_c profile from the convex hull (black dashed line) and the actual P_c profile (blue) assuming profile stationarity. The zoom-in plots show with greater clarity how the convex hull procedure, assuming stationarity, fail in some instances to capture the correct jump heights. The case shown is a time slice taken from `NL4096alpha1beta.6eta.01ms.015psi0c200`.

$\Delta x/l_{\mathrm{diff}}$) will not change the number of jumps per unit box length. Higher resolutions do seed smaller scale instabilities, as shown in Appendix A.2.

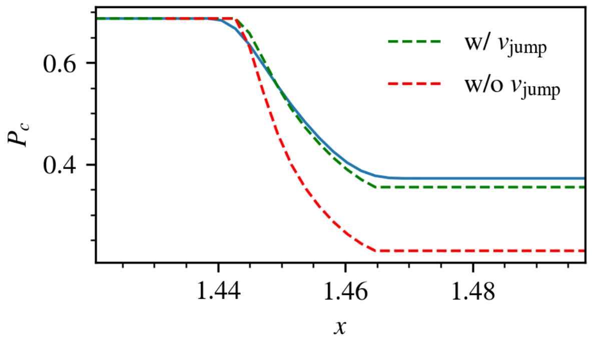

FIGURE 3.17: For a given density and velocity profile we evaluate the corresponding P_c profiles from eqn.3.28 and eqn.3.22 with and without including $v_{\rm jump}$ respectively and compare them against P_c from simulation. Blue solid line: Simulation data. Red dashed line: Estimated P_c profile without $v_{\rm jump}$. Green dashed line: Estimated P_c profile with $v_{\rm jump}$.

3.3.3.5 Bottleneck Effect with a Moving Staircase

In this section, we recall and extend our discussion of the bottleneck effect (§3.2.2) in the context of the non-linear profile arising from the acoustic instability (fig.3.10). In the presence of non-linear acoustic disturbances, the bottleneck effect causes a CR plateau to be formed on the rising side of the disturbance (viewed from the standpoint of the streaming CRs). Meanwhile CR and gas are coupled on the falling side, forming CR jumps. The plateaus and jumps occur one after another, in conjunction with successively rising and falling acoustic disturbances, forming a staircase. If the density and velocity profiles were stationary, with all the peaks held fixed, P_c would acquire a stationary profile as well, whose profile can be obtained through a 'convex hull' procedure, as shown by the dashed curve in the top plot of Fig.3.5. The convex hull is the minimal surface that encompasses the entire $(v+v_A)^{-1}$ profile[14]. P_c can then be obtained via equation 3.22. Fig.3.16 shows one such example of reconstructed P_c profile using the convex hull procedure. Comparing the reconstructed P_c profile against actual simulations shows that even though the locations of the P_c jumps can be identified reasonably, the magnitude of the individual jumps are incorrectly estimated.

---

[14] The steps to constructing a convex hull is described in greater detail here. 1. Identify the highest peak of the $(v+v_A)^{-1}$ profile. Incoming CRs will bottleneck all the way up to here. 2. Trace the

Clearly, the profiles are not stationary, since the jumps (and shocks) are propagating. Could this be the problem? Equation (3.22) only holds in the rest frame of the jumps. In the lab frame, the conserved quantity is thus:

$$P_c(v + v_A - v_{\rm bump})^{\gamma_c} = \text{const} \tag{3.46}$$

instead, where v is the lab frame velocity profile and $v_{\rm bump}$ is the propagation velocity of the jump determined by imposing continuity across the preceding hydrodynamic shock (eqn.3.44). This is the same as equation 3.28, aforementioned in §3.2.2. In fig.3.17, we show that once equation 3.28 is used, good agreement is restored. Since all the jumps propagate at different velocities, the frame transformation has to be applied separately to each jump to reconstruct an entire staircase, using the convex hull approach.

---

falling side of the $(v + v_A)^{-1}$ peak while searching for the next highest peak. CRs will bottleneck up to here next. 3. By repeating this procedure over successively lower $(v + v_A)^{-1}$ peaks a convex hull can be constructed for the $(v + v_A)^{-1}$ profile. The convex hull is given by the dashed line in the top plot of fig.3.16. 4. Finally, the P_c profile is obtained by applying equation 3.22 using the convex hull of $(v + v_A)^{-1}$.

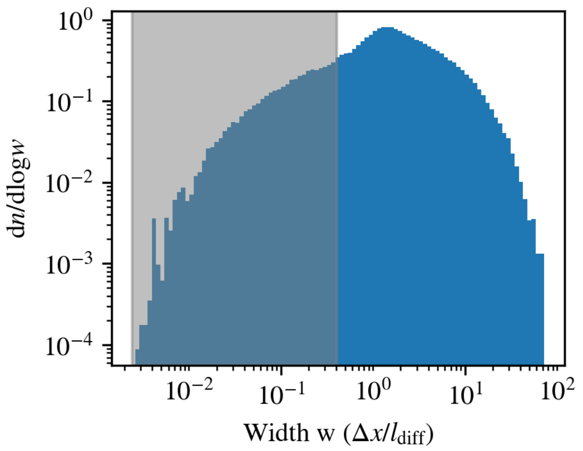

FIGURE 3.18: Distribution $(\mathrm{d}n/\mathrm{d}\ln w)$ of jump widths w (in units of $l_{\rm ldiff}$, i.e. $w \equiv \Delta x/l_{\rm diff}$), showing a peak at $\Delta x \sim l_{\rm diff}$ $(w \sim 1)$ and a cutoff above and below. Note that the diffusion length $l_{\rm diff}$ is calculated locally at each jump by averaging κ/c_s across the jump. The grey shaded region, with the limits obtained by dividing the grid size by the maximum and minimum local diffusion lengths respectively, denote jump widths that *may* be under-resolved (see the footnote in §3.3.3.6 for more details). The case shown is `NL16384alpha1beta.6eta.01ms.015psi0c200`.

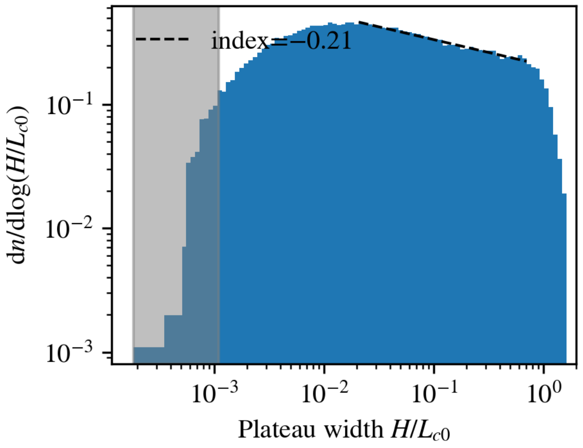

FIGURE 3.19: Distribution $(\mathrm{d}n/\mathrm{d}\ln(H/L_{c0}))$ of plateau widths H (in units of the initial background CR scale height L_{c0}). It has a power law index of -0.21 and is bounded by $H \sim L_{c0}$. The grey shaded region, with the limits obtained by dividing the grid size by the maximum and minimum L_{c0} respectively, denote plateau widths that *may* be under-resolved (see the footnote in §3.3.3.6 for more details). The case shown is `NL16384alpha1beta.6eta.01ms.015psi0c200`.

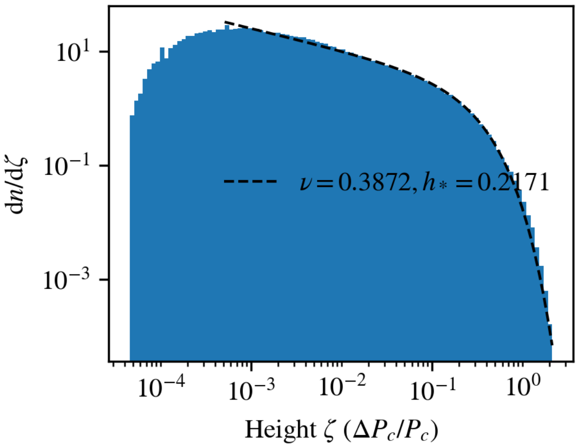

FIGURE 3.20: Distribution $(\mathrm{d}n/\mathrm{d}\zeta)$ of jump heights (in units of the local P_c) with fitting parameters ν and h_* (eqn.3.47). The case shown is `NL16384alpha1beta.6eta.01ms.015psi0c200`.

3.3.3.6 Jump Widths, Heights and Plateau Widths

We now discuss some characteristic scales in the staircase, such as the jump width, heights and plateau widths. We begin with the jump width Δx. As discussed in §3.2.1, the growth rate increases with wave number for $k\kappa/c_s \lesssim 1$, flattening to a constant value for $k\kappa/c_s \gtrsim 1$. With sufficient resolution, modes with wavelength less than $l_{\rm diff} \sim \kappa/c_s$ - the diffusion length, will grow the fastest and form non-linear stair jumps. Modes with wavelength close to the resolution grid size will be susceptible to numerical diffusion and damp. Thus we expect the distribution of stair widths Δx to be suppressed on small scales $\Delta x < \Delta x_{\rm res}$ due to numerical diffusion, and to be suppressed on large scales $\Delta x > l_{\rm diff}$ due to lower growth rates.

With the staircase finder one can also study the distribution of jump widths. We tally up the jump widths and display their distribution $\mathrm{d}n/\mathrm{d}\ln w$ in fig.3.18, where $w \equiv$

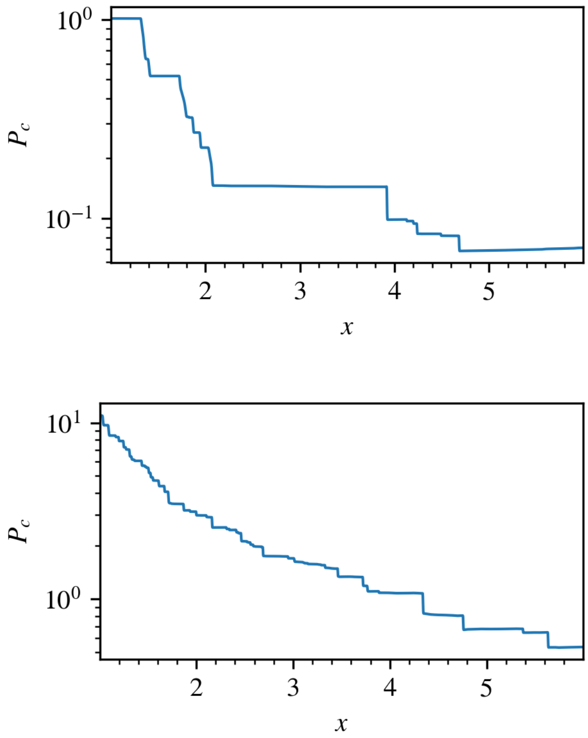

FIGURE 3.21: Two snapshots of P_c taken at the same time in which the bottom test case has a CR pressure 10 times higher than the top case, all other parameters held constant. The bottom test case has considerably smaller plateau widths and jump height than the top case, consistent with the discussion in §3.3.3.6. The cases shown are `NL4096alpha1beta1eta.01ms.015psi0c200` and `NL4096alpha10beta1eta.01ms.015psi0c200`.

$\Delta x / l_{\text{ldiff}}$ is the jump width normalized by the local diffusion length. The distribution peaks at $w \sim 1$, truncating above $w \sim 1$ exponentially and, as shown by the grey region[15], close to the grid scale. This shape is broadly consistent with expectations. In

---

[15] The lower and upper limits of the grey region in fig.3.18 are obtained by dividing the grid size Δx_{res} (which is uniform in our simulations) by the maximum and minimum local diffusion lengths registered at the jumps respectively. The local diffusion length at each jump is calculated by $\kappa / \langle c_s \rangle_{\text{jump}}$, where $\langle \cdot \rangle_{\text{jump}}$ indicates average across the jump. The grey region is therefore an approximate indication where jump widths may be under-resolved. Note that some well-resolved jumps may still fall within the grey region, for example, one can imagine a well-resolved jump width spanning q grids, i.e. $\Delta x = q \Delta x_{\text{res}}$. Then $\Delta x / l_{\text{diff}} = q \Delta x_{\text{res}} / l_{\text{diff}} = q(\Delta x_{\text{res}} / l_{\text{diff,min}})(l_{\text{diff,min}} / l_{\text{diff}})$. But note that $\Delta x_{\text{res}} / l_{\text{diff,min}}$ is the upper limit of the grey region, so if $q(l_{\text{diff,min}} / l_{\text{diff}}) < 1$, this jump width would still be placed in the grey region. Conversely, jump widths above the grey region is guaranteed to be resolved by more than one grids. Similarly, in 3.19, the lower and upper limits of the grey region are obtained by dividing the grid size Δx_{res} by the maximum and minimum local initial background CR scale heights at the plateaus. The local initial background CR scale height

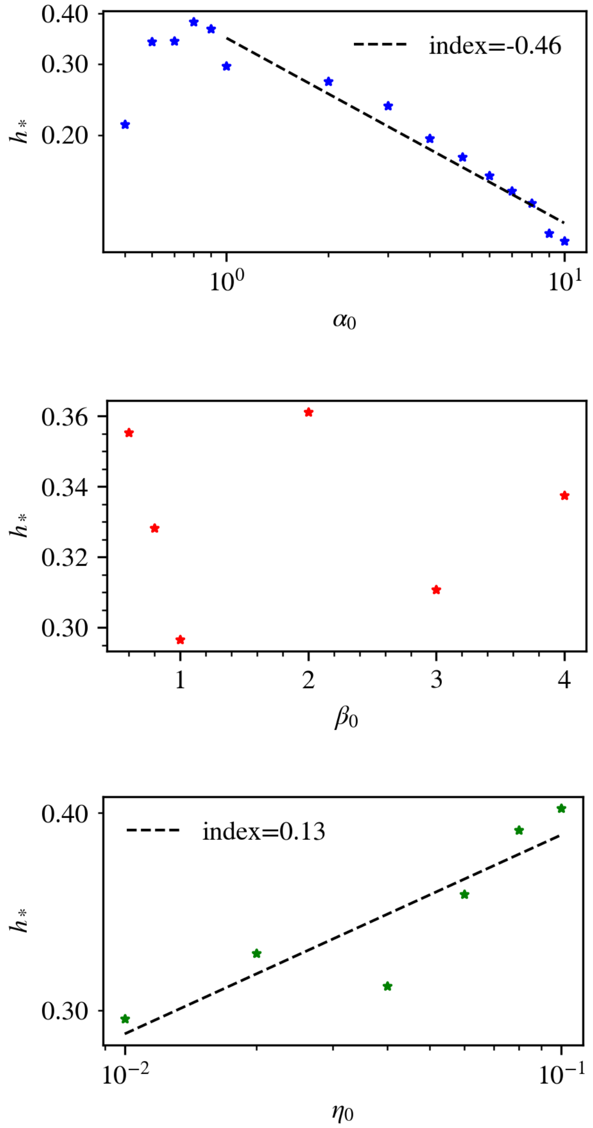

FIGURE 3.22: Variation of the characteristic jump height ζ_* (defined in eqn.3.47) for a range of $\alpha_0 = P_{c0}/P_{g0}$ (top, fixing $\beta_0 = 1, \eta_0 = 0.01$), $\beta_0 = 8\pi P_{g0}/B^2$ (middle, fixing $\alpha_0 = 1, \eta_0 = 0.01$) and $\eta_0 = \kappa/\gamma_c L_{c0} c_{s0}$ (bottom, fixing $\alpha_0 = 1, \beta_0 = 1$). The legends indicate the power law index found from logarithmic fitting when there is a prevailing trend. Log-log plotting is used for the top and bottom panel.

general, the jump width typically spans sizes of order the diffusion length, $\Delta x \sim l_{\rm diff}$. Substituting values appropriate for halo gas, $\kappa \sim 10^{28-29}$ cm^2 s^{-1} and $c_s \sim 100$ km s^{-1}, one would find that $l_{\rm diff} \sim 1 - 10$ kpc - orders of magnitude larger than small-scale cool structures in the CGM (which may be of order of a parsec; McCourt et al. [116]), and within reach of observational and cosmological simulation resolution limits. We briefly discuss observational consequences in §3.4.3.

Fig.3.19 shows a distribution of plateau widths H (in units of L_{c0}). A power law of index -0.21 emerges. The physics of these power laws is interesting, but we will defer exploration to future work. Note that the relatively flat distribution suggests the mean plateau width $\langle H \rangle = \int H \, {\rm d}n/{\rm d}H \, {\rm d}H$ would be skewed towards towards the higher end $\sim L_{c0}$, consistent with simulations, which shows that profile is dominated by large plateau widths. Thus, the CR scale height sets both an upper bound and a characteristic scale for plateau widths.

Finally, the distribution of jump heights $\Delta P_c/P_c$ is displayed in fig.3.20. It cutting off sharply as $\Delta P_c/P_c$ approaches unity. This distribution can be roughly characterized as a power-law followed by an exponential cutoff at some characteristic scale, and be reasonably fitted with a Schechter function

$$\frac{{\rm d}n}{{\rm d}\zeta} = N_0 \left(\frac{\zeta}{\zeta_*} \right)^{-\nu} e^{-\zeta/\zeta_*}, \tag{3.47}$$

---

at each plateau is calculated by $\langle L_{c0} \rangle_{\rm plateau}$, where $L_{c0} \equiv P_{c0}(x)/|\nabla P_{c0}(x)|$ is the CR scale height of the initial profile. There are also physical constraints on jump width set by CR mean free paths, which coincidentally are not very different from our numerical limits (see Appendix A.2).

where $\zeta \equiv \Delta P_c/P_c = \Delta \ln P_c$ is the logarithmic jump height, with ν and ζ_* denoting the power-law index and characteristic jump height respectively.

How do these scales change as we change physical parameters? For instance, in Fig.3.21 we show the effects of a higher CR pressure. The stairs appear more clustered and there are many more of them, meaning that both the plateau widths and the jump heights are reduced. In Fig. 3.22, we show how ζ_* (the exponential cutoff as defined in equation 3.47) changes as we change parameters at the base ($\alpha_0, \beta_0, \eta_0$, defined in equation 3.38). Since our pressure profiles are power-law, this amounts to an overall rescaling; note in particular that α_0 is independent of x. We find that $\zeta_* \propto \alpha_0^{-1/2} = (P_{c0}/P_{g0})^{-1/2}$ for $\alpha_0 > 1$ (and saturates at $\zeta_* = \Delta P_c/P_c \sim 0.4$ for $\alpha_0 < 1$). In addition, ζ_* shows little dependence on β_0, η_0.

These scaling relations are particular to our setup and likely sensitive to some key assumptions (e.g., about background profiles, as well as heating and radiative cooling). They should therefore be taken with a grain of salt; they are unlikely to be universal for CR staircases. We can nonetheless understand some qualitative features. Suppose the number of staircases per scale height is $n_c = L_c/H$, so that $\zeta_* = \Delta P_c/P_c \propto 1/n_c \propto H$, where both ζ_*, H are representative values of the logarithmic height and plateau width respectively. The steady state number of staircases arises from a balance between staircase production (via the acoustic instability) and destruction (via merging). From equation 3.21, the linear growth rate of the acoustic instability is:

$$\Gamma_{\text{grow}} \sim \frac{c_c^2}{\kappa}\left(1+\frac{1}{\beta^{1/2}}\right)^2 + \frac{1}{\rho c_s}\left(1+\frac{1}{\beta^{1/2}}\right)\frac{\mathrm{d}P_c}{\mathrm{d}x}. \tag{3.48}$$

$\mathrm{d}P_c/\mathrm{d}x$ can be approximated as $\Delta P_c/\Delta x$. The jump width scales roughly as the diffusion length while ΔP_c is observed to be at most of order P_c (e.g. in fig.3.10). Therefore the term in equation 3.48 involving $\mathrm{d}P_c/\mathrm{d}x$ is at most of order $(c_c^2/\kappa)(1 + 1/\beta^{1/2})$. A close examination (not shown) of the jumps shows that the first term in 3.48 usually dominates, and for simplicity we ignore the second term. On the other hand, the merger rate scales roughly as the shock crossing time across a plateau. We argued in §3.3.3.2 that the shock is driven by pressure gradients. The free energy for the shocks comes from cosmic rays, such that $P_c \sim \rho v_{\mathrm{sh}}^2$. Thus, the characteristic shock propagation velocity is $v_{\mathrm{sh}} \sim c_c \sim \sqrt{P_c/\rho}$. Staircases 'merge' when one shock (typically the stronger shock, which is propagating faster) overtakes another. If there is a distribution of shock speeds, and the characteristic spread is of order $\sim c_c$, then the merger rate is $\Gamma_{\mathrm{merge}} \sim H/c_c$. If we set $\Gamma_{\mathrm{grow}} \sim c_c^2/\kappa$ to $\Gamma_{\mathrm{merge}} \sim H/c_c$, we obtain $H \propto c_c^{-1} \propto P_c^{-1/2}$, which reproduces the scaling $\zeta_* \propto \alpha^{-1/2}$ for $\alpha_0 > 1$. However, we caution that the growth and merger rates estimates we use are very crude, and this argument do not capture the relative independence with respect to β_0, η_0. Since it is unclear how universal these scalings are, we do not pursue this further.

3.3.3.7 Dynamical Effect and Averaged Properties

The presence of staircases significantly changes outflow dynamics. The decoupling of gas from CRs at the plateaus deprives it of CR pressure support and Alfvenic heating. Great P_c support and intense heating do occur, however, at the CR jumps, so a fluid parcel not co-propagating with the staircase experiences alternating pressure support

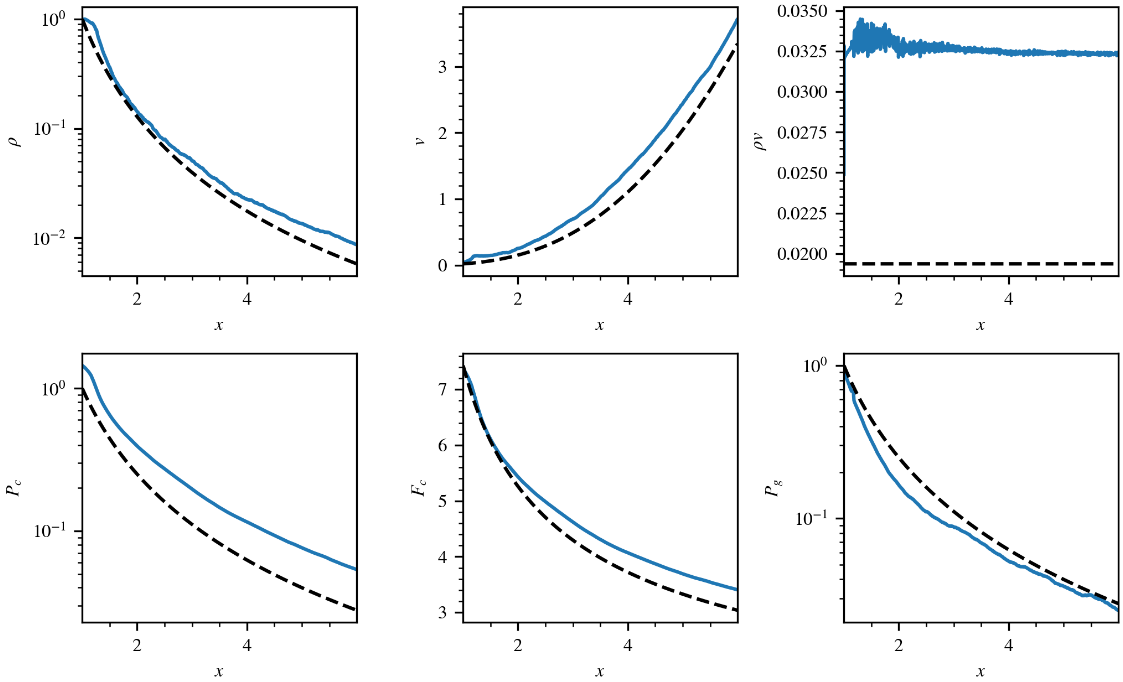

FIGURE 3.23: The blue solid lines denote the time averaged profile of density (top left), velocity (top middle), mass flux (top right), CR pressure (bottom left), CR flux (bottom middle) and gas pressure (bottom right). The black dashed lines show their respective initial profiles. The case shown is `NL4096alpha1beta.6eta.01ms.015psi0c200`.

and heating as it transverses plateaus and jumps. The question is: to what degree do the spasmodic pressure support and heating due to stair jumps balance the deficits at CR plateaus? And how does it affect the averaged profiles?

In §3.3.3.5 we observed for a moving stair jump, it is the quantity given by equation 3.28 that is conserved. A moving jump, as shown in fig.3.4 and 3.17, can cause the jump height to change as compared to when it is stationary[16]. In §3.2.2 we discussed, for a steady state profile, the total momentum and energy transfer are given

---

[16] If one estimates the ratio of P_c before and after the jump to be $P_{c,\text{after}}/P_{c,\text{before}} = A/B$, where $B > A$ then adding a positive constant C to the numerator and denominator would lead to an increase in the ratio, i.e. $(A+C)/(B+C) > A/B$. For example, adding 2 to the numerator and denominator of $1/4$ gives $3/5 > 1/4$. This means the jump height is lessened.

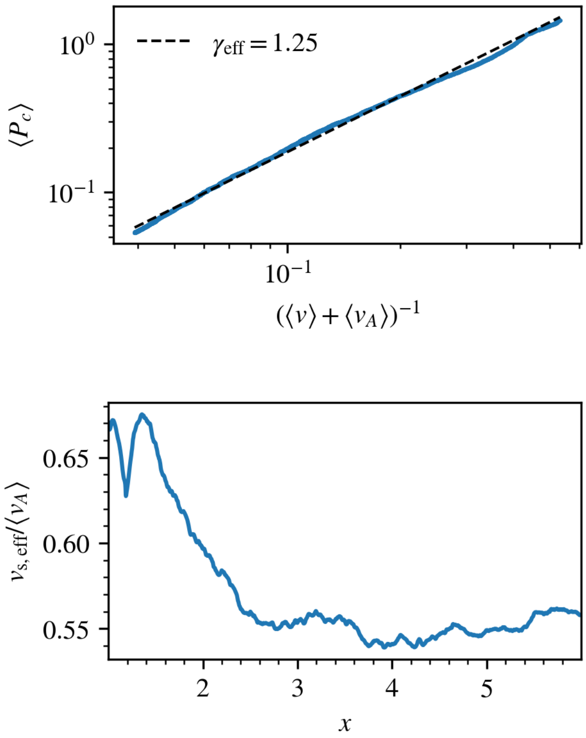

FIGURE 3.24: Top: Phase plot of $\langle P_c \rangle$ against $(\langle v \rangle + \langle v_A \rangle)^{-1}$ with the effective adiabatic index $\gamma_{\rm eff}$ (eqn.3.50) found from fitting. Bottom: Plot of the effect streaming speed $v_{\rm s,eff}$ (in units of the local time averaged Alfven speed). The case shown is `NL4096alpha1beta.6eta.01ms.015psi0c200`.

by ΔP_c and ΔF_c. We also showed, in fig.3.3 that provided none of the density bumps exceed the global maximum of the background and are stationary, there is no change in net momentum and energy transfer as compared to when there are no bumps. Now, the staircase is dynamically moving, merging and fragmenting, so a steady state profile in which all the time derivatives vanish is impossible. However, averaged over time, the time derivatives do vanish, and $\langle \Delta P_c \rangle$ and $\langle \Delta F_c \rangle$ do represent the time-averaged momentum and energy transfer (note that angle bracketed quantities are time averaged). Since ΔP_c is the sum of jump heights, in which each is affected by the jump velocity $v_{\rm jump}$, the time averaged momentum transfer therefore is deeply

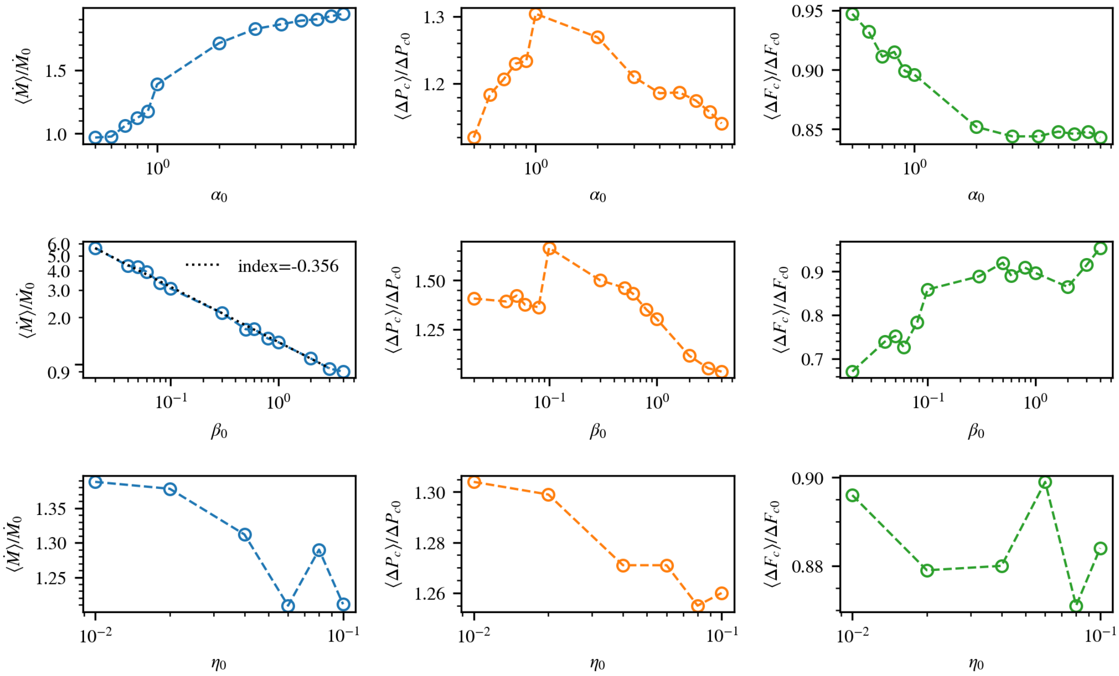

FIGURE 3.25: Time averaged quantities $\langle\dot{M}\rangle/\dot{M}_0$ (blue dashed line), $\langle\Delta P_c\rangle/\Delta P_{c0}$ (orange dashed line) and $\langle\Delta F_c\rangle/\Delta F_{c0}$ (green dashed line) for different α_0, β_0 and η_0. All changes are with respect to the new background profile for a given set of parameters.

related to the jumps' motion, as is the time averaged energy transfer.

In addition to $\langle\Delta P_c\rangle$ and $\langle\Delta F_c\rangle$, the time averaged mass flux $\langle\dot{M}\rangle$ is also a quantity of interest as in winds it controls the mass loading and transport of materials out to the CGM. We report numerical results for these quantities from our simulations, and suggest physical motivations for our findings. We defer detailed modeling to future work.

In fig.3.23 we present an example of the time averaged profiles resulting from the staircase. The time averaged profiles (blue solid lines) are placed in juxtaposition to the initial profiles (black dashed lines). Overall the change is quite modest. Apart from the shifts in $\langle P_c \rangle$ and mass flux $\langle \dot{M} \rangle = \langle \rho v \rangle$, the other profiles remain relatively close to the initial profiles. In table 3.2 and fig.3.25 we collect and display $\langle \dot{M} \rangle$, $\langle \Delta P_c \rangle$ and $\langle \Delta F_c \rangle$ for the test cases we have performed. Overall, the changes to $\langle \Delta P_c \rangle$ and $\langle \Delta F_c \rangle$ are very modest, of order $\sim 10\%$ over 1-2 decades in the parameters probed. The main interesting change is to the mass outflow rate, which changes by a factor of ~ 2 over 1.5 decades in α_0, and by a factor of ~ 6 over 2 decades in β_0.

It is perhaps surprising that changes to global energy and momentum transfer are so modest. After all, the CR staircase produces a drastic rearrangement of CR forces and heating – cutting it off through a majority of the profile, and leaving only a small fraction (the jumps) where the CRs are coupled, which receive intense forces and heating. If the staircase (and associated bottlenecks) were stationary, this state of affairs would indeed be deeply destabilizing. However, a flux tube threading *propagating bottlenecks* (in this case, shocks) still receives heat and momentum over its entire length, albeit in a very intermittent manner. Individual fluid elements experience brief periods of intense forcing and heating, followed by longer stretches without any CR interaction. But as we have seen, averaged over time, each fluid element receives heat and momentum comparable to the background profile. Thus, while there can be strong local fluctuations, the global flow is not destabilized. For instance, the timescale for a fluid element to fall out of force balance is the free fall time, which is of order the sound crossing time $t_{\rm sc} \sim L_{\rm P}/c_s$ in the quasi-hydrostatic part of the flow, where $L_{\rm P}$ is the pressure scale height. By contrast, the timescale to receive another 'hit' of CR forces is $H/v_{\rm bump}$; thus, $t_{\rm stair}/t_{\rm sc} \sim H/L_{\rm P}(c_s/v_{\rm bump}) < 1$. If the bottlenecks were stationary (e.g., a cloud co-moving with a hot wind), their effects would be much more severe.

Despite the modest changes in global momentum and energy transfer, it is interesting that the mass flux $\dot{M}$ can change so significantly. One way to understand this is as follows. We have a fixed flux of CRs at the base, which must be transported through the stratified atmosphere. Since CRs are trapped at bottlenecks, their effective streaming speed is reduced. In Fig. 3.24, we show:

$$v_{\rm s,eff} \equiv \frac{\langle F_c \rangle}{\langle P_c + E_c \rangle} - \langle v \rangle. \tag{3.49}$$

which is reduced by a factor of ~ 2 for the simulation shown. Plugging the escape valve for CRs leads to a larger overall CR pressure, required to sustain the same flux $F_c \approx 4P_c(v + v_{\rm s,eff})$. This increase in the normalization of $P_c \propto 1/v_{\rm s,eff}$ (already apparent at the base, where $v = 0$) is seen in the lower left panel of Fig. 3.23; it drives a stronger outflow. The advective flux increases to compensate for the decrease in streaming flux. The situation is similar to increasing the opacity in a radiation pressure driven wind – buildup in radiation pressure drives a stronger outflow. This increase in wind driving can be divorced from CR energy losses. For instance, consider purely diffusive models, where there are no CR heating losses. Nonetheless, for a fixed CR injection power, $\dot{M} \propto 1/\kappa$ increases as diffusivity κ falls, since the base CR pressure scales as $P_c \propto 1/\kappa$ [132]. Similar effects occur in streaming models as the effective streaming speed falls.

In Fig 3.25, we see that $\dot{M} \propto \beta_0^{-0.36}$. Why is the impact of CR staircases sensitive to the background β_0? As B-fields (and hence v_A) increases, the streaming flux is increasingly dominant over the advective flux, and thus the impact of bottlenecks grows. Furthermore, as $v_A/v_{\rm jump}$ increases, the attenuation of the bottleneck due to bump motion is lessened (equation 3.28); deeper bottlenecks imply greater build-up of CR pressure and stronger outflows. Accordingly, we find in our simulations that the suppression factor $f = v_{\rm s,eff}/\langle v_{\rm A}\rangle$ falls with decreasing β.

Quataert et al. [131] see a similar strong increase in $\dot{M}$ as CR bottlenecks develop in their isothermal wind simulations. This is consistent with an observed change in the apparent equation of state in the CRs, from the expected $P_c \propto \rho^{2/3}$ in their highly sub-Alfvenic flow to $P_c \propto \rho^{1/2}$. We also see this apparent change in the effective equation of state in our simulations. In Fig.3.24, we show the effective CR adiabatic index $\gamma_{\rm eff}$, defined by

$$\gamma_{\rm eff} = \frac{{\rm d}\ln\langle P_c\rangle}{{\rm d}\ln\left(\langle v\rangle + \langle v_A\rangle\right)^{-1}}. \tag{3.50}$$

We find that $\gamma_{\rm eff} \approx 1.2$ rather than 4/3, which naively corresponds to $P_c \propto \rho^{\gamma_{\rm eff}/2} \propto \rho^{0.6}$ in the sub-Alfvenic limit. Quataert et al. [131] note that over a large radial range, $F_c \approx 4P_c v_A \approx$const, which is consistent with $P_c \propto v_A^{-1} \propto \rho^{0.5}$. They also note that heating losses were $\sim 1/3$ of what one might expect from the time-averaged profile; if heating losses were negligible compared with the cosmic ray energy flux over a majority of the volume, this would explain $F_c \approx$ const.

In our simulations, the change in energy losses is mild, even when $\dot{M}$ changes significantly. Here, we offer a slightly different interpretation, which relies on the role of moving bottlenecks in the CR flux. By themselves, bottlenecks do not change the equation of state (e.g., consider the stationary flow in Fig 3.3, where $P_c \propto v_{\rm A}^{-4/3}$). However, the motion of the bottlenecks can change the apparent CR flux divergence and equation of state if not taken into account. For instance, as noted in §3.2, bump motion reduces $\nabla \cdot F$, with $\nabla \cdot F_c \rightarrow 0$, $F_c \rightarrow$const for $v_{\rm bump} \gg v, v_A$. Consider highly sub-Alfvenic motion (e.g., in very low β flows) , where one might expect $P_c \propto v_A^{-4/3} \propto \rho^{2/3}$. Instead, $v_{\rm A}$ falls at density jumps in shocks and can become comparable to $v - v_{\rm bump}$. Indeed, since the CRs are only coupled in dense regions, $v_{\rm A}$ should be evaluated here. From equation 3.28, we have:

$$\tilde{\gamma}_{\rm eff} \equiv \frac{{\rm d} \ln P_c}{{\rm d} \ln (v + v_A)^{-1}} = \gamma_c \frac{v + v_A}{v + v_A - v_{\rm bump}}, \tag{3.51}$$

where we have defined $\tilde{\gamma}_{\rm eff}$ separately from $\gamma_{\rm eff}$ as it is not derived from time averaged quantities. Only for stationary bumps $v_{\rm bump} = 0$ do we recover $\tilde{\gamma}_{\rm eff} = 4/3$. If the bumps propagate *up* the gradient (i.e. $v_{\rm bump} < 0$), the bottlenecks reduce the CR flux compared to the pure streaming case and $\tilde{\gamma}_{\rm eff} < \gamma_c$. This is the canonical case for the acoustic instability. Conversely, if the bumps propagate *down* the gradient (i.e. $v_{\rm bump} > 0$), the bottlenecks enhance outward CR transport relative to the pure streaming case and $\tilde{\gamma}_{\rm eff} > \gamma_c$. However, if $(v + v_{\rm A}) \gg v_{\rm bump}$, then $\tilde{\gamma}_{\rm eff} \rightarrow \gamma_c$. This is potentially at play in Fig.8 of Quataert et al. [131], which shows that while $P_c \propto \rho^{0.5}$ at the mid-range densities, at low densities (the outskirts, where flow becomes highly supersonic, with $v \gg v_{\rm bump}$), the effective adiabatic index steepens. While these effects are definitely present, whether they fully determine the change in apparent equation of state requires further quantitative study.

In summary, our simulation results are as follows: except in low β environments, the changes in net heating and mass flux are generally modest, reaching at most 85-90% and a factor of 2 respectively compared to no staircases. However, at low β, $\langle \dot{M} \rangle \propto \beta^{-0.36}$ changes more significantly, and can increase by an order of magnitude. This arises from the build-up of CR pressure due to stronger bottlenecks in low β flows. Our simulation results are consistent with the higher β (~ 1) study by Huang and Davis [82] and low β ($\ll 1$) study by Quataert et al. [131], the former reporting heating rates 95% of the background profile, and the latter finding a change of a factor of ~ 10 for $\langle \dot{M} \rangle$. Note that these three studies all make different assumptions about cooling/thermodynamics, as well as geometry, so the overall broad agreement is reassuring.

In our simulations, the time-averaged rate of global momentum and energy transfer is constrained if equilibrium is to hold. For instance, our cooling rates are time-steady, i.e. the total cooling luminosity of the simulation box is fixed. Hence, in global equilibrium, the time-averaged heat input from CRs – either in the form of direct $v_A \cdot \nabla P_c$ heating, or from shocks (which are ultimately powered by CRs) must balance this constant rate, and cannot deviate too much. In simulations with realistic radiative cooling, the global cooling luminosity and the density profile could change significantly. This could strongly affect momentum/energy transfer from the CRs. This will be the subject of future work.

3.4 Discussion and Conclusions

3.4.1 Brief Summary

In this paper, we carried out simulations of a CR driven acoustic instability [5], focussing on the streaming-dominated limit. The condition for this instability is strong B-fields ($\beta \lesssim 0.5$), so that CR heating $v_{\rm A} \cdot \nabla P_c$, which drives the instability, is sufficiently important[17]. In addition, a diffusion length $l_{\rm diffuse} \sim \kappa/c_s$ shorter than the background scale height L_c is required. If this is not satisfied, sound waves will still be unstable, but the staircase structure we focus on is washed out by diffusion. The instability becomes stronger at smaller lengthscales, with the growth time $t_{\rm grow} \sim \kappa/c_c^2 \sim \kappa\rho/P_c$ becoming independent of wavelength at scales below the diffusion length $l_{\rm diffuse}$.

As sound waves steepen and become non-linear, they turn into a quasi-periodic sequence of shocks. The density jumps at the shocks in turn create bottlenecks for CR streaming, resulting in a CR staircase structure. The jump widths are of order the diffusion length, while the jump heights depend on an equilibrium between staircase creation and mergers, and decrease with P_c. The CRs are uncoupled at staircase plateaus, but exert intense forces and heating at the staircase jumps. This rearrangement of CR pressure profiles has important consequences, which we now discuss.

---

[17] It also requires that CR heating contributes substantially to thermal balance, i.e. that cooling rates are comparable to CR heating rates.

3.4.2 Physical Significance

Some key physical consequences the CR acoustic instability and ensuing CR staircases are:

- *Shocks; density and velocity fluctuations.* The non-linear CR acoustic instability creates a propagating shock train. In our simulations, the shocks are initially fairly weak $\mathcal{M} \sim 1, \delta\rho/\rho \sim 1$, but they become stronger with the onset of cooling. The free energy for these shocks come from CRs, which thus result in significant density and velocity fluctuations. We anticipate this will drive turbulence in 2D and 3D simulations. These shocks are an important potential observational signature of the CR acoustic instability.
- *Spatial and temporal fluctuations in CR forces and heating.* CRs provide a steady body force ∇P_c and heating $v_A \cdot \nabla P_c$ when there is a global background gradient. The CR staircase breaks this up into patchy, highly intermittent momentum and energy transfer where (at any given instant) the CRs are uncoupled with the gas throughout most of the volume, but exert intense forces and heating over narrow regions with widths of order the diffusion length. Since these stair steps and associated shocks are rapidly propagating, averaged over time the entire gas volume does gain momentum and energy from the cosmic rays, but in an intermittent and stochastic fashion. We expect the intermittency—similar to the highly intermittent and fluctuating nature of turbulent dissipation

– to become more apparent in 2D and 3D simulations. The departure from local momentum and energy balance can drive dynamical and thermal instability, which deserve in depth investigation. In our simulations, the sudden loss of CR heating in plateaus drives rapid cooling and large gas pressure fluctuations.

- *Changes in net momentum and energy transfer.* CR staircases also affect the net momentum and energy transfer averaged over space and time once the system has reached a steady state, $\Delta P_c, \Delta F_c$. In our simulations, these changes are relatively modest, although they could potentially be more significant in simulations with realistic radiative cooling where the energy source terms evolve. More importantly, the CR staircase can significantly change mass outflow rates $\dot{M}$, as also seen by [131]. We interpret this as due to the build up in CR pressure due to reduced streaming speeds at bottlenecks, which ultimately drives a stronger outflow as advective flux outcompetes CR streaming flux; this becomes progressively more important at lower β where the bottlenecks are deeper and changes to CR streaming are stronger.

3.4.3 Applications

Can the acoustic instability and CR staircases arise in the CGM[18]? Depending on gas pressure profiles, this requires $B \sim 0.5 - \text{few}\,\mu$G in the CGM. Observations of the galaxy halo magnetic fields are challenging and sparse. Recent observations using an

---

[18] It is likely to also be relevant in the ISM, but our focus here is on the CGM.

FRB burst to observe Faraday rotation measured a parallel magnetic field $B_{\parallel} \sim 1\mu$G of order the estimated equipartition magnetic field, such that $\beta \sim 1$ [129], modulo uncertainties such as field geometry. For instance, field reversals reduce the rotation measure and lead to an underestimate of $B_{\parallel}$. Another caveat is that contribution to the Faraday rotation measure from the FRB engine, host galaxy, host galaxy's CGM, IGM, and intervening galaxy's CGM could not be separated. The inferred β is therefore a lower limit. van de Voort et al. [174] show from a suite of zoom-in cosmological simulations of galaxy formation that the plasma beta can reach as low as 0.01 in regions that coincide with the biconical outflow. The magnetic field can acquire such dominance from turbulent dynamo action and metal enriched cooling. It is quite likely that β fluctuates spatially in the CGM. Some regions may be unstable to the acoustic instability, while others are not.

If the acoustic instability is present, it has a very short growth time:

$$t_{\text{grow}} = 15\ \text{Myr}\left(\frac{\kappa}{10^{29}\ \text{cm}^2\,\text{s}^{-1}}\right)\left(\frac{c_s}{150\ \text{km}\,\text{s}^{-1}}\right)^{-2}\left(\frac{P_c/P_g}{1}\right), \tag{3.52}$$

where we have normalized to the (large) diffusion efficient $\kappa \sim 10^{29}\text{cm}^2\,\text{s}^{-1}$ that appears necessary to avoid overproducing γ-rays at a level inconsistent with observations [29]. This growth time is far shorter than the $0.1 - 1$ Gyr dynamical times typical of CGM processes (e.g., $L_c/c_s \sim 0.1$ Gyr for our fiducial parameters). The ratio of the diffusion length to the background scale height in galaxy halos is:

$$\eta = \frac{\kappa}{c_s L_c} \sim 0.1 \left(\frac{\kappa}{10^{29} \mathrm{cm}^2 \mathrm{s}^{-1}} \right) \left(\frac{c_s}{150\,\mathrm{km\,s}^{-1}} \right)^{-1} \left(\frac{L_c}{20\,\mathrm{kpc}} \right)^{-1} \tag{3.53}$$

which means that one can expect sharp staircase steps.

Of course, the CGM is multi-phase, and the cooler $T \sim 10^4$K component is a critical component. Indeed, it is generally the only component we directly observe. At face value, it might appear from equation 3.53 that we will not see the CR staircase in cooler $T \sim 10^4$K clouds, where both the sound speed c_s and CR scale height L_c can be much smaller. In particular, the interface between hot coronal gas and cold clouds has a very small scale height L_c, and naively, plugging in numbers into equation 3.53 would yield a very large η. This is not correct, because the ambient diffusion coefficient adjusts to local conditions. In the self-confinement picture, diffusion expresses transport relative to the Alfven wave frame, and can be written as:

$$\frac{\kappa}{v_A L_c} = \frac{v_D}{v_A} - 1 = \frac{l_{\mathrm{mfp}} c}{3 v_A L_c} \ll 1 \quad \text{(strong coupling)} \tag{3.54}$$

where v_D is the drift speed relative to the Alfven wave frame, and l_{mfp} is the CR mean free path $l_{\mathrm{mfp}} \sim r_g/(\delta B/B)^2$, where r_g is the CR gyroradius and the CR-excited Alfven wave amplitude $(\delta B/B)^2$ can be calculated in quasi-linear theory by balancing wave growth and damping rates [52, 181]. At ∼GeV energies (where most of the CR energy resides and the gyro-resonant streaming instability is strong), we expect $(v_D/v_A - 1) \sim 0.01 - 0.1$; i.e., the CRs are tightly locked to the Alfven wave frame.

See Wiener et al. [185] for expressions relevant to coronal gas, and Wiener et al. [183] for expressions relevant to $T \sim 10^4$K clouds and their interfaces with coronal gas. Our parameter η is directly related to this measure of CR coupling:

$$\eta = \frac{\kappa}{c_s L_c} \sim 0.1 \left(\frac{v_D/v_A - 1}{0.1} \right) \beta^{-1/2} \tag{3.55}$$

As a sanity check, note that for our fudicial assumptions of $c_s \sim 150\,\mathrm{km\,s^{-1}}$, $L_c \sim 20$ kpc, $\beta \sim 1$ in the coronal gas, equation 3.54 gives $\kappa \sim 10^{29}\mathrm{cm^2 s^{-1}}$ for $(v_D/v_A - 1) \sim 0.1$. Note that empirical measurements of κ in the ISM average over a multi-phase ISM and are likely dominated by regions where κ is largest.

It is also important to remember that CR staircases are not unique to the acoustic instability. They are seeded by density fluctuations, since overdense regions serve as streaming bottlenecks. They are agnostic as to the origin of these density fluctuations. Thus, overdensities created by thermal instability, or a network of overdense clouds in a multi-phase medium, can have similar effects. For this reason, CR staircases can show up in a wide range of scenarios.

Some potential applications include:

- *Galactic Winds.* Galactic winds driven by CRs have often been simulated in two limits: a diffusion dominated regime, due possibly to 'extrinsic confinement', where CRs are scattered by extrinsic turbulence, and/or due to various wave damping mechanisms (e.g. ion neutral damping) and streaming-dominated 'self confinement', where CRs are confined by Alfven waves they produce via the gyroresonant streaming instability. In the diffusive 'extrinsic confinement' case, CRs do not heat the gas[19]. In the streaming dominated 'self confinement' case, CR transport heats gas at a rate $v_A \cdot \nabla P_c$. The diffusive case fits γ ray observations better, because CRs can propagate out of the galaxy faster [29]. It is also much better at driving winds, because the CRs do not suffer strong energy losses via Alfven wave heating [71, 185]. However, we expect self-confinement to be very strong at the ~GeV energies where CR energy peaks [52, 106, 181], while extrinsic compressible turbulence is strongly damped at small scales, and unlikely to efficiently scatter ~GeV CRs [186]. Thus, CR winds should be streaming dominated and relatively inefficient. The CR staircase changes these dichotomies by changing the structure of the wind. We have seen how CR pressure can build up in streaming dominated simulations, due to trapping at bottlenecks. This increases mass outflow rates, similar to the effect of increased opacity in radiative outflows. In CR streaming simulations of isothermal winds where the CR acoustic instability arose, Quataert et al. [131] found an increase in wind mass loss rates by an order of magnitude, compared to analytic models without a CR staircase, illustrating the potential impact of CR staircases. High resolution cosmological zoom simulations of CR staircases are actually well within reach. As seen in Appendix §A.2, all that is required is that the diffusion length $l_{\rm diff} \sim \kappa/c_s \sim 2\,{\rm kpc}\,\left(\frac{\kappa}{10^{29}{\rm cm}^2{\rm s}^{-1}}\right)\left(\frac{c_s}{150\,{\rm km\,s}^{-1}}\right)^{-1}$ is resolved. However, to date only the FIRE collaboration has implemented the two moment method (capable of dealing with CR streaming) in such simulations, and– in contrast to, for instance, van de Voort et al. [174] – the plasma β in their winds is too high for the acoustic instability to develop [71]. But alternate setups where CR staircases appear are certainly numerically feasible.

---

[19] The only energy exchange is slow Fermi II acceleration of the CRs.

- *Thermal Instability.* As already seen in this paper, the patchy nature of heating due to a staircase structure can play an important role in thermal instability, if CR heating is significant in the background equilibrium profile. While CR heating is unlikely to be the sole source of heating over all galacto-centric radii, as in our simplified model, if it is significant even over a fraction of the profile (e.g., one or two scale height-heights), interesting effects can occur. We will study this in upcoming work (Tsung et al 2022, in preparation). The sudden loss of CR heating at plateaus triggers rapid cooling. The large gas pressure gradients and density fluctuations provide unusually non-linear, large-scale perturbations. It would be particularly interesting to see in 2D and 3D simulations if the high gas pressure gradients trigger 'shattering' of condensing large scale patches of cold gas, creating a 'fog' of cloudlets [60, 116]. The train of shocks which propagating over condensing cold gas can also play a role in subsequent dynamics, breaking up the cold gas further and driving baroclinic vorticity.

- *Thermal Interfaces.* CRs provide pressure support and heating to the interfaces between warm ($T \sim 10^4$K) photoionized gas and hot ($T \sim 10^6$K) coronal gas, thickening them and setting a characteristic temperature scale height. Similar to the case with thermal conduction, it is possible to solve for the steady state structure of CR mediated fronts [183]. These fronts are currently unresolved in simulations of cloud acceleration [16, 19] and their structure influences the strength of the 'bottleneck' and hence the momentum that is deposited towards cloud acceleration. It is therefore important to understand them in detail. The interfaces can be magnetically dominated due to flux freezing as hot gas condenses onto the interface [22, 59]. Therefore they are a likely breeding ground for the CR acoustic instability. If a CR staircase appears, the spatially fluctuating pressure and thermal balance triggers mixing, shocks and turbulence, which in term create dissipation and diffuse heat transport. The long term stability and structure of such fronts could change significantly, affecting the mass flux between the phases as well as observational diagnostics such as the ratio of low to high ionic species (e.g. N(CIV)/N(OVI)).

- *Observational Signatures.* Although the study of CR driven winds have become an intense area of activity, observational constraints are unfortunately few and far between. If seen, the quasi-periodic network of shocks due to the CR acoustic instability could provide a sorely needed observational diagnostic of the presence of cosmic rays in galaxy halos. For instance, they could potentially create widespread radio synchrotron emission from CR acceleration at shocks, at a level and with spectral indices inconsistent with transport of CR electrons out of galaxies, due to rapid synchrotron and inverse Compton cooling. However, further work is needed to see if this is an appreciable effect. The resultant density fluctuations could also potentially be probed by frequency-dependent temporal broadening of radio waves from Fast Radio Bursts [110, 129] passing through intervening galaxy halos. The challenge is in disentangling these effects from other sources of shocks and turbulence. Presumably the closely spaced, wide-spread nature of the shock train, as well as accompanying signatures of CRs (gamma-rays, synchrotron emission) help, but this must be studied in more detail. For instance, the passage of multiple weak shocks leaves a distinct spectral signature, with the spectrum flattening and the shock acceleration efficiency increasing at each shock [98].

Again, as mentioned in §3.3.3.6, the staircase jump width have typical size of a diffusion length, which for halo gas can be several kpc, i.e. it can be resolved by both observations and galaxy scale simulations. Provided that the shocks themselves do not decrease the diffusion coefficient (e.g., by increasing the scattering rate), this is a happy circumstance where shocks can be observationally resolved, and would be an interesting test of this physics. From the standpoint of galaxy scale simulations, the required dynamic range is feasible, since the diffusion length is routinely resolved. Some small scale structure may appear down to $\sim 10^{-2} l_{\rm diff}$ (though resolving such lengthscales is not necessary to obtain reliable results for the impact of the CR acoustic instability on $\dot{M}, \Delta P_c$). Below $\sim 10^{-2} l_{\rm diff}$, the CR fluid approximation no longer holds (see discussion in Appendix A.2).

The observation of a CR staircase can also be used as an observational diagnostic of CR streaming. [166] have argued, through observation of P_c plateaus at radio synchrotron harps in the Galactic Center, streaming transport is probably dominant there. These flat plateaus arise at CR maxima where CRs stream away from a source; there is only a single plateau (by constrast, diffusion produces a rounded, more Gaussian-like maxima). The staircase structure presented in this study produces a series of multiple successive plateau and jump features. It relies on the bottleneck effect, which only arises if CR transport is streaming dominated. It offers a more demanding test for the streaming versus diffusion picture.

3.4.4 Looking Forward

This paper is a first detailed study of CR staircases, which we expect to have broad applicability. Indeed, CR staircases due to the acoustic instability have just appeared in two recent preprints [82, 131]. More work is needed to clarify the impact of CR staircases on the interaction between gas and CRs. Some of the most pressing improvements include: (i) 2D and 3D MHD simulations, to assess the role of B-field geometry (particularly tangled magnetic fields, spatially varying B-fields, MHD forces and MHD acoustic modes), as well as the role of turbulence. For instance, in winds, one might expect the flow to develop significant anisotropy, depending on where bottlenecks develop and how field lines warp in response. (ii) Better treatment of the thermodynamics, and more realistic cooling functions. This is particularly important in assessing cooling at CR plateaus and the development of thermal instability. (iii)

Exploring parameter space with a wider range of background profiles which are less highly idealized.

Chapter 4

The Impact of Cosmic Rays on Thermal and Hydrostatic Stability in Galactic Halos

The research constituting this chapter was conducted in collaboration with Dr. Chad Bustard. This chapter has been reformatted and submitted to the Monthly Notices of the Royal Astronomical Society for which I am the lead author. In the following, I use 'we' to indicate my supervisor Prof. Siangpeng Oh, Dr. Chad Bustard and myself.

4.1 Introduction

In recent years, there has been a surge of interest in how cosmic rays (CRs) affect feedback in the circumgalactic medium (CGM) and intracluster medium (ICM), in particular on how they can drive a wind and provide thermal support. Unlike thermal gas, CRs do not suffer radiative losses and have smaller adiabatic index, making them able to sustain their pressure far away from their sources. Simulations have indeed shown that CRs can drive winds in the CGM [13, 31, 58, 65, 73, 96, 141, 146, 154, 172] and heat the ICM gas sufficiently to prevent a cooling catastrophe [61, 86, 139, 179], but these are apparently dependent on the model for CR transport and the gas properties, for which results can differ by orders of magnitude [18, 75, 81, 124]

To date, there is still considerable uncertainty about CR effects on galaxy evolution, despite herculean efforts to simulate CR-modulated feedback and compare to observations. To help dissect the influence of CRs, we take a distinctly different but complementary approach to that of usual feedback simulations. Our main science questions are as follows. For a hydrostatic atmosphere in initial thermal equilibrium supported by thermal gas, magnetic fields, and CRs, is this atmosphere thermally and dynamically stable? How do CRs affect local and global stability? Finally, in regimes where neither stability criterion holds, what is the nonlinear outcome? Our results confirm previous analytic expectations, illuminate connections between local and global instability, and reveal new insights into how CRs create and modify large-scale gas flows.

A key uncertainty in CR feedback models is the nature of CR transport. CRs scatter collisionlessly off magnetic turbulence, and the rapid scattering rate renders their behavior fluid-like. However the exact details of this process are still not yet fully understood, and sometimes at odds with observations in our Galaxy [80, 103]. CR transport is often divided into 2 distinct modes: CR streaming, and CR diffusion. In the self-confinement picture of CR transport, CRs are scattered by magnetic turbulence they generate and can lock themselves with self-excited Alfven waves. They advect or *stream* down the CR pressure gradients at the Alfven speed [107, 192]. In addition, since the CR scattering rate is finite, CRs are not completely locked to the Alfven waves, but drift slowly with respect to the Alfven wave frame. This can be represented as a field-aligned diffusion term. More generally, CRs undergo a random walk due to small-scale tangled B-fields, known as 'Field Line Wandering', even if CRs stream along B-field. In addition, CRs can random walk due to scattering by extrinsic turbulence[1]. This random walk renders CR transport diffusive, or even super-diffusive [118, 148, 187]. In reality, CRs are likely to both stream and diffuse; these processes must be considered in parallel.

There are two aspects of CR streaming which are germane to this paper. Streaming CRs locked with the Alfven waves transfer energy to the thermal gas at the rate $v_A \cdot \nabla P_c$, reflecting the work done by the CRs to excite magnetic waves, which then damp and heat the gas. This only takes place with CR streaming; there is no collisionless CR heating with CR diffusion. CR heating could plausibly explain elevated heating–

---

[1] Scattering by extrinsic turbulence is thought to be important only at higher energies, $E >$ 100GeV, with lower energy CRs – where the bulk of the energy resides– predominantly self-confined.

as inferred from line ratios– in the Reynolds layer of our Galaxy [181], reflecting its potential importance in the disk halo interface and CGM. It can drive acoustic waves unstable in sufficiently magnetized environments ($\beta \lesssim 0.5$, Begelman and Zweibel [6]) and may potentially have significant effect on wind driving in the CGM [83, 133, 169]. In another context, the ICM, CR heating has been shown able to balance radiative cooling and suppress cooling flows [61, 179]. Recently, Kempski and Quataert [102] explored, through linear analysis, the effect CR heating has on local thermal instability, finding it can cause thermal entropy modes to propagate and suppress the instability in certain parameter regimes. The nonlinear effects have not been explored yet.

Secondly, for the streaming instability to be excited, the drift speed must exceed the local Alfvén velocity $v_{\rm A}$. In regions where the CRs are isotropic ($\nabla P_{\rm c} = 0$), or have small drift speed, $v_{\rm D} < v_{\rm A}$, CRs will not scatter; they decouple from the gas and free stream out of these ‘optically thin’ regions at the speed of light. This leads to the ‘CR bottleneck effect’ [6, 156, 184], which can significantly modulate CR transport in a multi-phase medium. Since $v_{\rm D} \sim v_A \propto \rho^{-1/2}$, a cloud of warm ($T \sim 10^4$K) ionized gas embedded in hot ($T \sim 10^6$K) gas results in a minimum in drift speed. This produces a ‘bottleneck’ for the CRs: CR density is enhanced as CRs are forced to slow down, akin to a traffic jam. Since CRs cannot stream up a gradient, the system readjusts to a state where the CR profile is flat up to the minimum in v_A; thereafter the CR pressure falls again. If there are multiple bottlenecks, this produces a staircase structure in the CR profile [169]. Importantly, since $\nabla P_c = 0$ in the plateaus, CRs there are no longer coupled to the gas, and can no longer exert pressure forces or heat the gas. Instead, momentum and energy deposition is focused at the CR 'steps'. Small-scale density contrasts can thus have global influence on CR driving and heating.

The impact of CRs on halo gas is by now well-trodden ground; there is a vast and rapidly expanding literature on this topic. Nonetheless, as hinted above, there are several key aspects which motivate this study. Firstly, the influence of collisionless CR heating $v_{\rm A} \cdot \nabla P_c$ on thermal instability and the development of winds, which is a key prediction of the self-confinement theory of CR transport, is often neglected. To date thermal instability simulations with CR streaming do not have background CR heating–they either have horizontal B-fields, so that there is no CR streaming in the background profile [23], or take place in an unstratified medium [84]. Wind simulations are also often run in limits (e.g., ignoring streaming, isothermal winds, or considering high β winds) where only the momentum input of CRs drive the wind, while CR thermal driving is negligible. To date, there is only an analytic linear analysis [102] and 1D CR wind models [85, 119] where CR heating plays an important role in thermal instability and CR winds respectively. We suggest that CR heating could play a more crucial role than previously thought.

Secondly, we take care to consider the *combined* effects of CR streaming and diffusion, operating simultaneously. Until ~ 5 years ago, due to numerical challenges (see §4.2.1), CR streaming was either ignored or treated in limits where the Alfven speed changes only on large lengthscales[2]. These difficulties have since been overcome with the two moment method [29, 93, 165]. Nonetheless, wind studies often consider effective limits where either CR streaming *or* diffusion are dominant[3]. We shall see that the combined effects of diffusion and streaming can be non-trivial, as each can dominate in different regimes. For instance, diffusion can dominate in the disk, allowing CRs to escape without strong heating losses, while streaming dominates in the halo, which provides strong CR heating in a low density regime where radiative cooling is weak. By contrast, streaming-only simulations lead to strong CR losses at the disk-halo interface, while diffusion-only simulations ignore the effects of CR heating.

Finally, the impact of *local* thermal instability on *global* hydrostatic and thermal stability have not been sufficiently studied. CR winds are often studied in models where conditions in the wind base (e.g., star formation rate) change, leading to a higher CR momentum flux which drives an outflow. Our models consider the opposite case where conditions at the base are fixed, but conditions in the halo gas change. Local thermal instability reduces the background gas density, thereby reducing plasma β and radiative cooling rates and increasing Alfven speeds. It also introduces CR 'bottlenecks' in a multi-phase medium. These changes can lead to a loss of global hydrostatic and thermal stability, and the emergence of phenomena such as CR heated winds and fountain flows. We find it is particularly important to include and resolve the disk/halo interface, where sharp density gradients drive sharp gradients in Alfven speed and hence CR pressure. Winds and fountain flows are generally launched at this interface, and are qualitatively different if this phase transition is not modelled.

---

[2] This is not possible in a multi-phase medium, where $v_{\mathrm{A}} \sim \rho^{-1/2}$ change on the short lengthscale of the interface width between cold and hot phases.

[3] Of course, there are exceptions, such as the FIRE simulations [29, 79], which incorporate simultaneous streaming and diffusion with the two moment method. However, they run fully self-consistent simulations from cosmological initial conditions; the B-field strength and plasma β is not an adjustable parameter, as in our idealized simulations, but a simulation output. Thus, we have greater flexibility to survey parameter space. See additional discussion in §4.5.

This paper is organized as follows. In §4.2 we review the governing equations, and describe the simulation setup used for this study. In §4.3, we study the effect of CRs on linear thermal instability. In §4.4, we discusses the nonlinear results of the simulations, in particular the emergence of galactic fountain flows and winds. We discuss some implications in §4.5, and conclude in §4.6.

4.2 Methods

4.2.1 Governing equations

We utilize the two-moment method [93], which has been tested in stringent conditions (e.g. CR-modified shocks, Tsung et al. [168]). A merit of this method is its ability to handle CR pressure extrema self-consistently and efficiently, which previously resulted in grid-scale numerical instabilities which rapidly swamped the true solution. Previous remedies relied on ad-hoc regularization [153], where the timestep scales quadratically with resolution; this becomes prohibitively expensively at high resolution. The ability to resolve sharp gradients in Alfven speed is important in simulating the CR bottleneck effect [20, 169, 184], a crucial feature of CR streaming transport in multi-phase media where large volumes of zero CR pressure gradient are found.

Assuming the gas is fully ionized, the gas flow is non-relativistic and the gyroradii of the CRs are much smaller than any macro scale of interest, the two-moment equations governing the dynamics of a CR-MHD fluid are given by [93]:

$$\frac{\partial \rho}{\partial t} + \nabla \cdot (\rho \mathbf{v}) = 0, \tag{4.1}$$

$$\frac{\partial (\rho \mathbf{v})}{\partial t} + \nabla \cdot (\rho \mathbf{v}\mathbf{v} - \mathbf{B}\mathbf{B} + P^{*}\mathbf{I}) = \boldsymbol{\sigma}_c \cdot [\mathbf{F}_c - (E_c + P_c)\mathbf{v}] + \rho \mathbf{g}, \tag{4.2}$$

$$\frac{\partial E}{\partial t} + \nabla \cdot [(E + P^{*})\mathbf{v} - \mathbf{B}(\mathbf{B} \cdot \mathbf{v})] = (\mathbf{v} + \mathbf{v}_s) \cdot \boldsymbol{\sigma}_c \cdot$$

$$[\mathbf{F}_c - (E_c + P_c)\mathbf{v}] + \rho \mathbf{g} \cdot \mathbf{v} + \mathcal{L}, \tag{4.3}$$

$$\frac{\partial \mathbf{B}}{\partial t} = \nabla \times (\mathbf{v} \times \mathbf{B}), \tag{4.4}$$

$$\frac{\partial E_c}{\partial t} + \nabla \cdot \mathbf{F}_c = -(\mathbf{v} + \mathbf{v}_s) \cdot \boldsymbol{\sigma}_c \cdot [\mathbf{F}_c - (E_c + P_c)\mathbf{v}] + \mathcal{Q}, \tag{4.5}$$

$$\frac{1}{c_{\text{red}}^2} \frac{\partial \mathbf{F}_c}{\partial t} + \nabla P_c = -\boldsymbol{\sigma}_c \cdot [\mathbf{F}_c - (E_c + P_c)\mathbf{v}], \tag{4.6}$$

where c_{red} is the reduced speed of light, $\mathcal{L} = \mathcal{H} - \mathcal{C}$ is the net heating, defined by source heating minus cooling, $\mathcal{Q}$ is the CR source/sink term, $\mathbf{v}_s = -\mathbf{v}_A \text{sgn}(\mathbf{B} \cdot \nabla P_c)$ is the streaming velocity, where $\mathbf{v}_A = \mathbf{B}/\sqrt{\rho}$ is the Alfven velocity, $\mathbf{g}$ is the gravitational acceleration, $P^{*} = P_g + B^2/2$ is the total pressure, equal to the sum of thermal gas pressure and magnetic pressure, $E = \rho v^2/2 + P_g/(\gamma_g - 1) + B^2/2$ is the total energy density, equal to the sum of kinetic, thermal and magnetic energy densities and $\boldsymbol{\sigma}_c$ is the interaction coefficient defined by

$$\boldsymbol{\sigma}_c^{-1} = \boldsymbol{\sigma}_d^{-1} + \boldsymbol{\sigma}_s^{-1},$$

$$\boldsymbol{\sigma}_d^{-1} = \frac{\boldsymbol{\kappa}}{\gamma_c - 1}, \quad \boldsymbol{\sigma}_s^{-1} = \frac{\mathbf{B}}{|\mathbf{B} \cdot \nabla P_c|} \mathbf{v}_A (E_c + P_c), \tag{4.7}$$

where $\boldsymbol{\kappa}$ is the CR diffusion tensor. The interaction coefficient $\boldsymbol{\sigma}_c$ links the thermal gas with CRs and acts as a bridge for momentum and energy transfer (through the source terms $\boldsymbol{\sigma}_c \cdot [\mathbf{F}_c - (E_c + P_c)\mathbf{v}]$ and $\mathbf{v}_s \cdot \boldsymbol{\sigma}_c \cdot [\mathbf{F}_c - (E_c + P_c)\mathbf{v}]$). It describes the strength of the CR-gas coupling and consists of two parts: a streaming part $\boldsymbol{\sigma}_s$ and a diffusive part $\boldsymbol{\sigma}_d$, to model different modes of CR transport. The reduced speed of light $c_{\rm red}$, in combination with $\boldsymbol{\sigma}_c$, set the timescale for CRs to couple with thermal gas. $c_{\rm red}$ is designed to capture the speed of the free-streaming CRs, which in reality is close to the speed of light, though in practice it is always set much lower to allow for a longer Courant time-step; it has been shown that results are converged with respect to $c_{\rm red}$ as long as it is much greater than any other velocity in the system [93]. Note that if $\sigma_c c_{\rm red}^2 \Delta t \gg 1$ (where Δt is the time step), the time derivative $\partial \mathbf{F}_c / \partial t$ will be negligible and one would recover the steady-state CR flux

$$\mathbf{F}_{\rm c,steady} = (E_c + P_c)(\mathbf{v} + \mathbf{v}_s) - \frac{\boldsymbol{\kappa}}{\gamma_c - 1} \cdot \nabla P_c. \tag{4.8}$$

We see two components of CR transport in eqn.4.8, the first term showing CR energy advecting at the combined velocity $\mathbf{v} + \mathbf{v}_s$ and the second term depicting diffusion. Note that from eqn.4.7 $\sigma_c c_{\rm red}^2 \Delta t \gg 1$ is not possible if $\nabla P_c \approx 0$. In this case $\sigma_c \approx 0$, $\partial \mathbf{F}_c / \partial t$ is not negligible and no closed form expression for $\mathbf{F}_c$ exists. CR momentum and energy transfer ≈ 0. In this regime CRs are said to be uncoupled from the thermal gas and free streaming. On the other hand, if ∇P_c is finite and $c_{\rm red}$ is sufficiently large, the CR flux would be in steady-state (eqn.4.8) and CR-gas are said to be coupled. In this regime CRs transfer momentum and energy to the gas at the rates

$$\boldsymbol{\sigma}_c \cdot [\mathbf{F}_c - (E_c + P_c)\mathbf{v}] \rightarrow -\nabla P_c, \tag{4.9}$$

$$\mathbf{v}_s \cdot \boldsymbol{\sigma}_c \cdot [\mathbf{F}_c - (E_c + P_c)\mathbf{v}] \rightarrow -\mathbf{v}_s \cdot \nabla P_c. \tag{4.10}$$

Note that there is no heat transfer if $\mathbf{v}_s$ (or the magnetic field) is perpendicular to ∇P_c. Since $\mathbf{v}_s$ always points down the P_c gradient, CRs always heat the gas instead of the other way around.

The diffusion tensor can be expressed in general as $\boldsymbol{\kappa} = \kappa_{\parallel}\hat{\mathbf{b}}\hat{\mathbf{b}} + \kappa_{\perp}(\mathbf{I} - \hat{\mathbf{b}}\hat{\mathbf{b}})$, where $\kappa_{\parallel}$ and $\kappa_{\perp}$ are the field-aligned and cross-field diffusion coefficients. Cross-field diffusion is ignored in this study (i.e. $\kappa_{\perp} \approx 0$). We also ignore any CR collisional losses due to Coulomb collisions and hadronic interactions. In this context, $\boldsymbol{\kappa}$ accounts for the slippage from perfect wave locking due to damping. If damping is weak, slippage is small and $\kappa_{\parallel}$ will be small. In principle, $\kappa_{\parallel}$ is a function of various plasma parameters (e.g., Jiang and Oh 93, Wiener et al. 182), but to date the exact contributions from wave damping are unclear, so in this study unless otherwise stated we shall consider damping to be weak, and we will set $\kappa_{\parallel}$ to be a small constant. For an implementation of $\kappa_{\parallel}$ with non-negligible ion-neutral damping, for example, see Bustard and Zweibel [20].

4.2.2 Simulation Setup

In this section we describe the simulation setup that is used throughout the study. The simulations were performed with Athena++ [161], an Eulerian grid-based MHD code using a directionally unsplit, high-order Godunov scheme with the constrained transport (CT) technique. CR streaming was implemented with the two-moment method [93], which solves eqn.4.1-4.6. Cartesian geometry is used throughout.

We run our setup in 2D and 3D, 2D for high resolution and 3D for full dimensional coverage. The setup consists of a set of initial profiles, source terms and appropriate boundary conditions. Gravity defines the direction of stratification, which is taken to be in the x-direction ($\mathbf{g} = -g(x)\hat{\mathbf{x}}$). We sometimes use 'vertical' and 'horizontal' to denote stratification (x) and perpendicular (y, z) directions respectively. Both CR transport modes are present (streaming and diffusion).

4.2.2.1 Initial Profiles

The initial profiles are calculated by solving a set of ODEs assuming hydrostatic and thermal equilibrium. In the absence of any instability, the initial profiles will remain time-steady. We align the magnetic field with the direction of stratification for background CR heating. It is initially spatially constant ($\mathbf{B} = B\hat{\mathbf{x}}$)[4]. Gravity is

---

[4] By symmetry, the magnetic field can only vary along x, the direction of stratification, i.e. $\mathbf{B} = B(x)\hat{\mathbf{x}}$. To satisfy $\boldsymbol{\nabla} \cdot B = 0$, $\mathrm{d}B/\mathrm{d}x = 0$, i.e. the magnetic field is constant.

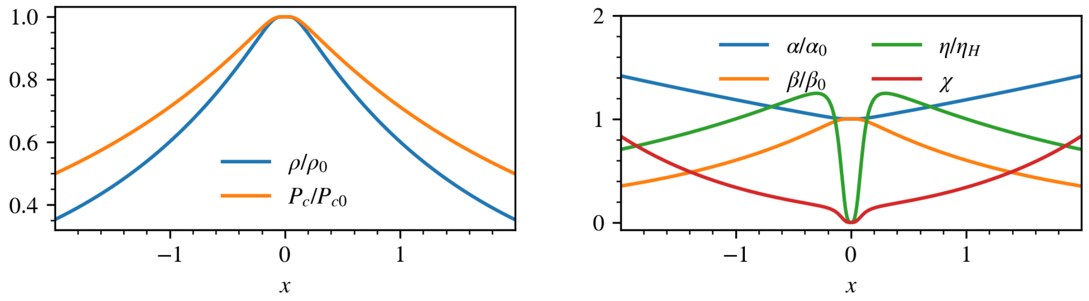

FIGURE 4.1: *Top*: Example of the initial density (blue) and P_c (orange) profiles. Found from solving eqn.4.14 numerically. Gravity is tapered to zero at $x = 0$, resulting in zero derivatives for ρ and P_c there. *Bottom*: Example of $\alpha, \beta, \eta, \chi$ for the same initial profile, normalized by their reference values. Note that $\alpha_0 = 1, \beta_0 = 5, \eta_H = 0.01$ and $\delta_H = 1$.

taken to be

$$g(x) = g_0 \frac{(x/a)^3}{1 + |x/a|^3}. \tag{4.11}$$

Thus, $g(x)$ approaches g_0, a constant, as $x \to \infty$ and approaches $g_0(x/a)^3$ when $x \ll a$. The smoothing parameter a tapers the gravitational field to zero as $x \to 0$ so as to avoid discontinuities in ∇P_g and ∇P_c. We found that this functional form maintains hydrostatic equilibrium better than the gravitational softening employed by McCourt et al. [115] and thereafter. In hydrostatic equilibrium,

$$\frac{\mathrm{d}P_g}{\mathrm{d}x} + \frac{\mathrm{d}P_c}{\mathrm{d}x} = -\rho g. \tag{4.12}$$

We take the initial profile to be isothermal with temperature T_0 such that $\mathrm{d}P_g/\mathrm{d}x = T_0\, \mathrm{d}\rho/\mathrm{d}x$. If CR transport is streaming dominated, $P_c = P_{c0}(\rho/\rho_0)^{\gamma_c/2}$, where ρ_0 and

P_{c0} are some reference density and CR pressure. Substituting into eqn.4.12,

$$\left[T_0+\frac{\gamma_c P_{c0}}{2\rho_0}\left(\frac{\rho}{\rho_0}\right)^{\gamma_c/2-1}\right]\frac{\mathrm{d}\rho}{\mathrm{d}x}=-\rho g. \tag{4.13}$$

Integrating both sides,

$$\ln\left(\frac{\rho}{\rho_0}\right)+\frac{\gamma_c}{2-\gamma_c}\frac{P_{c0}}{P_{g0}}\left[1-\left(\frac{\rho}{\rho_0}\right)^{\gamma_c/2-1}\right]=-\frac{1}{T_0}\int_0^x g(x')\,\mathrm{d}x'\,, \tag{4.14}$$

where $P_{g0}=\rho_0 T_0$ is some reference gas pressure. The density profile $\rho(x)$ is then found numerically from eqn.4.14 using a numerical integrator and root-finder. The gas and CR pressure, CR flux profiles are then found from $P_g=\rho T_0$, $P_c=P_{c0}(\rho/\rho_0)^{\gamma_c/2}$ and

$$F_c(x)=\frac{\gamma_c}{\gamma_c-1}P_c v_A-\frac{\kappa_\parallel}{\gamma_c-1}\frac{\mathrm{d}P_c}{\mathrm{d}x}, \tag{4.15}$$

where we have used eqn.4.8. See the top panel of fig.4.1 for an example of the density and P_c profile. Here we discuss several important ratios characterizing our initial profiles:

$$\alpha=\frac{P_c}{P_g},\ \beta=\frac{2P_g}{B^2},\ \eta=\frac{\kappa_\parallel}{\gamma_c v_A L_c},\ \delta=\frac{t_{\rm cool}}{t_{\rm ff}},\ \chi=\frac{v_A|\nabla P_c|}{\rho^2\Lambda}, \tag{4.16}$$

which determine the CR to gas (α), magnetic to gas (β) pressure ratios, diffusive to streaming flux ratio (η) and the ratio of cooling to free-fall time (δ) and CR heating to radiative cooling (χ). $L_c=P_c/|\nabla P_c|$ is the CR scale height. η, the ratio of the diffusive to streaming flux, is small if streaming transport dominates. As ρ, P_c, P_g in the initial profiles are functions of x, the ratios in eqn.4.16 in general also vary with x.

The density profile can be fully determined given $g_0, a, \rho_0, T_0, \alpha_0$. The reference values ρ_0, α_0 are set at the base $x = 0$. Note that T_0 is a constant in our isothermal profile. With $\rho(x)$ determined, $P_g(x), P_c(x)$ can be obtained easily from the ideal gas law and $P_c \propto \rho^{\gamma_c/2}$. The latter is true for steady-state, static streaming dominated flows[5] [15, 184]. The magnetic field can be obtained by specifying β_0, i.e. β at $x = 0$. Note that in our setup the field is aligned with gravity. The diffusion coefficient $\kappa_{\parallel}$ is found by setting η *not* at $x = 0$ as L_c is infinite there but at a thermal scale height $x = H = T_0/g_0$ (we shall denote this by η_H, with subscript H meaning it is set at $x = H$). Without loss of generality, we shall set g_0, T_0, ρ_0 all to 1 and $a = 0.1H$. In fig.4.1 we show an example of the how these profiles (top panel) and the respective ratios α, β, η (bottom panel) vary in space. Since CR pressure declines more weakly with density ($P_c \propto \rho^{2/3}$) than isothermal gas pressure ($P_{\rm g} \propto \rho$), the profile becomes slightly more CR dominated the further out. Plasma β decreases with height as the B-field is spatially constant. Apart from the peak at $x \sim a$ where $|\nabla P_c|$ is maximized, η generally decreases with increasing x.

---

[5] We ignore CR diffusion in our initial profiles. Thus, our background profiles are not exactly in steady state, particularly in profiles where diffusion is comparable to streaming, $\eta_{\rm H} \sim 1$. In practice, we have found that our results are not sensitive to the initial deviation from perfect equilibrium. We also find that the global background profile eventually always evolves significantly, once thermal instability triggers mass dropout.

4.2.2.2 Source Terms

We adopt a power law cooling function

$$\Lambda = \Lambda_0 (T/T_0)^{\Lambda_T}. \tag{4.17}$$

Using the density and P_c profiles found from §4.2.2.1, the cooling strength Λ_0 is determined by δ or χ. The cooling index Λ_T can be adjusted to mimic the cooling curve in cluster ($\Lambda_T = 0.5$) and galaxy halo ($\Lambda_T = -2/3$; we use this exclusively in this paper) contexts.

When δ_H (i.e. δ at a thermal scale-height) is specified, the cooling strength is given by

$$\Lambda_0 = \frac{T_0}{(\gamma_g - 1)\delta_H \rho_H t_{\mathrm{ff,H}}}, \tag{4.18}$$

where $t_{\mathrm{ff,H}}$ is the free-fall time at $x = H$ defined by

$$t_{\mathrm{ff}} = \sqrt{\frac{2x}{g_0}}, \tag{4.19}$$

with x replaced by H. The subscript H again denotes quantity evaluated at $x = H$. When χ_H is specified, the cooling strength is:

$$\Lambda_0 = \frac{|v_{A,H} \nabla P_{c,H}|}{\chi_H \rho_H^2}. \tag{4.20}$$

Thus, we can specify either δ or χ to our desired value for the purpose of the study.

Unless $\chi = 1$ everywhere, CR heating cannot fully balance radiative cooling. The residual heating needed to attain thermal balance is provided by 'feedback heating' (or 'magic heating') $\mathcal{H}$ [115, 151], a phenomenological heating model where global thermal equilibrium is enforced by fiat. At each time-step, uniform heating is input at a rate given by the spatially averaged cooling rate at a given height (or radius), so that the average net cooling is zero. However, the fluctuations in the net cooling rate can give rise to thermal instability. In our system, this means that the heating rate is given by:

$$\mathcal{H}(x,t) = \langle \rho^2 \Lambda + v_A \nabla P_c \rangle, \tag{4.21}$$

where $\langle \cdot \rangle$ denotes spatial average over the y, z-slice at any particular x. This term is activated only when the RHS of eqn.4.21 is greater than zero; $\mathcal{H}$ will be set to zero if the RHS is negative. $\mathcal{H}$ can be interpreted physically as other sources of heating, such as thermal star formation or AGN feedback.

In the absence of a CR source at the base ($x = 0$), the CR profiles will not maintain steady state as CRs stream away, causing the P_c profile to flatten (see fig.1 of Jiang and Oh [93] for an example). We supply CRs at the base by fixing the CR pressure P_c as

$$P_c(x,t) = \alpha_0 P_g(x,t) \tag{4.22}$$

for $|x| < 0.7\Delta x$, where Δx is the grid size. Physically this represents sources of CRs from the galactic disk (e.g., due to supernovae or AGN). An alternative is to fix the

CR flux F_c at the base. We show some results from this in Appendix B.3. There is no qualitative change in our conclusions.

4.2.2.3 Simulation Box and Boundary Conditions

The simulation box extends symmetrically in all directions about the origin for 2 thermal scale-heights H, employing hydrostatic boundary conditions in the x-direction and periodic boundaries otherwise. Hydrostatic boundaries mandate

$$\left.\frac{\mathrm{d}P_g}{\mathrm{d}x}\right|_{\mathrm{bond}} + \left.\frac{\mathrm{d}P_c}{\mathrm{d}x}\right|_{\mathrm{bond}} = -\left.\rho g\right|_{\mathrm{bond}} \tag{4.23}$$

at the ghost zone cell faces. We provide details of our boundary implementation in Appendix B.2. In §4.4 we shall see that in some cases the flow could become non-hydrostatic, but no significant difference is seen when we adopt an outflow type boundary condition (see Appendix B.2). We refrain from extending the box beyond $2H$ to prevent plasma β from dropping below ~ 0.5 and exciting acoustic instabilities right from the beginning of the simulation [6, 169]. It is also to prevent $\chi > 1$ at large x (see fig.4.1) for which overheating occurs and the gas would be out of thermal equilibrium.

To prevent spurious numerical behavior, we apply buffers with thickness a near the x boundaries and the base. There is no cooling or CR heating within these buffers.

4.2.2.4 Resolution, Reduced Speed of Light and Temperature Floors

We run our simulations in 2D with 1024×512 grids (higher resolution along the x-axis). In Appendix B.4 we run a selected subset of cases in higher resolution (2048×512) and in 3D with $256 \times 128 \times 128$ grids and show that our conclusions remain unchanged. We use a reduced speed of light $c_{\rm red} = 200$, which is much greater than any other velocity scale in the problem (in most cases this should be sufficient, though in some cases with particularly strong magnetic field and low density, for which v_A is large, we increase $c_{\rm red}$ accordingly). The temperature floor is set to $T_0/100$ while the ceiling is set to $5T_0$. In general, in a multi-phase medium, cooling is dominated by the cool gas, so enforcing global thermal equilibrium means that the hot gas, where cooling is inefficient, could be heated up to even higher temperatures. It is customary, in thermal instability studies, to set a temperature ceiling to prevent the time-step from becoming extremely small. However, given the possibility that CR heating can potentially heat the gas to very high temperatures in the nonlinear evolution, we remove the ceiling for simulations in §4.4.

4.2.2.5 Simulation Runs

Table 4.1 summarizes the test cases used to produce the results shown in this study. As previously discussed, the initial profile is characterized by $g_0, \rho_0, T_0, a, \alpha_0, \beta_0, \eta_H$ while the cooling term is determined by the cooling index Λ_T, and χ_H or δ_H. These parameters are defined therein. Without loss of generality, we set $g_0, \rho_0, T_0 = 1$ in all

Identifier	α_0	β_0	η_H	χ_H	δ_H	Λ_T	Resolution	c_{red}	Remarks
Test cases for §4.3.2									
a1b3k.01c.4in.67res1024c200single	1	3	0.01	0.4	-	-2/3	1024 × 512	200	-
a.5b3k.01c.3in.67res1024c200single	0.5	3	0.01	0.3	-	-2/3	1024 × 512	200	-
a5b100k.01c.7in.67res1024c200single	5	100	0.01	0.7	-	-2/3	1024 × 512	200	-
a1b3k.01c.4in.67res1024c200single − nocrh	1	3	0.01	0.4	-	-2/3	1024 × 512	200	No CR heating
a.5b3k.01c.3in.67res1024c200single − nocrh	0.5	3	0.01	0.3	-	-2/3	1024 × 512	200	No CR heating
a5b100k.01c.7in.67res1024c200single − nocrh	5	3	0.01	0.7	-	-2/3	1024 × 512	200	No CR heating
a1b3k1c.4in.67res1024c200single	1	3	1	0.4	-	-2/3	1024 × 512	200	-
Test cases for §4.3.3									
a1b3k.01c.4in.67res1024c200	1	3	0.01	0.4	-	-2/3	1024 × 512	200	-
a1b3k.01c.4in.67res1024c200 − nocrh	1	3	0.01	0.4	-	-2/3	1024 × 512	200	No CR heating
a1b3k1c.4in.67res1024c200	1	3	1	0.4	-	-2/3	1024 × 512	200	-
a1b3k.01c1in.67res1024c200	1	3	0.01	1	-	-2/3	1024 × 512	200	-
a1b3k.01c1in.67res1024c200 − nocrh	1	3	0.01	1	-	-2/3	1024 × 512	200	No CR heating
a1b3k1c1in.67res1024c200	1	3	1	1	-	-2/3	1024 × 512	200	-
a1b3k.01c2.5in.67res1024c200	1	3	0.01	2.5	-	-2/3	1024 × 512	200	-
a1b3k.01c2.5in.67res1024c200 − nocrh	1	3	0.01	2.5	-	-2/3	1024 × 512	200	No CR heating
a1b3k1c2.5in.67res1024c200	1	3	1	2.5	-	-2/3	1024 × 512	200	-
Test cases for §4.4									
a1b5k.0001d1in.67res1024c200	1	5	0.0001	-	1	-2/3	1024 × 512	200	-
a1b5k.001d1in.67res1024c200	1	5	0.001	-	1	-2/3	1024 × 512	200	-
a1b5k.01d1in.67res1024c200	1	5	0.01	-	1	-2/3	1024 × 512	200	'slow wind'
a1b5k.01d1in.67res1024c200 − nocrh	1	5	0.01	-	1	-2/3	1024 × 512	200	'slow wind' (nocrh)
a1b5k.1d1in.67res1024c200	1	5	0.1	-	1	-2/3	1024 × 512	200	-
a1b5k.5d1in.67res1024c200	1	5	0.5	-	1	-2/3	1024 × 512	200	-
a1b5k1d1in.67res1024c200	1	5	1	-	1	-2/3	1024 × 512	200	'fast wind'
a1b5k1d1in.67res1024c200 − nocrh	1	5	1	-	1	-2/3	1024 × 512	200	'fast wind' (nocrh)
a1b5k5d1in.67res1024c1000	1	5	5	-	1	-2/3	1024 × 512	1000	-
a5b5k1d1in.67res1024c3000	10	5	1	-	1	-2/3	1024 × 512	3000	-
a10b5k.01d1in.67res1024c1000	10	5	0.01	-	1	-2/3	1024 × 512	1000	-
a1b10k1d1in.67res1024c200	1	10	1	-	1	-2/3	1024 × 512	200	-
a1b30k1d1in.67res1024c200	1	30	1	-	1	-2/3	1024 × 512	200	-
a1b50k1d1in.67res1024c200	1	50	1	-	1	-2/3	1024 × 512	200	-
a1b100k1d1in.67res1024c200	1	100	1	-	1	-2/3	1024 × 512	200	-
a1b300k.01d1in.67res1024c200	1	300	0.01	-	1	-2/3	1024 × 512	200	-
a1b300k1d1in.67res1024c200	1	300	1	-	1	-2/3	1024 × 512	200	'fountain'
a1b300k1d1in.67res1024c200 − nocrh	1	300	1	-	1	-2/3	1024 × 512	200	'fountain' (nocrh)
a1b300k10d1in.67res1024c200	1	300	10	-	1	-2/3	1024 × 512	200	-
a1b1000k10d1in.67res1024c200	1	1000	1	-	1	-2/3	1024 × 512	200	-
a1b10000k10d1in.67res1024c200	1	10000	1	-	1	-2/3	1024 × 512	200	-
a10b300k.01d1in.67res1024c1000	10	300	0.01	-	1	-2/3	1024 × 512	1000	-
a10b300k1d1in.67res1024c1000	10	300	1	-	1	-2/3	1024 × 512	1000	-
a.3b300k.01d1in.67res1024c200	0.3	300	0.01	-	1	-2/3	1024 × 512	200	-
a.1b300k1d1in.67res1024c200	0.1	300	1	-	1	-2/3	1024 × 512	200	-
a.1b5k1d1in.67res1024c200 − nocrh	0.1	5	1	-	1	-2/3	1024 × 512	200	No CR heating
a.01b5k1d1in.67res1024c200 − nocrh	0.01	5	1	-	1	-2/3	1024 × 512	200	No CR heating
Test cases for Appendix B.4									
a1b5k.01d1in.67res2048c200	1	5	0.01	-	1	-2/3	2048 × 512	200	-
a1b5k1d1in.67res2048c200	1	5	1	-	1	-2/3	2048 × 512	200	-
a1b300k1d1in.67res2048c200	1	300	1	-	1	-2/3	2048 × 512	200	-
a1b5k.01d1in.67res256c2003d	1	5	0.01	-	1	-2/3	256 × 128 × 128	200	-
a1b5k1d1in.67res256c2003d	1	5	1	-	1	-2/3	256 × 128 × 128	200	-
a1b300k1d1in.67res256c2003d	1	300	1	-	1	-2/3	256 × 128 × 128	200	-

TABLE 4.1: Test cases used in this study. Each test case has an identifier, listed in column 1. Identifiers suffixed with 'single' have a single density bump as initial perturbation while 'nocrh' denotes no CR heating. Column 2 and 3 list the profile parameters α_0, β_0 used in determining the initial profiles ρ, P_g, P_c (α_0 and β_0 are the initial ratio of CR to gas pressure and magnetic to gas pressure at $x = 0$, respectively). With the initial ρ, P_g, P_c, column 4 to 7 are parameters used to determine the CR diffusivity κ, cooling normalization Λ_0 and cooling index Λ_T, which are constants throughout the simulation. η_H refers to the initial ratio of CR diffusive to streaming flux at a scaleheight H, and similarly for χ_H and δ_H. Please refer to §4.2.2.1 and §4.2.2.2 for complete description. The resolution, reduced speed of light and box domain are listed in column 8 to 10.

our simulations. The scale height H should always be understood as the *initial* gas scale height $x = H = T_0/g_0 = 1$, which is therefore a constant. Although we report all our results in code units, we translate our results into physical units scaled to the Milky Way in §4.5.1.

4.3 Linear Evolution: Thermal Instability

4.3.1 Previous Work; Analytic Expectations

Local thermal instability is caused by runaway radiative cooling, i.e. hot gas that has been cooled slightly becomes denser, causing it to cool faster. In gravitationally stratified media, however, buoyant oscillations can damp local thermal instability [115, 151]. Stability is determined by the ratio of two timescales: the cooling time $t_{\rm cool}$ and the free fall $t_{\rm ff}$, where $t_{\rm ff} \approx \sqrt{2h/g}$ for the constant gravity setup in this paper. If cooling acts faster than buoyant damping, the instability can proceed, otherwise it is damped. This idea has been pursued by many others in various geometries and background profiles, generally leading to an instability condition of $t_{\rm cool}/t_{\rm ff} \lesssim 10$, although in our particular setup, where we evaluate $t_{\rm cool}/t_{\rm ff}$ at a scale-height, the condition is $t_{\rm cool}/t_{\rm ff} \lesssim 1$[6]. Observationally, this threshold has been quite successful in flagging clusters which host substantial cold gas [37], though the applicability to galaxy halos, which are not in hydrostatic or thermal equilibrium, and where large amplitude density perturbations are present, is less clear [49, 123].

---

[6] This result only holds for small linear perturbations. Choudhury et al. [34] have shown that buoyant oscillations cannot suppress large amplitude perturbations $\delta\rho/\rho \sim \mathcal{O}(1)$, where thermal instability is independent of $t_{\rm cool}/t_{\rm ff}$ and only depends on $t_{\rm cool}$.

Non-thermal forces can modify thermal instability. Magnetic tension suppresses buoyant oscillations, leading to instability even when the threshold is exceeded [87]. This effect takes hold even for high plasma $\beta \sim 300$ and is independent of field orientation relative to the gravitational field. Magnetic fields can also provide pressure support for the cold clouds, so that they can be vastly out of thermal pressure balance with the surrounding. While CRs can similarly provide non-thermal pressure support [84], their impact *does* depend on the orientation of magnetic fields. Butsky et al. [23] include CR streaming transport in their stratified simulations. However, the magnetic field is oriented perpendicular to gravity in the study, making CR streaming heating, $-v_s \cdot \nabla P_c$, non-existent in the background and only a second order effect in the evolution of the instability. In this case, the main influence of CRs is via their pressure support. Cold gas is underdense relative to the purely thermal case (reducing net density fluctuations $\delta\rho/\rho$ in the atmosphere), and thus more buoyant; they can levitate for longer and TI saturation is less sensitive to $t_{\rm cool}/t_{\rm ff}$. However, if the magnetic field is aligned with gravity (as should be the case if there are outflows), the background heating will change the nature of thermal instability. This has been studied in a linear stability analysis by Kempski and Quataert [102], although it has not yet been simulated.

We now review analytic expectations for the CR-modified thermal instability when the magnetic field is aligned with gravity [102]. The relevant dimensionless parameters are the cooling index $\Lambda_T \equiv \partial \ln \Lambda / \partial \ln T$, the ratio of CR pressure to gas pressure $\alpha = P_c/P_g$, and

$$\xi = \frac{\kappa_{\parallel}}{\alpha t_{\rm cool} v_A^2} \sim \left(\frac{F_{\rm c,diff}}{F_{\rm c,st}}\right)\left(\frac{t_{\rm heat}}{t_{\rm cool}}\right) \sim \frac{\eta}{\chi} \tag{4.24}$$

where in the last equality of equation 4.24, we have used the diffusive flux $F_{\rm c,diff} \sim \kappa_{\parallel}\nabla P_c$, the streaming flux $F_{\rm c,st} \sim P_c v_A$, and the heating time $t_{\rm heat} \sim P_g/v_A \cdot \nabla P_c$; the symbols η, χ are defined in equation 4.16. In the limit where background cooling is balanced by CR heating, $t_{\rm cool} \sim t_{\rm heat}$, ξ is simply the ratio of diffusive to streaming flux. For fiducial values in galaxies, it is of order unity:

$$\xi \sim 1 \frac{(\kappa_{\parallel}/10^{28}\ {\rm cm^2 s^{-1}})(\beta/10)}{(\alpha/1)(t_{\rm cool}/30\ {\rm Myr})(c_s/100\ {\rm kms^{-1}})^2}. \tag{4.25}$$

The CR to gas pressure α determines how gas density changes with cooling. If $\alpha \gg 1$, CR pressure dominates and cooling is isochoric ($\Delta P_g/P_g \gg \delta\rho/\rho$), while if $\alpha \ll 1$, cooling is isobaric ($\Delta P_g/P_g \ll \delta\rho/\rho$) [7]. The cooling index Λ_T determines if the gas is isobarically ($\Lambda_T < 2$) and/or isochorically ($\Lambda_T < 0$) thermally unstable [54]. Ignoring the influence of cosmic ray transport for now, this means that gas will be thermally unstable for $\Lambda_T < 2$ when $\alpha \ll 1$ (and cooling is isobaric), and it will be thermally unstable for $\Lambda_T < 0$ when $\alpha \gg 1$ (and cooling is isochoric). In between, there is a critical cooling index $0 \lesssim \Lambda_{\rm T,c}(\alpha) \lesssim 2$, for which gas with $\Lambda_T < \Lambda_{\rm T,c}(\alpha)$ will be thermally unstable. As ambient hot galaxy halo gas in the temperature range

---

[7] Assuming that the perturbation $l \ll c_s t_{\rm cool}$, where $c_s t_{\rm cool}$ is evaluated at the background temperature, so that it is in sonic contact with its surroundings. Note that as the perturbation cools to lower temperatures and $c_s t_{\rm cool}$ falls, it can fall out of pressure balance and be subject to fragmentation by 'shattering' [117], but this is immaterial in the linear evolution.

$10^5 < T < 10^7$K always has $\Lambda_T < 0$ (we adopt $\Lambda_{\rm T} = -2/3$ in our simulations), it will always be thermally unstable. It turns out that inclusion of CR transport changes some details, but does not change the conclusion that CRs do not generally suppress thermal instability (except in specific conditions described below) [102].

The perturbed CR heating rate due to CR streaming has two potential effects [102]. If it is in phase with the perturbed cooling rate, and also is sufficiently strong, it can suppress thermal instability. If CR heating is out of phase with the perturbed cooling rate, which is more generally the case, the associated gas pressure fluctuations will drive an acoustic mode[8]. In this case, thermally unstable modes result in overstable oscillations which propagates at the characteristic velocity of the heating front, i.e. the Alfven velocity.

We can gain some intuition from the perturbation equations. In Appendix B.1, we present a fuller analysis, but below we outline the main elements. The perturbed CR heating is

$$\delta(-\mathbf{v}_A \cdot \nabla P_c) = -i\omega_A \delta P_c, \tag{4.26}$$

while the perturbed cooling is

$$\delta\big(-\rho^2\Lambda\big) = -\rho^2\Lambda(2-\Lambda_T)\frac{\delta\rho}{\rho} - \rho^2\Lambda\Lambda_T\frac{\delta P_g}{P_g}. \tag{4.27}$$

---

[8] For adiabatic sound waves, this can drive an acoustic instability, where sound waves grow in amplitude and steepen into shocks [6, 169].

If the background is in thermal equilibrium, local thermal stability is then determined by the perturbed CR heating and gas cooling rates. Their ratio in the isobaric ($\delta P_g/P_g \ll \delta\rho/\rho$) and isochoric ($\delta P_g/P_g \gg \delta\rho/\rho$) cases is:

$$\frac{\delta(\text{CR Heating})}{\delta(\text{Cooling})} = \begin{cases} \frac{i\omega_A}{(2-\Lambda_T)\omega_c}\frac{\delta P_c/P_g}{\delta\rho/\rho} & \text{Isobaric} \\ \\ \frac{i\omega_A}{\omega_c\Lambda_T} & \text{Isochoric,} \end{cases} \tag{4.28}$$

where $\omega_c = \rho^2\Lambda/P_c$ is the cooling rate and we have used $\delta P_c \sim -\delta P_g$ in the isochoric case. In the isochoric case, the perturbed CR heating is always $\pi/2$ out of phase with cooling. Thus, they cannot cancel. The effect of CR heating in this case is to cause the modes to oscillate and propagate at frequency $\propto \omega_A$ up the CR pressure gradient, as Kempski and Quataert [102] has shown. In the isobaric case, CR heating can suppress cooling if there is an out of phase component between δP_c and $\delta\rho$. CR diffusion can provide this phase shift. In the strong diffusion limit ($k\kappa_\parallel/v_A \gg 1$), δP_c will scale as $\delta P_c/P_g \sim i(\alpha\omega_A/\omega_d)(\delta\rho/\rho)$, i.e. shifted by a phase of $\pi/2$ from $\delta\rho$. Substituting this into eqn.4.28 gives

$$\frac{\delta(\text{CR Heating})}{\delta(\text{Cooling})} \sim -\frac{\alpha v_A^2 t_{\text{cool}}}{\kappa_\parallel} = -\xi^{-1}, \tag{4.29}$$

where the minus sign indicates the opposite nature of CR heating and cooling. The perturbed CR heating suppresses cooling only if diffusion is subdominant in the background ($\xi < 1$). Then, on small scales where CR diffusion across the perturbation dominates ($k\kappa/v_A \gg 1$), there is a CR 'Field length' λ_{CRF} below which the perturbed heating balances cooling [102]. Thermal instability is suppressed for $\lambda < \lambda_{\rm CRF}$, where

$$\lambda_{\rm CRF} \sim \min(\alpha^{1/2}, \alpha^{-1/2})\sqrt{\kappa t_{\rm cool}}. \tag{4.30}$$

Note the close analogy to the Field length $\lambda_{\rm F} \sim \sqrt{\kappa_{\rm cond} t_{\rm cool}}$ set by thermal conduction, where $\kappa_{\rm cond}$ is the heat diffusion coefficient associated with thermal electrons.

To summarize, isochoric modes ($\Lambda_{\rm T} < 0$) are always thermally unstable. In addition, if $\xi > 1$, all isobaric modes are unstable. If $\xi < 1$, then small scale modes are stabilized, but large scale modes $\lambda > \lambda_{\rm CRF}$ are still unstable. In general, CRs are unable to directly quench thermal instability in galaxy halos, where $\Lambda_{\rm T} < 0$. We shall see this is consistent with our simulations.

However, the phase velocity of thermal modes up the CR pressure gradient, which can be approximated as [102]:

$$v_{\rm ph} \sim \min(\frac{2}{3}, \frac{4}{15}\alpha) \;\; v_A \tag{4.31}$$

is potentially of more interest. The ratio of the crossing time $t_{\rm cross} \sim L/v_{\rm ph}$ to the cooling time $t_{\rm cool}$ is:

$$\theta \equiv \frac{t_{\rm cool}}{t_{\rm cross}} \sim \left(\frac{t_{\rm cool}}{t_{\rm heat}}\right)\left(\frac{t_{\rm heat}}{t_{\rm cross}}\right) \sim \chi\frac{L_c}{L} \;\; \min(\frac{2}{3}\alpha^{-1}, \frac{4}{15}), \tag{4.32}$$

where $L_c = P_c/\nabla P_c$, and $t_{\rm heat} \sim P_g/(v_A \cdot \nabla P_c)$, and we have used equation 4.31. If $\theta > 1$, then thermal modes will propagate out of the system before cooling significantly.

In general, we expect $\theta < 1$, since $\chi = t_{\rm cool}/t_{\rm heat} < 1$ (otherwise the background will be overheated), and we also expect $L_c/L \lesssim 1$. We can also see this from the parametrization:

$$\theta \equiv \frac{t_{\rm cool}}{t_{\rm cross}} \sim \left(\frac{t_{\rm cool}}{t_{\rm ff}}\right)\left(\frac{t_{\rm ff}}{t_{\rm cross}}\right) \sim \frac{\delta}{\beta^{1/2}} \;\; \min(\frac{2}{3}, \frac{4}{15}\alpha) \tag{4.33}$$

so that when there is thermal instability in our setup, $\delta = t_{\rm cool}/t_{\rm ff} < 1$, the fact that $\beta \gtrsim 1$ means that $\theta < 1$.

However, there is sufficient uncertainty that it is worth investigating numerically how the propagation of thermal modes affect thermal instability. In addition, Kempski and Quataert [102] suggest that the oscillations induced by mode propagation could also potentially damp thermal instability and change the threshold for thermal instability, particularly if the oscillation frequency $\omega_{\rm A}$ is higher than the free-fall frequency. We now address this in our simulations.

4.3.2 Propagation of modes

We begin by verifying that thermal entropy modes do propagate at the expected velocity given by linear analysis. To do this we insert a Gaussian density bump of form

$$\delta\rho = \mathcal{A}\rho(x_b)e^{-\left(\frac{(x-x_b)^2+(y-y_b)^2}{\Delta}\right)}, \tag{4.34}$$

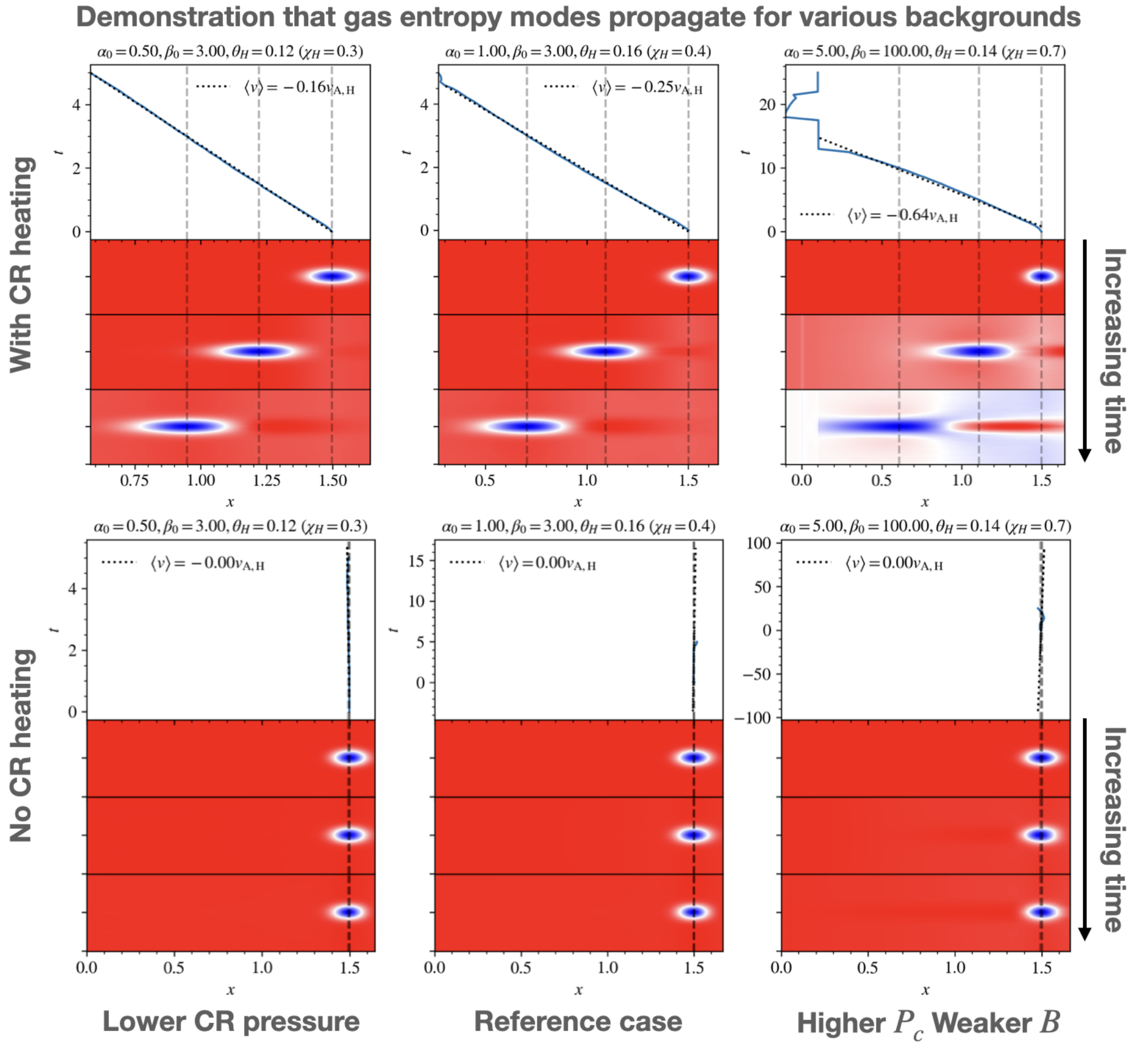

FIGURE 4.2: Propagation of thermal entropy modes for different values of $\alpha_0, \beta_0, \theta_H = t_{\rm cool,H}/t_{\rm cross,H}$ with (top row) and without (bottom row) CR heating (note that θ_H is related to χ_H, the ratio of CR heating to radiative cooling through eqn.4.32). Note that subscripts 0 and H means quantities evaluated at the base $x = 0$ and at the initial gas scale-height $x = H = T_0/g_0 = 1$ respectively. A Gaussian density bump is placed at $x = 1.5$ initially and its trajectory followed. In each panel we trace the location of the bump with time, showing snapshots of the temperature field. With CR heating, the bump is clearly moving. No propagation is seen without CR heating. We fit the slope of the $x - t$ plot while the bump is in its linear phase (i.e. $\delta\rho/\rho < 1$) to extract its propagation velocity $\langle v \rangle$ (in units of $v_{A,H}$). The propagation speeds are consistent with that predicted from linear theory eqn.4.31. The propagating mode appear stretched out due to slight differences in $v_{\rm ph}$ across its width.

where $\mathcal{A}$ is the amplitude (in units of $\rho(x_b)$, the local background density), (x_b, y_b) is the location of the bump and Δ is the width. We place the bump at $(1.5H, 0)$, with amplitude $\mathcal{A} = 0.01$ and width $0.1H$. The other parameters used are listed on top of each panel in fig.4.2 and the resulting evolution is shown. In each panel we plot the $x - t$ trajectory of the perturbation and display snapshots of the temperature field at different times. The perturbation is tracked by finding the location with minimum temperature. CR heating to the thermal gas $-v_A \cdot \nabla P_c$ is switched off for the bottom row as a control to illustrate the effect of CR heating. To ensure the background is in steady state while the mode is propagating (for the sake of clarity in our demonstration), we impose the CR source term $\mathcal{Q}$ (*only* for the studies of mode propagation in §4.3; we do not include such source terms in §4.4) on the right hand side of equation 4.5:

$$\mathcal{Q}(x) = \frac{\mathrm{d}F_c}{\mathrm{d}x} - v_A \frac{\mathrm{d}P_c}{\mathrm{d}x}. \tag{4.35}$$

Since $P_c \propto \rho^{\gamma_c/2}$ initially, this simplifies to

$$\mathcal{Q}(x) = -\frac{\kappa}{\gamma_c - 1} \frac{\mathrm{d}^2 P_c}{\mathrm{d}x^2} = -\frac{\gamma_c}{\gamma_c - 1} \eta L_c v_A \frac{\mathrm{d}^2 P_c}{\mathrm{d}x^2}. \tag{4.36}$$

In fig.4.2 we present three test cases, corresponding (from left to right) to parameters $(\alpha_0, \beta_0, \eta_H, \theta_H) = (0.5, 3, 0.01, 0.12)$, $(1, 3, 0.01, 0.16)$ and $(5, 100, 0.01, 0.14)$. CR streaming dominate the transport as $\eta_H \ll 1$. Note that θ_H is adjusted through χ_H via eqn.4.32. Changing β_0 changes the Alfven speed v_A while changing α_0 affects the fraction of the Alfven speed the modes propagate at. Using the $(1, 3, 0.01, 0.16)$

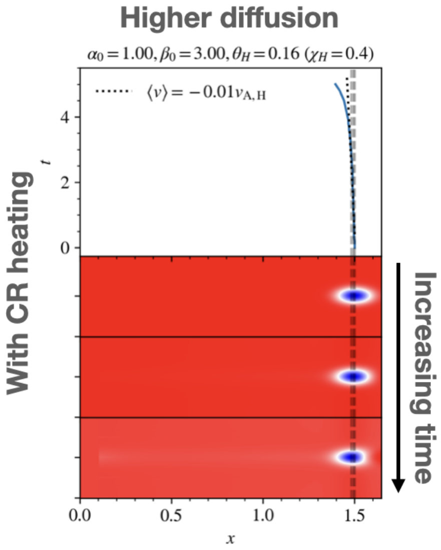

FIGURE 4.3: Same as the middle column of fig.4.2 but with enhanced CR diffusion ($\eta_H = 1$). There is no propagation in this case even when CR heating is present.

(middle column) as a reference case, halving the CR pressure roughly halves the propagation speed while increasing it by 5 times boosts the propagation to the asymptotic limit of $v \sim -2v_A/3 \sim -0.67v_A$. The propagation speed of the reference case, $\langle v \rangle = -0.25v_{A,H}$, is consistent with $-4\alpha v_A/15$ predicted from linear theory (eqn.4.31). Note that the mode velocity displayed in the figure $\langle v \rangle$ is given in terms of $v_{A,H}$, the Alfven velocity at a thermal scale-height. v_A varies with density along the profile, so the slight difference found in our test cases from that predicted from linear theory is to be expected. The minus sign in the propagation speeds indicate the modes are propagating up the P_c gradient.

The bottom row of fig.4.2, with CR heating switched off, shows no propagation of the modes and reflects clearly that propagation is completely due to CR heating. In fig.4.3 we show again the middle column case ($\alpha_0 = 1, \beta_0 = 3, \theta_H = 0.16$) but with increased diffusion ($\eta_H = 1$, i.e. the diffusive flux is equal to the streaming flux at a thermal scale-height). There is no mode propagation in this case. The reason is diffusion causes CRs to slip out of the perturbation before they can heat the gas, thus removing the effects of CR heating.

From these test cases we have shown that CR streaming, through streaming heating, can cause thermal entropy modes to propagate at some fraction of the Alfven velocity consistent with linear theory. If one removes the effect of CR heating, either by switching off the source term $-v_A \cdot \nabla P_c$ or by increasing diffusion, the modes do not propagate.

4.3.3 Does propagation suppress thermal instability?

Having shown in §4.3.2 that thermal entropy modes propagate in a CR streaming dominated flow under the effect of CR heating, we consider whether thermal instability can be suppressed as proposed in §4.3.1, that is, if mode propagation sets a time limit t_{cross} on how much the perturbations can grow before moving out of the cooling region. If $t_{\text{cross}} \ll t_{\text{cool}}$, perturbations can hardly grow before they propagate out of the cooling region, effectively suppressing the instability.

In this section, we initiate a stratified profile in hydrostatic and thermal balance and seed random isobaric perturbations:

$$\frac{\delta\rho}{\rho} = \begin{cases} \sum_{mn} \frac{4A_{mn}}{\sqrt{N}} \sin\left(\frac{2\pi n x}{L_x} + \phi_{x,n}\right) \sin\left(\frac{2\pi m y}{L_y} + \phi_{y,m}\right), & \text{(2D)} \\ \sum_{lmn} \frac{8A_{lmn}}{\sqrt{N}} \sin\left(\frac{2\pi n x}{L_x} + \phi_{x,n}\right) \sin\left(\frac{2\pi m y}{L_y} + \phi_{y,m}\right) & \text{(3D)} \\ \qquad \sin\left(\frac{2\pi l z}{L_z} + \phi_{z,l}\right), & \end{cases} \tag{4.37}$$

where $1 \leq n, m, l \leq 10$, ϕ_x, ϕ_y, ϕ_z are phase shifts selected randomly from $(0, 2\pi)$, L_x, L_y, L_z are domain sizes in the x, y, z directions, A_{lmn} are mode amplitudes selected randomly from a Gaussian pdf with $(\mu, \sigma) = (0, 0.1)$ and N is the total number of modes.

We then let the simulation evolve, and record the amount of cold gas formed near a thermal scale-height ($0.9H < x < 1.1H$). As a comparison, we also run simulations without CR heating and with higher CR diffusion. Switching off CR heating allows us to isolate the effect of CR heating on thermal instability, whereas increasing CR diffusion allows us to isolate the effect of mode propagation (see results from §4.3.2). In particular, recall that in our setup, $\theta_{\rm H} \propto \chi_{\rm H}$ (eqn.4.32). Thus, if thermal instability is suppressed, it is difficult to tell if this is due to mode propagatiion ($\theta > 1$) or CR overheating ($\chi > 1$). In order to break this degeneracy and isoloate the effects of mode propagation, we utilize the fact that increasing CR diffusion can suppress mode propagation. We saw this explicitly in §4.3.2, when $\eta_{\rm H} = 1$. Our 'enhanced diffusion' tests here use the same value of $\eta_{\rm H}$.

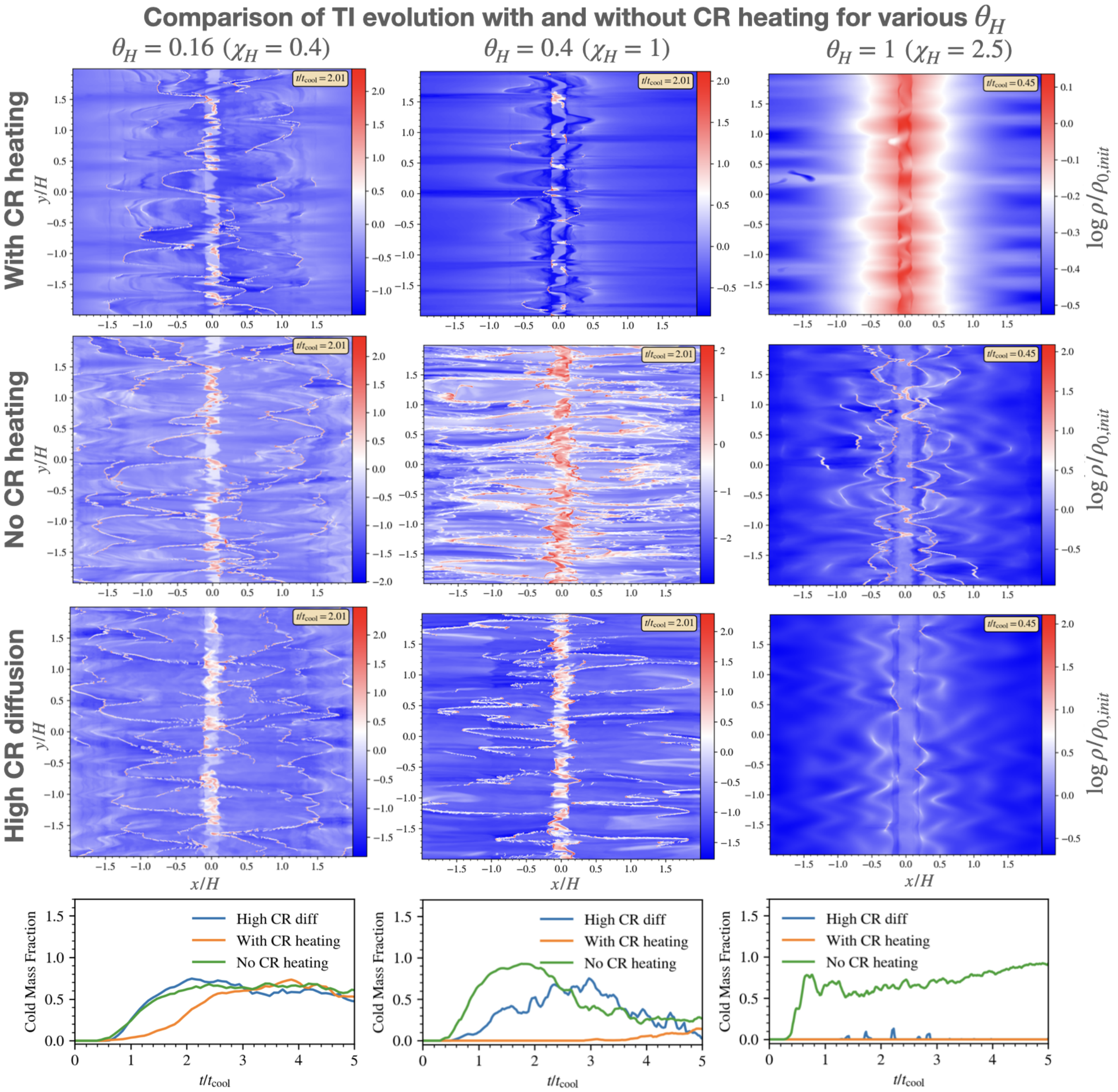

FIGURE 4.4: Comparison of thermal instability evolution with (top row) and without (second row) CR heating for streaming dominated transport ($\eta_H = 0.01$), and with higher diffusion (third row, $\eta_H = 1$) for (from left to right) $\theta_H = t_{\rm cool,H}/t_{\rm cross,H} = 0.16, 0.4, 1$. The bottom row displays the cold mass fraction taken near a thermal scale-height ($0.9H < x < 1.1H$) as a function of time $t/t_{\rm cool,H}$. The density slices displayed are taken roughly at times where the cold mass fraction peaks. Note that quantities with subscript H are taken at the initial gas scale-height $x = T_0/g_0 = 1$. The remaining parameters required to uniquely determine the initial profiles for these test cases are $\alpha_0 = 1, \beta_0 = 3$. The conversion from θ_H to χ_H in our setup is given by eqn.4.32.

In fig.4.4 we compare the evolution of thermal instability with (top row) and without (second row) CR heating for streaming dominated transport ($\eta_H = 0.01$), and with enhanced diffusion (third row, $\eta_H = 1$), for (from left to right) $\theta_H = 0.16, 0.4, 1$. The bottom row displays the cold mass fraction taken near a thermal scale-height ($0.9H < x < 1.1H$) as a function of time $t/t_{\rm cool,H}$. The density slices displayed are taken roughly at times where the cold mass fraction peaks. The initial profile parameters for these test cases are $\alpha_0 = 1, \beta_0 = 3$. Note that $\theta_H, \chi_H, t_{\rm cool,H}$, with the subscript H, are parameters evaluated at $x = H$ (where H is the thermal scale-height of the initial profile). Note also that the initial density, P_c and P_g profiles and magnetic field strength of the test cases displayed in fig.4.4 are all the same. Thus, initial background CR forces ∇P_c and heating rates $v_A \cdot \nabla P_c$ are identical in all cases. This remains true even when we change the amplitude of CR diffusion, which ordinarily would change CR profiles and heating rates. However, the CR source terms implemented in equations 4.35 and 4.36 guarantee identical $P_c(x)$ profiles. We emphasize that this is a numerical convenience to isolate the impact of mode propagation by enabling the background $P_c(x)$ profile to be held fixed. We do *not* include source terms $Q(x)$ in our study of non-linear outcomes in §4.4.

Let us first compare the left ($\chi_{\rm H} = 0.4$)) and rightmost ($\chi_{\rm H} = 2.5$) columns in Fig 4.4, which correspond to the cases where CR heating provides only a fraction of the heating rate ($\chi_{\rm H} = 0.4$)) and overheats the gas ($\chi_{\rm H} = 2.5$)). As one might expect, when there is CR heating, there is ample cold gas in the former case (broadly comparable to the 'no CR heating' case), and almost no cold gas in the latter case. The strong

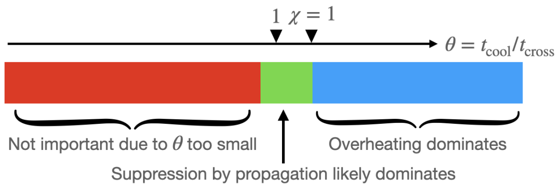
1
$\chi = 1$
$\theta = t_{\rm cool}/t_{\rm cross}$
Not important due to θ too small
Overheating dominates
Suppression by propagation likely dominates

FIGURE 4.5: A color-bar illustrating the effect of mode propagation on TI for various regimes of $\theta = t_{\rm cool}/t_{\rm cross}$.

suppression in the overheated $\chi_{\rm H} = 2.5$ case is still present when CR diffusion is included. This suggests that overheating, rather than mode propagation (which is absent once CR diffusion is included), suppresses thermal instability. On the other hand, when CR heating marginally balances cooling, for $\chi_{\rm H} = 1, \theta_{\rm H} = 0.4$, the case including CR heating has almost no cold gas, but including CR diffusion allows ample cold gas to form. This suggests that mode propagation, rather than overheating, is responsible for the suppression of thermal instability. We have verified this directly by examining heating rates, as well as observing the propagation of cooling gas clouds.

Thus, suppression of TI by propagation effects can occur. However, it only occurs in a narrow range around $\theta \approx 1$, as illustrated in Fig 4.5: for low values of θ, mode propagation is too slow, while for high values of θ, overheating suppresses thermal instability. Thus, mode propagation is unlikely to play an important role in regulating the abundance of cold gas. In fact, overheating during the non-linear stages is much more interesting. We turn to this next.

4.4 Nonlinear Outcomes: Winds and fountain flows

Since suppression of TI by mode propagation is at best marginally important, thermal instability will likely develop in a system in global thermal equilibrium, i.e. when there is no overheating. What would be the nonlinear outcome of TI then, particularly when CR heating plays an important thermodynamic role in the system? Note that we started with a profile in both hydrostatic and thermal balance,

$$\nabla P_g + \nabla P_c = -\rho g, \tag{4.38}$$

$$\rho^2 \Lambda = -v_A \cdot \nabla P_c + \mathcal{H}. \tag{4.39}$$

As TI develops, it draws mass out of the atmosphere and causes the density to decrease. It is not immediately clear, in the subsequent evolution, that both hydrostatic and thermal balance will be maintained. In particular, since radiative cooling varies with density much more sensitively than CR heating, one could imagine in the nonlinear evolution, the energy budget is likely dominated by CR heating. This could eventually drive the system out of both hydrostatic and thermal balance. Indeed, we shall see that this is exactly what happens. We shall also see that the reduced gas density also reduces gas pressure, causing β to decrease in the atmosphere.

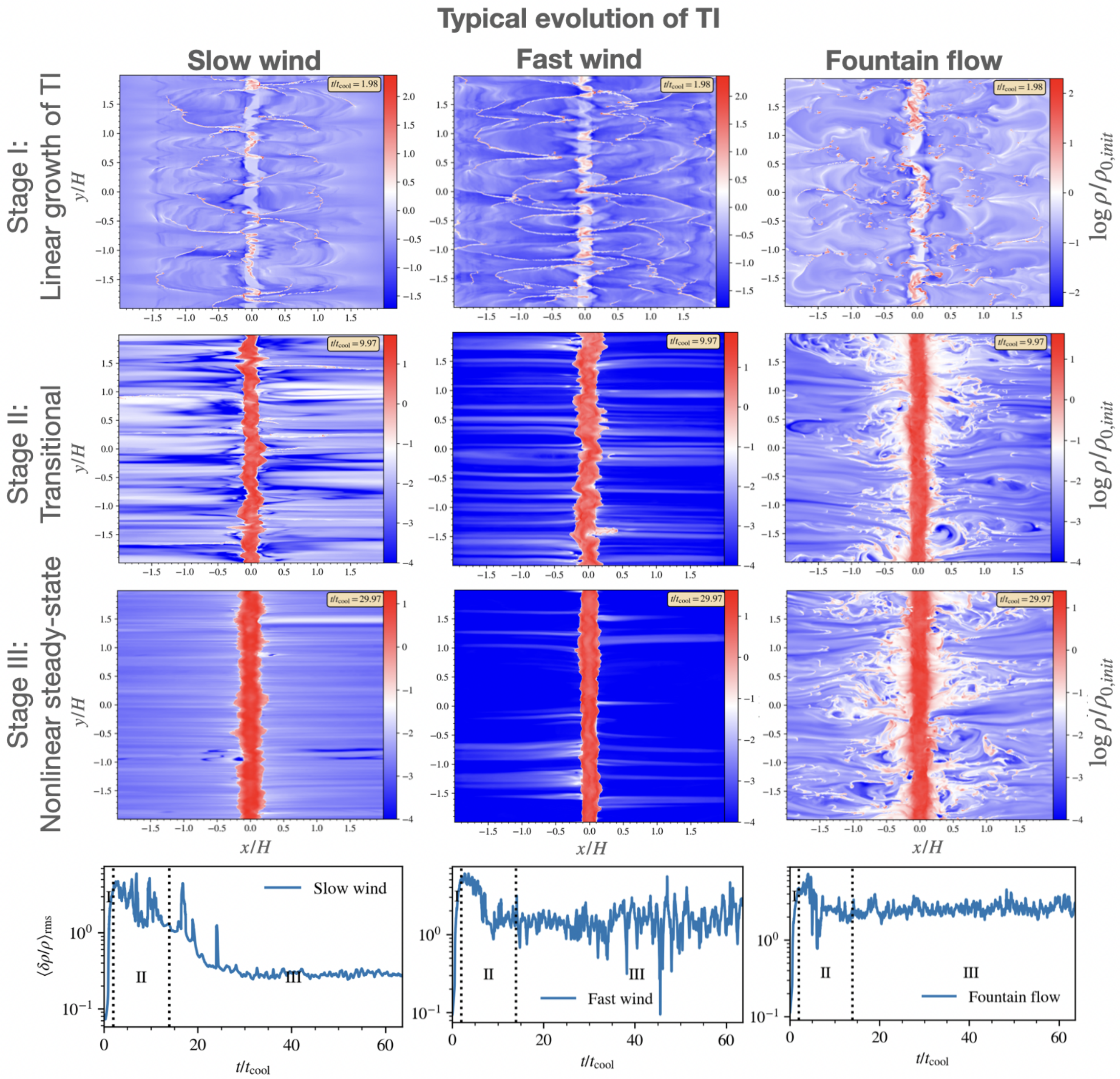

FIGURE 4.6: Typical evolution of TI with CR heating. Shown above are density slices at $t = 2, 10, 30 t_{\rm cool}$ for the three categories of outcomes - slow wind, fast wind and fountain flow, with blue and red coloring indicating less dense and denser gas respectively. In this figure, $t_{\rm cool}$ refers to the initial cooling time at $x = H$. Shown at the bottom are $\langle \delta\rho/\rho \rangle_{\rm rms}$ (r.m.s. fractional density deviation from the mean) as a function of time taken at a strip near a scale height ($0.9H < x < 1.1H$) for the three cases shown, with the black dotted line demarcating different stages of evolution. The case identifier for the three cases shown are: 'slow wind' - a1b5k.01d1in.67res1024c200; 'fast wind' - a1b5k1d1in.67res1024c200; 'fountain flow' - a1b300k1d1in.67res1024c200. $\rho_{0,init}$ with the extra subscript *init* is added for clarity and is synonymous to $\rho_0 = 1$, the density at the base of the initial profile.

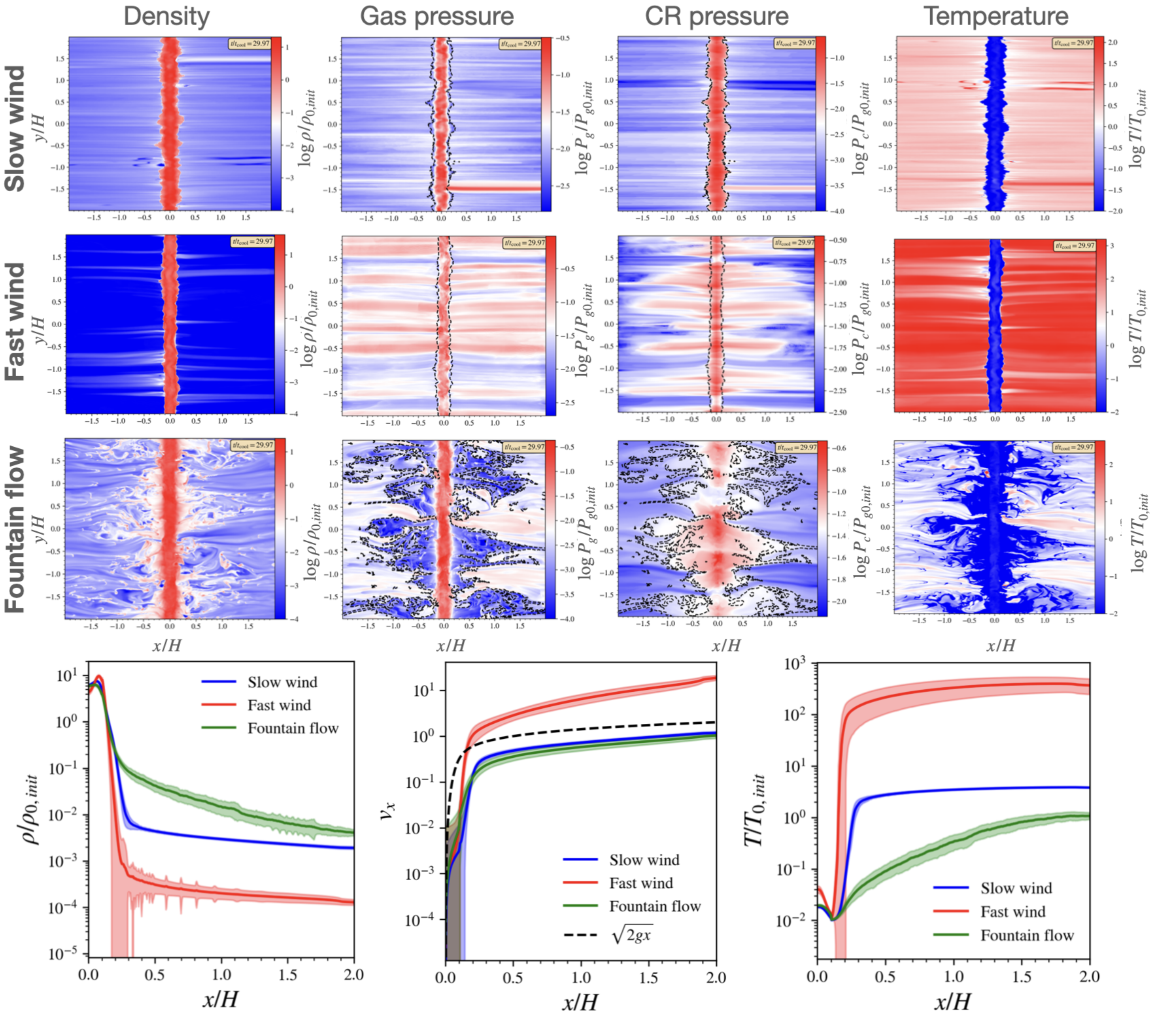

FIGURE 4.7: Nonlinear outcomes of TI with CR heating. Density, gas pressure, CR pressure and temperature slices at $t = 30t_{\mathrm{cool}}$. t_{cool} shown in this figure refers to the initial cooling time at $x = H$. The black dashed contours in the gas and CR pressure slices demarcate gas with temperature below and above $0.3T_{0,init}$, where $T_{0,init}$ is the temperature of the initial profile and is synonymous to $T_0 = 1$ (similarly for $\rho_{0,init} = \rho_0 = 1$ and $P_{g0,init} = P_{g0} = 1$, the added subscript *init* for added clarity). Shown at the bottom are the time averaged projection plots of the density, outflow velocity and temperature for the three cases shown. Time average projection refers to averaging from $t = 31.8t_{\mathrm{cool}}$ to $63.6t_{\mathrm{cool}}$, when the flows have settled onto their nonlinear steady-states, and then spatial averaging over y. t_{cool} refers to the initial cooling time at a $x = H$. The shaded regions denote 1σ variations throughout the time averaging. The case identifiers are the same as fig.4.6.

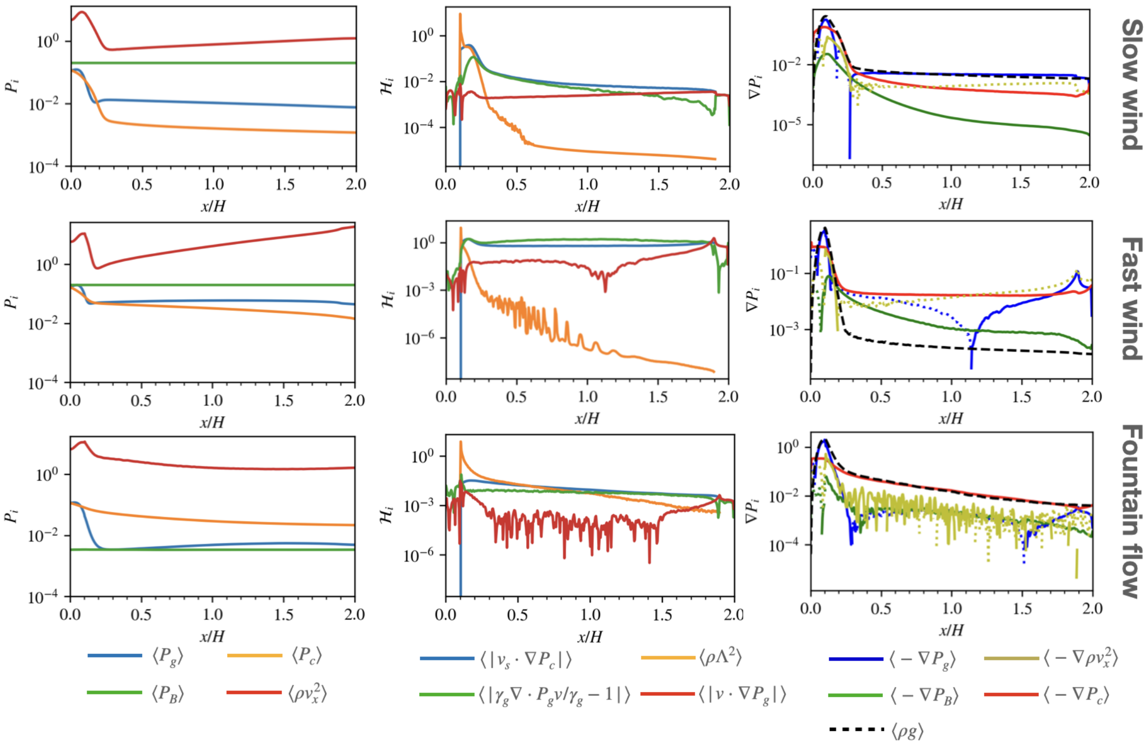

FIGURE 4.8: Time averaged projection plots of the pressures (left column), energy terms (center column) and pressure gradients (right column) for the three categories of outcomes. Time average projection refers to averaging from $t = 31.8t_{\text{cool}}$ to $63.6t_{\text{cool}}$, when the flows have settled onto their nonlinear steady-states, and then spatial averaging over y. t_{cool} refers to the initial cooling time at $x = H$. The cases displayed are the same as that in fig.4.7. In the pressure plots (left column), the pressures are represented by: gas pressure $\langle P_g \rangle$ - blue; CR pressure $\langle P_c \rangle$ - orange; magnetic pressure $\langle B^2/2 \rangle$ - green; ram pressure $\langle \rho v_x^2 \rangle$ - red. In the energy plots (center column): CR heating $\langle |\mathbf{v}_s \cdot \nabla P_c| \rangle$ - blue; cooling $\langle \rho^2 \Lambda \rangle$ - orange; enthalpy flux $\langle |\gamma_g \nabla \cdot P_g \mathbf{v}|/\gamma_g - 1 \rangle$ - green; gas work done $\langle |\mathbf{v} \cdot \nabla P_g| \rangle$ - red; There is no cooling and CR heating within the buffer zones ($0 < x < a$ and $2H - a < x < 2H$). In the pressure gradient plots: $\langle -\nabla P_g \rangle$ - blue; $\langle -\nabla P_c \rangle$ - red; $\langle -\nabla P_B \rangle$ - green; $\langle -\nabla \rho v_x^2 \rangle$ - yellow. Positive values are represented by solid curves, negative by dotted lines. $\langle \rho g \rangle$, the gravitational force, is denoted by a black dashed line. The angled brackets indicate the time average projection, they are omitted in the legend and in other plots to reduce clutter.

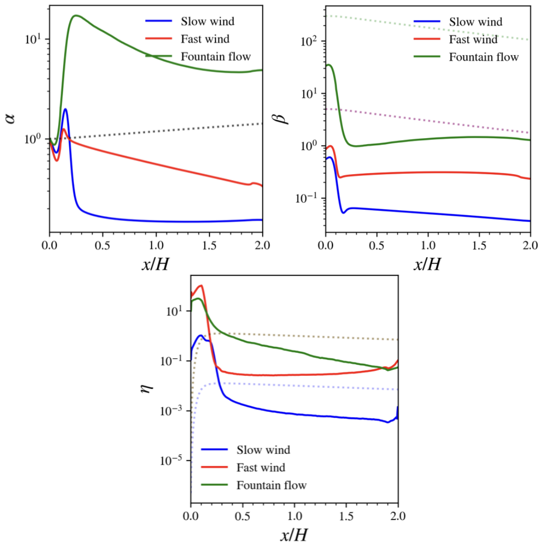

FIGURE 4.9: α, β, η are in general functions of position and time. The figure show the time average projection plots of α, β, η when steady state has been reached (solid lines) in comparison to their initial values (dotted line). Time average projection refers to averaging from $t = 31.8t_{\rm cool}$ to $63.6t_{\rm cool}$, when the flows have settled onto their nonlinear steady-states, and then spatial averaging over y. $t_{\rm cool}$ refers to the initial cooling time at $x = H$. Note that due to mass draw-out from TI, the ending α, β, η could be very different from their starting values.

4.4.1 Overview of simulation outcomes

There are in general three categories of outcomes for nonlinear TI with CR heating[9]. Here, we analyze 3 prototypical simulations which exemplify these outcomes: 'slow wind' ($\beta_0 = 5, \eta_{\rm H} = 0.01$), 'fast wind' ($\beta_0 = 5, \eta_{\rm H} = 1$), and 'fountain flow' ($\beta_0 = 300, \eta_{\rm H} = 1$). All simulations have $\delta_{\rm H} = 1, \alpha_0 = 1$. We run the simulations for up to $60t_{\rm cool,H}$, long enough for the flow to settle onto a nonlinear steady state. Although we fix CR pressure at the base, in Appendix B.3 we show that similar outcomes arise if we fix the CR flux. As mentioned in §4.2.2.4, with the expectation that CR heating dominates the nonlinear evolution, we henceforth remove the temperature ceiling.

---

[9] The reader can view videos pertaining to the discussion in this section at the following link: `https://www.youtube.com/playlist?list=PLQqhpX30dsYq2cD51L4M2pNQAlm0GSle9`.

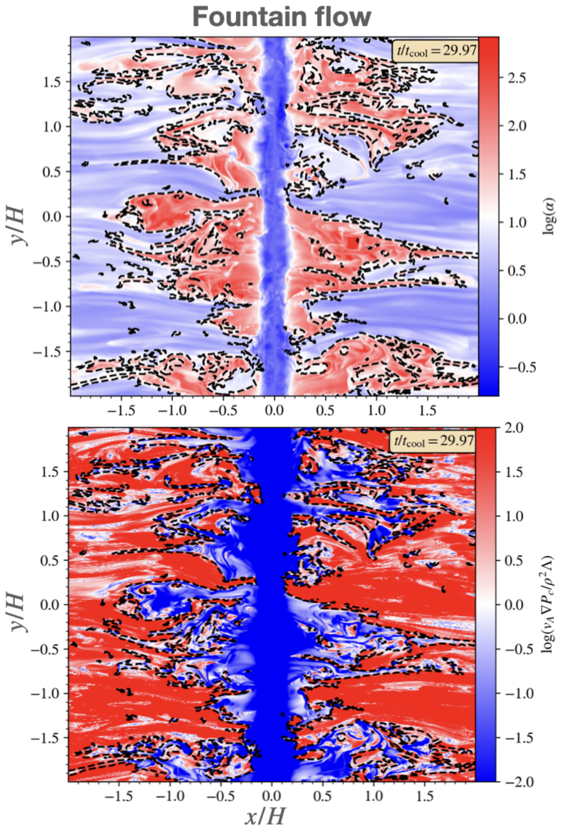

FIGURE 4.10: Ratio of CR to gas pressure $\alpha = P_c/P_g$ (top) and CR heating to radiative cooling $|v_A \nabla P_c|$ (bottom) for the fountain flow case at $t = 30t_{\rm cool}$. $t_{\rm cool}$ refers to the initial cooling time at $x = H$. Contours demarcating cold gas ($T < 0.3T_{0,init}$) from the hotter gas are marked by black dashed lines.

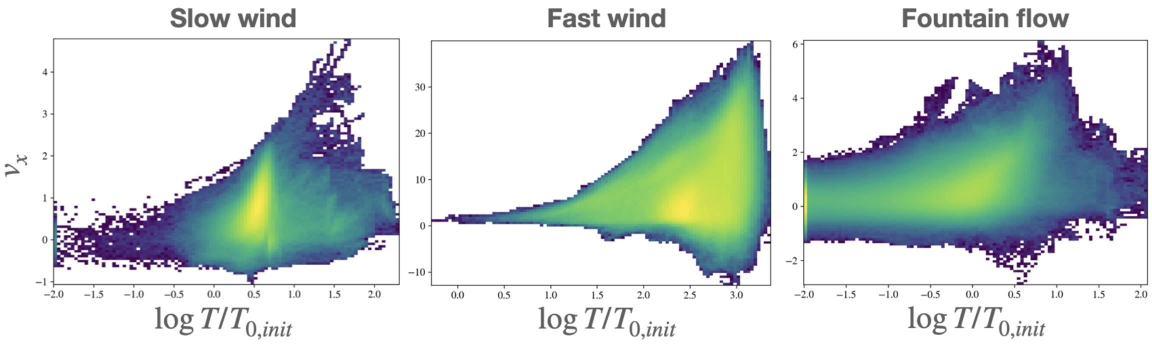

FIGURE 4.11: $v_x - T$ (velocity vs. temperature) phase plots for the three displayed cases in fig.4.6: slow wind case on the left; fast wind in the middle; fountain flow on the right. The $v_x - T$ plots are constructed from binning the gas cells by their x velocity and temperature from $21.2 - 24.7t_{\rm cool}$. $t_{\rm cool}$ refers to the initial cooling time at $x = H$. $T_{0,init}$ refers to the initial profile temperature, i.e. $T_{0,init} = T_0 = 1$, the extra subscript *init* for added clarity.

The typical evolution of these simulations are shown in fig.4.6, showing the density slices at $t = 2, 10, 30t_{\rm cool}$, which mark the three stages of TI evolution: stage I, linear growth of TI; stage II, the transitional phase; stage III, the nonlinear steady-state. Shown at the bottom of the figure are the r.m.s density variations $\langle \delta\rho/\rho \rangle_{\rm rms}$ as a function of time for the three displayed cases, with black dotted lines demarcating the different stages of evolution. In stage I, seed density perturbations grow to nonlinear amplitudes over several $t_{\rm cool}$ (from $t = 0$ to $\sim 2 - 3t_{\rm cool}$ in our sims with 10% seed amplitude). Over this time, $\langle \delta\rho/\rho \rangle_{\rm rms}$ grows exponentially. In stage II, cold, dense gas formed from TI collapses under gravity, forming a dense mid-plane disk. Stage II marks the transitional period where such a two-phase medium (a cold, dense mid-plane disk bounded by hot, rarefied halo gas) is formed. This is the typical end state of TI simulations [23, 87, 115]. However, in the presence of CR heating, this two-phase hydrostatic disk-halo medium can be globally unstable, and TI generally veers towards one of three possible outcomes in Stage III, the non-linear steady state.

The first outcome is a slow wind, where the disk-halo structure is well maintained and the interface clearly defined. A wind with velocity less than the local escape velocity ($\sqrt{2gx}$) develops. The second outcome is a fast wind, where again the disk-halo structure is well maintained with a distinctive interface, but the wind has a velocity greater than the local escape velocity, so that much of the gas in the halo are blown away, leaving the halo much more rarefied compared to the weak-wind case. The third outcome is a fountain flow, characterized by filaments of cold, dense gas rising and falling from the central disk. The warmer gas is generally outflowing, leaking through the space between the cold tendrils, occasionally entraining several tiny cold clouds out. The halo gas flow is turbulent.

The transition from linear TI to these outcomes through the formation of a disk-halo structure takes around $10t_{\rm cool}$, marked by high values of $\langle \delta\rho/\rho \rangle_{\rm rms} \sim 5$. The density fluctuations and flow structure then stabilize during stage III, the nonlinear steady-state. Surveying parameter space, we have found that slow winds are typically associated with low β, low CR diffusivity (or streaming dominated) flows, fast wind with low β, high CR diffusivity flows, whereas fountain flows happen mostly for high β flows. We will quantify these criteria and supply theoretical explanations.

We describe the flow properties of these three outcome categories in greater detail using fig.4.7, which shows the density, gas pressure, CR pressure, temperature slices at $t = 30t_{\rm cool}$ (top 3 rows) and the time averaged projection plots[10] of the density, outflow velocity and temperature (bottom row). From the slice plots, one can observe the aforementioned disk-halo structure. The central disk, spanning a height of $\sim 0.2H \approx 2a$ (where a is the smoothing length of the gravitational field) is made up of cold gas near the temperature floor. The flow patterns of the slow-wind and fast-wind case appear collimated, with the major differences being: 1. the outflow velocity of the fast-wind case can exceed the local escape speed (bottom central panel), 2. the density is significantly lower for the fast-wind case and 3. the temperature is appreciably higher for the fast-wind case. The gas and CR pressures of the fast wind case are also greater. Some minor differences between the slow and fast wind case include smaller variability for the weak-wind (as indicated by the shaded regions in the time averaged plots). Note that once out of the central disk, the flows become isothermal[11] for both the slow and fast wind cases (from $x \approx 0.3H$ outwards). The density and hence pressure is also relatively constant. The fountain flow is vastly different from the other two outcomes, showing more turbulent dynamics. Despite the relatively similar time averaged outflow velocity profile with the slow-wind case, both of which are sub-escape speed, the cold gas is far more extended in the fountain flow case, leading to higher average density and lower average temperature. The cold gas extending away from the disk is also low in gas pressure but high in CR pressure.

---

[10] The time averaged projection plots are obtained by first averaging the slices across the y-axis (projection) and then time averaging over $t = 31.8 - 63.6t_{\rm cool}$, when the flow is well within stage III, the nonlinear steady-state.

Due to mass drop-out in the atmosphere from TI, which produces the cold gas disk in the mid-plane, the ending α, β, η profiles could be vastly different from what it started with. For example, in fig.4.9, the time averaged projection plots of α, β, η for the slow wind, fast wind and fountain flow cases (denoted respectively by blue, red and greed solid lines) are different from the initial profiles (denoted by dotted lines) by orders of magnitude. In particular, for the slow and fast winds, the halo α decreases over time while the fountain flow case seems to have accumulated CR pressure. The halo β and η can decrease by orders of magnitude due to the substantial decrease in halo gas density (thus increasing v_A) and pressure.

---

[11] Isothermal in the sense that the temperature profile appears spatially constant, not that the equation of state is isothermal.

4.4.2 Energetics and dynamics of the nonlinear steady-state

- *Slow and fast wind case.* To understand the energetics and dynamics of the nonlinear steady-state, we plot in fig.4.8 the time averaged projection plots of the pressures, energies and pressure gradient terms corresponding to the three displayed outcomes. For energetics, the gas energy equation (eqn.4.3) in time-steady state can be expressed as

$$\frac{\gamma_g}{\gamma_g - 1}\nabla \cdot (P_g \mathbf{v}) = \mathbf{v} \cdot \nabla P_g + |v_A \cdot \nabla P_c| - \rho^2 \Lambda + \mathcal{H}(x), \tag{4.40}$$

i.e. the gas enthalpy flux (LHS) is the sum of gas work done, CR heating, radiative cooling and residual feedback heating (RHS). Near the central disk, the density and radiative cooling rate is high, cooling some of the gas to the temperature floor. The drop in density away from the disk causes an abrupt change in the energetics. CR heating is a much weaker function of density than radiative cooling. In a streaming dominated flow with $v_x \ll v_A$ and B-field is constant (as in our setup), CR heating $v_A \nabla P_c \propto \rho^{1/6}$ (since $v_A \propto \rho^{-1/2}, P_c \propto \rho^{2/3}$ for constant B-fields) while cooling $\rho^2 \Lambda \propto \rho^2$. Thus we can reasonably expect $v_A \nabla P_c \gg \rho^2 \Lambda$ at the halo outskirts in the nonlinear steady state (thus, for the wind cases, the residual feedback heating $\mathcal{H}(x) = 0$; however, it can be non-zero in the fountain flow case we later discuss). It is clear from the figure that this is indeed the case, at least for the slow and fast wind case (compare the blue and orange curves in fig.4.8, central column, top and middle row). Thus the halo gas is overheated. At the transition region where CR heating starts to dominate over cooling ($x \approx 0.2H$), the velocity is low and the gas is heated to high temperatures (see the abrupt rise in temperature there, fig.4.7, bottom right panel). Further out, when gas acceleration is greater, energy balance is maintained by an enthalpy flux commensurate with the overheating rate.

We can gain intuition by noting that the steady-state gas energy equation (equation 4.40) can be rewritten as:

$$v_x \nabla \ln \mathrm{K} = \frac{\gamma_g - 1}{t_{\mathrm{netheat}}} \Rightarrow v_x \nabla \mathrm{K} = \frac{(\gamma_g - 1)\mathrm{K}}{t_{\mathrm{netheat}}} \tag{4.41}$$

where $K \equiv P_g/\rho^{5/3}$, and $t_{\mathrm{netheat}} = P_g/(|v_{\mathrm{A}} \nabla P_c| - \rho^2 \Lambda) = 1/(1/t_{\mathrm{heat}} - 1/t_{\mathrm{cool}})$ ($\approx t_{\mathrm{heat}}$ if CR heating dominates). This form implies that any increase in gas entropy due to heating is balanced by outward advection of entropy. It also implies that the velocity of a thermal wind driven by heating is given by $v_x \approx L_{\mathrm{K}}/t_{\mathrm{heat}} \approx 3/2 L_\rho/t_{\mathrm{heat}}$ where $L_{\mathrm{K}} \equiv K/\nabla K$, i.e. $v_{\mathrm{x}} \propto t_{\mathrm{heat}}^{-1}$. Alternatively, note that the enthalpy flux $\gamma_g \nabla P_g v_x/(\gamma_g - 1)$ consists of two terms, first due to adiabatic expansion $\propto P_g \nabla v_x$ and the second due to work done on the gas by the flow $\propto v_x \nabla P_g$). From fig.4.7 (central column, top and middle row) it is apparent the enthalpy flux term is dominant over the work done term for at least a scale height above the disk (compare the green and red curves), thus the energetics there are controlled by a simple balance between CR heating and adiabatic expansion, i.e. $P_g \nabla v_x \sim -v_A \nabla P_c$. At the escape velocity $v_{\mathrm{esc}} \sim \sqrt{2gx}$, we have $\nabla v_{\mathrm{esc}} \sim (g/x)^{1/2} \sim t_{\mathrm{ff}}^{-1}/\sqrt{2}$. This suggests:

$$v_{\mathrm{x}} \sim \zeta v_{\mathrm{esc}} \left(\frac{t_{\mathrm{ff}}}{t_{\mathrm{heat}}} \right)^{-1} \tag{4.42}$$

where $\zeta \sim 0.4$ is a fudge factor which we later calibrate numerically. We investigate this scaling further in §4.4.3. In short, the energetics of the slow and fast wind case can be described by a cool inner disk region followed abruptly by an overheated outskirt, driving a sharp rise in temperature and then a balance between CR heating and adiabatic expansion, which generates the required enthalpy flux carrying the heated gas parcels away.

For dynamics, we refer to the left column of fig.4.8. Although magnetic pressure dominates the the slow and fast wind case, it is unimportant in the overall dynamics of the flow due to its constancy, except for setting the Alfven/streaming speed v_A (hence the CR heating rate) and collimating flows via the high magnetic tension. Since we have set $\alpha_0 = P_{c0}/P_{g0} = 1$ at the base for the displayed cases (see §4.2.2), CR and gas pressures are comparable at the disk. However, CR pressure varies with density differently than the gas pressure, so they develop different profiles at the disk-halo interface, leading to different outskirt pressures. In particular, for streaming dominated flows where $v_x \ll v_A$, $P_c \propto \rho^{\gamma_c/2}$. This implies a precipitous decline in CR pressure at the disk halo interface, where there is a steep density gradient to offset the sharp change in temperature (see bottom panels of fig.4.7). By contrast, the gas pressure suffers a much smaller decline in the disk, where the rise in temperature at the disk halo interface compensates for the reduced density. Thus, for streaming dominated flows, $P_c \ll P_g$ in the halo, resulting in a slow wind.

If, instead diffusion dominates out to at least the disk halo interface, i.e. $\kappa\nabla P_c \sim \kappa P_c/a > v_A P_c \Rightarrow \kappa > v_A a$, then for $F_c \sim \kappa\nabla P_c \sim$ const (i.e., consistent with these assumptions, streaming losses $v_A \cdot \nabla P_c$ are negligible), CR suffer a linear rather than exponential decline with distance:

$$P_c \approx P_{c0} - \frac{(\gamma_c - 1)F_{c0}}{\kappa} x. \tag{4.43}$$

Diffusion decouples CR pressure from the gas at the steep density drop, avoiding the heavy 'tax' at the disk-halo interface. Since P_c is higher in the halo, this allows for stronger heating at the the lower densities when radiative cooling is weak. The smaller drop in CR pressure also means that the CR pressure gradient $\nabla P_c \gg \rho g$ dominates in the more diffusive, fast wind case, while the gas pressure gradient $\nabla P_g \sim \rho g$ dominates in the streaming dominated, slow wind case (right column, Fig 4.8).

As the gas drops in density, heating starts to exceed cooling, and gas is abruptly heated to high temperature. The heating of the gas halts the rapid decline in gas pressure in the disk; the hot gas now has a much larger scale height $H_{\rm gas} \propto T$. The phase transition from cool to hot gas takes place in a very thin layer. To a rough approximation, it takes place isobarically, so that $\rho_h/\rho_c \sim T_c/T_h \ll 1$. Due to the low gas densities in the halo, CR transport becomes streaming dominated ($v_{\rm A} \propto \rho^{-1/2}$), with $P_c \propto \rho^{2/3}$ tracking the very gentle density decline in the halo. This change in transport is responsible for the sharp change in ∇P_c gradient at the disk-halo boundary. Note that rapid evolution in gas and CR properties typically occurs only at the disk halo interface, where gas is being heated and accelerated by CRs; fluid gradients are much gentler in the halo, where gravitational stratification is much weaker for the hot gas. The evaporative flow at the disk halo interface gives rise to a single-phase hot wind in the halo, whose velocity is given by equation 4.42.

In summary, the slow and fast wind cases are driven by CR heating, which causes the cold gas to evaporate at the disk-halo interface, boosting the gas pressure and driving an enthalpy flux out. They differ in strength because CR heating is weaker in one case and stronger in the other. The intensity of CR heating at the halo depends on the supply of CR at the base (adjusted through α_0 in our sims) and their transport. In particularly, for a given supply of CRs, streaming dominated flows generally lead to sharp decrease in CR energy at the interface, whereas higher diffusivity helps CRs to leak out. As we will see next, fountain flows are instead driven by CR pressure forces.

- *fountain flow case.* The fountain flow case is characterized by cold, dense gas being flung out of the disk. As we shall see, this is wholly due to CR forces, rather than CR heating. When the Alfven speed v_{A} is small due to weak magnetic fields, the momentum input of CRs, ∇P_c, is much more important than the heat input $v_{\mathrm{A}} \cdot \nabla P_c$. Due to the high density of the gas, radiative cooling is strong and the gas remains at the temperature floor. Bounded by gravity, there is a maximum height this cold gas can reach (around a scale height H in the case shown in fig.4.8), beyond which the gas is low in density and warm. CR heating regains dominance and the system transitions into a slow wind, with CR heating balanced by the enthalpy flux.

In terms of pressure, the disk region is well supported by both the gas and CRs, but the flow becomes vastly CR dominated in the halo. The high gas density requires a high level of pressure support, most of which are provided by the CRs.

Given the turbulent dynamics of the fountain flows, it may be more instructive to look at particular snapshots of the flow, so we refer the reader back to the slice plots shown in fig.4.8. There is a clear distinction in how pressure is partitioned between the gas and CR components for the cold, fountain gas and the surrounding warm gas. The cold gas is heavily CR dominated, whereas gas pressure is comparable to CR pressure in warm/hot gas. Outside the cold gas, gas pressure rises and CR pressure drops. Fig.4.10 shows this more clearly: the cold gas is distinctively higher in $\alpha = P_c/P_g$ than the surrounding gas. The cold gas is also radiative cooling dominated. Thus, in contrast to the slow and fast wind case where the outflow is driven by CR heating, the cold, fountain flows here are driven by CR pressure. In particular, the presence of high levels of CR pressure extending from the disk at the cold gas indicates they are peeled off from the surface of the disk.

To supplement our discussion on the energetics and dynamics of the three flow outcomes, we plot, in fig.4.11, the $v_x - T$ phase plots for the three cases. In line with our expectations and observations above, faster outflow gas is generally higher in temperature. Cold gas with temperature $\lesssim 0.3T_{0,init}$, if present, is slower and roughly equally distributed between outflows and inflows - this is particularly the case for the fountain flow, in which the cold gas is gravitationally bound and continuously circulating.

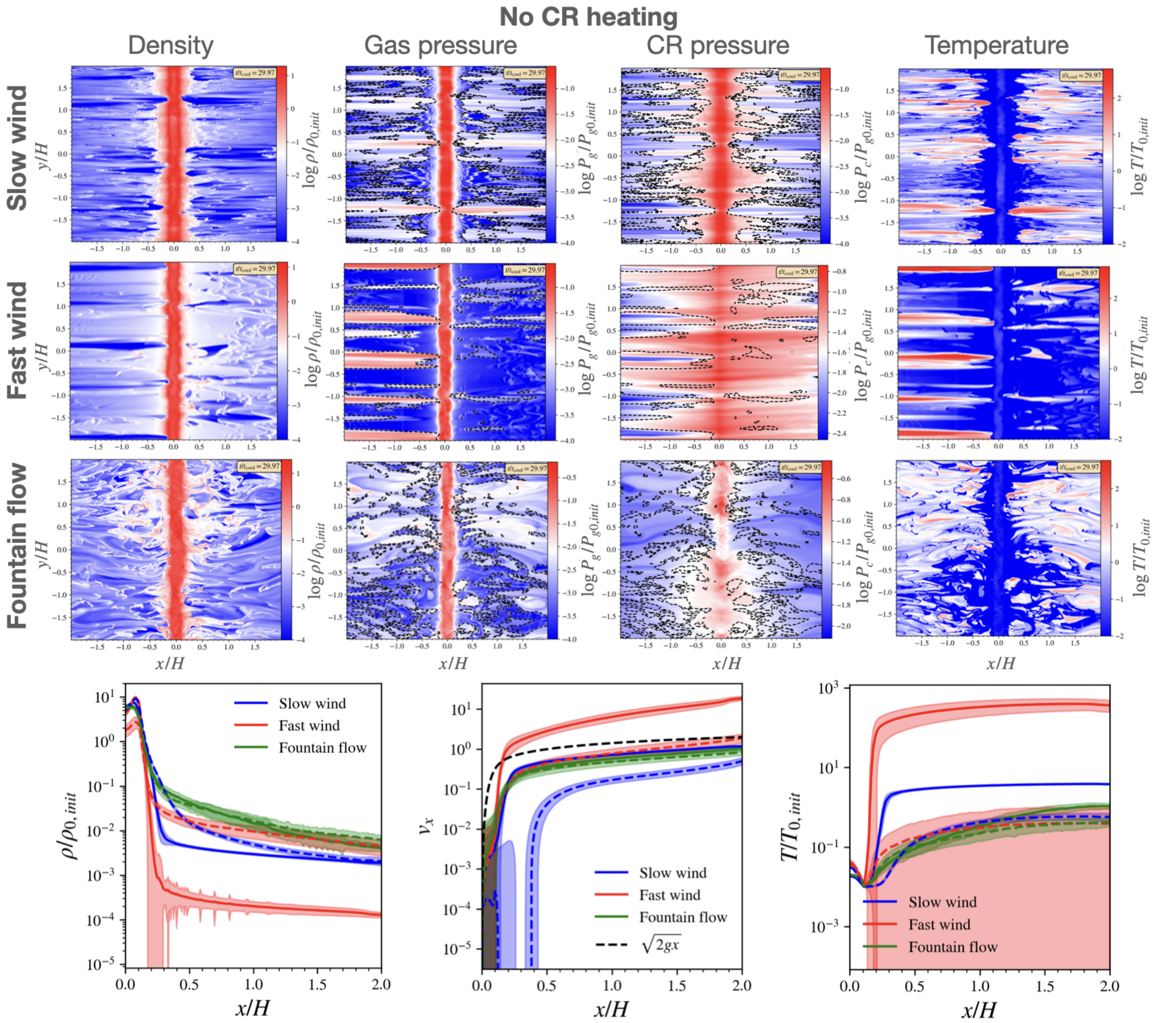

FIGURE 4.12: Nonlinear outcomes of TI with CR but without CR heating. Plots are the same as fig.4.7, except the dashed lines at the bottom are time averaged projection quantities of runs without CR heating.

4.4.3 Effect of CR heating

In §4.4.2 we claimed that the slow and fast wind cases are driven by CR heating while the dynamics of the cold, fountain flow is driven by CR pressure. We demonstrate these claims further by re-running these fiducial cases, but removing CR heating to the thermal gas[12]. The results are shown in fig.4.12 and 4.13. We can see that

---

[12] In these runs, we remove the $v_A \cdot \nabla P_c$ term from the gas energy equation, yet keeping collisionless losses $v_A \cdot \nabla P_c$ in the CR energy equation.

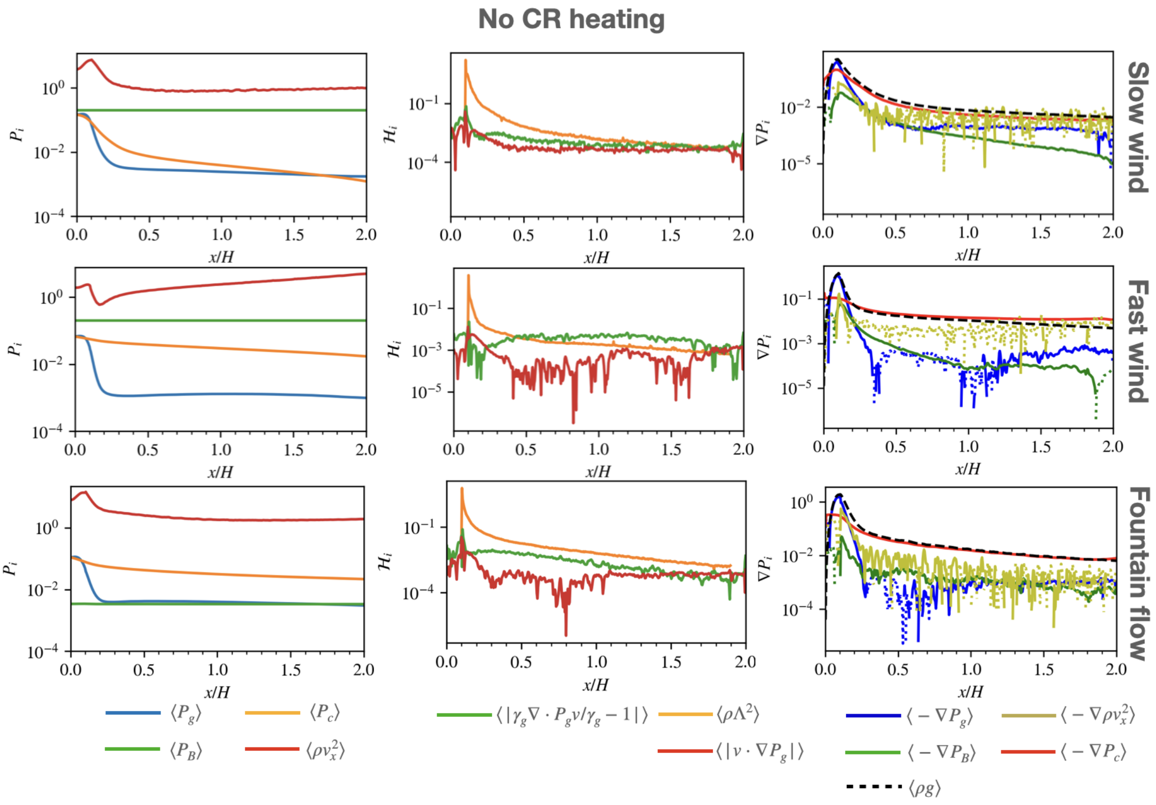

FIGURE 4.13: Same as fig.4.8 but without CR heating.

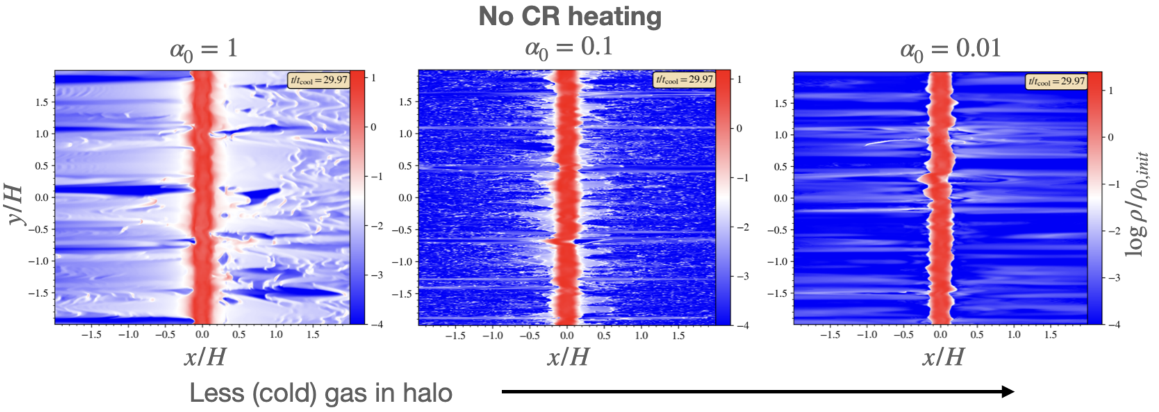

FIGURE 4.14: Density snapshots at $t = 30t_{\rm cool}$ for cases with different base CR pressure (as measured by $\alpha_0 = P_{c0}/P_{g0}$, which in our simulation setup, is fixed) but the same starting β_0 and η_H. $t_{\rm cool}$ refers to the initial cooling time at $x = H$ Less cold, dense gas appears in the halo as the base CR pressure support decreases. The identifiers for the three cases displayed are (from left to right) 'a1b5k1d1in.67res1024c200-nocrh', 'a.1b5k1d1in.67res1024c200-nocrh' and 'a.01b5k1d1in.67res1024c200-nocrh'

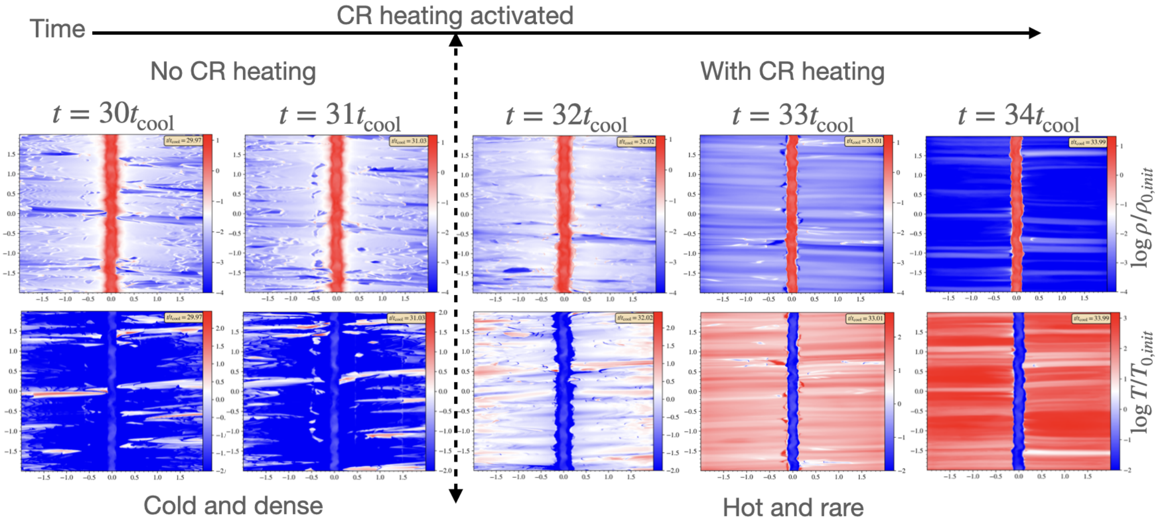

FIGURE 4.15: Transition from a cold, dense flow to a hot, fast wind case upon activation of CR heating at $t \approx 32t_{\rm cool}$. $t_{\rm cool}$ refers to the initial cooling time at $x = H$. The case shown is a continuation of the middle row of fig.4.12, with identifier 'a1b5k1d1in.67res1024c200-nocrh'.

switching off CR heating has a significant effect on the slow and fast wind cases, but changes the fountain flow case minimally. In particular, the slice plots in fig.4.12 for the slow and fast wind cases show that the density is much higher and cold gas is more prevalent. The difference is greatest for the 'fast wind' case, where removing CR heating results in an increase in halo density by 2 orders of magnitude, a decrease of outflow speed to sub-escape speeds, and a drastic decrease in halo temperature by 3 orders of magnitude, according to the time averaged projection plots in Fig.4.12. The slow wind case also sees an increase in halo density and decrease in outflow speed and temperature, but the magnitude of the changes are considerably smaller. This reflects the importance of CR heating in driving the outflow dynamics as shown in Fig.4.7. The fountain flow case continues to display fountain flow features even without CR heating, with hardly any change to the halo density, outflow velocity and temperature. This further shows that the cold, fountain flows are not a result of CR heating, but

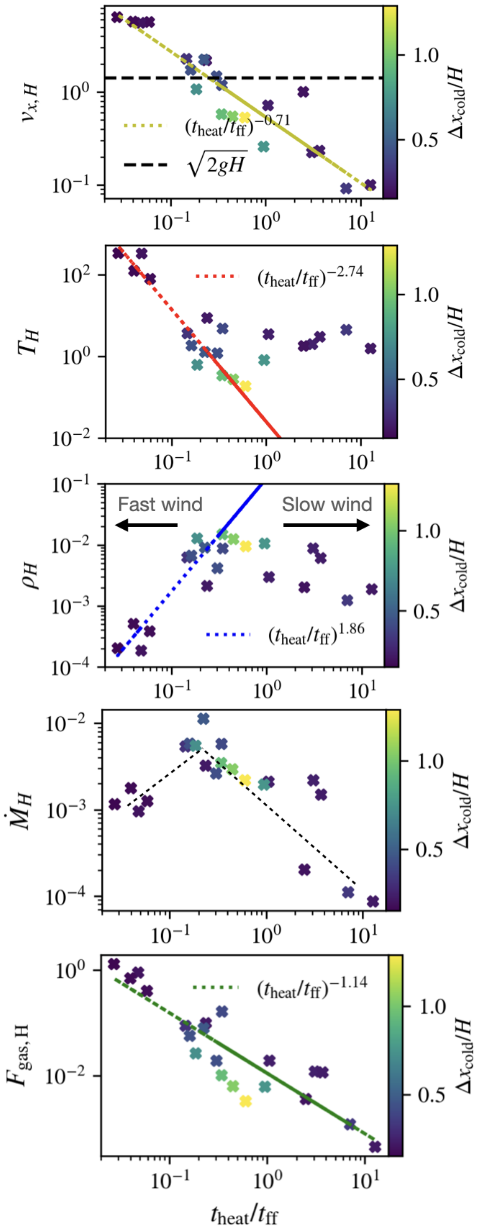

FIGURE 4.16: Plot of (from top to bottom) outflow velocity v_x, temperature T, density ρ, mass flux ρv_x and gas energy flux $F_{\rm gas} = \rho v_x^3/2 + \gamma_g P_g v_x/(\gamma_g - 1)$ at a scaleheight $x = H$ against $t_{\rm heat}/t_{\rm ff}$ (also taken at a scaleheight $x = H$) for all the cases listed in table 4.1 under §4.4. Note that $v_x, T, \rho, \rho v_x, F_{\rm gas}$ and $t_{\rm heat}/t_{\rm ff}$ are taken from their time averaged projection profiles. Time average projection refers to averaging from $t = 31.8 t_{\rm cool}$ to $63.6 t_{\rm cool}$, when the flows have settled onto their nonlinear steady-states, and then spatial averaging over y. $t_{\rm cool}$ refers to the initial cooling time at $x = H$. The scatter points are color-coded by their cold width $\Delta x_{\rm cold}/H$, which is a measure of the extend of fountain flows. $\Delta x_{\rm cold}$ is defined in fig.4.18. The regimes for slow and fast wind are indicated by arrows in the density plot. The dashed lines in the mass flux plot are for indicating the general trend above and below $t_{\rm heat}/t_{\rm ff} \sim 0.4$.

of CR forces.

In terms of energetics and dynamics, Fig.4.13 shows that in the absence of CR heating, gas pressure support drops, making CR pressure the dominant source of support against gravity in the halo. However, now the much higher gas densities mean that radiative cooling is important throughout the system. Note that excess radiative cooling is balanced by an artificial heating source term (equation 4.21), which is not shown in Fig.4.13. Looking again at the slice plots in fig.4.12, the presence of nearly volume-filling quantities of cold gas in the fast wind case (middle row of fig.4.12) is striking. The morphology of this cold gas is different from the cool clouds which typically form during thermal instability. Similar to the cold fountain flows seen in the fountain flow case, the cold halo gas here, which also has high levels of CR pressure extending from the disk, is a result of cold dense gas being flung off the disk by CR pressure. If one decreases the CR pressure at the base, e.g. by varying α_0, as in fig.4.14, the amount of cold gas in the halo decreases. Unlike the fountain flows seen in the fountain flow case though, the cold gas appears to be moving outwards in a monotonic wind instead of continuously recycling. The weak B-fields in the fountain case allow CRs to be alternatively trapped and released by transverse/vertical B-fields, producing outflow/infall, whereas the B-fields remain relatively straight when they are stronger. The slow wind case exhibits less cold gas in the halo. This is because the streaming-dominated CRs sustain stronger losses in the sharp density drop at the disk halo interface. The increased diffusion in the fast wind case allows CRs to leak out of the disk and act on the less dense gas, which is easier to push.

To further demonstrate the role of CR heating, we perform simulations starting without it, letting the flow settle onto a nonlinear steady state as shown in Fig.4.12, then re-activating CR heating. An example of this is shown in Fig.4.15 (which corresponds to a continuation of the middle row case in Fig.4.12). The cold, dense flow quickly transitions into a hot and low density wind (in just $\approx 2t_{\rm cool}$ for the case shown in fig.4.15). For the case shown, the low β and high CR diffusivity generates intense heating at the halo, and results in a quick transition into a fast wind (i.e. similar to the middle row of fig.4.7). CR heating evaporates initially cool gas leaving the disk, transforming it to a low density wind which is easy to accelerate. From equation 4.42, we see that for the flow to exceed the escape velocity, we require $t_{\rm heat}/t_{\rm ff} < 1$.

In Fig.4.16 we plot the time averaged outflow velocity, temperature and density at a scale height $x = H$ against $t_{\rm heat}/t_{\rm ff}$ (also taken at a scaleheight). The plots shows a clear transition around $t_{\rm heat} \sim 0.4 t_{\rm ff}$ when $v_x \sim v_{\rm esc} = \sqrt{2gx}$. For $t_{\rm heat}/t_{\rm ff} > 0.4$, the density and temperature of the flow is roughly independent of $t_{\rm heat}/t_{\rm ff}$, while for $t_{\rm heat}/t_{\rm ff} < 0.4$, the temperature/density of the flow increase/decrease continuously as $t_{\rm heat}/t_{\rm ff}$ falls. By contrast, the velocity $v_{\rm x} \propto (t_{\rm heat}/t_{\rm ff})^{-0.7}$, varies continuously with $t_{\rm heat}/t_{\rm ff}$, in rough accordance with equation 4.42. Surprisingly, the mass flux peaks at $t_{\rm heat}/t_{\rm ff} \sim 0.4$; it falls as heating becomes stronger. The scatter points are also color-coded by their cold width $\Delta x_{\rm cold}$, which measures the extent of fountain flows, and defined in fig.4.18. Fountain flows will be discussed in more detail in the next section, but for now we simply note that while fountain flows are mostly slower, colder, denser, and have a lower gas enthalpy flux, they account for the highest mass flux

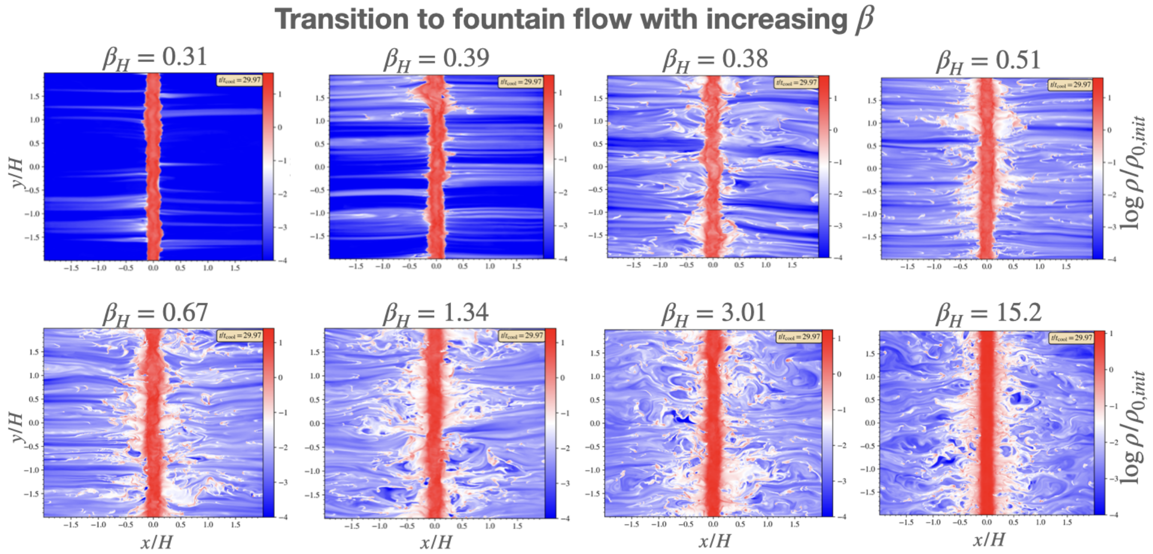

FIGURE 4.17: Density slices at $t = 30t_{\rm cool}$ for various cases with different β (the time average projection of β at $x = H$ is listed on top of each panel), showing the transition to fountain flows as the magnetic field weakens. $t_{\rm cool}$ refers to the initial cooling time at $x = H$. $\alpha_0 = 1$ and $\eta_H = 1$ for these cases (α_0 refers the initial ratio of CR to gas pressure at the base, which in our simulations, is kept fixed. η_H is the initial ratio of CR diffusive to streaming flux at $x = H$). The initial plasma β (at $x = 0$) for these cases are: 5 (top left); 10 (top second left); 30 (top second right); 50 (top right); 100 (bottom left); 300 (bottom second left); 1000 (bottom second right); 1000 (bottom right). The respective case identifiers are: ‘a1b5k1d1in.67res1024c200’ (top left); ‘a1b10k1d1in.67res1024c200’ (top second left); ‘a1b30k1d1in.67res1024c200’ (top second right); ‘a1b50k1d1in.67res1024c200’ (top right); ‘a1b100k1d1in.67res1024c200’ (bottom left); ‘a1b300k1d1in.67res1024c200’ (bottom second left); ‘a1b1000k1d1in.67res1024c200’ (bottom second right); ‘a1b10000k1d1in.67res1024c200’ (bottom right). Note that due to reduction in gas pressure, the simulations ended up with a reduced β compared to the initial value.

among our test cases. We shall see that while the cold gas recycles in fountain flows, the warm/hot component moves monotonically outward, and because of its higher density relative to the slow/fast wind cases, it has a higher mass flux.

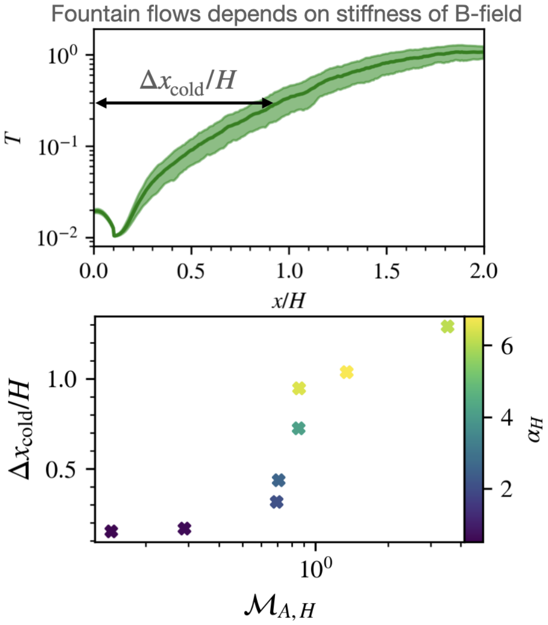

FIGURE 4.18: Bottom panel: With of cold mass $\Delta x_{\rm cold}$ against the Alfven Mach number $\mathcal{M}_{A,H} = v_H/v_{A,H}$. v_H and $v_{A,H}$ are taken at a scaleheight from the time-averaged projection profiles of v and v_A. The ratio of CR to gas pressure at a scaleheight α_H is color-coded into the scatter points. α_H is also taken from the time averaged projection profile of α. The top panel is a diagram showing how the width of the cold mass is defined: from the time-averaged projection temperature profile, measure the width from the base for which the temperature is $\leq 0.3T_{0,init}$.

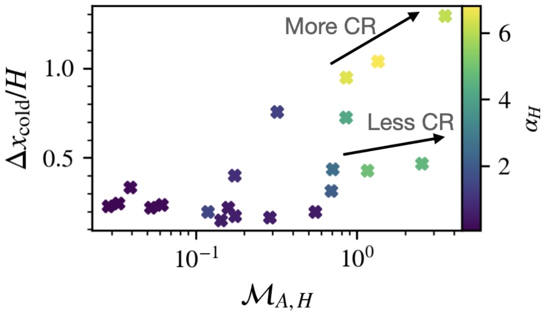

FIGURE 4.19: Same as the bottom panel of fig.4.18, including all cases listed under §4.4 in table 4.1 with CR heating. The width of the cold region, which is a marker of fountain flows vs winds, decreases as $\alpha_{\rm H}$ is smaller. Both $\mathcal{M}_{\rm A,H} > 1$ and $\alpha_{\rm H} > 1$ are generally required for fountain flows, though the two parameters are correlated – $\alpha_{\rm H}$ typically jumps once $M_{\rm A} > 1$.

4.4.4 Transition to fountain flows

In previous sections, we focused a lot on the transition from slow winds to fast winds, and discussed how it relates to $t_{\rm heat}/t_{\rm ff}$. Here, we also want to understand the criterion for fountain flow. We discussed in previous sections that fountain flows are driven by CR pressure as they are a flow feature that do not vanish when CR heating is turned off. When the presence of CRs in the halo is decreased, either when the base supply of CRs is lowered or when the diffusivity is reduced, so too does the extent of fountain flows. The strength of the magnetic field affects fountain flows too. In the discussion and figures shown up to this point, fountain flows appear only in high β cases. In fact, as we vary β_0 as shown in fig.4.17, we could see a clear transition to a fountain flow as it increases.

In fig.4.18, we show how the extent of the fountain flow (as measured by the width of the cold mass $\Delta x_{\rm cold}$ (defined by the extent in x where $T < 0.3$) depends on the Alfven Mach number $\mathcal{M}_A$ (measured at a scaleheight). There is a clear transition at $\mathcal{M}_A \sim 1$, below which there is generally single-phase hot gas, and above which there is cool fountain flow. This is straightforward to understand: CRs do work by direct acceleration at a rate $v \cdot \nabla P_c$, while the CR heating rate is $v_A \cdot \nabla P_c$. Thus, cool momentum driven winds arise when $\mathcal{M}_A > 1$, and hot thermally driven winds arise when $\mathcal{M}_A < 1$.

Consistent with fig.4.10, the fountain cold gas is associated with CR pressure dominance, as indicated by the high ratio of CR to gas pressure α. At low β, characterized by $\mathcal{M}_A \ll 1$, the magnetic field is stiff and CRs are transported monotonically outwards, producing winds. As β increases, and $\mathcal{M}_A \gtrsim 1$, the magnetic field becomes more flexible and can wrap around cold gas, trapping CRs. The accumulated CRs build up in pressure and loft the cold, dense gas up, creating fountain flows (and significantly more turbulence). The trapping of CRs is a crucial factor in the appearance of fountain flows. In our simulations where the initial field is vertical, this realignment only happens with weak fields, though realistically it could also happen when the galactic B-field is aligned with the disk, i.e. horizontal.

Although the mean radiative cooling rate in fountain flows is significantly larger than the mean CR heating, this does not mean the flow is exclusively a cool isothermal wind. Instead, strong gas density and CR pressure fluctuations – seeded by the magnetic 'shrink wrap' – cause the gas to fragment into a multi-phase flow. The dense cold gas, which is gravitationally bound, is confined to low galactic heights, circulating in a fountain whose width increases with $\mathcal{M}_{\rm A}$. At higher galactic heights, the flow becomes more single phase, though some cold gas remains. Unlike the fountain flow cool gas, the hotter, lower density phase moves monotonically outward. Indeed, because the density of this phase is higher than in the hot wind case, the outward mass flux is *larger* for fountain flows than for hot, thermally driven winds (fig.4.16)

To further demonstrate the effect of CR pressure on fountain flows, in fig.4.19 we replot the $\Delta x_{\rm cold}$ against $\mathcal{M}_A$ graph, including all other cases listed in table 4.1 under §4.4 with CR heating. Again, there is no fountain flow for $\mathcal{M}_A \ll 1$. For $\mathcal{M}_A \gtrsim 1$,

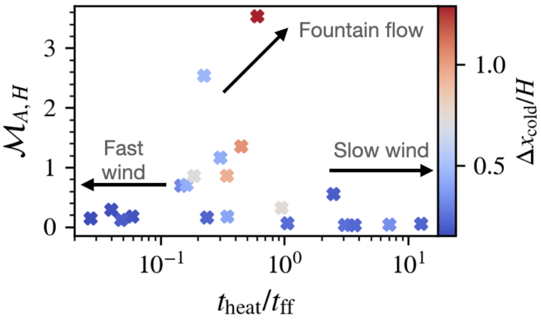

FIGURE 4.20: Alfven Mach number $\mathcal{M}_{A,H}$ against $t_{\rm heat}/t_{\rm ff}$ with $\Delta x_{\rm cold}/H$ color-coding. $\mathcal{M}_A, t_{\rm heat}/t_{\rm ff}$ and $\Delta x_{\rm cold}/H$ are taken at a scaleheight $x = H$ from the time averaged projection profiles of $\mathcal{M}_A, t_{\rm heat}/t_{\rm ff}, \alpha$. Time average projection refers to averaging from $t = 31.8 t_{\rm cool}$ to $63.6 t_{\rm cool}$, when the flows have settled onto their nonlinear steady-states, and then spatial averaging over y. $t_{\rm cool}$ refers to the initial cooling time at $x = H$. The region of parameter space typical for each nonlinear TI outcome is indicated by arrows.

greater α_H (i.e., greater CR dominance) leads to greater $\Delta x_{\rm cold}$. Thus, both super-Alfvenic flows $\mathcal{M}_{\rm A} > 1$ and CR dominance $\alpha_{\rm H} > 1$ are required for fountain flows, although in practice the two parameters are strongly correlated, since $\alpha_{\rm H}$ increases sharply at $\mathcal{M}_{\rm A} > 1$.

4.4.5 Understanding Mass Outflow Rates; 1D Models

From our discussion above, the nonlinear outcome of TI with CR heating can be summarized with the aid of fig.4.20, which shows the variation of the Alfven Mach number $\mathcal{M}_A$ against $t_{\rm heat}/t_{\rm ff}$ with $\Delta x_{\rm cold}/H$ (width of the cold gas) color-coding. As shown by the figure, cases with $t_{\rm heat}/t_{\rm ff} \lesssim 0.4$ result in a fast wind, as gas expansion caused by intense CR heating drives a super-escape speed flow. The halo structure is characterized by a hot, rarefied single phase where cold gas is evaporated. As $t_{\rm heat}/t_{\rm ff}$ increases beyond ~ 0.4, the outcome bifurcates to either a slow wind or a fountain

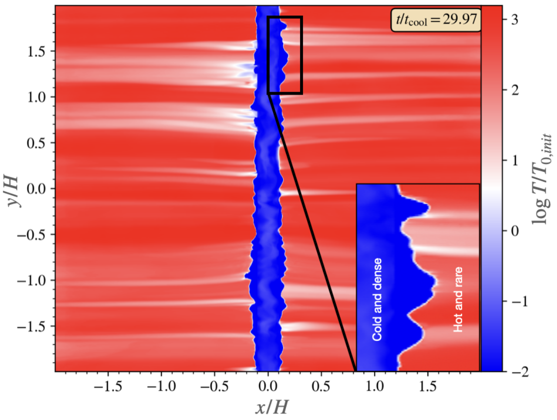

FIGURE 4.21: Zoom-in on a part of the interface region of the fast wind case, showing the multiphase structure of the interface region. The color scale shows the temperature, with blue representing cold gas and red representing hot gas.

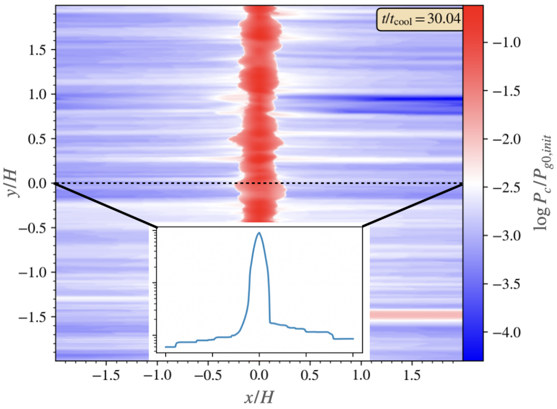

FIGURE 4.22: Top: Plot of P_c at $t = 30t_{\rm cool}$ for the slow wind case with an inset box indicating the P_c profile through the dotted line. CR staircases can be clearly seen.

flow. If the magnetic field is weak, such that the Alfven Mach number $\mathcal{M}_A > 1$ and the easily bent magnetic field 'shrink-warps' CRs (such that $\alpha > 1$), multi-phase fountain flows where cold, dense gas is flung out of the disk ensue. Otherwise, a slow wind results.

Ideally, a predictive theory should be able to tell us what the outcome is given input parameters such as g, κ, B and boundary conditions like $\rho_0, \alpha_0, F_{c,0}$. A common

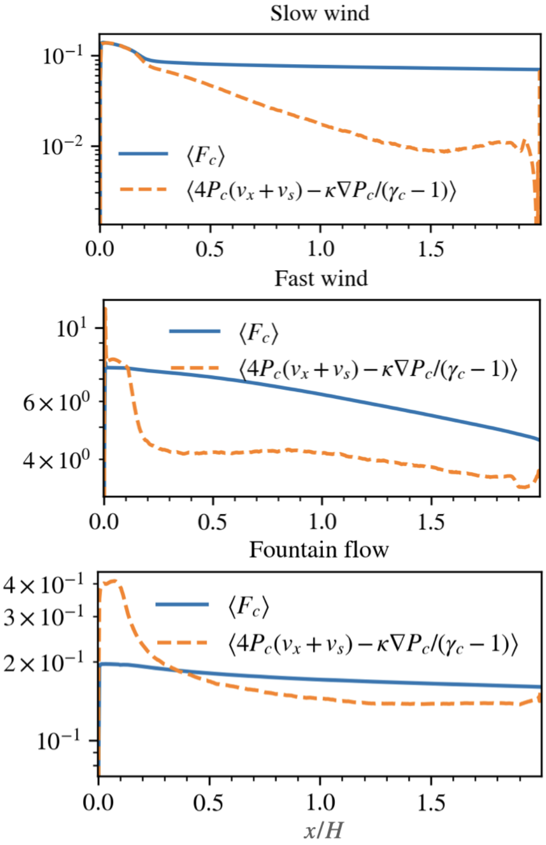

FIGURE 4.23: Comparison of the time averaged projection profile of F_c and the steady state form of F_c (eqn.4.8), showing there is a mismatch between the two. Time averaged projection refers to averaging from $t = 31.8t_{\rm cool}$ to $63.6t_{\rm cool}$, when the flows have settled into their nonlinear steady-state, and then spatial averaging over y. $t_{\rm cool}$ refers to the initial cooling time at $x = H$.

approach is to solve the steady-state 1D ODEs for mass, momentum and energy conservation (i.e. 1D version of eqn.4.1 to 4.6 omitting the time derivatives) using appropriate boundary conditions at the base, to derive the wind solution, similar to what has been done in the past (Mao and Ostriker [113], Modak et al. [119], Quataert et al. [133, 135], except (i) the isothermal assumption has to be dropped, as in Modak et al. [119], and (ii) *both* streaming and diffusion has to be incorporated, rather than considering only streaming dominated or diffusion dominated solutions, as in all of the cited works). In principle, one could then estimate what $t_{\rm heat}/t_{\rm ff}$ and $\mathcal{M}_A$ are,

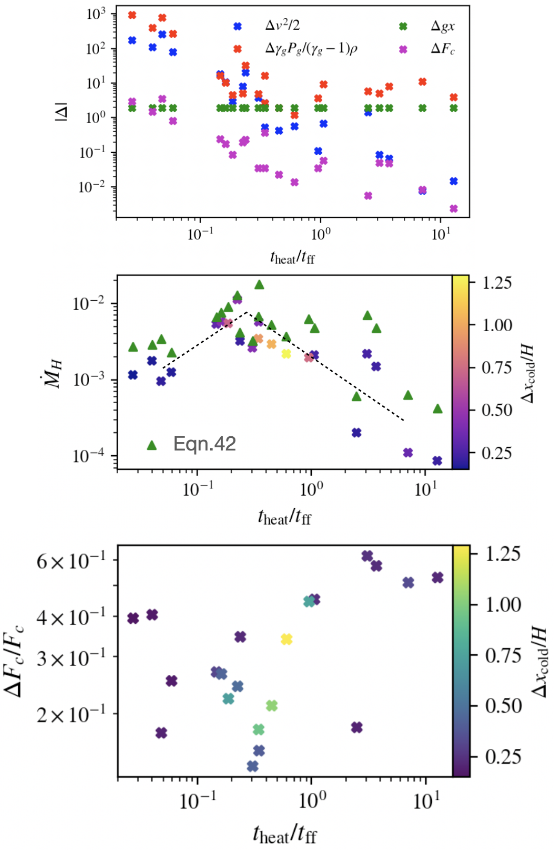

FIGURE 4.24: Top: Breaking up of the different terms in the RHS of eqn.4.45. Blue - $\Delta v^2/2$; green - $\Delta\phi$, where ϕ is estimated as gx; red - $\Delta\gamma_g P_g/(\gamma_g-1)\rho$; magenta - ΔF_c. Note that ΔF_c, which is the numerator of eqn.4.45, has different units form the rest. ΔQ of a generic quantity Q is estimated roughly from the difference $Q(x=a)-Q(x=2H)$ whereas $t_{\rm heat}/t_{\rm ff}$ is measured at a scaleheight $x=H$ of the time averaged projection profiles. Time average projection refers to averaging from $t=31.8t_{\rm cool}$ to $63.6t_{\rm cool}$, when the flows have settled onto their nonlinear steady-states, and then spatial averaging over y. $t_{\rm cool}$ refers to the initial cooling time at $x=H$. Middle: Mass flux $\dot{M}_H=\rho_H v_{x,H}$ measured at a scaleheight $x=H$ against $t_{\rm heat}/t_{\rm ff}$ for all the cases listed in table 4.1 under §4.4. Scatter points marked with 'X' and color-coded by $\Delta x_{\rm cold}/H$ are the true mass flux taken from the time averaged projection profiles while the green triangles are estimates of $\dot{M}_H$ using eqn.4.45 and the Δ estimates in the top panel. Bottom: Fractional change in the CR flux, $\Delta F_c/F_c$, against $t_{\rm heat}/t_{\rm ff}$ with $\Delta x_{\rm cold}/H$ color-coding. Note that we calculate the Δ's by taking the difference between $x=a=0.1H$ and $x=2H$ (the outer boundary) rather than at $x=0$ because CR heating is not added to the thermal gas in the buffer region $x=-a$ to a (see §4.2.2)

e.g. at a scale height, and determine using fig.4.20 and the conditions discussed above what the outcome would be.

However, in practice, 1D models will likely require substantial modification; naive application of time-steady 1D fluid equations do not reproduce higher dimensional simulation results. This is obvious for the fountain flow case, where the multi-phase nature of the flow, and the effects of B-field draping which traps CRs, cannot be trivially reproduced in 1D. Surprisingly, it is also true in the slow and fast wind cases, where the gas appears mostly single phase at a given galactic height x, and the B-fields are relatively straight. If we compare the simulation results to the steady-state fluid equations, they do not match.

The culprit is the disk-halo interface, where cold gas is accelerated and heated. In Fig 4.23, we show that the time-averaged simulated CR flux does not assume its steady state form, as given by equation 4.8. There are two reasons for this. Firstly, the interface is multi-phase, with fingers of cold gas protruding into the hot medium; accurately capturing the multi-phase character generally requires 2D or 3D simulations. Secondly, the interface can be unstable to the CR acoustic instability[13] [6, 169], particularly for low β fast winds. As seen in Fig 4.21, the density perturbations due to these effects produce CR staircases due to the bottleneck effect [169], which result in alternating regions of flat and intensely dropping ∇P_c, producing haphazard regions of CR coupling to gas variables (Tsung et al. 169; $\nabla P_c \neq 0$ is required for CR to couple with the thermal gas). The intermittent coupling causes the steady-state equation 4.8, which assumes continuous coupling, to fail. It may be possible to produce models with effective coupling which can reproduce our simulation results (as has been done for multi-phase turbulent mixing layers, Tan and Oh 163, Tan et al. 164), but it is beyond the scope of this paper.

---

[13] The CR acoustic instability, which operates when $\beta \lesssim 0.5$, causes CRs to amplify sound waves, which grow non-linearly into weak shocks. The growth time $t_{\rm grow} \sim \kappa\beta/c_c^2$, where $c_c = (\gamma_c P_c/\rho)^{1/2}$ is the CR sound speed, is short compared to other timescales in our setup. For instance, for the fast wind case (in code-unit, $\rho \sim 2 \times 10^{-4}$, $P_c \sim 0.03$, $\kappa = 2.92$, $\beta \sim 0.3$), $t_{\rm grow} = 1/\gamma_{\rm grow} \sim 4 \times 10^{-3} \sim 3 \times 10^{-3} t_{\rm cool} \sim 10^{-2} L/v_x$, where $t_{\rm cool}$ is the initial cooling time, L is the domain size and v_x is the outflow speed of the fast wind.

How can we understand the mass flux $\dot{M}$ of the flows, which is key to describing the strength of an outflow? We note that total energy conservation gives:

$$\nabla \cdot \left[\dot{M}\left(\phi + \frac{3}{2}c_s^2 + \frac{1}{2}v^2\right) + F_c\right] = -\rho^2\Lambda(T). \tag{4.44}$$

In the nonlinear regime, cooling is negligible (fig.4.8), thus we can estimate the mass flux, assuming $\dot{M}$ is constant, as

$$\dot{M} \approx -\frac{\Delta F_c}{\Delta\left(\phi + 3c_s^2/2 + v^2/2\right)}, \tag{4.45}$$

where ΔF_c is the net change in the CR flux, and $\Delta\left(\phi + 3c_s^2/2 + v^2/2\right)$ is the total change in the specific energy of the gas, including gravitational, thermal, and kinetic energy components (ϕ is approximated by gx for this study). What eqn.4.45 says is that since the total energy flux is conserved, any increase in the gas energy flux comes entirely from CR, through the decrease of F_c. For a fixed ΔF_c, a larger change in the specific energy requires a lower mass flux to ensure energy conservation.

In fig 4.24, we compare simulation results against equation 4.45. The agreement is generally good, though eqn.4.45 does tend to overestimate $\dot{M}_H$ slightly as $\dot{M}$ generally is not constant near the base. Modak et al. [119], who arrive at similar estimates, assume that $\Delta F_c \sim F_{c0}$ and $\Delta(\phi + v^2/2 + 3c_s^2/) \sim v_{\rm esc,Herquist}^2$, where $v_{\rm esc,Herquist}$ is the escape speed from the base of a Herquist model gravitational potential, giving rise to an estimated mass flux of $\dot{M}_{\rm Modak} \approx F_{c0}/v_{\rm esc,Herquist}^2$. In our simulation, we can see that this estimate is justified for $t_{\rm heat}/t_{\rm ff} > 1$, corresponding to slow wind cases, as $\Delta\phi$ does contribute significantly to the change in the specific energy (top panel of fig.4.24) and ΔF_c is of order (but not exactly) F_c (bottom panel of fig.4.24). This is indeed the case that Modak et al. [119] simulated. As one transitions to the $t_{\rm heat} < t_{\rm ff}$ regime, however, this estimation is no longer valid, as the change in the specific energy is now dominated by the kinetic and thermal energy terms. Accurate estimation of Δv^2 and ΔT are needed. This requires knowledge of the wind solutions, which from our discussion above, is left for future work. Observe also that $\Delta F_c/F_c$ tends to be larger for the slow wind cases ($t_{\rm heat}/t_{\rm ff} > 1$). One reason for this is that the slow wind cases generally have smaller η (CR diffusivity). The CRs are therefore more strongly coupled to the gas, and lose most of their energy. Overall, $\Delta F_c/F_c \sim 0.1 - 0.6$, i.e. the halo is at best marginally optically thick. Echoing our discussion in §4.4.3, the trends in $\dot{M}_H$ as shown in fig.4.16 (and in the middle panel fig.4.24) can be explained as follows: For $t_{\rm heat}/t_{\rm ff} > 1$, the tight coupling between CRs and the thermal gas implies greater CR losses by proportion, with $\Delta F_c \sim 0.6 F_c$. The change in the specific energy is of order $\Delta\phi$, which in our simulations is fixed.

Reducing $t_{\rm heat}/t_{\rm ff}$, for example by increasing the CR supply at the base, increases ΔF_c and therefore $\dot{M}$. As $t_{\rm heat}/t_{\rm ff}$ is reduced below 0.4, the opposite trend occurs. Due to increased η (CR diffusivity) for the fast wind cases, CR losses decrease by proportion ($\Delta F_c/F_c$ decreases). Furthermore, the gas specific energy is no longer fixed by $\Delta\phi$, but is dominated by the (much larger) kinetic and thermal energy, which leads to a drop in $\dot{M}$. Thus, the maximum $\dot{M}$ occurs at the transition $t_{\rm heat}/t_{\rm ff} \sim 0.4 - 1$.

4.5 Discussion

4.5.1 Translating from Code to Physical Units

The fluid equations we solve are scale-free, and our results are characterized essentially by dimensionless ratios. The only constraint is that the cooling index we used, $-2/3$, necessarily requires the initially condensing gas to be between $10^5 - 10^6$ K. With this constraint, our results can be dimensionalized if the reference quantities ρ_0, T_0, g_0 in physical units are given (they are all set to 1 in our simulations). If we set the reference gravitational acceleration, temperature and density to be $g_0 = 10^{-8}$ cm s^{-2} (as appropriate for the Milky Way disk; Benjamin and Danly 9), $T_0 = 10^6$ K and $\rho_0 = 10^{-26}$ g cm^{-1} ($n_0 \sim 10^{-2}$cm^{-3}) respectively, the other reference quantities would then scale as: length $H = k_B T_0/m_u g_0 = 2.7$ kpc, pressure $P_0 = \rho_0 k_B T_0/m_u = 8.3 \times 10^{-13}$ erg cm^{-3}, velocity $v_0 = (k_B T_0/m_u)^{1/2} = 91$ km s^{-1}, and the flux $F_0 = P_0 v_0 = 7.5 \times 10^{-6}$ erg s^{-1} cm^{-2}, where k_B and m_u are the Boltzmann constant and the atomic mass unit[14]. From fig.4.7 we can see that at $x = H$ the fast wind can acquire velocity ~ 600 km s^{-1} (or generally hundreds of km s^{-1}) whereas the slow wind is around ~ 60 km s^{-1} (or generally tens of km s^{-1}). The halo density can get to as low as 10^{-30} g cm^{-3} ($n_0 \sim 10^{-6}$cm^{-3}) and 10^{-28} g cm^{-3} ($n_0 \sim 10^{-4}$cm^{-3}) for the fast and slow wind respectively while the temperature remains $T \sim 10^6$ K for the slow wind but can reach up to $T \sim 10^8$ K for the fast wind. Scaling the CR diffusivity by $\kappa_{\rm ref} = Hv_0 = 7.6 \times 10^{28}$ cm^2 s^{-1}, the slow, fast wind and fountain case diffusion coefficients κ are 2.2×10^{27} cm^2 s^{-1}, 2.2×10^{29} cm^2 s^{-1} and 2.9×10^{28} cm^2 s^{-1} respectively.

A key physical quantity for winds is the mass loading factor, which expresses the mass outflow rate per unit star formation rate (SFR) ($\dot{M}_{\rm wind}/\dot{M}_*$). In physical units, the mass loss rate $\dot{M}_{\rm wind}$ can be expressed as $\rho v A$, where A is the cross-sectional area the wind passes through. To get the SFR, we make several simplifying assumptions to connect the CR flux at the base F_{c0} to $\dot{M}_*$. First, assuming all of the CRs originate from supernovae (SN), we can express $F_{c0} \approx \epsilon_{\rm SN} E_{\rm SN} \dot{N}_{\rm SN}/A$, where $\epsilon_{\rm SN} \approx 0.1$ is the CR acceleration efficiency by SN, $E_{\rm SN} \sim 10^{51}$ erg is the energy released from each SN event, $\dot{N}_{\rm SN}$ is the SN rate. If we make the further assumption that a fraction $f_{\rm SN}$ of the stars formed becomes SN, i.e. $\dot{N}_{\rm SN} = f_{\rm SN}(\dot{M}_*/\bar{M})$, where $\bar{M}$ is the mean stellar mass, then $\dot{M}_* \approx F_{c0} A \bar{M}/\epsilon_{\rm SN} f_{\rm SN} E_{\rm SN}$ and the mass loading factor $\dot{M}_{\rm wind}/\dot{M}_* = (\rho v/F_{c0})(\epsilon_{\rm SN} f_{\rm SN} E_{\rm SN}/\bar{M})$. Again, crudely estimating $f_{\rm SN}$ and $\bar{M}$ using the initial-mass-function ϕ (IMF): $f_{\rm SN} \approx \int_{8M_\odot}^{20M_\odot} \phi \, {\rm d}M \,/ \int_{0.1M_\odot}^{20M_\odot} \phi \, {\rm d}M$ and

---

[14] Note that all of these quantities are equal to 1 in code-units. By expressing the ideal gas law as $P_g = \rho T$ in the code, we have absorbed factors of k_B into T and m_u into ρ.

$\bar{M} \approx \int_{0.1M_\odot}^{20M_\odot} M\phi \, \mathrm{d}M \, / \int_{0.1M_\odot}^{20M_\odot} \phi \, \mathrm{d}M$, we get, if we adopt a power law IMF with index -2.35 [147], $f_{\mathrm{SN}} \approx 0.002$, $\bar{M} \approx 0.33 M_\odot$. At the top of fig.4.25 we plot the mass loading factor against $t_{\mathrm{heat}}/t_{\mathrm{ff}}$ using these conversion and scaling factors. As discussed in §4.4.3, despite the high outflow velocity of fast winds ($t_{\mathrm{heat}}/t_{\mathrm{ff}} \lesssim 0.4$), they are inefficient in carrying mass out. Slow winds ($t_{\mathrm{heat}}/t_{\mathrm{ff}} \gtrsim 0.4$) appear more efficient, and the mass loading factor seems to be roughly independent of $t_{\mathrm{heat}}/t_{\mathrm{ff}}$. The result for slow winds is in agreement with the literature that shows that the mass loading factor depends generally on the escape velocity, which is held fixed in our study. We note that one should take the numerical values for the mass loading in fig.4.25 with a grain of salt, as it involved some simplifying assumptions and depends quite heavily on the reference values we used to map our code-units to physical units (e.g. if the reference temperature T_0 is decreased by a factor of 10 to 10^5 K, as one might imagine for less massive galaxies with lower virial temperature, the mass loading would be boosted by a factor of 10). Also, the mass loading calculated here takes into account only the effect of CRs; the total mass loading is likely a culmination of many factors (direct mechanical injection from SNe, radiation, and from multiphase clouds). With just CRs alone, the mass loading factor of fast winds is low compared to that observed (e.g. $\dot{M}_{\mathrm{wind}}/\dot{M}_* \sim 0.3$ for $M_* \approx 10^{11} M_\odot$ galaxies and $\dot{M}_{\mathrm{wind}}/\dot{M}_* \sim 3$ for $M_* \approx 10^9 M_\odot$ galaxies, see Chisholm et al. [33]), whereas the slow wind regime mass loading appears higher and more consistent. In any case, the trend shows that fast winds have appreciably lower mass loading than the slow wind.

Similarly, the energy loading factor $\dot{E}_{\mathrm{wind}}/\dot{E}_*$, compares thermal and kinetic power in the wind to the rate of energy input from stellar feedback. Here, we only consider CR feedback, and write $\dot{E}_{\rm wind} = F_{\rm wind}A$ and $F_{\rm c0} = \epsilon_{\rm SN}\dot{E}_*/A$ to obtain $\dot{E}_{\rm gas}/\dot{E}_* = \epsilon_{\rm SN}F_{\rm wind}/F_{\rm c0}$. We plot the energy loading factor $\dot{E}_{\rm gas}/\dot{E}_* = \epsilon_{\rm SN}F_{\rm wind}/F_{\rm c0}$ at the bottom panel of fig.4.25 (the numerator $F_{\rm wind}$, which varies in the flow, is evaluated at $x = H$). We again caution the reader to take the numerical values with a grain of salt, but the trend is clear: the energy loading increases gently from slow to fast winds, while the fountain flow cases (circled in the plot) show distinctively low energy loading. This echos existing studies showing that hot, fast outflows are generally more efficient in energy loading but less so in mass loading, while the opposite is true for colder flows [55, 109]. Given the drastic change in fluid properties of the fast wind cases from the slow wind case, it might seem surprising that the rise in energy loading is so gentle across the two regimes. The energy loading factor is given by

$$\begin{aligned}\frac{\dot{E}_{\rm wind}}{\dot{E}_*} &= \epsilon_{\rm SN}\frac{F_{\rm gas}}{F_{\rm c0}} \approx \epsilon_{\rm SN}\frac{\Delta(F_{\rm gas}+F_{\rm grav})}{F_{\rm c0}}\frac{\Delta F_{\rm gas}}{\Delta(F_{\rm gas}+F_{\rm grav})} \\ &\approx \epsilon_{\rm SN}\frac{\Delta F_c}{F_{\rm c0}}\frac{\Delta(v^2/2+c_s^2/(\gamma_g-1))}{\Delta(\phi+v^2/2+c_s^2/(\gamma_g-1))},\end{aligned} \tag{4.46}$$

where we have approximated $F_{\rm gas}$ by $\Delta F_{\rm gas}$ in the first step as the gas energy flux near the base is negligible, and used the fact that $\Delta(F_{\rm gas}+F_{\rm cr}+F_{\rm grav}) = 0$ (for negligible radiative cooling) in the second step, where $\Delta F_{\rm grav}$ is the work done against gravity. In the slow wind regime, the change in gravitational potential dominates (fig.4.24), so the last term in eqn.4.46 can be approximated by $\Delta(v^2/2+c_s^2/(\gamma_g-1))/\Delta\phi$; it decreases as $t_{\rm heat}/t_{\rm ff}$ increases. However, this term approaches 1 in the fast wind regime, when the flow is dominated by kinetic and thermal energy. On the other hand, faster winds are usually associated with higher CR diffusivity in our study (since we fix the base CR pressure, greater CR heating in the halo is brought on by either increasing the magnetic field or allowing CRs to diffuse faster out of the disk by increasing κ), thus the coupling between the thermal gas and CR is generally weaker for fast wind in our study, leading to a smaller $\Delta F_c/F_{c0}$. The overall increase in the energy loading factor across the slow wind regime to the fast wind regime is thus gentle. We note that $t_{\rm heat}/t_{\rm ff}$ can be changed in a number of ways, so the steepness of this scaling may change in other scenarios with different boundary conditions (for instance, fixing $F_{\rm c}$ rather than $P_{\rm c}$ in the central disk).

One of the most interesting outcomes of this study is the presence of fountain flows when $\mathcal{M}_A > 1$, characterized by circulation of cold gas. The extent of the cold gas, from fig.4.18, can reach up to H (or more). From the right-most panel of fig.4.11, we can see that cold gas with $T < 0.1T_{0,\rm init}$ is distributed roughly equally between outflows and inflows, indicative of a circulation, with velocity of order ± 1 (in code-units). Using the scaling factors as discussed above, $H \sim 2.7$ kpc and the cold gas circulation speed ~ 90 km s^{-1}. These values are consistent with the observed intermediate-velocity-clouds (IVC, Marasco et al. 114), which appear also to be circulating above the galactic disk at a height of $\sim$ kpc with velocity $\lesssim 90$ km s^{-1}.

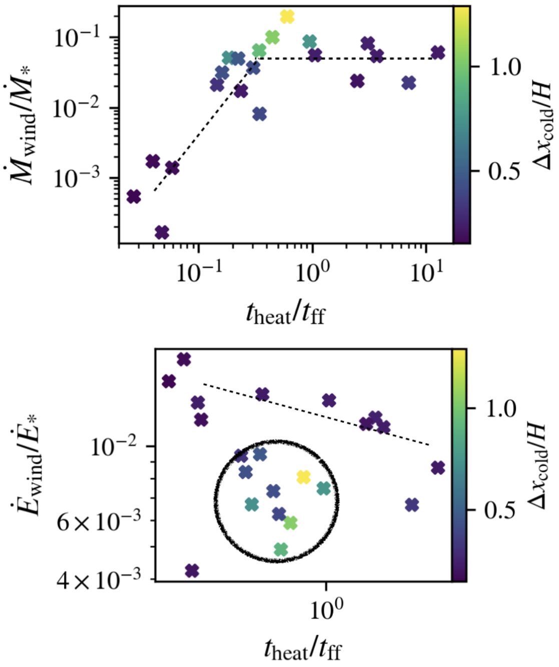

FIGURE 4.25: Top: Mass loading factor $\dot{M}_{\rm wind}/\dot{M}_*$ against $t_{\rm heat}/t_{\rm ff}$ with $\Delta x_{\rm cold}/H$ color-coding. Bottom: Energy loading factor $\dot{E}_{\rm wind}/\dot{E}_*$ against $t_{\rm heat}/t_{\rm ff}$ with $\Delta x_{\rm cold}/H$ color-coding. In both plots, the dotted lines are there to highlight the general trend. In the bottom plot (energy loading), fountain flow cases are circled and the trend for energy loading to increase with stronger heating (indicated by the dashed line) applies only for the wind cases.

4.5.2 Comparisons against larger scale simulations

An obvious question is whether any of the phenomenon we discuss can be seen in existing CR wind simulations, particularly those which are larger scale and less idealized. We have already discussed how the slow heated wind has been studied in 1D by Modak et al. [119]. We mention two potential cases where previous simulations are in the right parameter regime for CR fountain flows and heated winds. Of course, a positive identification requires further detailed analysis. We merely show that existing simulation runs often lie in the parameter regimes we describe, and show similar behavior. They can be reanalysed with these considerations in mind.

A number of FIRE simulations, with CR physics incorporated in a two-moment formalism [30, 73, 90], are potentially in the fountain flow regime. Their simulated CGM has high plasma $\beta \gg 1$ and therefore has a low CR heating rate and high Alfven Mach number, as required for fountain flows. Indeed, cold gas which circulates in a fountain is seen [31, 91]. Their disk-halo interface has significant gas motions near the disk, and is more hydrostatic further out (with gravity balanced primarily by CR pressure), as in our fountain flow picture (see fig.4.8). They found that CR feedback causes a greater uplift of gas, with gas of all phases (both cold and hot) more abundant above the disk. The hot gas moves further out, while the cold, $T \sim 10^4$ K gas is generally more confined. Our simulation set-ups are of course very different, but this broad-brush agreement is encouraging.

AREP0 simulations also include CR physics in a two-moment formalism [167]. In contrast to the FIRE simulations, their CR-driven wind is strongly magnetized ($\beta < 1$), with magnetic fields relatively collimated and vertical in the inner parts of the wind, and low in Alfven Mach number. In the innermost CGM, B-field lines are vertical, as in our setup. The authors describe a wind launched by CR pressure at the disk-halo interface. However, their wind also exhibits properties consistent with a CR-heated wind. From their Fig 3, we can see that $t_{\rm heat}/t_{\rm cool} \ll 1$ at the wind launch region at $z \gtrsim 0.6$ kpc, where (from the slice plots in their Fig 1) it is heated to high temperatures and low densities. Thus, a phase transition mediated by CR heating, similar to what we see, seems plausible. The heating of the disk gas is crucial: it reduces its density so that $\nabla P_c \gg \rho g$; without CR heating, the wind is much weaker

(§4.4.3). The inner disk wind ($R_{\rm disk} < 1$ kpc) shows wind velocities comparable to the escape velocity $v \sim 200\,{\rm km\,s^{-1}}$, and indeed crude estimates[15] from their figures show that $t_{\rm heat}/t_{\rm ff} \sim 0.2$. This is consistent with our 'fast wind regime' where $v \sim v_{\rm esc}$ for $t_{\rm heat}/t_{\rm ff} \sim 0.2$ in Fig 4.16. Similar to our fast wind simulations (Fig 4.8), in their simulations CR pressure gradients dominate in the hot wind above the disk. Regions of weak coupling between the CRs and the thermal gas (which the authors called 'dark Alfven regions') are found within the wind, and the transport speed of the CRs is frequently found to lag the Alfven speed. This echos our claim that the CR flux is, for the most part, not given by the steady-state form (eqn.4.8, and see fig.4.23). The authors attribute the 'dark Alfven regions' to field lines perpendicular to the CR gradient, so that there is no streaming instability. We note that the low plasma β of the gas implies that the CR acoustic instability [169] can potentially also play a role, particularly further out in the CGM. This can also cause regions of flat CR pressure where the CR streaming instability does not develop, and subsequent onset of the bottleneck effect causes a slowing of the CRs transport speed [169], which is limited by the Alfven speed at bottlenecks.

4.6 Conclusions

In this study we explored the effect of CR heating on TI, both in the linear and nonlinear phase, using a gravitationally stratified setup with vertical magnetic fields and streaming CRs. In the linear phase, we found that in accordance to linear theory [102], CR heating can cause gas entropy modes to propagate at some velocity proportional the Alfven velocity up the P_c gradient. The propagation of the modes is a result of differential CR heating on different parts of the gas perturbation, resulting in a net phase velocity. We verified with simulations that the modes propagate at the expected velocity (see §4.3.2 and fig.4.2). This propagation is subdued when we increase CR diffusivity (fig.4.3), as CRs diffuse out of the perturbation before they have time to heat it.

---

[15] We estimate $t_{\rm heat} \sim P_g/\Gamma \sim 0.5\,{\rm Myr}$, from $P_g \sim 10^{-2}$ eV cm^{-3}, $\Gamma \sim 10^{-27}\,{\rm erg\,s^{-1}\,cm^{-3}}$, while $t_{\rm ff} \sim r/v_{\rm esc} \sim 3\,{\rm Myr}$.

Mode propagation, under the action of CR heating, in a streaming dominated flow could in principle suppress TI. The idea is that if the time it takes for the modes to propagate across a cooling radius $t_{\rm cross}$ is less than the time it takes the modes to grow, which scales as $t_{\rm cool}$, the perturbations would not reach nonlinear amplitudes and become cold clouds. However, since both the crossing time $t_{\rm cross} \sim L/v_{\rm A}$ and the heating time $t_{\rm heat} \sim L/v_{\rm A}$ are closely related, there is only a small range of $\theta = t_{\rm cool}/t_{\rm heat}$ near unity where suppression by propagation effects operates, before the gas becomes over-heated.

Our most interesting results do not relate to the linear thermal instability, but rather the non-linear outcome of our simulations. There are two important things to note. Firstly, thermal instability causes substantial mass dropout and evolution in CGM properties. A cold disk containing most of the mass forms in the mid-plane, while the density and pressure of extraplanar gas is significantly reduced. Thus, initial values of

$\alpha = P_c/P_g$, $\beta = P_g/P_B$ evolve substantially during the non-linear stage[16]. The strong phase transition from cool disk gas to hot atmosphere has important consequences for CR wind properties, different from calculations which assume single-phase isothermal winds. Secondly, the dual role of CRs in pushing (∇P_c) and heating ($v_A \cdot \nabla P_c$) the gas implies that global thermal and hydrostatic equilibrium is not possible without fine-tuning. Indeed, the gas generally loses force and/or thermal balance at the disk halo interface, leading to the development of winds. The sharp reduction in gas density at the disk halo interface $\rho_{\rm h} \sim \rho_c(T_c/T_h)$ reduces radiative cooling ($\propto \rho^2$) and gravitational forces ($-\rho g$). The resulting loss of dynamical and thermal equilibrium can cause gas to accelerate outwards and heat up. CR winds and fountain flows are most efficient if diffusion is sufficiently strong such that transport is diffusion dominated until the flow reaches low densities (i.e., in the halo). Otherwise, since $P_{\rm c} \propto \rho^{2/3}$ for streaming dominated flows (assuming B $\approx$const), the sharp density gradient means that CRs suffer strong losses at high densities, when radiative cooling is still efficient. Since $v_{\rm A}$ increases strongly as the atmosphere thins due to mass dropout, in our simulations flows are typically streaming dominated in the halo, even if they are diffusion dominated near the disk.

We find two general classes of solutions, depending on whether the momentum or heat imparted by CRs dominates. CRs do work by direct acceleration at a rate $v \cdot \nabla P_c$, while the CR heating rate is $v_A \cdot \nabla P_c$. Thus, momentum driven winds arise when

---

[16] For instance, in our 'fountain flow' simulations, $\beta_{H,i} = 300$ becomes $\beta_{\rm H,f} \approx 1$, due to the reduction in gas pressure. See Fig 4.17 for other examples.

$M_A > 1$, and thermally driven winds arise when $M_A < 1$. This typically means that momentum or energy driven winds arise for high and low β atmospheres respectively.

- *Momentum-Driven Winds; Fountain Flows* ($M_A > 1$; high β; typically $\alpha = P_c/P_g > 1$). Cool disk gas is accelerated directly via CR forces – indeed, winds with almost unchanged characteristics are launched if CR heating is turned off. Since the flow is super-Alfvenic, magnetic fields are easily warped; as they wrap around rising gas they can trap CRs, with a consequent strong jump in CR dominance $\alpha = P_c/P_g$ once $M_{\rm A} > 1$. Density fluctuations result in a multi-phase fountain flow at low galactic heights, with the cold dense gas being lifted off the disk and falling back, while hotter gas flows outwards. At larger distances, when CR heating exceeds radiative cooling, the gas becomes hotter and mostly single phase. The extent of the fountain region increases with $\mathcal{M}_{\rm A}$ and CR dominance $\alpha_{\rm H}$.

- *Energy-Driven Winds* ($M_A < 1$; low β; typically $\alpha = P_c/P_g < 1$). Cool disk gas is strongly heated and evaporated at the disk halo interface, resulting in a hot wind powered by CR heating. In steady state, the divergence of the enthalpy flux of the hot gas balances CR heating. The sharp transition to a hot phase leads to a strong drop in gas density at the disk halo interface, with $\rho_{\rm h} \sim \rho_{\rm c}(T_{\rm c}/T_{\rm h})$. This low wind gas density means that the mass flux of CR heated winds is relatively low; they are an inefficient form of feedback compared to cool, denser momentum-driven winds, even though a large fraction of the latter circulates in a fountain flow. The velocity of the wind is $v \sim 0.4 v_{\rm esc} (t_{\rm heat}/t_{\rm ff})^{-1}$, i.e. the flow exceeds the escape velocity once $t_{\rm heat} \sim t_{\rm ff}$. The flow becomes even hotter and lower density for these fast winds, leading to very low mass fluxes. The strong magnetic tension in these sub-Alfvenic flows means there is little warping of field lines, and the single-phase wind flows monotonically outward.

There are numerous potential avenues for future work. A key issue is geometry. We have simulated a plane parallel Cartesian setup. This is appropriate close to the disk; thus, our simulation domain of $\sim 2H$ is relatively small. As the flow opens up, a spherical geometry becomes appropriate further away. The flow properties become quite different, as do the density, velocity, B-field and hence Alfven speed profiles. Thus, our simulations do not address the asymptotic properties of the flow far out in the CGM; also, Parker-type sonic points do not develop in plane-parallel flows. Our work is complementary to 1D models which use spherical geometry [85, 112, 119, 134, 136], but make other idealizations which we relax. Other possible extensions include: (i) using more physically motivated diffusion coefficients which depend on plasma conditions – e.g., from quasi-linear self-confinement theory [182], or using a model for field-line wandering [148]; (ii) incorporating other sources of thermal and momentum driving besides CRs, and understanding their mutual interaction; (iii) considering more complex B-field geometry (e.g., tangled fields due to turbulence). One interesting avenue for future work include formulating an 'effective' 1D model which takes the effect of multi-phase structure and CR bottlenecks into account, to match our time-averaged multi-dimensional flows (similar to effective 1D models for turbulent mixing layers; Chen et al. 32, Tan and Oh 163, Tan et al. 164). Another would be to make predictions for the nature of CR outflows for different galaxies lying on the SFR-M_* relation (which, in our language, correspond to different values of F_{c0} and gravity g respectively, leading to different values of $t_{\mathrm{heat}}/t_{\mathrm{ff}}$). It would also be interesting to make observational predictions (e.g., in gamma-ray emission) for CR dominated fountain flows. Of course, the biggest unknowns are still the strength of magnetic fields in the CGM, and the nature of CR transport, particularly the relative importance of streaming and diffusive transport.

Appendix A

Appendix for chapter 3

A.1 Linear Growth Rates in 1D including Background Gradient

Here, we provide a concise derivation of linear growth rates for the acoustic instability. More details can be found in Begelman and Zweibel [5].

A.1.1 Adiabatic EOS for Finite Diffusion Coefficient

In the well coupled limit, the time-dependent flux term in equation 4.6 can be ignored, reducing equations 4.1-4.6 to the one-moment equations. Expressing the equations in

1D and in primitive form,

$$\frac{\partial \rho}{\partial t} + \frac{\partial}{\partial x}(\rho v) = 0 \tag{A.1}$$

$$\frac{\partial v}{\partial t} + v\frac{\partial v}{\partial x} = -\frac{1}{\rho}\frac{\partial}{\partial x}(P_g + P_c) + \rho g \tag{A.2}$$

$$\frac{\partial P_g}{\partial t} + v\frac{\partial P_g}{\partial x} + \gamma_g P_g \frac{\partial v}{\partial x} = -(\gamma_g - 1)v_A \frac{\partial P_c}{\partial x} + (\gamma_g - 1)\mathcal{L} \tag{A.3}$$

$$\frac{\partial P_c}{\partial t} + (v + v_A)\frac{\partial P_c}{\partial x} = -\gamma_c P_c \frac{\partial}{\partial x}(v + v_A) + \frac{\partial}{\partial x}\kappa\frac{\partial P_c}{\partial x} \tag{A.4}$$

$$\tag{A.5}$$

For simplicity we assume the diffusion coefficient κ is constant. We perform a WKB analysis similar to Drury and Falle [40]. Assume all quantities Y can be expanded as a background plus fluctuating part

$$Y(x,t) \rightarrow Y(x) + \tilde{Y}(x,t), \tag{A.6}$$

where $\tilde{Y} \ll Y$. Keeping terms up to the first order in the fluctuating quantities gives (note that going from eqn.A.1 - A.4 to eqn.A.7 - A.10 we have performed a change of variables $Y \rightarrow Y + \tilde{Y}$. Quantities without a tilde now represents the unperturbed background rather than the full variation.)

$$\frac{\partial \tilde{\rho}}{\partial t} + \frac{\partial}{\partial x}(\rho \tilde{v} + \tilde{\rho} v) = 0, \tag{A.7}$$

$$\frac{\partial \tilde{v}}{\partial t} + v\frac{\partial \tilde{v}}{\partial x} + \tilde{v}\frac{\partial v}{\partial x} = -\frac{1}{\rho}\frac{\partial \tilde{P}_g}{\partial x} - \frac{1}{\rho}\frac{\partial \tilde{P}_c}{\partial x} + \frac{\tilde{\rho}}{\rho^2}\frac{\partial P_g}{\partial x} + \frac{\tilde{\rho}}{\rho^2}\frac{\partial P_c}{\partial x}, \tag{A.8}$$

$$\begin{aligned} &\frac{\partial \tilde{P}_g}{\partial t} + v\frac{\partial \tilde{P}_g}{\partial x} + \tilde{v}\frac{\partial P_g}{\partial x} + \gamma_g P_g \frac{\partial \tilde{v}}{\partial x} + \gamma_g \tilde{P}_g \frac{\partial v}{\partial x} = \\ &-(\gamma_g - 1) v_A \frac{\partial \tilde{P}_c}{\partial x} + (\gamma_g - 1)\frac{v_A}{2\rho}\tilde{\rho}\frac{\partial P_c}{\partial x} + (\gamma_g - 1)\left(\tilde{\rho}\frac{\partial \mathcal{L}}{\partial \rho} + \tilde{T}\frac{\partial \mathcal{L}}{\partial T}\right), \end{aligned} \tag{A.9}$$

$$\begin{aligned} &\frac{\partial \tilde{P}_c}{\partial t} + (v + v_A)\frac{\partial \tilde{P}_c}{\partial x} + (\tilde{v} + \tilde{v}_A)\frac{\partial P_c}{\partial x} = \\ &-\gamma_c P_c \frac{\partial}{\partial x}(\tilde{v} + \tilde{v}_A) - \gamma_c \tilde{P}_c \frac{\partial}{\partial x}(v + v_A) + \kappa \frac{\partial^2 \tilde{P}_c}{\partial x^2}. \end{aligned} \tag{A.10}$$

In WKB analysis we assume the fluctuating length and timescales are much smaller than the scales on which the background varies. The fluctuating quantity $\tilde{Y}$ can be expanded as

$$\tilde{Y}(x,t) = \sum_{n=0}^{\infty} \epsilon^n Y_n(x,t) e^{i\theta/\epsilon}, \tag{A.11}$$

where ϵ is a small parameter and $\partial\theta/\partial t = \omega, \partial\theta/\partial x = -k$. Note that $\partial\omega/\partial x + \partial k/\partial t = 0$. Substituting into equation A.7-A.10, we find to the lowest order ϵ^{-2}, (note that the expansion of the fluctuating quantity $\tilde{Y}$ begins with the subscript 0, i.e. the subscript 0 means it is the lowest order fluctuation, not the unperturbed background.)

$$k^2 \kappa P_{c0} = 0, \implies P_{c0} = 0. \tag{A.12}$$

To order ϵ^{-1},

$$\bar{\omega}\rho_0 = k\rho v_0, \tag{A.13}$$

$$\bar{\omega}\rho v_0 = kP_{g0}, \tag{A.14}$$

$$\bar{\omega}P_{g0} = k\gamma_g P_g v_0, \tag{A.15}$$

$$k^2\kappa P_{c1} = ik\gamma_c P_c\left(v_0 - \frac{v_A}{2\rho}\rho_0\right), \tag{A.16}$$

where $\bar{\omega} = \omega - kv$. Solving for $\bar{\omega}$ from equation A.13-A.15 we obtain the dispersion relation of a sound wave

$$\bar{\omega} = \pm kc_s, \tag{A.17}$$

where $c_s = \sqrt{\gamma_g P_g/\rho}$.

Now we have found that sound wave is a mode to the perturbed equation, what is its growth rate? As a wave packet transverse through a varying background, it changes in amplitude due to 1. adiabatic compression and 2. growth or damping due to instabilities. It is the latter we are interested in. To separate the two contributions, note that the wave action density $\mathcal{A}$, defined by dividing the wave energy density by its propagation frequency

$$\mathcal{A} = \frac{\rho v_0^2}{\bar{\omega}}, \tag{A.18}$$

is conserved under adiabatic compression. If the evolution of $\mathcal{A}$ can be expressed as a conservation equation, the non-conservative contribution would be due to instabilities, the growth rate which we can read off easily. Such a conservation equation can be derived by substituting eqn.A.13 - A.16 back to eqn.A.7 - A.10 and rearranging. Below is the result.

$$\begin{aligned}\frac{\partial \mathcal{A}}{\partial t} + \frac{\partial}{\partial x}[(v \pm c_s)\mathcal{A}] = & \frac{\mathcal{A}}{\rho c_s^2}\gamma_g(\gamma_g - 1)\left(v_A \frac{\partial P_c}{\partial x} - \mathcal{L}\right) \\ & - \frac{c_c^2 \mathcal{A}}{\kappa}\left[1 \pm (\gamma_g - 1)\frac{v_A}{c_s}\right]\left(1 \mp \frac{v_A}{2c_s}\right) \\ & \pm \frac{\mathcal{A}}{\rho c_s}\left(1 \pm (\gamma_g - 1)\frac{v_A}{2c_s}\right)\frac{\partial P_c}{\partial x} \\ & + \mathcal{A}\frac{(\gamma_g - 1)}{c_s^2}\left(\frac{\partial \mathcal{L}}{\partial \rho} + (\gamma_g - 1)\frac{T}{\rho}\frac{\partial \mathcal{L}}{\partial T}\right), \end{aligned} \tag{A.19}$$

where $c_c = \sqrt{\gamma_c P_c / \rho}$. This equation governs the evolution of the wave action density as it propagates through a background. The LHS describes the adiabatic change due to a varying background whereas the RHS describes growth/damping due to instabilities. Without loss of generality, we group the prefactors of $\mathcal{A}$ on the RHS into a term $\mathcal{G}(x)$ such that

$$\frac{\partial \mathcal{A}}{\partial t} + \frac{\partial}{\partial x}[(v \pm c_s)\mathcal{A}] = \mathcal{G}(x)\mathcal{A}. \tag{A.20}$$

Growth occurs when $\mathcal{G} > 0$ while damping occurs otherwise. For purpose of linear analysis assume the velocity perturbation has a form

$$v_0(x,t) = \hat{v}(x)\exp\{i\omega t - ikx\} \tag{A.21}$$

and the background gradients can be neglected over some region x_{inj} to x such that ω, k can be considered constants, it can be easily shown that

$$\frac{\partial}{\partial x} \ln \rho \hat{v}^2 = \pm \frac{\mathcal{G}}{c_s}. \tag{A.22}$$

Solving gives

$$\hat{v}(x) = \hat{v}(x_{\mathrm{inj}}) \exp\left\{ \frac{1}{2} \ln \frac{\rho_{\mathrm{inj}}}{\rho} + \frac{1}{2} \mathcal{I}(x, x_{\mathrm{inj}}) \right\}, \tag{A.23}$$

where $\mathcal{I}(x, x_{\mathrm{inj}})$, given by

$$\mathcal{I}(x, x_{\mathrm{inj}}) = \int_{x_{\mathrm{inj}}}^{x} \pm \frac{\mathcal{G}}{c_s} \, \mathrm{d}x \, , \tag{A.24}$$

is the integral of the RHS of A.22 from the location where the wave is injected $x_{\mathrm{x,inj}}$ to some location x later in its path. The first term within the brace bracket of A.23 denotes the adiabatic change in wave amplitude due to background profile change while the second term represent that due to genuine growth. The phase velocity of a sound wave is $\mathrm{d}x/\mathrm{d}t = \pm c_s$, so $\mathcal{I}$ in A.24 is equivalent to integrating the function $\mathcal{G}$ over time from the moment of injection to some later time t

$$\mathcal{I}(x, x_{\mathrm{inj}}) = \int_{t_{\mathrm{inj}}}^{t} \mathcal{G} \, \mathrm{d}t' \, . \tag{A.25}$$

Differentiating the expression within the brace bracket by time t we obtain an expression for the growth rate Γ_{grow}

$$\Gamma_{\mathrm{grow}} = \frac{\mathcal{G}}{2}. \tag{A.26}$$

A.1.2 Adiabatic EOS with a Small Diffusion Coefficient

If the diffusion coefficient κ were small such that the term $k^2\kappa P_{c0}$ is of the same order as the other perturbed terms in the CR energy equation, equation A.12 may not be valid. This implies $P_{c0} \neq 0$. Including this term at order ϵ^{-1} yields

$$\bar{\omega}\rho_0 = k\rho v_0, \tag{A.27}$$

$$\bar{\omega}\rho v_0 = kP_{g0} + kP_{c0}, \tag{A.28}$$

$$\bar{\omega}P_{g0} = k\gamma_g P_g v_0 + (\gamma_g - 1)kv_A P_{c0}, \tag{A.29}$$

$$\left(\bar{\omega} - kv_A - ik^2\kappa\right)P_{c0} = k\gamma_c P_c\left(v_0 - \frac{v_A}{2\rho}\rho_0\right). \tag{A.30}$$

Rearranging, we obtain

$$\begin{aligned}\bar{\omega}\left(\bar{\omega}^2 - k^2c_s^2\right)\left(\omega - kv_A - ik^2\kappa\right) =\\ k^2c_c^2[\bar{\omega} + (\gamma_g - 1)kv_A]\left(\bar{\omega} - \frac{kv_A}{2}\right)\end{aligned} \tag{A.31}$$

as the dispersion equation. In the limit where $k\kappa/c_s \to \infty$ we recover the gas acoustic mode $\omega \approx \pm kc_s$, though at moderate values of $k\kappa/c_s$ the gas acoustic mode is clearly not a solution. This equation has been solved in various limits in Begelman and Zweibel [5]. In particular, in the limit $v_A \gg c_c \gg c_s$, an unstable hybrid mode with phase speed intermediate between the gas sound speed and the Alfven speed appears

$$\bar{\omega}^3 = \frac{(\gamma_g - 1)k^3v_A^2c_c^2}{2}\frac{v_A - ik\kappa}{v_A^2 + k^2\kappa^2}. \tag{A.32}$$

For $k\kappa \ll v_A$

$$\bar{\omega} = \left[\frac{(\gamma_g - 1)k^3 v_A c_c^2}{2}\right]^{1/3} \left(-\frac{1}{2} - \frac{\sqrt{3}}{2}i\right), \tag{A.33}$$

while for $k\kappa \gg v_A$

$$\bar{\omega} = \left[\frac{(\gamma_g - 1)k^2 v_A^2 c_c^2}{2\kappa}\right]^{1/3} \left(\pm\frac{\sqrt{3}}{2} - \frac{1}{2}i\right). \tag{A.34}$$

These modes are mediated by gas pressure perturbations, but are driven unstable by CR heating. The growth rate scales as the wavenumber so higher resolution simulations can potentially seed faster growth. The transition from the acoustic mode to these hybrid modes occurs at $k\kappa/c_s \sim 1$.

Solving equation A.31 numerically, one finds that the growth rate for $k\kappa/c_s \lesssim 1$ increases with wavenumber (equation A.33) and then flattens off with respect to wavenumber for $k\kappa/c_s \gtrsim 1$ (as one would expect from looking at the RHS of equation A.19, which is independent of k). As discussed in §4.2, for converged simulations, the diffusion length must be resolved. This implies that in the simulations, our fastest growing modes are always in the limit $k\kappa/c_s \gtrsim 1$, and hence we are dominated by acoustic modes.

A.1.3 Isothermal EOS with Finite Diffusion Coefficient

For isothermal EOS, equation A.9 is ignored. The gas pressure relates to the density by

$$P_g = c_s^2 \rho,$$

with the sound speed c_s a constant. Repeating the calculation above gives

$$\bar{\omega} = \pm k c_s \tag{A.35}$$

as the dispersion relation and

$$\frac{\partial \mathcal{A}}{\partial t} + \frac{\partial}{\partial x}[(v \pm c_s)\mathcal{A}] = \pm \frac{\mathcal{A}}{\rho c_s}\frac{\partial P_c}{\partial x} - \frac{c_c^2}{\kappa}\mathcal{A}\left(1 \mp \frac{v_A}{2c_s}\right) \tag{A.36}$$

as the wave action equation, which is simply equation A.19 with $\gamma_g = 1$ and without the heating/cooling terms. Condition for genuine growth is again

$$\Gamma(x) = \pm \frac{1}{\rho c_s}\frac{\partial P_c}{\partial x} - \frac{c_c^2}{\kappa}\left(1 \mp \frac{v_A}{2c_s}\right) > 0. \tag{A.37}$$

A.2 Resolution and Reduced Speed of Light Study

Acoustic waves with wavelengths much shorter than the diffusion length $l_{\rm diff} = \kappa/c_s$ grow in the linear phase at a rate independent of the wavelength, as discussed in §3.2.1 and §A.1. If the diffusion length is well resolved, the characteristic staircase scales should $\sim l_{\text{diff}}$ (see §3.3.3.6). As the resolution decreases, so that the diffusion length is no longer resolved, the wavelength of the growing modes will also increase. In particular, for $kl_{\text{diff}} \lesssim 1$, the acoustic mode will bifurcate into hybrid modes which propagate at some modified sound speed, with growth rate that decreases linearly with the wavenumber k (see §A.1.2). Thus, decreasing resolution will 1. cause slower growth of the staircase and 2. smooth out small scale stairs and render stair sizes larger.

In this section we rerun the test case `NLalpha1beta1eta.01phi2` (table 3.2) with several resolutions and reduced speed of light c, comparing their time averaged mass flux $\langle \dot{M} \rangle$, $\langle \Delta P_c \rangle$ and $\langle \Delta F_c \rangle$. We shall also discuss the effect of resolution on the distributions of stair width, plateau width and jump height. A summary of the resolution, reduced speed of light and time averaged quantities is drawn up in table A.1.

In fig.A.1 we plot $\langle \dot{M} \rangle / \dot{M}_0$, $\langle \Delta P_c \rangle / \Delta P_{c0}$ and $\langle \Delta F_c \rangle / \Delta F_{c0}$ as function of $\langle l_{\text{diff}} \rangle / \Delta x$, the number of grids the mean diffusion length is resolved with. Overall, despite small fluctuations at large $\langle l_{\text{diff}} \rangle / \Delta x$, the time averaged quantities appear reasonably robust to resolution. Although there are secular trends with resolution, the changes are small. Deviations appear when the mean diffusion length is under-resolved, i.e. $\langle l_{\text{diff}} \rangle / \Delta x < 1$, yet even in the lowest resolution explored (i.e. $\langle l_{\text{diff}} \rangle / \Delta x = 0.0588$), a staircase structure can be clearly seen (fig.A.2). Generally, effects of the staircase on $\langle \dot{M} \rangle / \dot{M}_0, \langle \Delta P_c \rangle, \langle \Delta F_c \rangle$ dwindle with resolution in the under-resolved regime, yet even in the lowest resolution explored the time-averaged quantities deviate from the

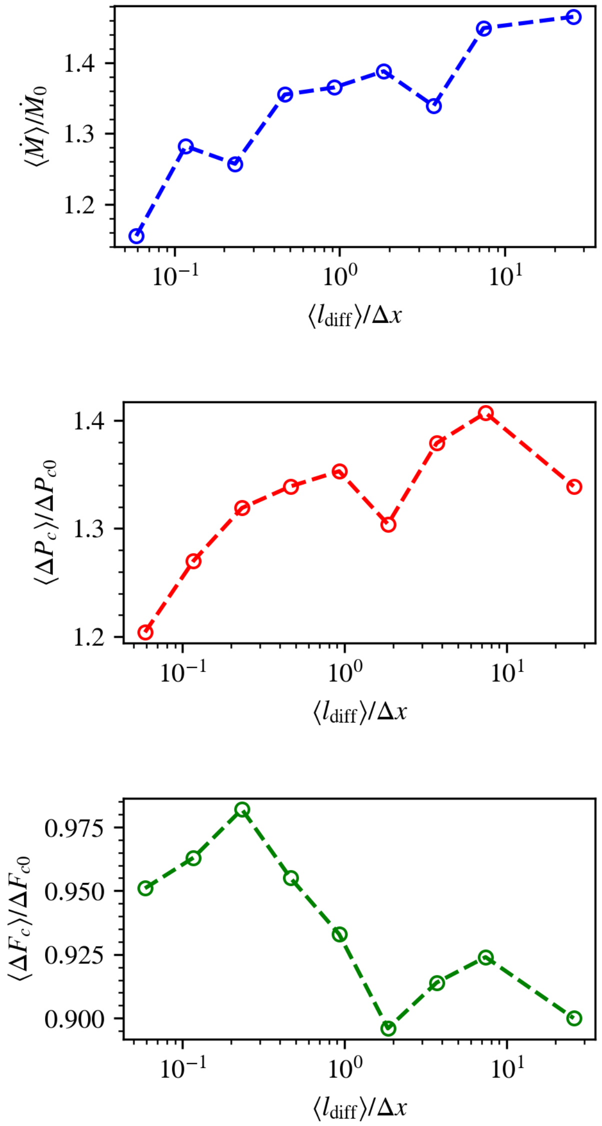

FIGURE A.1: Time average quantities ($\langle \dot{M} \rangle / \dot{M}_0$, $\langle \Delta P_c \rangle / \Delta P_{c0}$, $\langle \Delta F_c \rangle / \Delta F_{c0}$) as function of resolution. Resolution given in the x-axis denotes the number of grids the mean diffusion length is resolved with ($\langle l_{\rm diff} \rangle / \Delta x$), the larger this is the higher the resolution.

Test case: `NL4096alpha1beta1eta.01ms.015phi2c200`

Resolution Δx ($\langle l_{\text{diff}}\rangle/\Delta x$)	c	$\langle \dot{M}\rangle/\dot{M}_0$	$\langle \Delta P_c\rangle/\Delta P_{c0}$	$\langle \Delta F_c\rangle/\Delta F_{c0}$
7.03×10^{-2} (0.0588)	200	1.155	1.204	0.951
3.52×10^{-2} (0.1168)	200	1.282	1.270	0.963
1.76×10^{-2} (0.233)	200	1.257	1.319	0.982
8.79×10^{-3} (0.465)	200	1.355	1.339	0.955
4.39×10^{-3} (0.926)	200	1.365	1.353	0.933
2.20×10^{-3} (1.85)	200	1.384	1.309	0.907
2.20×10^{-3} (1.85)	400	1.382	1.321	0.890
2.20×10^{-3} (1.85)	800	1.375	1.313	0.883
2.20×10^{-3} (1.85)	1000	1.446	1.310	0.868
1.10×10^{-3} (3.70)	200	1.339	1.379	0.914
5.49×10^{-4} (7.41)	200	1.449	1.407	0.924
5.49×10^{-4} (7.41)	400	1.408	1.395	0.918
1.37×10^{-4} (25.9)	400	1.465	1.339	0.900

Table A.1: Re-running with different resolutions and reduced speed of light. Column 1: Resolution given in grid spacing with (the bracketed quantities show the number of grids the mean diffusion length is resolved with, i.e. $\langle l_{\text{diff}}\rangle/\Delta x$). Column 2: Reduced speed of light. Column 3-5: Time averaged mass flux $\dot{M}$, ΔP_c and ΔF_c (in units of the initial, unperturbed $\dot{M}_0$, ΔP_{c0} and $\Delta F_{c,0}$).

resolved runs by less than 20%. This suggests effects on the time averaged quantities is due mainly to the bigger stairs, with minor modifications from the small stairs.

Visually inspecting fig.A.2, which shows the P_c profile taken at the same time for the lowest and highest resolutions explored, it is observed that more small scale structures arise when the resolution is high. Only the largest jumps are resolvable at low resolution, details of the small scale jumps smoothed out.

In fig.A.3 we plot the distributions of stair width, plateau width and jump height for the highest and lowest resolutions explored, finding there to be more small scale structures (smaller widths and heights) for the more resolved run while the low resolution run have more large scale structures (larger widths and heights). In particular, the peak at $\sim l_{\text{diff}}$ for the jump width is recovered only if the diffusion length is resolved.

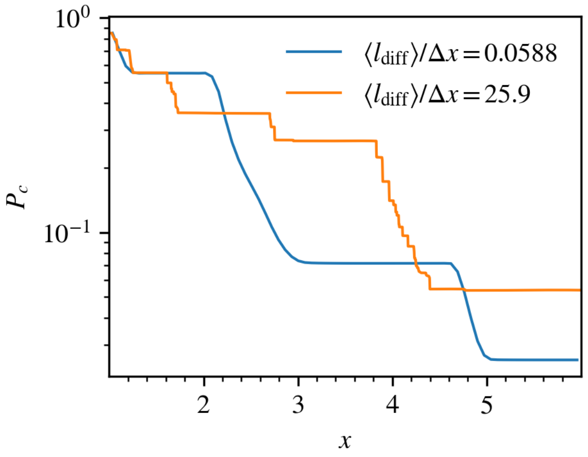

Figure A.2: P_c profile taken at the same time instance for a low ($\langle l_{\rm diff}\rangle/\Delta x = 0.0588$) and high resolution run ($\langle l_{\rm diff}\rangle/\Delta x = 25.9$). Many more small jumps are resolved in the high resolution run. The P_c profile is a stochastic, time-varying quantity, and this is an instantaneous snapshot. The difference in the time-averaged quantity between these two resolutions ($\langle P_c\rangle/\Delta P_{c0} = 1.204, 1.339$ respectively) is small (Table A.1), despite the factor ~ 400 change in resolution.

This lies within expectation as under-resolving the diffusion length would cause small scale jumps (typically having size of the diffusion length) to be smoothed out into a bigger jump.

All in all, in practice (e.g. in galaxy scale simulations), for the purpose of eliciting the staircase and its time averaged effects, it appears acceptable to resolve the diffusion length by a few cells. However, should effects of individual stairs be important (e.g. cloud survival under bombardment of a few of these stairs), higher resolution is probably necessary.

On that note, it is tempting to raise the resolution in attempt to reveal more small-scale phenomenon. Yet in the fluid approximation, one must beware not to go below the CR mean free path, given by $\sim \kappa/c$, where it breaks down. In CGM conditions the

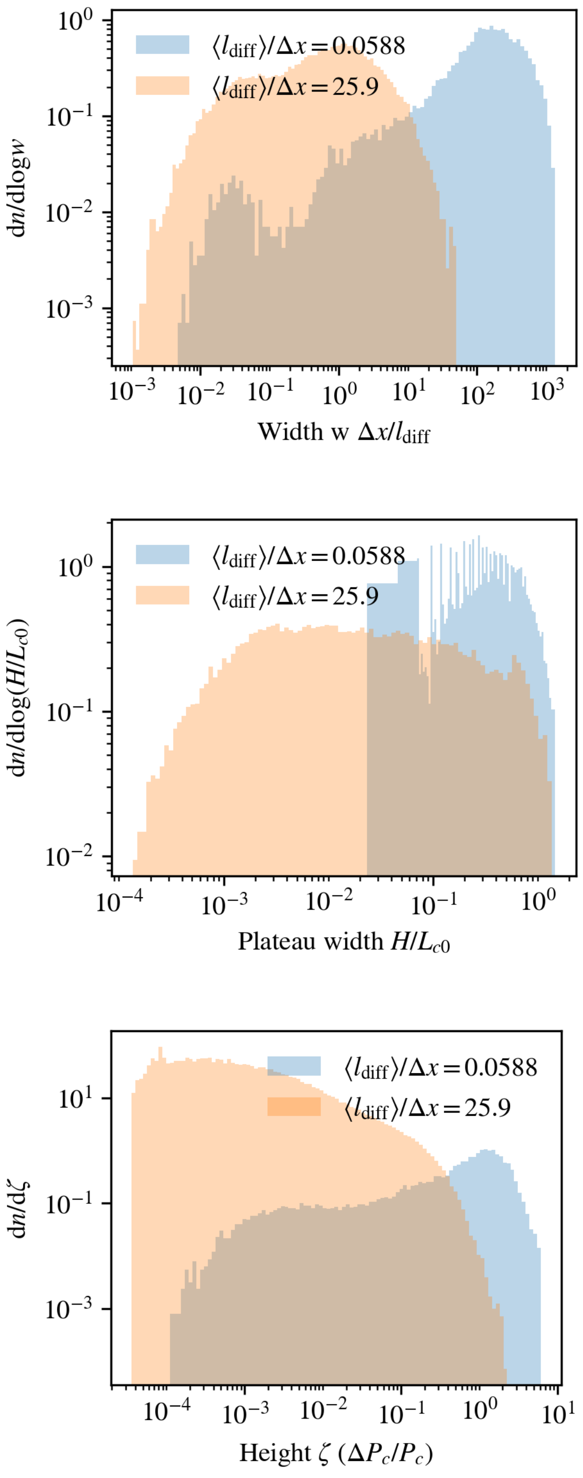

FIGURE A.3: Distributions of jump width (top), plateau width (middle) and jump height (bottom) for low ($\langle l_{\rm diff}\rangle/\Delta x = 0.0588$) and high resolutions ($\langle l_{\rm diff}\rangle/\Delta x = 25.9$).

ratio of the diffusion length to the CR mean free path is $\sim c/c_s \sim 3000(c_s/100 \text{ km s}^{-1})$, meaning there is no use resolving the diffusion length by more than a few hundred to a thousand grids. We shall see, particularly in fig.A.3 that with the resolution we employed, structures 0.001 times the local diffusion length do arise. Going to higher resolutions may allow one to resolve some of these structures better, but the physical validity of these smaller structures is questionable given that the fluid approximation no longer holds, so pushing to higher resolution may be unwarranted and unrealistic. Finally, convergence can be set by other physics as well, particularly in higher dimensional simulations, by implementing physical dissipation.

On a shorter note, changing the reduced speed of light c appears to have little effect on our results as long as it is much greater than any other velocity scales present (e.g. c, c_s, c_c, v_A). This is consistent with Jiang and Oh [92]. Numerically, the reduced speed of light c should not affect the simulation much if it is way above any other velocity scales, any effect due to c would be of order $O(v/c)$ or less. In reality, the speed of light $c_{\text{true}} \approx 3000(c_s/100 \text{ km s}^{-1})$. In our simulations we often invoke a reduced speed of light that is a factor $200c_s$, i.e. $\sim 0.1c_{\text{true}}$.

Appendix B

Appendix for chapter 4

B.1 1D Linearized Equations in Uniform Medium

Kempski and Quataert [102] showed that 1D calculations can approximately capture the behavior of CR-modified thermal modes in the linear regime as perturbations perpendicular to the magnetic field is usually small. In the 1D, fully-coupled limit, eqn.4.1-4.6 reduces to

$$\frac{\partial\rho}{\partial t}+v\frac{\partial\rho}{\partial x}+\rho\frac{\partial v}{\partial x}=0, \tag{B.1}$$

$$\frac{\partial v}{\partial t}+v\frac{\partial v}{\partial x}=-\frac{1}{\rho}\frac{\partial P_g}{\partial x}-\frac{1}{\rho}\frac{\partial P_c}{\partial x}-g, \tag{B.2}$$

$$\frac{\partial P_g}{\partial t}+v\frac{\partial P_g}{\partial x}+\gamma_g P_g\frac{\partial v}{\partial x}=-(\gamma_g-1)v_s\frac{\partial P_c}{\partial x}+(\gamma_g-1)\mathcal{L}, \tag{B.3}$$

$$\frac{\partial P_c}{\partial t}(\gamma_c-1)\frac{\partial F_c}{\partial x}=(\gamma_c-1)(v+v_s)\frac{\partial P_c}{\partial x}+(\gamma_c-1)\mathcal{Q}, \tag{B.4}$$

$$F_c=\frac{\gamma_c}{\gamma_c-1}P_c(v+v_s)-\frac{\kappa_\parallel}{\gamma_c-1}\frac{\partial P_c}{\partial x}, \tag{B.5}$$

where we have used the fact that the magnetic field **B** is constant in 1D. The streaming velocity $v_s=-v_A\mathrm{sgn}(\partial P_c/\partial x)$. Ignoring contributions from CR sources $\mathcal{Q}$ and assuming the background is nearly uniform such that we can ignore derivatives of the background but CRs remain coupled to gas, the linearized equations are

$$-\frac{\omega}{\omega_s}\frac{\delta\rho}{\rho}+\frac{\delta v}{c_s}=0, \tag{B.6}$$

$$-\frac{\omega}{\omega_s}\frac{\delta v}{c_s}+\frac{1}{\gamma_g}\frac{\delta P_g}{P_g}+\frac{1}{\gamma_g}\frac{\delta P_c}{P_g}=0, \tag{B.7}$$

$$\begin{aligned}\left[-i(\gamma_g-1)\frac{\omega_c}{\omega_s}\Lambda_T-\frac{\omega}{\omega_s}\right]\frac{\delta P_g}{P_g}-i(\gamma_g-1)\frac{\omega_c}{\omega_s}(2-\Lambda_T)\frac{\delta\rho}{\rho}&\\+\gamma_g\frac{\delta v}{c_s}+(\gamma_g-1)\frac{\omega_A}{\omega_s}\frac{\delta P_c}{P_g}=0,&\end{aligned} \tag{B.8}$$

$$\gamma_c\alpha\frac{\delta v}{c_s}-\frac{\gamma_c\alpha\omega_A}{2\omega_s}\frac{\delta\rho}{\rho}+\left(\frac{\omega_A}{\omega_s}-i\frac{\omega_d}{\omega_s}-\frac{\omega}{\omega_s}\right)\frac{\delta P_c}{P_g}=0, \tag{B.9}$$

where $c_s=\sqrt{\gamma_g P_g/\rho}$ is the adiabatic sound speed, $\omega_s=kc_s$, $\omega_A=kv_A$, $\omega_d=k^2\kappa_\parallel$, $\omega_c=\rho^2\Lambda/P_g$, $\alpha=P_c/P_g$ and we have assumed the background flow is static.

Substituting δv in eqn.B.6 into eqn.B.7-B.9, the equations simplify to

$$\frac{\delta P_g}{P_g} + \frac{\delta P_c}{P_c} = \gamma_g \left(\frac{\omega}{\omega_s} \right)^2 \frac{\delta \rho}{\rho}, \tag{B.10}$$

$$\begin{aligned} i\omega \left(\gamma_g \frac{\delta \rho}{\rho} - \frac{\delta P_g}{P_g} \right) &= -(\gamma_g - 1)\omega_c \left[(2 - \Lambda_T) \frac{\delta \rho}{\rho} + \Lambda_T \frac{\delta P_g}{P_g} \right] \\ &\quad -i(\gamma_g - 1)\omega_A \frac{\delta P_c}{P_g}, \end{aligned} \tag{B.11}$$

$$\frac{\delta P_c}{P_g}(\omega - \omega_A + i\omega_d) = \gamma_c \alpha \left(\omega - \frac{\omega_A}{2} \right) \frac{\delta \rho}{\rho}. \tag{B.12}$$

For thermally unstable modes, we expect $\omega \sim \omega_c$. If $\omega_c \gg \omega_s$, i.e. the cooling time is shorter than the sound crossing time, $\delta\rho/\rho \ll \delta P_g/P_g$ from eqn.B.10, i.e. the mode is isochoric. If $\omega_c \ll \omega_s$, the otherwise is true and the mode is pressure balanced.

The ratio of perturbed CR heating to cooling is

$$\frac{\delta(\text{CRHeating})}{\delta(\text{Cooling})} = \frac{i\omega_A(\delta P_c/P_g)}{\omega_c[(2 - \Lambda_T)(\delta\rho/\rho) + \Lambda_T(\delta P_g/P_g)]}. \tag{B.13}$$

Eqn.B.13 reduces to eqn.4.28 in the isochoric and isobaric limits. The ratio $(\delta P_c/P_g)/(\delta\rho/\rho)$ is given directly by eqn.B.12

$$\frac{(\delta P_c/P_g)}{(\delta\rho/\rho)} = \gamma_c \alpha \frac{\omega - \omega_A/2}{\omega - \omega_A + i\omega_d}. \tag{B.14}$$

For $\omega_c \ll \omega_A$ (small scale modes) and $\omega_d \gg \omega_A$, the RHS is purely imaginary, i.e. δP_c is $\pi/2$ out of phase with $\delta\rho$. This phase shift allows CR heating to counteract cooling.

B.2 Hydrostatic Boundary Conditions for Eulerian Grid Codes

We employ hydrostatic boundary conditions in the x-direction, which requires eqn.4.23 to be satisfied at the boundaries. In a grid code, cell-center values are indicated with subscripts i, j, k, all of them integers, representing cells in the x, y, z-directions respectively. Below we will shorten the notation to i to reduce clutter, the relations derived in the following are implied for all j, k. We shall use is and ie to denote the first and last active zones in the x-directions. The cell-center ghost zones are expressed by $is - n$ and $ie + n$, where $n = 1, \ldots, n_g$, n_g is the number of ghost zones (typically 2 for piecewise linear method (PLM)). We want eqn.4.23 to hold at the boundary cell face, for example at the outer-x boundary

$$\left.\frac{\mathrm{d}P_g}{\mathrm{d}x}\right|_{ie+n-1/2} + \left.\frac{\mathrm{d}P_c}{\mathrm{d}x}\right|_{ie+n-1/2} = -\left.\rho\right|_{ie+n-1/2} \left.g\right|_{ie+n-1/2}, \tag{B.15}$$

where the fractional index indicates cell faces. The cell-faced values are approximated linearly as

$$\frac{P_{g,ie+n} - P_{g,ie+n-1}}{\Delta x} + \frac{P_{c,ie+n} - P_{c,ie+n-1}}{\Delta x} = -\frac{1}{2}(\rho_{ie+n} + \rho_{ie+n-1}) g_{ie+n-1/2}, \tag{B.16}$$

we do not need to approximate g because it is a given function. Using the ideal gas law $P_g = \rho T$ and since our initial profiles are isothermal and $P_c \propto \rho^{\gamma_c/2}$ for streaming dominated flows,

$$r - 1 + \alpha\left(r^{\gamma_c/2} - 1\right) = -\xi(r+1), \tag{B.17}$$

where α, ξ, r are defined by

$$\alpha = \frac{P_{c,ie+n-1}}{P_{g,ie+n-1}}, \quad \xi = \frac{\rho_{ie+n-1} g_{ie+n-1/2} \Delta x}{2P_{g,ie+n-1}}, \quad r = \frac{\rho_{ie+n}}{\rho_{ie+n-1}}. \tag{B.18}$$

Rearranging,

$$\alpha r^{\gamma_c/2} + (1+\xi)r - (1+\alpha-\xi) = 0. \tag{B.19}$$

Solving for r (e.g. using a non-linear root finder) gives us the value for ρ_{ie+n} in terms of quantities in the $ie+n-1$ cell-centers, which we can use to determine $P_{g,ie+n}$ and $P_{c,ie+n}$. $F_{c,ie+n}$ can be obtained from the CR equation by imposing time steadiness, i.e.

$$\left.\frac{\mathrm{d}F_c}{\mathrm{d}x}\right|_{\text{bond}} = \left.v_A\right|_{\text{bond}} \left.\frac{\mathrm{d}P_c}{\mathrm{d}x}\right|_{\text{bond}} \tag{B.20}$$

Performing a linear approximation,

$$\begin{aligned} F_{c,ie+n} &= F_{c,ie+n-1} \\ &\quad + \frac{1}{2}(v_{A,ie+n} + v_{A,ie+n-1})(P_{c,ie+n} - P_{c,ie+n-1}). \end{aligned} \tag{B.21}$$

We copy the velocity of the last active zone to the ghost zones if the flow is outbound and set them to zero otherwise.

The same can be performed for the inner-x boundary, an equation similar to B.19 arises,

$$\alpha r^{\gamma_c/2} + (1-\xi)r - (1+\alpha+\xi) = 0, \tag{B.22}$$

where now α, ξ, r are defined by

$$\alpha = \frac{P_{c,is-n+1}}{P_{g,is-n+1}}, \quad \xi = \frac{\rho_{is-n+1} g_{is-n+1/2} \Delta x}{2P_{g,is-n+1}}, \quad r = \frac{\rho_{is-n}}{\rho_{is-n+1}}. \tag{B.23}$$

$F_{c,is-n}$ is given by

$$\begin{split} F_{c,is-n} = F_{c,is-n+1} \\ + \frac{1}{2}(v_{A,is-n} + v_{A,is-n+1})(P_{c,is-n} - P_{c,is-n+1}). \end{split} \tag{B.24}$$

The magnetic field is set to the value of the nearest x-layer. Note that we assume an isothermal background. If this assumption is relaxed, the energy eqn.4.3 will have to be invoked.

In §4.4 we see that the nonlinear evolution of thermal instability with CR heating can lead to winds, bringing the system out of hydrostatic equilibrium. Using the fast wind case as an example, in fig.B.1 we show that there is no significant difference when one

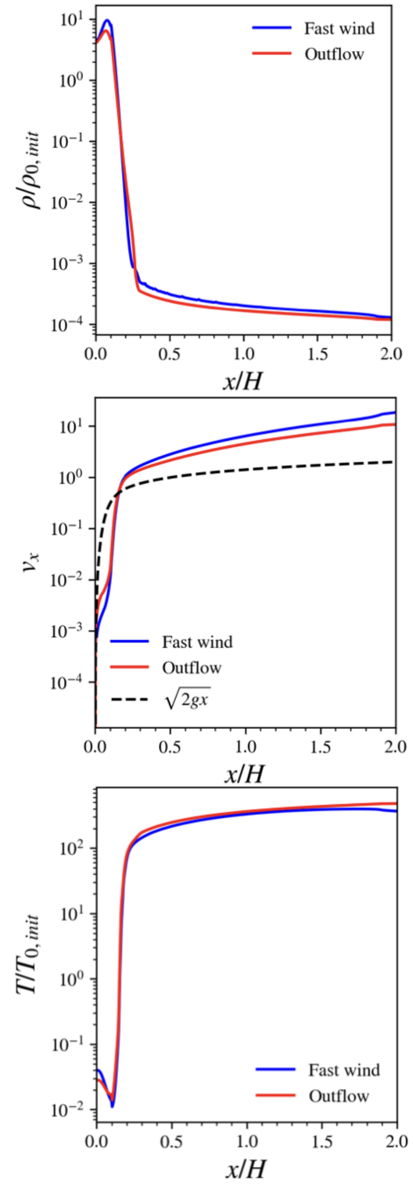

FIGURE B.1: Comparison of the fast wind case using different boundary conditions: hydrostatic (blue) and outflowing (red), as described in the text, showing no significant difference is found.

uses an outflow type condition along the x-boundaries. We copy the density and gas pressure of the last active zone to the ghost zones and adopted a diode condition for the x-velocity (i.e. the x-velocity of the last active zone is copied to the ghost zone if the gas is outflowing, and zero otherwise). The y-velocity at the last active zone is copied to the ghost zones. As for the CR pressure and x-flux, we set the ghost zone values to be 0.99 times the value at the previous cell. We note that simply copying the CR pressure and x-flux at the last active zone to the ghost zones would lead to unphysical confinement of CRs as there would be no CR gradient to transport the CRs out. The CR y-flux at the last active zone is copied to the ghost zones.

B.3 Simulations fixing the base CR flux instead of pressure

As discussed in §4.4, the nonlinear outcome of TI depends heavily on the CR heating time $t_{\rm heat}$ at the halo, which depends on the halo gas, CR pressure and Alfven speed. In our simulations, we control these quantities through specifying α_0, which sets the CR pressure at the base, β_0, which sets the magnetic field, and η_H, which sets the CR diffusion coefficient and therefore how much of the base CRs will leak into the halo. Moreover, these quantities evolve as mass dropout proceeds in the halo, and the gas pressure P_g and Alfven speed evolve. Nonetheless, it is important to understand the sensitivity of our results to boundary conditions at the disk. Instead of specifying α_0, which sets P_c at the base, we could alternatively specify F_{c0}, the base CR flux.

The combination of F_{c0}, β_0, η_H will self-consistently determine what the base P_c will be, and is therefore just a different way of specifying $\alpha_0, \beta_0, \eta_H$. The advantage of setting $\alpha_0, \beta_0, \eta_H$ instead of F_{c0}, β_0, η_H is that the former involves only dimensionless parameters whereas the latter requires physical units[1]. As we shall demonstrate, our conclusions remain unchanged whether you choose to fix F_{c0} or α_0. For example, increasing F_{c0} for a fixed CR transport model will result in greater presence of CRs in the halo, and is equivalent to increasing α_0.

What value of F_{c0} should we set? Let's assume, in galaxies, all of the CRs are generated from supernovae. Each supernova releases about 10^{51} ergs of energy, for which around 10% goes into accelerating CRs [24]. Supernovae occur around once per 100 years, so if we assume all of the CRs produced eventually make it out of the disk, the rate of CRs released into the halo, would on averaged be $\dot{E}_c \sim 10^{51}$ ergs $* 0.1/(100$ yr$) \sim 3 \times 10^{40}$ ergs s^{-1}. Assuming CRs escape mostly perpendicular to the disk, we can relate the CR flux F_c with $\dot{E}_c$ through $F_c A \approx \dot{E}_c$, where A is the galactic disk face area. For a disk with radius 10 kpc, the CR flux would then be $F_c \sim 10^{-5}$ ergs s^{-1} cm^{-2}. Let's convert this to code units. In our simulations we set g_0, T_0, ρ_0 all to unity (see §4.2.2.1). If these variables scale, in real units as $g_0 = 10^{-8}$ cm s^{-2}, $T_0 = 10^6$ K and $\rho_0 = 10^{-26}$ g cm^{-3}, as typically in galactic environments, then the scale-height $H = k_B T_0 / m_u g_0 = 2.7$ kpc, pressure $P_0 = \rho_0 k_B T_0 / m_u = 8.3 \times 10^{-13}$ erg cm^{-3}, velocity $v_0 = (k_B T_0 / m_u) = 1 = 91$ km s^{-1}, and the CR flux $F_{c0} = P_0 v_0 = 1 = 7.5 \times 10^{-6}$ ergs cm^{-2} s^{-1}. In code units, the CR flux

---

[1] One could specify a parameter like $P_{\mathrm{c},0}/(P_{\mathrm{g},0} v_{\mathrm{esc}})$, but this is similar to our definition of α_0.

$F_c \sim 10^{-5}$ ergs s^{-1} cm^{-2} would then be ~ 1.3. In reality galaxies could, depending on e.g. the star formation rate, size and structure, be supplying CRs at different rates, thus we also explore different values of F_{c0}.

In fig.B.2 we display the nonlinear outcome of TI for various combinations of F_{c0}, β_0, η_H. Once again we observe the three outcomes discussed in §4.4: slow wind, fast wind and fountain flows. The fast wind is again marked by a single phase, rarefied halo (e.g. middle and right panels of the second row) while fountain flows are marked by filamentary cold flows (e.g. right panel of the third row and the middle and right panels of the bottom row). By varying F_{c0}, we can observe the transition into different outcomes clearly. For example, from a slow wind to a fast wind in the second row and into a fountain flow in the third and bottom row. All these are the result of greater supply of CRs to the halo, which increases both CR pressure support and heating.

In fig.B.3 we again plot the outflow velocity v_x against $t_{\rm heat}/t_{\rm ff}$ (taken at a scale height), recovering the same trend as in fig.4.16 that the flow transitions to a fast wind when $t_{\rm heat} \ll t_{\rm ff}$. In short, there is no fundamental difference whether one fixes F_{c0} or α_0 at the base. All that matters is $t_{\rm heat}$ in the halo.

B.4 Resolution and 3D

We rerun the 'slow wind', 'fast wind' and 'fountain flow' cases in §4.4 with higher resolution and in 3D to check that our results hold. For increased resolution, we

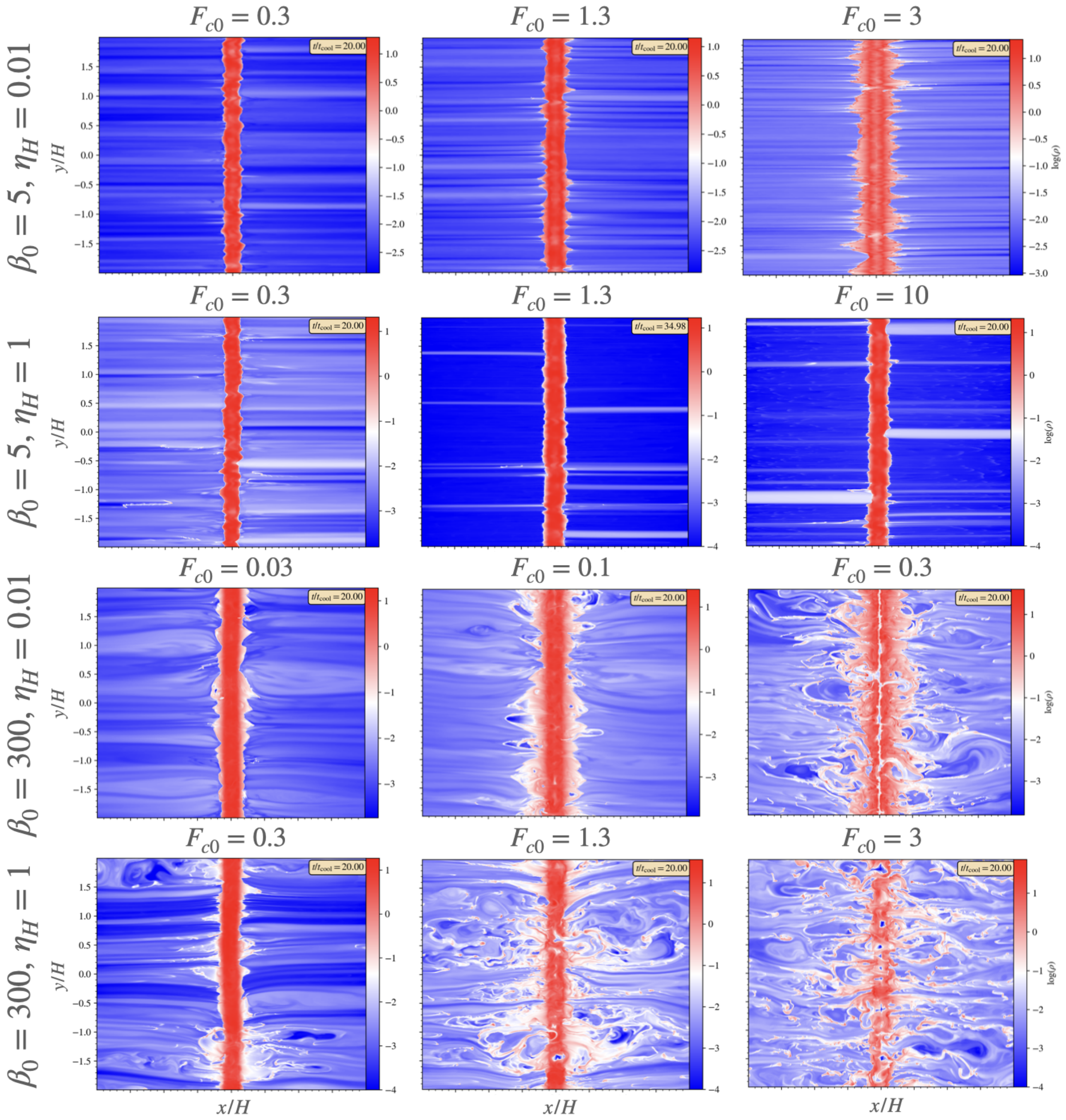

FIGURE B.2: Density slice plots at $t = 20t_{\rm cool}$ for a variety of test cases fixing the base CR flux F_{c0}. F_{c0} is given in code-units, but conversion to real units for scenario specific flows can be found in Appendix B.3. The nonlinear outcomes of TI are explored for varying F_{c0}, β_0, η_H. Specifically, the first row displays flows that are low in β and streaming dominated, the second row for low β and higher diffusivity. The third and forth row are replica of the first and second row at higher β.

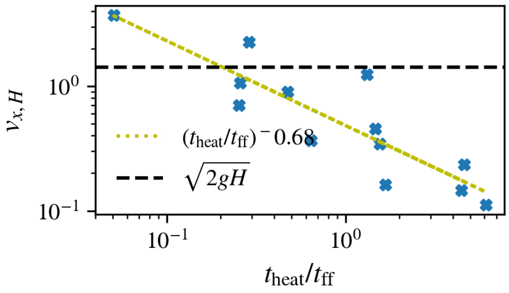

FIGURE B.3: v_x against $t_{\rm heat}/t_{\rm ff}$ at a scaleheight for the cases shown in fig.B.2, which the base CR flux is fixed instead of CR pressure.

resolve the simulation domain ($-2H < x < 2H$) by 2048×512 grids (doubling the x-resolution) whereas for 3D simulations, the grid resolution is reduced to $256 \times 128 \times 128$ (again higher resolution along the x-axis) to save computational time. Further details regarding the setup are listed in table 4.1. As shown in fig.B.4, the fluid properties of the higher resolution and 3D runs are all in line with the trends given by simulations with fiducial resolution. Our conclusions remain unchanged. While there is some scatter as resolution and dimensionality change, the scatter lies along the trends we have already found. In fig.B.5 we compare the time averaged projection plots of the density, velocity and temperature for all three solution outcomes. The fiducial and the high resolution 2D profiles are very similar. The 3D profiles also give very similar outcomes. The time-averaged profiles do deviate somewhat more: for instance, up to a factor of ~ 2 in asymptotic temperatures or densities, though at least part of this is due to the much lower resolution in our 3D sims.

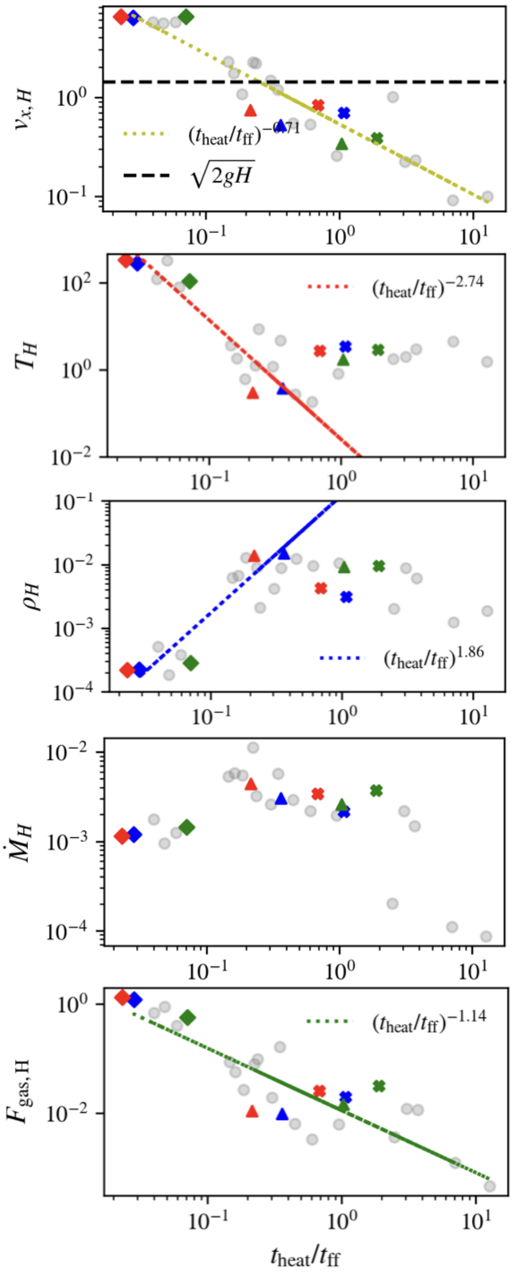

FIGURE B.4: Same as fig.4.16 including cases 2D standard resolution (blue) with 2D higher resolution (red) and lower-resolution 3D (green markings). The markers indicate ‘slow wind’ (crosses) ‘fast wind’ (diamond) and ‘fountain flow’ (triangular) profile parameters respectively. Test cases with flow parameters other than the three mentioned are indicated by grey circles and are shown for reference.

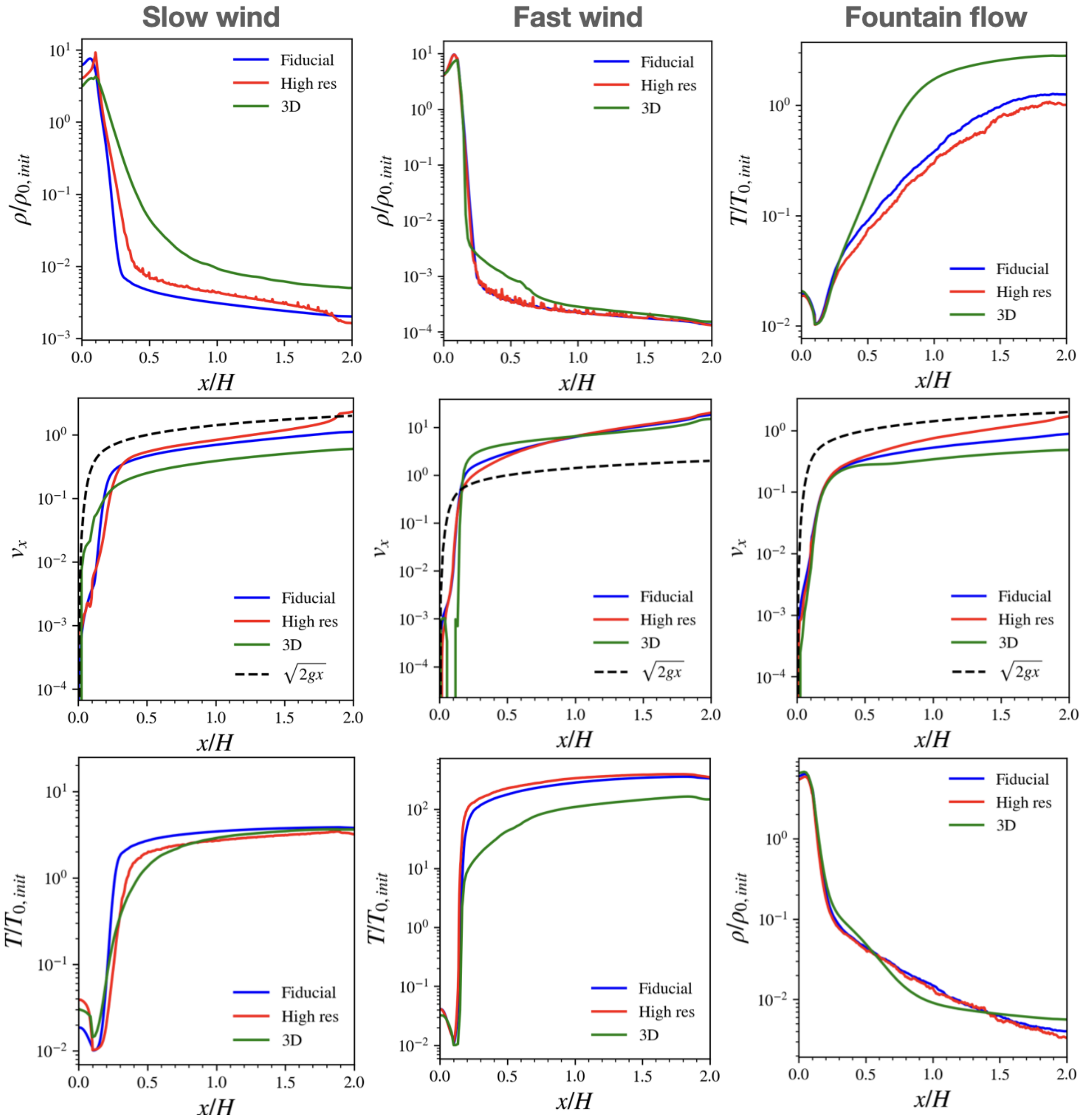

FIGURE B.5: Time averaged projection plots of the density, velocity and temperature for the 'slow wind', 'fast wind' and 'fountain flow' cases. In each case, the fiducial profile (blue) is compared against the higher resolution profile (red) and the 3D profile (green).

Bibliography

[1] A. Achterberg, R. Blandford, and V. Periwal. Two-fluid models of cosmic ray shock acceleration. *AAP*, 132(1):97–104, March 1984.

[2] W. I. Axford, E. Leer, and G. Skadron. The Acceleration of Cosmic Rays by Shock Waves. In *International Cosmic Ray Conference*, volume 11 of *International Cosmic Ray Conference*, page 132, January 1977.

[3] Jean Ballet. X-ray synchrotron emission from supernova remnants. *Advances in Space Research*, 37(10):1902–1908, January 2006. doi: 10.1016/j.asr.2005.03.047.

[4] Peter A. Becker and Demosthenes Kazanas. Exact Expressions for the Critical Mach Numbers in the Two-Fluid Model of Cosmic-Ray-modified Shocks. *ApJ*, 546(1):429–446, January 2001. doi: 10.1086/318257.

[5] Mitchell C. Begelman and Ellen G. Zweibel. Acoustic Instability Driven by Cosmic-Ray Streaming. *ApJ*, 431:689, August 1994. doi: 10.1086/174519.

[6] Mitchell C. Begelman and Ellen G. Zweibel. Acoustic Instability Driven by Cosmic-Ray Streaming. *ApJ*, 431:689, August 1994. doi: 10.1086/174519.

[7] A. R. Bell. The acceleration of cosmic rays in shock fronts - I. *MNRAS*, 182: 147–156, January 1978. doi: 10.1093/mnras/182.2.147.

[8] A. R. Bell. Turbulent amplification of magnetic field and diffusive shock acceleration of cosmic rays. *MNRAS*, 353(2):550–558, September 2004. doi: 10.1111/j.1365-2966.2004.08097.x.

[9] Robert A. Benjamin and Laura Danly. High-Velocity Rain: The Terminal Velocity Model of Galactic Infall. *ApJ*, 481(2):764–774, May 1997. doi: 10.1086/304078.

[10] R. D. Blandford and J. P. Ostriker. Particle acceleration by astrophysical shocks. *ApJL*, 221:L29–L32, April 1978. doi: 10.1086/182658.

[11] Roger Blandford and David Eichler. Particle acceleration at astrophysical shocks: A theory of cosmic ray origin. *Phys. Rep.*, 154(1):1–75, October 1987. doi: 10.1016/0370-1573(87)90134-7.

[12] C. M. Booth, Oscar Agertz, Andrey V. Kravtsov, and Nickolay Y. Gnedin. Simulations of Disk Galaxies with Cosmic Ray Driven Galactic Winds. *ApJL*, 777(1):L16, November 2013. doi: 10.1088/2041-8205/777/1/L16.

[13] C. M. Booth, Oscar Agertz, Andrey V. Kravtsov, and Nickolay Y. Gnedin. Simulations of Disk Galaxies with Cosmic Ray Driven Galactic Winds. *ApJL*, 777(1):L16, November 2013. doi: 10.1088/2041-8205/777/1/L16.

[14] A. Botteon, G. Brunetti, D. Ryu, and S. Roh. Shock acceleration efficiency in radio relics. *AAP*, 634:A64, February 2020. doi: 10.1051/0004-6361/201936216.

[15] D. Breitschwerdt, J. F. McKenzie, and H. J. Voelk. Galactic winds. I. Cosmic ray and wave-driven winds from the galaxy. *AAP*, 245:79, May 1991.

[16] Marcus Brüggen and Evan Scannapieco. The Launching of Cold Clouds by Galaxy Outflows. IV. Cosmic-Ray-driven Acceleration. *ApJ*, 905(1):19, December 2020. doi: 10.3847/1538-4357/abc00f.

[17] Tobias Buck, Christoph Pfrommer, Rüdiger Pakmor, Robert J. J. Grand, and Volker Springel. The effects of cosmic rays on the formation of Milky Way-mass galaxies in a cosmological context. *MNRAS*, 497(2):1712–1737, September 2020. doi: 10.1093/mnras/staa1960.

[18] Tobias Buck, Christoph Pfrommer, Rüdiger Pakmor, Robert J. J. Grand, and Volker Springel. The effects of cosmic rays on the formation of Milky Way-mass galaxies in a cosmological context. *MNRAS*, 497(2):1712–1737, September 2020. doi: 10.1093/mnras/staa1960.

[19] Chad Bustard and Ellen G. Zweibel. Cosmic Ray Transport, Energy Loss, and Influence in the Multiphase Interstellar Medium. *arXiv e-prints*, art. arXiv:2012.06585, December 2020.

[20] Chad Bustard and Ellen G. Zweibel. Cosmic-Ray Transport, Energy Loss, and Influence in the Multiphase Interstellar Medium. *ApJ*, 913(2):106, June 2021. doi: 10.3847/1538-4357/abf64c.

[21] Chad Bustard, Ellen G. Zweibel, and Cory Cotter. Cosmic Ray Acceleration by a Versatile Family of Galactic Wind Termination Shocks. *ApJ*, 835(1):72, January 2017. doi: 10.3847/1538-4357/835/1/72.

[22] Iryna S. Butsky, Drummond B. Fielding, Christopher C. Hayward, Cameron B. Hummels, Thomas R. Quinn, and Jessica K. Werk. The Impact of Cosmic Rays on Thermal Instability in the Circumgalactic Medium. *ApJ*, 903(2):77, November 2020. doi: 10.3847/1538-4357/abbad2.

[23] Iryna S. Butsky, Drummond B. Fielding, Christopher C. Hayward, Cameron B. Hummels, Thomas R. Quinn, and Jessica K. Werk. The Impact of Cosmic Rays on Thermal Instability in the Circumgalactic Medium. *ApJ*, 903(2):77, November 2020. doi: 10.3847/1538-4357/abbad2.

[24] D. Caprioli and A. Spitkovsky. Simulations of Ion Acceleration at Non-relativistic Shocks. I. Acceleration Efficiency. *ApJ*, 783(2):91, March 2014. doi: 10.1088/0004-637X/783/2/91.

[25] D. Caprioli and A. Spitkovsky. Simulations of Ion Acceleration at Non-relativistic Shocks. I. Acceleration Efficiency. *ApJ*, 783(2):91, March 2014. doi: 10.1088/0004-637X/783/2/91.

[26] D. Caprioli and A. Spitkovsky. Simulations of Ion Acceleration at Non-relativistic Shocks. II. Magnetic Field Amplification. *ApJ*, 794(1):46, October 2014. doi: 10.1088/0004-637X/794/1/46.

[27] D. Caprioli, P. Blasi, E. Amato, and M. Vietri. Dynamical Effects of Self-Generated Magnetic Fields in Cosmic-Ray-modified Shocks. *ApJl*, 679(2):L139, June 2008. doi: 10.1086/589505.

[28] D. Caprioli, P. Blasi, E. Amato, and M. Vietri. Dynamical feedback of self-generated magnetic fields in cosmic ray modified shocks. *MNRAS*, 395(2):895–906, May 2009. doi: 10.1111/j.1365-2966.2009.14570.x.

[29] T. K. Chan, D. Kereš, P. F. Hopkins, E. Quataert, K. Y. Su, C. C. Hayward, and C. A. Faucher-Giguère. Cosmic ray feedback in the FIRE simulations: constraining cosmic ray propagation with GeV γ-ray emission. *MNRAS*, 488 (3):3716–3744, September 2019. doi: 10.1093/mnras/stz1895.

[30] T. K. Chan, D. Kereš, P. F. Hopkins, E. Quataert, K. Y. Su, C. C. Hayward, and C. A. Faucher-Giguère. Cosmic ray feedback in the FIRE simulations: constraining cosmic ray propagation with GeV γ-ray emission. *MNRAS*, 488 (3):3716–3744, September 2019. doi: 10.1093/mnras/stz1895.

[31] T. K. Chan, Dušan Kereš, Alexander B. Gurvich, Philip F. Hopkins, Cameron Trapp, Suoqing Ji, and Claude-André Faucher-Giguère. The impact of cosmic rays on dynamical balance and disc-halo interaction in L$\star$ disc galaxies. *MNRAS*, 517(1):597–615, November 2022. doi: 10.1093/mnras/stac2236.

[32] Zirui Chen, Drummond B. Fielding, and Greg L. Bryan. The Anatomy of a Turbulent Radiative Mixing Layer: Insights from an Analytic Model with Turbulent Conduction and Viscosity. *arXiv e-prints*, art. arXiv:2211.01395, November 2022. doi: 10.48550/arXiv.2211.01395.

[33] John Chisholm, Christy A. Tremonti, Claus Leitherer, and Yanmei Chen. The mass and momentum outflow rates of photoionized galactic outflows. *MNRAS*, 469(4):4831–4849, August 2017. doi: 10.1093/mnras/stx1164.

[34] Prakriti Pal Choudhury, Prateek Sharma, and Eliot Quataert. Multiphase gas in the circumgalactic medium: relative role of t_{cool}/t_{ff} and density fluctuations. *MNRAS*, 488(3):3195–3210, September 2019. doi: 10.1093/mnras/stz1857.

[35] Roland M. Crocker, Mark R. Krumholz, and Todd A. Thompson. Cosmic rays across the star-forming galaxy sequence - I. Cosmic ray pressures and calorimetry. *MNRAS*, 502(1):1312–1333, March 2021. doi: 10.1093/mnras/stab148.

[36] Roland M. Crocker, Mark R. Krumholz, and Todd A. Thompson. Cosmic rays across the star-forming galaxy sequence. II: Stability limits and the onset of cosmic ray-driven outflows. *MNRAS*, February 2021. doi: 10.1093/mnras/stab502.

[37] Megan Donahue and G. Mark Voit. Baryon cycles in the biggest galaxies. *PhysRep*, 973:1–109, August 2022. doi: 10.1016/j.physrep.2022.04.005.

[38] D. J. Donohue and G. P. Zank. Steady state and dynamical structure of a cosmic-ray-modified termination shock. *JGR*, 98(A11):19005–19026, November 1993. doi: 10.1029/93JA01948.

[39] E. A. Dorfi and L. O. Drury. a Cosmic Ray Driven Instability. In *19th International Cosmic Ray Conference (ICRC19), Volume 3*, volume 3 of *International Cosmic Ray Conference*, page 121, August 1985.

[40] L. O. Drury and S. A. E. G. Falle. On the Stability of Shocks Modified by Particle Acceleration. *MNRAS*, 223:353, November 1986. doi: 10.1093/mnras/223.2.353.

[41] L. O'C. Drury. Reaction effects in diffusive shock acceleration. *Advances in Space Research*, 4(2-3):185–191, January 1984. doi: 10.1016/0273-1177(84)90311-9.

[42] L. O'C. Drury and T. P. Downes. Turbulent magnetic field amplification driven by cosmic ray pressure gradients. *MNRAS*, 427(3):2308–2313, December 2012. doi: 10.1111/j.1365-2966.2012.22106.x.

[43] L. O'C. Drury and J. H. Voelk. Hydromagnetic shock structure in the presence of cosmic rays. *ApJ*, 248:344–351, August 1981. doi: 10.1086/159159.

[44] Yohan Dubois and Benoît Commerçon. An implicit scheme for solving the anisotropic diffusion of heat and cosmic rays in the RAMSES code. *AAP*, 585: A138, January 2016. doi: 10.1051/0004-6361/201527126.

[45] Yohan Dubois, Benoît Commerçon, Alexand re Marcowith, and Loann Brahimi. Shock-accelerated cosmic rays and streaming instability in the adaptive mesh refinement code Ramses. *AAP*, 631:A121, November 2019. doi: 10.1051/0004-6361/201936275.

[46] P. Duffy, L. O'C. Drury, and H. Voelk. Cosmic ray hydrodynamics at shock fronts. *AAP*, 291:613–621, November 1994.

[47] D. Eichler. Particle acceleration in collisionless shocks: regulated injection and high efficiency. *ApJ*, 229:419–423, April 1979. doi: 10.1086/156969.

[48] D. C. Ellison and D. Eichler. Monte Carlo shock-like solutions to the Boltzmann equation with collective scattering. *ApJ*, 286:691–701, November 1984. doi: 10.1086/162644.

[49] Clarke J. Esmerian, Andrey V. Kravtsov, Zachary Hafen, Claude-André Faucher-Giguère, Eliot Quataert, Jonathan Stern, Dušan Kereš, and Andrew Wetzel. Thermal instability in the CGM of $L_\star$ galaxies: testing 'precipitation' models with the FIRE simulations. *MNRAS*, 505(2):1841–1862, August 2021. doi: 10.1093/mnras/stab1281.

[50] S. A. E. G. Falle and J. R. Giddings. Time-dependent cosmic ray modified shocks. *MNRAS*, 225:399–423, March 1987. doi: 10.1093/mnras/225.2.399.

[51] R. Farber, M. Ruszkowski, H. Y. K. Yang, and E. G. Zweibel. Impact of Cosmic-Ray Transport on Galactic Winds. *ApJ*, 856(2):112, April 2018. doi: 10.3847/1538-4357/aab26d.

[52] Alison J. Farmer and Peter Goldreich. Wave Damping by Magnetohydrodynamic Turbulence and Its Effect on Cosmic-Ray Propagation in the Interstellar Medium. *ApJ*, 604(2):671–674, April 2004. doi: 10.1086/382040.

[53] G. B. Field, D. W. Goldsmith, and H. J. Habing. Cosmic-Ray Heating of the Interstellar Gas. *ApJL*, 155:L149, March 1969. doi: 10.1086/180324.

[54] George B. Field. Thermal Instability. *ApJ*, 142:531, August 1965. doi: 10.1086/148317.

[55] Drummond B. Fielding and Greg L. Bryan. The Structure of Multiphase Galactic Winds. *ApJ*, 924(2):82, January 2022. doi: 10.3847/1538-4357/ac2f41.

[56] Adam Frank, T. W. Jones, and Dongsu Ryu. Oblique Magnetohydrodynamic Cosmic-Ray–modified Shocks: Two-Fluid Numerical Simulations. *ApJS*, 90:975, February 1994. doi: 10.1086/191935.

[57] Akimi Fujita, Crystal L. Martin, Mordecai-Mark Mac Low, Kimberly C. B. New, and Robert Weaver. The Origin and Kinematics of Cold Gas in Galactic Winds: Insight from Numerical Simulations. *ApJ*, 698(1):693–714, June 2009. doi: 10.1088/0004-637X/698/1/693.

[58] Philipp Girichidis, Thorsten Naab, Stefanie Walch, Michał Hanasz, Mordecai-Mark Mac Low, Jeremiah P. Ostriker, Andrea Gatto, Thomas Peters, Richard Wünsch, Simon C. O. Glover, Ralf S. Klessen, Paul C. Clark, and Christian

Baczynski. Launching Cosmic-Ray-driven Outflows from the Magnetized Interstellar Medium. *ApJL*, 816(2):L19, January 2016. doi: 10.3847/2041-8205/816/2/L19.

[59] Max Gronke and S. Peng Oh. How cold gas continuously entrains mass and momentum from a hot wind. *MNRAS*, 492(2):1970–1990, February 2020. doi: 10.1093/mnras/stz3332.

[60] Max Gronke and S. Peng Oh. Is multiphase gas cloudy or misty? *MNRAS*, 494(1):L27–L31, May 2020. doi: 10.1093/mnrasl/slaa033.

[61] Fulai Guo, S. Peng Oh, and M. Ruszkowski. A Global Stability Analysis of Clusters of Galaxies with Conduction and AGN Feedback Heating. *ApJ*, 688(2):859–874, December 2008. doi: 10.1086/592320.

[62] Siddhartha Gupta, Biman B. Nath, Prateek Sharma, and David Eichler. Lack of thermal energy in superbubbles: hint of cosmic rays? *MNRAS*, 473(2):1537–1553, January 2018. doi: 10.1093/mnras/stx2427.

[63] Siddhartha Gupta, Prateek Sharma, and Andrea Mignone. Non-uniqueness of cosmic ray two-fluid equations at shocks and possible remedies. *arXiv e-prints*, art. arXiv:1906.07200, June 2019.

[64] Colby C. Haggerty and Damiano Caprioli. Kinetic Simulations of Cosmic-Ray-modified Shocks. I. Hydrodynamics. *ApJ*, 905(1):1, December 2020. doi: 10.3847/1538-4357/abbe06.

[65] M. Hanasz, H. Lesch, T. Naab, A. Gawryszczak, K. Kowalik, and D. Wółtański. Cosmic Rays Can Drive Strong Outflows from Gas-rich High-redshift Disk Galaxies. *ApJL*, 777(2):L38, November 2013. doi: 10.1088/2041-8205/777/2/L38.

[66] Evan Heintz and Ellen G. Zweibel. The Parker Instability with Cosmic-Ray Streaming. *ApJ*, 860(2):97, June 2018. doi: 10.3847/1538-4357/aac208.

[67] Evan Heintz, Chad Bustard, and Ellen G. Zweibel. The Role of the Parker Instability in Structuring the Interstellar Medium. *ApJ*, 891(2):157, March 2020. doi: 10.3847/1538-4357/ab7453.

[68] Tsun Hin Navin Tsung, S. Peng Oh, and Yan-Fei Jiang. Fluid Simulations of Cosmic Ray Modified Shocks. *arXiv e-prints*, art. arXiv:2008.10537, August 2020.

[69] Cole Holcomb and Anatoly Spitkovsky. On the Growth and Saturation of the Gyroresonant Streaming Instabilities. *ApJ*, 882(1):3, September 2019. doi: 10.3847/1538-4357/ab328a.

[70] F. Holguin, M. Ruszkowski, A. Lazarian, R. Farber, and H. Y. K. Yang. Role of cosmic-ray streaming and turbulent damping in driving galactic winds. *MNRAS*, 490(1):1271–1282, November 2019. doi: 10.1093/mnras/stz2568.

[71] Philip F. Hopkins, T. K. Chan, Shea Garrison-Kimmel, Suoqing Ji, Kung-Yi Su, Cameron B. Hummels, Dušan Kereš, Eliot Quataert, and Claude-André

Faucher-Giguère. But what about...: cosmic rays, magnetic fields, conduction, and viscosity in galaxy formation. *MNRAS*, 492(3):3465–3498, March 2020. doi: 10.1093/mnras/stz3321.

[72] Philip F. Hopkins, Iryna S. Butsky, Georgia V. Panopoulou, Suoqing Ji, Eliot Quataert, Claude-Andre Faucher-Giguere, and Dusan Keres. First Predicted Cosmic Ray Spectra, Primary-to-Secondary Ratios, and Ionization Rates from MHD Galaxy Formation Simulations. *arXiv e-prints*, art. arXiv:2109.09762, September 2021.

[73] Philip F. Hopkins, T. K. Chan, Suoqing Ji, Cameron B. Hummels, Dušan Kereš, Eliot Quataert, and Claude-André Faucher-Giguère. Cosmic ray driven outflows to Mpc scales from L_* galaxies. *MNRAS*, 501(3):3640–3662, March 2021. doi: 10.1093/mnras/staa3690.

[74] Philip F. Hopkins, T. K. Chan, Suoqing Ji, Cameron B. Hummels, Dušan Kereš, Eliot Quataert, and Claude-André Faucher-Giguère. Cosmic ray driven outflows to Mpc scales from L_* galaxies. *MNRAS*, 501(3):3640–3662, March 2021. doi: 10.1093/mnras/staa3690.

[75] Philip F. Hopkins, T. K. Chan, Jonathan Squire, Eliot Quataert, Suoqing Ji, Dušan Kereš, and Claude-André Faucher-Giguère. Effects of different cosmic ray transport models on galaxy formation. *MNRAS*, 501(3):3663–3669, March 2021. doi: 10.1093/mnras/staa3692.

[76] Philip F. Hopkins, T. K. Chan, Jonathan Squire, Eliot Quataert, Suoqing Ji, Dušan Kereš, and Claude-André Faucher-Giguère. Effects of different cosmic ray transport models on galaxy formation. *MNRAS*, 501(3):3663–3669, March 2021. doi: 10.1093/mnras/staa3692.

[77] Philip F. Hopkins, Jonathan Squire, and Iryna S. Butsky. A Consistent Reduced-Speed-of-Light Formulation of Cosmic Ray Transport Valid in Weak and Strong-Scattering Regimes. *arXiv e-prints*, art. arXiv:2103.10443, March 2021.

[78] Philip F. Hopkins, Jonathan Squire, and Iryna S. Butsky. A consistent Reduced-Speed-of-Light formulation of Cosmic Ray transport valid in weak and strong-scattering regimes. *MNRAS*, October 2021. doi: 10.1093/mnras/stab2635.

[79] Philip F. Hopkins, Jonathan Squire, T. K. Chan, Eliot Quataert, Suoqing Ji, Dušan Kereš, and Claude-André Faucher-Giguère. Testing physical models for cosmic ray transport coefficients on galactic scales: self-confinement and extrinsic turbulence at ∼GeV energies. *MNRAS*, 501(3):4184–4213, March 2021. doi: 10.1093/mnras/staa3691.

[80] Philip F. Hopkins, Jonathan Squire, Iryna S. Butsky, and Suoqing Ji. Standard self-confinement and extrinsic turbulence models for cosmic ray transport are fundamentally incompatible with observations. *MNRAS*, 517(4):5413–5448, December 2022. doi: 10.1093/mnras/stac2909.

[81] Philip F. Hopkins, Jonathan Squire, Iryna S. Butsky, and Suoqing Ji. Standard self-confinement and extrinsic turbulence models for cosmic ray transport

are fundamentally incompatible with observations. *MNRAS*, 517(4):5413–5448, December 2022. doi: 10.1093/mnras/stac2909.

[82] Xiaoshan Huang and Shane W. Davis. The launching of cosmic ray driven outflows, 2021.

[83] Xiaoshan Huang and Shane W. Davis. The launching of cosmic ray-driven outflows. *MNRAS*, 511(4):5125–5141, April 2022. doi: 10.1093/mnras/stac059.

[84] Xiaoshan Huang, Yan-fei Jiang, and Shane W. Davis. Cosmic-Ray-driven Multiphase Gas Formed via Thermal Instability. *ApJ*, 931(2):140, June 2022. doi: 10.3847/1538-4357/ac69dc.

[85] F. M. Ipavich. Galactic winds driven by cosmic rays. *ApJ*, 196:107–120, February 1975. doi: 10.1086/153397.

[86] Svenja Jacob and Christoph Pfrommer. Cosmic ray heating in cool core clusters - II. Self-regulation cycle and non-thermal emission. *MNRAS*, 467(2):1478–1495, May 2017. doi: 10.1093/mnras/stx132.

[87] Suoqing Ji, S. Peng Oh, and Michael McCourt. The impact of magnetic fields on thermal instability. *MNRAS*, 476(1):852–867, May 2018. doi: 10.1093/mnras/sty293.

[88] Suoqing Ji, T. K. Chan, Cameron B. Hummels, Philip F. Hopkins, Jonathan Stern, Dušan Kereš, Eliot Quataert, Claude-André Faucher-Giguère, and Norman Murray. Properties of the circumgalactic medium in cosmic ray-dominated

galaxy haloes. *MNRAS*, 496(4):4221–4238, June 2020. doi: 10.1093/mnras/staa1849.

[89] Suoqing Ji, T. K. Chan, Cameron B. Hummels, Philip F. Hopkins, Jonathan Stern, Dušan Kereš, Eliot Quataert, Claude-André Faucher-Giguère, and Norman Murray. Properties of the circumgalactic medium in cosmic ray-dominated galaxy haloes. *MNRAS*, 496(4):4221–4238, August 2020. doi: 10.1093/mnras/staa1849.

[90] Suoqing Ji, T. K. Chan, Cameron B. Hummels, Philip F. Hopkins, Jonathan Stern, Dušan Kereš, Eliot Quataert, Claude-André Faucher-Giguère, and Norman Murray. Properties of the circumgalactic medium in cosmic ray-dominated galaxy haloes. *MNRAS*, 496(4):4221–4238, August 2020. doi: 10.1093/mnras/staa1849.

[91] Suoqing Ji, Dušan Kereš, T. K. Chan, Jonathan Stern, Cameron B. Hummels, Philip F. Hopkins, Eliot Quataert, and Claude-André Faucher-Giguère. Virial shocks are suppressed in cosmic ray-dominated galaxy haloes. *MNRAS*, 505(1):259–273, July 2021. doi: 10.1093/mnras/stab1264.

[92] Yan-Fei Jiang and S. Peng Oh. A New Numerical Scheme for Cosmic-Ray Transport. *ApJ*, 854(1):5, February 2018. doi: 10.3847/1538-4357/aaa6ce.

[93] Yan-Fei Jiang and S. Peng Oh. A New Numerical Scheme for Cosmic-Ray Transport. *ApJ*, 854(1):5, February 2018. doi: 10.3847/1538-4357/aaa6ce.

[94] Frank C. Jones and Donald C. Ellison. The plasma physics of shock acceleration. *SSR*, 58(1):259–346, December 1991. doi: 10.1007/BF01206003.

[95] Thomas W. Jones and Hyesung Kang. Time-dependent Evolution of Cosmic-Ray–mediated Shocks in the Two-Fluid Model. *ApJ*, 363:499, November 1990. doi: 10.1086/169361.

[96] M. Jubelgas, V. Springel, T. Enßlin, and C. Pfrommer. Cosmic ray feedback in hydrodynamical simulations of galaxy formation. *AAP*, 481(1):33–63, April 2008. doi: 10.1051/0004-6361:20065295.

[97] Byung-Il Jun and T. W. Jones. The Density Spike in Cosmic-Ray-Modified Shocks: Formation, Evolution, and Instability. *ApJ*, 481(1):253–262, May 1997. doi: 10.1086/304030.

[98] Hyesung Kang. Diffusive Shock Acceleration by Multiple Weak Shocks. *arXiv e-prints*, art. arXiv:2106.08521, June 2021.

[99] Hyesung Kang and T. W. Jones. Diffusive Cosmic-Ray Acceleration: Two-Fluid Models with In Situ Injection. *ApJ*, 353:149, April 1990. doi: 10.1086/168601.

[100] Hyesung Kang, T. W. Jones, and Dongsu Ryu. Acoustic Instability in Cosmic-Ray Mediated Shocks. *ApJ*, 385:193, January 1992. doi: 10.1086/170927.

[101] Philipp Kempski and Eliot Quataert. Thermal instability of halo gas heated by streaming cosmic rays. *MNRAS*, 493(2):1801–1817, April 2020. doi: 10.1093/mnras/staa385.

[102] Philipp Kempski and Eliot Quataert. Thermal instability of halo gas heated by streaming cosmic rays. *MNRAS*, 493(2):1801–1817, April 2020. doi: 10.1093/mnras/staa385.

[103] Philipp Kempski and Eliot Quataert. Reconciling cosmic ray transport theory with phenomenological models motivated by Milky-Way data. *MNRAS*, 514(1):657–674, July 2022. doi: 10.1093/mnras/stac1240.

[104] G. F. Krymskii. A regular mechanism for the acceleration of charged particles on the front of a shock wave. *Soviet Physics Doklady*, 22:327, June 1977.

[105] Yuki Kudoh and Tomoyuki Hanawa. Approximate Riemann solvers for the cosmic ray magnetohydrodynamical equations. *MNRAS*, 462(4):4517–4531, November 2016. doi: 10.1093/mnras/stw1937.

[106] Russell Kulsrud and William P. Pearce. The Effect of Wave-Particle Interactions on the Propagation of Cosmic Rays. *ApJ*, 156:445, May 1969. doi: 10.1086/149981.

[107] Russell Kulsrud and William P. Pearce. The Effect of Wave-Particle Interactions on the Propagation of Cosmic Rays. *ApJ*, 156:445, May 1969. doi: 10.1086/149981.

[108] Takuhito Kuwabara and Chung-Ming Ko. Analysis of Magnetorotational Instability with the Effect of Cosmic-Ray Diffusion. *ApJ*, 798(2):79, January 2015. doi: 10.1088/0004-637X/798/2/79.

[109] Miao Li and Greg L. Bryan. Simple Yet Powerful: Hot Galactic Outflows Driven by Supernovae. *ApJL*, 890(2):L30, February 2020. doi: 10.3847/2041-8213/ab7304.

[110] Jean-Pierre Macquart and Jun Yi Koay. Temporal Smearing of Transient Radio Sources by the Intergalactic Medium. *ApJ*, 776(2):125, October 2013. doi: 10.1088/0004-637X/776/2/125.

[111] M. A. Malkov. Bifurcation, Efficiency, and the Role of Injection in Shock Acceleration with the Bohm Diffusion. *ApJ*, 491(2):584–595, December 1997. doi: 10.1086/304990.

[112] S. Alwin Mao and Eve C. Ostriker. Galactic Disk Winds Driven by Cosmic Ray Pressure. *ApJ*, 854(2):89, February 2018. doi: 10.3847/1538-4357/aaa88e.

[113] S. Alwin Mao and Eve C. Ostriker. Galactic Disk Winds Driven by Cosmic Ray Pressure. *ApJ*, 854(2):89, February 2018. doi: 10.3847/1538-4357/aaa88e.

[114] Antonino Marasco, Filippo Fraternali, Nicolas Lehner, and J. Christopher Howk. Intermediate- and high-velocity clouds in the Milky Way - II. Evidence for a Galactic fountain with collimated outflows and diffuse inflows. *MNRAS*, 515 (3):4176–4190, September 2022. doi: 10.1093/mnras/stac1172.

[115] Michael McCourt, Prateek Sharma, Eliot Quataert, and Ian J. Parrish. Thermal instability in gravitationally stratified plasmas: implications for multiphase structure in clusters and galaxy haloes. *MNRAS*, 419(4):3319–3337, February 2012. doi: 10.1111/j.1365-2966.2011.19972.x.

[116] Michael McCourt, S. Peng Oh, Ryan O'Leary, and Ann-Marie Madigan. A characteristic scale for cold gas. *MNRAS*, 473(4):5407–5431, February 2018. doi: 10.1093/mnras/stx2687.

[117] Michael McCourt, S. Peng Oh, Ryan O'Leary, and Ann-Marie Madigan. A characteristic scale for cold gas. *MNRAS*, 473(4):5407–5431, February 2018. doi: 10.1093/mnras/stx2687.

[118] Philipp Mertsch. Test particle simulations of cosmic rays. *APSS*, 365(8):135, August 2020. doi: 10.1007/s10509-020-03832-3.

[119] Shaunak Modak, Eliot Quataert, Yan-Fei Jiang, and Todd A. Thompson. Cosmic-Ray Driven Galactic Winds from the Warm Interstellar Medium. *arXiv e-prints*, art. arXiv:2302.03701, February 2023. doi: 10.48550/arXiv.2302.03701.

[120] M. Mond and L. O'C. Drury. Acoustic emission and corrugational instability of shocks modified by strong particle acceleration. *AAP*, 332:385–390, April 1998.

[121] G. Morlino, E. Amato, P. Blasi, and D. Caprioli. Spatial structure of X-ray filaments in SN 1006. *MNRAS*, 405(1):L21–L25, June 2010. doi: 10.1111/j.1745-3933.2010.00851.x.

[122] Norman Murray, Brice Ménard, and Todd A. Thompson. Radiation Pressure from Massive Star Clusters as a Launching Mechanism for Super-galactic Winds. *ApJ*, 735(1):66, July 2011. doi: 10.1088/0004-637X/735/1/66.

[123] Dylan Nelson, Prateek Sharma, Annalisa Pillepich, Volker Springel, Rüdiger Pakmor, Rainer Weinberger, Mark Vogelsberger, Federico Marinacci, and Lars Hernquist. Resolving small-scale cold circumgalactic gas in TNG50. *MNRAS*, 498(2):2391–2414, October 2020. doi: 10.1093/mnras/staa2419.

[124] R. Pakmor, C. Pfrommer, C. M. Simpson, and V. Springel. Galactic Winds Driven by Isotropic and Anisotropic Cosmic-Ray Diffusion in Disk Galaxies. *ApJL*, 824(2):L30, June 2016. doi: 10.3847/2041-8205/824/2/L30.

[125] Rüdiger Pakmor, Freeke van de Voort, Rebekka Bieri, Facundo A. Gómez, Robert J. J. Grand, Thomas Guillet, Federico Marinacci, Christoph Pfrommer, Christine M. Simpson, and Volker Springel. Magnetizing the circumgalactic medium of disc galaxies. *MNRAS*, 498(3):3125–3137, November 2020. doi: 10.1093/mnras/staa2530.

[126] C. Pfrommer, V. Springel, T. A. Enßlin, and M. Jubelgas. Detecting shock waves in cosmological smoothed particle hydrodynamics simulations. *MNRAS*, 367(1):113–131, March 2006. doi: 10.1111/j.1365-2966.2005.09953.x.

[127] C. Pfrommer, R. Pakmor, K. Schaal, C. M. Simpson, and V. Springel. Simulating cosmic ray physics on a moving mesh. *MNRAS*, 465(4):4500–4529, March 2017. doi: 10.1093/mnras/stw2941.

[128] Anders Pinzke, S. Peng Oh, and Christoph Pfrommer. Giant radio relics in galaxy clusters: reacceleration of fossil relativistic electrons? *MNRAS*, 435(2): 1061–1082, October 2013. doi: 10.1093/mnras/stt1308.

[129] J. Xavier Prochaska, Jean-Pierre Macquart, Matthew McQuinn, Sunil Simha, Ryan M. Shannon, Cherie K. Day, Lachlan Marnoch, Stuart Ryder, Adam Deller, Keith W. Bannister, Shivani Bhandari, Rongmon Bordoloi, John Bunton, Hyerin Cho, Chris Flynn, Elizabeth K. Mahony, Chris Phillips, Hao Qiu, and Nicolas Tejos. The low density and magnetization of a massive galaxy halo exposed by a fast radio burst. *Science*, 366(6462):231–234, October 2019. doi: 10.1126/science.aay0073.

[130] V. S. Ptuskin. Influence of cosmic rays on propagation of long magnetohydrodynamic waves. *ApSS*, 76(2):265–278, May 1981. doi: 10.1007/BF00687494.

[131] Eliot Quataert, Yan-Fei Jiang, and Todd A. Thompson. The Physics of Galactic Winds Driven by Cosmic Rays II: Isothermal Streaming Solutions. *arXiv e-prints*, art. arXiv:2106.08404, June 2021.

[132] Eliot Quataert, Todd A. Thompson, and Yan-Fei Jiang. The Physics of Galactic Winds Driven by Cosmic Rays I: Diffusion. *arXiv e-prints*, art. arXiv:2102.05696, February 2021.

[133] Eliot Quataert, Fei Jiang, and Todd A. Thompson. The physics of galactic winds driven by cosmic rays - II. Isothermal streaming solutions. *MNRAS*, 510 (1):920–945, February 2022. doi: 10.1093/mnras/stab3274.

[134] Eliot Quataert, Yan-Fei Jiang, and Todd A. Thompson. The physics of galactic winds driven by cosmic rays - II. Isothermal streaming solutions. *MNRAS*, 510 (1):920–945, February 2022. doi: 10.1093/mnras/stab3274.

[135] Eliot Quataert, Todd A. Thompson, and Yan-Fei Jiang. The physics of galactic winds driven by cosmic rays I: Diffusion. *MNRAS*, 510(1):1184–1203, February 2022. doi: 10.1093/mnras/stab3273.

[136] Eliot Quataert, Todd A. Thompson, and Yan-Fei Jiang. The physics of galactic winds driven by cosmic rays I: Diffusion. *MNRAS*, 510(1):1184–1203, February 2022. doi: 10.1093/mnras/stab3273.

[137] Timour Radko. Mechanics of merging events for a series of layers in a stratified turbulent fluid. *Journal of Fluid Mechanics*, 577:251, April 2007. doi: 10.1017/S0022112007004703.

[138] L. F. S. Rodrigues, G. R. Sarson, A. Shukurov, P. J. Bushby, and A. Fletcher. The Parker Instability in Disk Galaxies. *ApJ*, 816(1):2, January 2016. doi: 10.3847/0004-637X/816/1/2.

[139] Mateusz Ruszkowski, H. Y. Karen Yang, and Christopher S. Reynolds. Cosmic-Ray Feedback Heating of the Intracluster Medium. *ApJ*, 844(1):13, July 2017. doi: 10.3847/1538-4357/aa79f8.

[140] Mateusz Ruszkowski, H. Y. Karen Yang, and Ellen Zweibel. Global Simulations of Galactic Winds Including Cosmic-ray Streaming. *ApJ*, 834(2):208, January 2017. doi: 10.3847/1538-4357/834/2/208.

[141] Mateusz Ruszkowski, H. Y. Karen Yang, and Ellen Zweibel. Global Simulations of Galactic Winds Including Cosmic-ray Streaming. *ApJ*, 834(2):208, January 2017. doi: 10.3847/1538-4357/834/2/208.

[142] Dongsu Ryu, Hyesung Kang, and T. W. Jones. The Stability of Cosmic-Ray–dominated Shocks: A Secondary Instability. *ApJ*, 405:199, March 1993. doi: 10.1086/172353.

[143] Dongsu Ryu, Jongsoo Kim, Seung Soo Hong, and T. W. Jones. The Effect of Cosmic-Ray Diffusion on the Parker Instability. *ApJ*, 589(1):338–346, May 2003. doi: 10.1086/374392.

[144] Tatsuhiko Saito, Masahiro Hoshino, and Takanobu Amano. Stability of Cosmic-Ray Modified Shocks: Two-fluid Approach. *ApJ*, 775(2):130, October 2013. doi: 10.1088/0004-637X/775/2/130.

[145] Munier Salem and Greg L. Bryan. Cosmic ray driven outflows in global galaxy disc models. *MNRAS*, 437(4):3312–3330, February 2014. doi: 10.1093/mnras/stt2121.

[146] Munier Salem and Greg L. Bryan. Cosmic ray driven outflows in global galaxy disc models. *MNRAS*, 437(4):3312–3330, February 2014. doi: 10.1093/mnras/stt2121.

[147] Edwin E. Salpeter. The Luminosity Function and Stellar Evolution. *ApJ*, 121:161, January 1955. doi: 10.1086/145971.

[148] Matt L. Sampson, James R. Beattie, Mark R. Krumholz, Roland M. Crocker, Christoph Federrath, and Amit Seta. Turbulent diffusion of streaming cosmic rays in compressible, partially ionized plasma. *MNRAS*, 519(1):1503–1525, February 2023. doi: 10.1093/mnras/stac3207.

[149] Mohsen Shadmehri. Thermal instability and the effects of cosmic-ray diffusion. *MNRAS*, 397(3):1521–1527, August 2009. doi: 10.1111/j.1365-2966.2009.15047.x.

[150] Mohamad Shalaby, Timon Thomas, and Christoph Pfrommer. A New Cosmic-Ray-driven Instability. *ApJ*, 908(2):206, February 2021. doi: 10.3847/1538-4357/abd02d.

[151] P. Sharma, M. McCourt, E. Quataert, and I. J. Parrish. Thermal instability and the feedback regulation of hot haloes in clusters, groups and galaxies. *MNRAS*, 420:3174–3194, March 2012. doi: 10.1111/j.1365-2966.2011.20246.x.

[152] Prateek Sharma, Phillip Colella, and Daniel Martin. Numerical implementation of streaming down the gradient: Application to fluid modeling of cosmic rays and saturated conduction. *Siam Journal on Scientific Computing*, 32, 09 2009. doi: 10.1137/100792135.

[153] Prateek Sharma, Phillip Colella, and Daniel F. Martin. Numerical Implementation of Streaming Down the Gradient: Application to Fluid Modeling of Cosmic Rays and Saturated Conduction. *arXiv e-prints*, art. arXiv:0909.5426, September 2009.

[154] Christine M. Simpson, Rüdiger Pakmor, Federico Marinacci, Christoph Pfrommer, Volker Springel, Simon C. O. Glover, Paul C. Clark, and Rowan J. Smith. The Role of Cosmic-Ray Pressure in Accelerating Galactic Outflows. *ApJL*, 827 (2):L29, August 2016. doi: 10.3847/2041-8205/827/2/L29.

[155] J. Skilling. Cosmic ray streaming - I. Effect of Alfvén waves on particles. *MNRAS*, 172:557–566, September 1975. doi: 10.1093/mnras/172.3.557.

[156] John Skilling. Cosmic Rays in the Galaxy: Convection or Diffusion? *ApJ*, 170: 265, December 1971. doi: 10.1086/151210.

[157] J. Smak. Outbursts of dwarf novae. *PASP*, 96:5–18, January 1984. doi: 10.1086/131295.

[158] Martin Sparre, Christoph Pfrommer, and Kristian Ehlert. Interaction of a cold cloud with a hot wind: the regimes of cloud growth and destruction and the impact of magnetic fields. *MNRAS*, 499(3):4261–4281, December 2020. doi: 10.1093/mnras/staa3177.

[159] Jonathan Squire, Philip F. Hopkins, Eliot Quataert, and Philipp Kempski. The impact of astrophysical dust grains on the confinement of cosmic rays. *MNRAS*, 502(2):2630–2644, April 2021. doi: 10.1093/mnras/stab179.

[160] James M. Stone, Kengo Tomida, Christopher J. White, and Kyle G. Felker. The Athena++ Adaptive Mesh Refinement Framework: Design and Magnetohydrodynamic Solvers. *ApJS*, 249(1):4, July 2020. doi: 10.3847/1538-4365/ab929b.

[161] James M. Stone, Kengo Tomida, Christopher J. White, and Kyle G. Felker. The Athena++ Adaptive Mesh Refinement Framework: Design and Magnetohydrodynamic Solvers. *ApJS*, 249(1):4, July 2020. doi: 10.3847/1538-4365/ab929b.

[162] Akihiro Suzuki, Hiroyuki R. Takahashi, and Takahiro Kudoh. Linear Growth of the Kelvin-Helmholtz instability with an Adiabatic Cosmic-Ray Gas. *ApJ*, 787(2):169, June 2014. doi: 10.1088/0004-637X/787/2/169.

[163] Brent Tan and S. Peng Oh. A model for line absorption and emission from turbulent mixing layers. *MNRAS*, 508(1):L37–L42, November 2021. doi: 10.1093/mnrasl/slab100.

[164] Brent Tan, S. Peng Oh, and Max Gronke. Radiative mixing layers: insights from turbulent combustion. *MNRAS*, 502(3):3179–3199, April 2021. doi: 10.1093/mnras/stab053.

[165] T. Thomas and C. Pfrommer. Cosmic-ray hydrodynamics: Alfvén-wave regulated transport of cosmic rays. *MNRAS*, 485(3):2977–3008, May 2019. doi: 10.1093/mnras/stz263.

[166] Timon Thomas, Christoph Pfrommer, and Torsten Enßlin. Probing Cosmic-Ray Transport with Radio Synchrotron Harps in the Galactic Center. *ApJL*, 890(2):L18, February 2020. doi: 10.3847/2041-8213/ab7237.

[167] Timon Thomas, Christoph Pfrommer, and Rüdiger Pakmor. Cosmic ray-driven galactic winds: transport modes of cosmic rays and Alfvén-wave dark regions.

arXiv e-prints, art. arXiv:2203.12029, March 2022. doi: 10.48550/arXiv.2203.12029.

[168] Tsun Hin Navin Tsung, S. Peng Oh, and Yan-Fei Jiang. Fluid simulations of cosmic ray-modified shocks. *MNRAS*, 506(3):3282–3300, September 2021. doi: 10.1093/mnras/stab1926.

[169] Tsun Hin Navin Tsung, S. Peng Oh, and Yan-Fei Jiang. The cosmic-ray staircase: the outcome of the cosmic-ray acoustic instability. *MNRAS*, 513(3):4464–4493, July 2022. doi: 10.1093/mnras/stac1123.

[170] Jason Tumlinson, Molly S. Peeples, and Jessica K. Werk. The Circumgalactic Medium. *ARAA*, 55(1):389–432, August 2017. doi: 10.1146/annurev-astro-091916-055240.

[171] M. Uhlig, C. Pfrommer, M. Sharma, B. B. Nath, T. A. Enßlin, and V. Springel. Galactic winds driven by cosmic ray streaming. *MNRAS*, 423(3):2374–2396, July 2012. doi: 10.1111/j.1365-2966.2012.21045.x.

[172] M. Uhlig, C. Pfrommer, M. Sharma, B. B. Nath, T. A. Enßlin, and V. Springel. Galactic winds driven by cosmic ray streaming. *MNRAS*, 423(3):2374–2396, July 2012. doi: 10.1111/j.1365-2966.2012.21045.x.

[173] Freeke van de Voort and Joop Schaye. Properties of gas in and around galaxy haloes. *MNRAS*, 423(4):2991–3010, July 2012. doi: 10.1111/j.1365-2966.2012.20949.x.

[174] Freeke van de Voort, Rebekka Bieri, Rüdiger Pakmor, Facundo A. Gómez, Robert J. J. Grand, and Federico Marinacci. The effect of magnetic fields on properties of the circumgalactic medium. *MNRAS*, 501(4):4888–4902, March 2021. doi: 10.1093/mnras/staa3938.

[175] M. Vergassola, B. Dubrulle, U. Frisch, and A. Noullez. Burgers' equation, Devil's staircases and the mass distribution for large-scale structures. *AAP*, 289:325–356, September 1994.

[176] H. J. Voelk, L. O'C. Drury, and J. F. McKenzie. Hydrodynamic estimates of cosmic ray acceleration efficiencies in shock waves. *AAP*, 130(1):19–28, January 1984.

[177] A. Y. Wagner and G. V. Bicknell. Relativistic Jet Feedback in Evolving Galaxies. *ApJ*, 728(1):29, February 2011. doi: 10.1088/0004-637X/728/1/29.

[178] A. Y. Wagner, S. A. E. G. Falle, T. W. Hartquist, and J. M. Pittard. Two-fluid models of cosmic ray modified radiative shocks. *AAP*, 452(3):763–771, June 2006. doi: 10.1051/0004-6361:20064885.

[179] Chaoran Wang, Mateusz Ruszkowski, and H. Y. Karen Yang. Chaotic cold accretion in giant elliptical galaxies heated by AGN cosmic rays. *MNRAS*, 493 (3):4065–4076, April 2020. doi: 10.1093/mnras/staa550.

[180] G. M. Webb, L. O'C. Drury, and H. J. Volk. Cosmic-ray shock acceleration in oblique MHD shocks. *AAP*, 160(2):335–346, May 1986.

[181] Joshua Wiener, S. Peng Oh, and Fulai Guo. Cosmic ray streaming in clusters of galaxies. *MNRAS*, 434(3):2209–2228, September 2013. doi: 10.1093/mnras/stt1163.

[182] Joshua Wiener, S. Peng Oh, and Fulai Guo. Cosmic ray streaming in clusters of galaxies. *MNRAS*, 434(3):2209–2228, September 2013. doi: 10.1093/mnras/stt1163.

[183] Joshua Wiener, S. Peng Oh, and Ellen G. Zweibel. Interaction of cosmic rays with cold clouds in galactic haloes. *MNRAS*, 467(1):646–660, May 2017. doi: 10.1093/mnras/stx109.

[184] Joshua Wiener, S. Peng Oh, and Ellen G. Zweibel. Interaction of cosmic rays with cold clouds in galactic haloes. *MNRAS*, 467(1):646–660, May 2017. doi: 10.1093/mnras/stx109.

[185] Joshua Wiener, Christoph Pfrommer, and S. Peng Oh. Cosmic ray-driven galactic winds: streaming or diffusion? *MNRAS*, 467(1):906–921, May 2017. doi: 10.1093/mnras/stx127.

[186] Huirong Yan and A. Lazarian. Scattering of Cosmic Rays by Magnetohydrodynamic Interstellar Turbulence. *PRL*, 89(28):281102, December 2002. doi: 10.1103/PhysRevLett.89.281102.

[187] Huirong Yan and A. Lazarian. Scattering of Cosmic Rays by Magnetohydrodynamic Interstellar Turbulence. *PRL*, 89(28):281102, December 2002. doi: 10.1103/PhysRevLett.89.281102.

[188] H. Y. K. Yang, M. Ruszkowski, P. M. Ricker, E. Zweibel, and D. Lee. The Fermi Bubbles: Supersonic Active Galactic Nucleus Jets with Anisotropic Cosmic-Ray Diffusion. *ApJ*, 761(2):185, December 2012. doi: 10.1088/0004-637X/761/2/185.

[189] A. P. Zank and J. F. McKenzie. Instabilities in Decelerating Supersonic Flows with Applications to Cosmic Ray Shocks. In *19th International Cosmic Ray Conference (ICRC19), Volume 3*, volume 3 of *International Cosmic Ray Conference*, page 111, August 1985.

[190] Ya. B. Zel'dovich and Yu. P. Raizer. *Physics of shock waves and high-temperature hydrodynamic phenomena.* 1967.

[191] Ellen G. Zweibel. The basis for cosmic ray feedback: Written on the wind. *Physics of Plasmas*, 24(5):055402, May 2017. doi: 10.1063/1.4984017.

[192] Ellen G. Zweibel. The basis for cosmic ray feedback: Written on the wind. *Physics of Plasmas*, 24(5):055402, May 2017. doi: 10.1063/1.4984017.